

Automated Aerial Refueling of a Large Receiver Aircraft

by

Steven Cornelius Kriel



*Dissertation presented for the degree of Doctor of Philosophy in
Electrical and Electronic Engineering in the Faculty of Engineering at
Stellenbosch University*

Supervisor: Prof T. Jones

Co-supervisor: Mnr. J. Engelbrecht

March 2016

Declaration

By submitting this dissertation electronically, I declare that the entirety of the work contained therein is my own, original work, that I am the sole author thereof (save to the extent explicitly otherwise stated), that reproduction and publication thereof by Stellenbosch University will not infringe any third party rights and that I have not previously in its entirety or in part submitted it for obtaining any qualification.

Date:

Copyright © 2016 Stellenbosch University
All rights reserved.

Abstract

Automated Aerial Refueling of a Large Receiver Aircraft

SC Kriel

*Department of Electrical and Electronic Engineering
Stellenbosch University
Matieland, South Africa*

Dissertation: PhD (E&E)

March 2016

Performing aerial refueling of a large receiver is an extremely strenuous task for a pilot. Automating the aerial refueling for a large receiver is thus highly desirable. While significant research has been performed on the autonomous aerial refueling of unmanned and fighter-sized aircraft, the challenges of autonomously refueling a large receiver are largely unknown. This thesis seeks to investigate these challenges. Primarily it seeks to determine whether the long distance between the centre of gravity (CG) and refueling receptacle (RR) has a meaningful impact on controller design.

A linear model is derived to describe the movement of the receiver aircraft's refueling receptacle during aerial refueling. This novel linear model is compared to existing linear aircraft models. Through analysis it is shown that the distance between the CG and the RR must be included in the dynamic model of the receiver. A novel normal controller is designed using a new architecture that takes the relative movement of the CG and the RR into account. An axial controller is derived using an innovative high-drag configuration in order to combat the slow engine response of large aircraft. Optimal control is used to design an RR specific lateral controller.

Other challenges relating to the refueling of a large receiver are also investigated. A control strategy for the tanker is developed using existing FBW control inputs and hold modes. The tanker control is designed to be supplied by a pilot and does not require any customisation of flight software. It is expected that tanker downwash will have a significant effect on the receiver. The linear models and non-linear simulation are adapted to include uncertain downwash disturbances. The controllers are customised to control the receiver in various trajectories: approach, toboggan, and racetrack. The linear models are augmented with a linearised model of the Airbus A330 MRTT's fly-by-wire (FBW) system. The FBW system is slightly adapted to be suited to automatic control. The controllers are redesigned to operate through the FBW.

The designed controllers are tested in a non-linear simulation. Simulations are performed in light and medium turbulence, as defined in MIL-STD-1797. Robustness tests are performed

with regard to downwash and sensor delays. Through numerous non-linear simulations on two different simulators, it is shown that the control system is capable of performing automated aerial refueling in light and medium turbulence.

Uittreksel

Automated Aerial Refueling of a Large Receiver Aircraft

SC Kriel

*Departement Elektriese en Elektroniese Ingenieurswese
Stellenbosch Universiteit
Matieland, Suid Afrika*

Proefskrif: PhD (E&E)

Maart 2016

Om brandstofaanvulling van 'n groot ontvangervliegtuig in die lug uit te voer, is vir 'n vlieënier 'n uiters veeleisende taak. Dit is dus wenslik om hierdie taak te outomatiseer. Terwyl 'n aansienlike hoeveelheid navorsing reeds gedoen is oor die outonome brandstofhervulling van onbemande en veggrootte-vliegtuie in die lug, is die uitdagings verbonde aan die outonome hervulling van 'n groot ontvangervliegtuig steeds grotendeels onbekend. Hierdie tesis ondersoek hierdie uitdagings. Die navorsing in hierdie tesis poog hoofsaaklik om te bepaal of die lang afstand tussen die swaartepunt en die hervullingspoort 'n betekenisvolle impak op beheerontwerp het.

'n Lineêre model word afgelei om die beweging van die ontvangervliegtuig se hervullingspoort tydens hervulling in die lug te beskryf. Hierdie nuwe lineêre model word dan met bestaande lineêre vliegtuigmodelle vergelyk. Deur ontleding word daar gewys dat die afstand tussen die swaartepunt en die hervullingspoort in die dinamiese model van die ontvangervliegtuig ingesluit moet word. 'n Nuwe normaalbeheerder word ontwerp deur 'n nuwe argitektuur te gebruik wat die relatiewe momente van die swaartepunt en hervullingspoort in ag neem. 'n Aksiaalbeheerder word afgelei deur 'n innoverende hoësluur-konfigurasie te gebruik, met die doel om die stadige enjinrespons van groot vliegtuie teen te werk. Optimaalbeheer word gebruik om 'n hervullingspoort-spesifieke laterale beheerder te ontwerp.

Ander uitdagings wat verband hou met die hervulling van 'n groot ontvangervliegtuig word ook ondersoek. 'n Beheerstrategie vir die tenkvliegtuig word ontwikkel deur bestaande elektroniese ("fly-by-wire") beheerinsette en houmodusse te gebruik. Die tenkvliegtuigbeheer word ontwerp om deur 'n vlieënier gedoen te kan word, en vereis geen pasmaking van die vliëgsageware nie. Daar word verwag dat die tenkvliegtuig se neerstroming 'n beduidende effek op die ontvangervliegtuig sal hê. Die lineêre modelle en nie-lineêre simulاسies word aangepas om die wisselvallige neerstromingsteurings in te sluit. Die beheerders word pasgemaak om die ontvangervliegtuig in verskeie trajekte te beheer, naamlik nadering ("approach"), rodelslee ("toboggan"), en renbaan ("racetrack"). Die lineêre modelle word aangevul deur 'n

gelineariseerde model van die Airbus A330 MRTT se elektroniese beheerstelsel (“fly-by-wire”). Hierdie stelsel word effens aangepas om geskik te wees vir outomatiese beheer. Die beheerders word dan herontwerp om deur hierdie stelsel te kan funksioneer.

Die ontwerpte beheerders word in ’n nie-lineêre simulاسie getoets. Simulasies word uitgevoer in ligte en matige turbulensie, soos in MIL-STD-1797 gedefinieer. Robuustheidstoetse word uitgevoer met betrekking tot neerstroming en sensorvertraging. Uit veelvuldige nie-lineêre simulاسies op twee verskillende simulators word daar gewys dat die beheerstelsel wel in staat is tot geoutomatiseerde brandstofhervulling in die lug, in ligte sowel as matige turbulensie.

Acknowledgements

To my supervisor, Thomas Jones: Thank you for your support throughout this project and for the insight you provided.

To my co-supervisor, Japie Engelbrecht: Thank you for your continuous encouragement and useful comments.

To my current boss, Iain Peddle: Thank you for allowing me the flexibility to finish this project.

To my girlfriend, Jolette Roodt: Thank you for all the emotional and editorial support. I could not have done this without you.

To all my friends for showing interest in my work, enquiring after my progress (and health), and generally being there for me.

Emmanuel Cortet, Daniel Cazy and Jérôme Gauvain at Airbus Operations, Stability and Control Department for all their assistance and for making this project possible.

The financial assistance of the National Research Foundation (NRF), Airbus SAS, and the National Aerospace Centre of Excellence (NACoE) towards this research is hereby acknowledged. Opinions expressed and conclusions arrived at, are those of the author and are not necessarily to be attributed to the NRF or Airbus.

Hierdie tesis word opgedra aan my ouers. Baie dankie dat julle oor 26 jaar my opvoeding ondersteun het. Dankie vir al die rekenaars, elektronika en boeke wat my toekoms as 'n ingenieur van kleintyd vasgelê het. Dankie dat julle my toegelaat het om goed uitmekaar te haal. Pa, dankie vir al die tyd saam in die garage. Ma, dankie vir al die middae in koffiewinkels tussen skool en Rekenaarwetenskap. Hierdie tesis sou nie bestaan het sonder julle liefde en ondersteuning nie.

Contents

Declaration	i
Abstract	ii
Uittreksel	iv
Acknowledgements	vi
Contents	viii
Nomenclature	ix
List of Figures	xiii
List of Tables	xiv
1 Introduction	1
1.1 Overview	1
1.2 Requirements	1
1.3 Problem Statement	2
1.4 Document Overview	3
1.5 Reference Frames and Axis Systems	4
1.5.1 Notation	5
1.5.2 Transformation	5
1.6 Aerial Refueling	6
1.6.1 Flying Boom	6
1.6.1.1 Mechanics	7
1.6.1.2 Boom Envelope	8
1.6.1.3 Calculation	10
Boom Position	10
Boom Parameters	11
Velocities	11
1.6.2 Flight Points	12
1.6.3 Trajectories	12
1.6.3.1 Straight and Level	13
1.6.3.2 Racetrack	13

1.6.3.3	Toboggan	13
1.6.3.4	Approach	14
1.6.4	Turbulence	14
2	Modelling	15
2.1	Overview	15
2.2	Non-linear Receptacle Dynamics	16
2.2.1	Overview	16
2.2.2	Velocity	17
2.2.3	Position	19
2.3	Linear Longitudinal Receptacle Dynamics	20
2.3.1	Axial Component	20
2.3.2	Normal Component	22
2.3.3	State Space	23
2.3.4	Longitudinal Decoupling	25
2.3.4.1	Normal	25
2.3.4.2	Axial	26
2.4	Linear Lateral Receptacle Dynamics	27
2.4.1	State Space	28
2.5	Tanker Downwash	29
2.5.1	Literature Study	29
2.5.1.1	Bloy et al.	30
2.5.2	Dogan et al.	31
2.5.3	Ryan et al.	32
2.5.4	Downwash Modeling Overview	33
2.5.5	Downwash Angle Modelling	33
2.5.6	Downwash Dynamics	35
2.5.6.1	Lift	36
2.5.6.2	Side Force	37
2.5.6.3	Pitching Moment	37
2.5.6.4	Rolling Moment	38
2.5.6.5	Yawing Moment	38
2.6	Engine	38
2.6.1	Architecture	39
2.6.2	Responses	41
2.6.2.1	Small Steps	41
2.6.2.2	Half to Full	41
2.6.2.3	Idle to Full	42
2.6.2.4	Reducing Thrust	42
2.7	Summary	43
3	Analysis	44
3.1	Overview	44

3.2	Normal System	45
3.2.1	Poles and Zeros	45
3.2.2	Downwash Angle	47
3.2.3	Control System	48
3.2.3.1	Tanker Tracking	49
3.2.3.2	Disturbance Rejection	50
3.2.4	Architectures	50
3.2.4.1	CG Model - CG Feedback	51
3.2.4.2	CG Model - RR Feedback	51
3.2.4.3	RR Model - RR Feedback	52
3.2.5	Results	52
3.2.5.1	CG Model - CG Feedback	52
3.2.5.2	CG Model - RR Feedback	54
3.2.5.3	RR Model - RR Feedback	55
3.3	Lateral	57
3.3.1	Zeros	58
3.3.2	Closed Loop	58
3.4	Summary	60
4	Tanker Control	62
4.1	Overview	62
4.2	Normal Control	62
4.3	Lateral Control	63
4.4	Axial Control	64
4.5	Racetrack Trajectory	65
4.5.1	Normal Control	65
4.5.2	Lateral Control	65
4.5.3	Axial Control	67
4.6	Summary	68
5	Receiver Control	69
5.1	Overview	69
5.2	Normal	69
5.2.1	Receptacle-Specific Control	70
5.2.1.1	Linear Simulation	72
5.2.2	Compensating for Receptacle Dynamics	72
5.2.2.1	Cancelling Receptacle Dynamics	72
5.2.2.2	Optimal Control	75
5.2.3	Summary	78
5.3	Axial: Thrust Only	80
5.4	Axial: High-Drag Configuration	81
5.4.1	Overview	81
5.4.2	Modeling	82

<i>CONTENTS</i>	xi
5.4.3 Control	83
5.4.4 Coupling	86
5.4.5 Flight Points	86
5.4.5.1 Summary	88
5.5 Lateral	89
5.6 Banked Turn	93
5.6.1 Normal	93
5.6.2 Lateral	93
5.6.3 Axial	93
5.7 Summary	93
6 Results	95
6.1 Overview	95
6.2 Light Turbulence	95
6.3 Flight-Point Parameters	98
6.3.1 Calibrated Airspeed	98
6.3.2 Flight Level	99
6.3.3 Tanker Mass	99
6.3.4 Tanker CG Position	100
6.3.5 Receiver Mass	100
6.3.6 Receiver CG	101
6.3.7 Downwash	101
6.4 High-Drag Configuration	102
6.5 Trajectories	104
6.5.1 Racetrack Trajectory	104
6.5.2 Toboggan Trajectory	106
6.5.3 Approach Trajectory	107
6.6 Medium Turbulence	108
6.7 Downwash Dynamics	111
6.7.1 Axial Displacement	112
6.7.2 Lateral Displacement	113
6.7.3 Summary	115
6.8 High-Fidelity Simulator Verification	115
6.9 Simulator	115
6.10 Results	116
7 Fly-by-Wire	119
7.1 Overview	119
7.2 Modeling	119
7.2.1 Longitudinal FBW System	120
7.2.1.1 Architecture	120
7.2.1.2 State Space	122
7.2.2 Lateral FBW System	123

7.2.2.1	Architecture	123
7.2.2.2	State Space	125
7.3	Control	127
7.3.1	Longitudinal Normal Law Model	128
7.3.2	Lateral Normal Law Model	128
7.4	Results	128
7.5	Summary	130
8	Conclusion and Recommendations	133
8.1	Summary	133
8.2	Contributions to the Field	134
8.3	Suggestions for Future Work	135
	Appendices	136
A	Model Derivation	137
A.1	Non-linear Equations	137
A.2	Aerodynamic Forces	138
A.3	Longitudinal Model	139
A.3.1	Straight and Level Flight	139
A.4	Lateral Model	140
A.5	Aerodynamic Derivatives	141
A.6	Model Verification	142
B	Axes System Transformations	143
B.1	Body Axes	143
B.1.1	Aerodynamic Axes & Error Axes	143
C	Simulation Setup	144
C.1	Airbus A330 MRTT Model	144
C.1.1	Initialisation Scripts	144
C.1.2	Aerodynamic Calculations	145
C.1.3	Aircraft Kinematics	145
C.1.4	Sensor Model	145
C.1.5	Actuator Model	145
C.1.6	Fly-by-wire System	145
C.1.7	Hold Modes	145
C.2	Aerial Refueling Simulation	146
C.2.1	Control Scripts	146
C.2.2	AAR System	146
C.2.3	Simulation Process	146
D	Unabridged Results	148
	Bibliography	155

Nomenclature

Refueling:

rr	Refueling Receptacle
cg	Centre of Gravity
t	Tanker
r	Receiver

Physical:

b	Wingspan
c	Mean Aerodynamic Chord
m	Mass
S	Surface Area
A	Aspect Ratio
e	Efficiency
I	Moment of Inertia Matrix
I_{xx}	Moment of Inertia X-axis
I_{yy}	Moment of Inertia Y-axis
I_{zz}	Moment of Inertia Z-axis

Natural Constants:

ρ	Air Pressure
g	Gravitational Acceleration

Aerodynamic:

q	Dynamic Pressure
CL	Aerodynamic Lift Coefficient
CL	Aerodynamic Side Force Coefficient
CD	Aerodynamic Drag Coefficient
$CI\bar{L}$	Aerodynamic Roll Coefficient
CM	Aerodynamic Pitch Coefficient
CN	Aerodynamic Yaw Coefficient

C_X	Aerodynamic Axial Force Coefficient
C_Y	Aerodynamic Lateral Force Coefficient
C_Z	Aerodynamic Normal Force Coefficient

Linear Quadratic Regulator:

LQR	Linear Quadratic Regulator
J	Cost Function
Q	State Weighting matrix
R	Actuator Weighting matrix

Position and Orientation:

p	Position Vector
N	North Position
E	East Position
D	Down Position
α	Angle of Attack
β	Angle of Side Slip
γ	Flight Path Angle
q_{1-4}	Quaternions
ϕ	Roll Angle
θ	Pitch Angle
ψ	Yaw Angle
DCM	Direction Cosine Matrix

Velocity and Rotation:

V	Velocity Vector
\bar{V}	Airspeed
U, u	Axial Velocity
V, v	Lateral Velocity
W, w	Normal Velocity
ω	Angular Velocity
α	Angular Acceleration
P, p	Roll Rate
Q, q	Pitch Rate
R, r	Yaw Rate

Forces, Moments and Accelerations:

L	Lift Force
-----	------------

S	Side Force
D	Drag Force
M	Moment Vector
\bar{L}	Roll Moment
M	Pitch Moment
N	Yaw Moment
F	Force Vector
X	Axial Force
Y	Lateral Force
Z	Normal Force

Flight Point:

FL	Flight Level (100ft)
V_c	Calibrated Airspeed

Actuation:

T	Thrust
δ_e	Elevator Deflection
δ_h	Horizontal Tailplane Deflection
δ_a	Aileron Deflection
δ_s	Collective Spoiler Deflection
δ_d	Drag Virtual-actuator Deflection
δ_{av}	Effective Aileron Deflection
δ_r	Rudder Deflection
δ_p	Lateral Stick Deflection (Fly-by-wire)
δ_Q	Longitudinal Stick Deflection (Fly-by-wire)
δ_R	Pedal Deflection (Fly-by-wire)

System:

A	Continuous System Matrix
B	Continuous Input Matrix
C	Output Matrix
D	Feed-through Matrix
K	Gain Matrix
K_x	Gain for State x

Superscripts and Subscripts:

b	Coordinated in Body Axes
-----	--------------------------

e	Coordinated in Inertial Axes
w	Coordinated in Aerodynamic Axes
0	Static or Initial value
cmd	Commanded Value
eff	Effective Actuation
$-f$	Filtered State
$-i$	Integrated State

Trigonometric Functions:

S_x	Sine of x , used as alternative to $\sin(x)$ to save space
C_x	Cosine of x , used as alternative to $\cos(x)$ to save space

Poles and Zeroes:

ζ	Damping ratio of pole pair
ω_p	Frequency of pole
ω_z	Frequency of zero

Other:

AAR	Automated Aerial Refueling
FBW	Fly by Wire
PIO	Pilot Induced Oscillation
MRTT	Multi Role Tanker Transport

List of Figures

1.1	A tanker refueling a helicopter using the probe-and-drogue system [35]	6
1.2	A tanker refueling a fighter aircraft using the flying boom system [36]	7
1.3	Flying boom degrees of freedom (not to scale)	7
1.4	Boom envelopes in three dimensions	9
1.5	Three-dimensional and two-dimensional views of side envelope plot	9
1.6	Three-dimensional and two-dimensional views of rear envelope plot	9
1.7	Calculating boom position	10
1.8	Calculating boom parameters from boom position	11
1.9	Flight envelope for AAR	13
1.10	Racetrack trajectory [2]	13
1.11	Observation position [2]	14
1.12	Pre-contact position [2]	14
2.1	Effect of the relative distance between CG and RR	15
2.2	Illustration of frames of reference in the AAR scenario	17
2.3	Vector diagram of receiver in tanker downwash	34
2.4	Illustration of expected downwash below and behind tanker	35
2.5	Change in the receiver's lift due to X-position and Y-position	37
2.6	Change in the receiver's pitching moment due to change in X-position and Y-position	37
2.7	Change in the receiver's pitching moment due to change in X-position and Y-position	38
2.8	Change in the receiver's rolling moment due to change in Y-position	38
2.9	Change in the receiver's rolling moment due to change in Y-position	39
2.10	Basic architecture of the non-linear engine model	39
2.11	Illustration of engine slew rates	40
2.12	Rising and falling engine thrust slew-rate limits	40
2.13	Small thrust step around steady state	41
2.14	Thrust step from half to maximum thrust	42
2.15	Thrust step from engine idle to maximum thrust	42
2.16	Reducing thrust from maximum to idle	43
3.1	Pole and zero positions and step responses for various receptacle positions in transfer function from elevator to normal acceleration	46
3.2	Visualisation of reference used in CG-CG architecture	51
3.3	Visualisation of reference used in CG-RR architecture	52

3.4	Visualisation of reference used in RR-RR architecture.	52
3.5	CG Model - CG Feedback: Time response of the RR and the CG to a CG position step command	53
3.6	CG Model - CG Feedback: Frequency response of the CG and the RR to a CG position command	53
3.7	CG Model - CG Feedback: Time response of the CG and the RR to a downwash step disturbance	54
3.8	CG Model - CG Feedback: Frequency response of the CG and the RR to a downwash disturbance	54
3.9	CG Model - RR Feedback: Frequency response of the CG and the RR to a downwash step disturbance	55
3.10	CG Model - RR Feedback: Step response of the CG and the RR to a step command .	55
3.11	RR Model - RR Feedback: Frequency response of the CG and the RR to a downwash disturbance	56
3.12	RR Model - RR Feedback: Time response of the CG and the RR to a downwash step disturbance	56
3.13	RR Model - RR Feedback: Step response of the CG and the RR to a step command .	57
3.14	Poles and zeros of system from aileron input to lateral acceleration of RR	58
3.15	Poles and zeros of system from rudder input to lateral acceleration of RR	59
3.16	Response of the CG and the RR to a lateral step command using primarily bank-to-turn	60
3.17	Response of the CG and the RR to a lateral step command using primarily skid-to-turn	60
4.1	Change in Z position and velocity of tanker CG and desired receiver RR position for tanker exposed to medium turbulence	63
4.2	Change in East position and velocity of tanker CG and desired receiver RR position for tanker exposed to medium turbulence	64
4.3	Difference in East position of tanker CG and desired receiver RR position for tanker exposed to medium turbulence	64
4.4	Ground speed of tanker when exposed to medium turbulence with constant throttle position at flight point $FL = 100$, $V_c = 200kt$, $m_t = 125t$	65
4.5	Racetrack trajectory segments	66
4.6	Bank and heading angle of tanker entering banked turn	66
4.7	Bank and heading angle of tanker leaving banked turn	67
4.8	Ground speed and altitude of tanker over course of banked turn without increasing thrust	67
4.9	Ground speed and altitude of tanker over course of banked turn when increasing thrust	68
5.1	RR and CG response to a position step command	71
5.2	RR and CG response to a position step command at various flight points using constant closed loop pole positions	71

5.3	RR command, position and error in medium turbulence with zero frequency of 1.65 rad/s	72
5.4	RR command, position and error in medium turbulence with zero frequency of 2.62 rad/s	73
5.5	RR command, position and error in medium turbulence with zero frequency of 3.57 rad/s	73
5.6	RR and CG response to a step command. (a) Unmodified control scheme. (b) Cancelling zero, without elevator model. (c) Cancelling zero with elevator model included	74
5.7	RR and CG response to a step command with 15 degree separation between zero and cancelling pole for various closed loop bandwidths. (a) Unmodified control scheme (b) Cancelling zero, without elevator model (c) Cancelling zero with elevator model included	74
5.8	Closed loop pole positions for values of r in range 0.1 to 10. (Increasing zero frequencies correspond to higher r values.)	75
5.9	RR and CG response to position command step for values of r in range 0.1 to 10. (Decreasing rise times correspond to higher r values.)	76
5.10	RR and CG response to position command step for values of r in range 0.1 to 10 when assigning a weight to the CG velocity	77
5.11	RR and CG response to position command step for values of r in range 0.1 to 10 when assigning a weight to the CG velocity	77
5.12	Block diagram for normal receptacle controller	78
5.13	Block diagram of controller implementation in non-linear simulation	79
5.14	Illustration detailing \dot{T}_{max} and ΔT_{max}	80
5.15	Simplified block diagram of axial system	81
5.16	Steady-state parameters for various spoiler deflections	82
5.17	Block diagram of high-drag axial system	83
5.18	High-drag axial system actuator response to a 0.5 m position disturbance	85
5.19	High-drag axial system response to a 0.1 m/s velocity disturbance	85
5.20	X- and Z-position response to an axial position step of the longitudinal system controlled by decoupled controllers	87
5.21	X- and Z-position response to a normal position step of the longitudinal system controlled by decoupled controllers	87
5.22	Tanker and receiver when tanker is disturbed by lateral wind	89
5.23	Block diagram of lateral system	90
5.24	RR and CG response to a lateral RR position step command at four flight points . . .	91
5.25	RR command, position and error in light turbulence at $V_c = 300$ kt, FL = 300 and $m_r = 225$ t	91
5.26	RR command, position and error in light turbulence at $V_c = 225$ kt, FL = 300 and $m_r = 225$ t	92
5.27	RR command, position and error in light turbulence at $V_c = 300$ kt, FL = 300 and $m = 125$ t	92
6.1	Good, average and poor performance at various flight points in light turbulence . .	96

6.2	Good, average and poor performance at various flight points in light turbulence . . .	97
6.3	Control system performance at baseline flight point	98
6.4	Simulation results for receivers with different airspeed in light turbulence	99
6.5	Simulation results for receivers with mass in light turbulence	101
6.6	Simulation results for receivers with varying CG location	101
6.7	Simulation results for receivers experiencing different downwash angles	102
6.8	Commanded thrust over the course of simulation for different downwash angles . . .	102
6.9	Simulation results for receivers with and without high-drag configuration at flight point: $FL = 100$, $V_c = 250$ kt, $m_r = 225$ t, $m_t = 175$ t	103
6.10	Thrust and spoiler actuation with and without high-drag configuration	104
6.11	Control system performance in light turbulence during racetrack trajectory	105
6.12	Path flown by tanker and receiver during racetrack trajectory	105
6.13	Control system performance in light turbulence during stages of racetrack trajectory	105
6.14	Control system performance in light turbulence during straight and level flight with high steady-state thrust requirement	106
6.15	Control system performance in light turbulence during toboggan trajectory with high steady-state thrust requirement	106
6.16	Thrust command comparison between straight and level flight and toboggan trajec- tory	107
6.17	North, East and Down separation between tanker and receiver CGs during approach.	107
6.18	Location of RR in boom envelope as receiver transitions from pre-contact to contact position	108
6.19	Good, average, poor and infeasible performance at various flight points in medium turbulence	109
6.20	Good, average, poor and infeasible performance at various flight points in medium turbulence	110
6.21	Infeasible control system performance in medium turbulence	111
6.22	Effect of $C_{L_{xcg}}$ on closed loop normal and axial system	112
6.23	Effect of $C_{M_{xcg}}$ on closed loop normal and axial system	113
6.24	Effect of $C_{S_{ycg}}$ on closed loop normal and axial system	113
6.25	Effect of $C_{L_{ycg}}$ on closed loop normal and axial system	114
6.26	Effect of $C_{N_{ycg}}$ on closed loop normal and axial system	114
6.27	Good, average and poor performance at various flight points in medium turbulence using high-fidelity simulator	117
6.28	Good, average and poor performance at various flight points in medium turbulence using high-fidelity simulator	118
7.1	Normal FBW system: input state	120
7.2	Normal FBW system: load factor calculation	120
7.3	Normal FBW system	121
7.4	Normal FBW system - output	121
7.5	Change in longitudinal pole and zero positions when fly-by-wire system is engaged	123
7.6	Lateral FBW system - input	124

7.7	Lateral FBW system - lateral stick (roll)	124
7.8	Lateral FBW system - pedal (sideslip)	125
7.9	Comparison between pole and zero positions between aileron and lateral stick inputs	127
7.10	Comparison between pole and zero positions between rudder and pedal inputs . . .	127
7.11	Good control system performance in medium turbulence in high-fidelity simulator .	129
7.12	Average control system performance in medium turbulence in high-fidelity simulator	129
7.13	Poor control system performance in medium turbulence in high-fidelity simulator .	130
7.14	Good control system performance in medium turbulence in high-fidelity simulator .	130
7.15	Average control system performance in medium turbulence in high-fidelity simulator	131
7.16	Poor control system performance in medium turbulence in high-fidelity simulator .	131

List of Tables

1.1	Overview of vector notation	6
1.2	Rigid boom envelope definitions	8
2.1	Receiver trim values for different downwash angles at 250kts, 20,000ft, 175,000kg and CG at 30%	35
2.2	Engine parameters at two flight points	41
3.1	Accuracy of zeros' position approximation at two flight points	47
3.2	Change in steady-state values for receiver exposed to three degree downwash	48
3.3	LQR state weightings used for analysis of lateral RR-system	59
5.1	Max deviations for axial LQR control system	81
5.2	Maximum deflections for axial system LQR	84
5.3	Steady-state thrust at various flight points in high-drag configuration	88
5.4	Steady-state thrust at various flight points in high-drag configuration and toboggan trajectory	88
5.5	Maximum deviation for lateral LQR controller	89
6.1	Standard deviation of boom-parameter errors over course of refueling simulation for different calibrated airspeeds	98
6.2	Standard deviation of boom parameters over course of refueling simulation for different flight levels	99
6.3	Standard deviation of boom parameters over course of refueling simulation for different tanker masses	100
6.4	Standard deviation of boom parameters over course of refueling simulation for different tanker CG locations	100
6.5	Standard deviation of boom parameters over course of refueling simulation for different receiver masses	100
6.6	Change in boom parameters when changing receiver CG location	101
6.7	Change in boom parameters when changing downwash angles	102
6.8	Standard deviation of boom parameters and thrust, and mean thrust for thrust-only system (A) and high-drag configuration (B)	104
D.1	Boom parameters during straight and level flight in light turbulence	148
D.1	Boom parameters during straight and level flight in light turbulence	149

D.1 Boom parameters during straight and level flight in light turbulence	150
D.1 Boom parameters during straight and level flight in light turbulence	151
D.2 Boom parameters during straight and level flight in medium turbulence	151
D.2 Boom parameters during straight and level flight in medium turbulence	152
D.2 Boom parameters during straight and level flight in medium turbulence	153
D.2 Boom parameters during straight and level flight in medium turbulence	154

Chapter 1

Introduction

1.1 Overview

Aerial refueling refers to the transfer of fuel from one aircraft (tanker) to another (receiver) during flight. While the majority of aerial refueling is performed with relatively small receiver aircraft, large aircraft have also been successfully refueled manually.

Aerial refueling holds significant benefits for unmanned aerial vehicles (UAVs) [28], resulting in an interest in the complete automation of aerial refueling. The modelling and control [17,21,24,27,31,40] of UAVs (or other relatively small aircraft), and the estimation of relative aircraft states [12,26,37,41] are currently very active research fields. There also exists an interest in the refueling of large piloted aircraft. The station keeping of a large aircraft with slow dynamics over a longer refueling time is a very strenuous task for the pilot. The automation of a large receiver aircraft during refueling will thus be beneficial.

When refueling fighter-sized aircraft, automatic control for station keeping of the receiver amounts to relative position control. For a large receiver aircraft, on the other hand, a few complications arise. Firstly, the natural dynamics of a large aircraft are much slower than those of a fighter aircraft. Secondly, for the aircraft considered here, the refueling boom connects to the front of the aircraft. The significant moment arm between the centre of gravity (CG) and the refueling receptacle (RR) introduces additional movement into the system that cannot be controlled with a tradition station keeping controller which regulates the position of the centre of gravity. The primary goal of this research project is to investigate the effect of this distance. It should be noted that, in this thesis, the term "large receiver" refers to an aircraft of size comparable to that of the tanker with a length of over 50m. However, in other literature, the same term sometimes refers to much smaller aircraft, e.g. a Learjet.

1.2 Requirements

This project was co-funded by Airbus and the National Aerospace Centre of Excellence. Airbus provided the data required to create the aircraft models and non-linear simulations, as well as an outline of the requirements for an AAR controller. These requirements will dictate several choices made in this thesis.

- The tanker and receiver aircraft will be Airbus A330 MRTTs.

- The flying boom refueling system will be used.
- The newly designed controller will control the receiver. The flight software of the tanker may not be changed.

The controller must:

- Move the receiver from the observation position to the contact position. (These terms will be defined later in this chapter.)
- Regulate the position of the RR inside boom envelopes.
- Perform these tasks in light and medium turbulence.
- Perform these tasks over the full mass and CG-position domain.
- Perform these tasks in the toboggan, racetrack, and approach trajectories. (These trajectories will be defined later in this chapter.)
- Use realistic sensor delays.

Airbus has made a Matlab Simulink model and engine response data available to Stellenbosch University. The architecture of the model and its simulation results will be shown throughout the thesis. However, at Airbus's request, the thesis will not list detailed information on the model, e.g. actuator limits and fly-by-wire system feedback gains.

1.3 Problem Statement

The primary research objective of this thesis is to create a control system to regulate a large receiver aircraft during aerial refueling. The general case of a large receiver is investigated, but the practical aspects of a specific aircraft – the Airbus A330 MRTT – are also addressed. The primary question this thesis seeks to answer is whether the large distance between the receiver's centre of gravity and its refueling receptacle prevents the use of existing station keeping controllers to achieving automated aerial refueling.

As secondary objectives, this thesis investigates several practical aspects that arise when automating a large receiver aircraft:

- Large aircraft have slower dynamics than small, fighter-sized aircraft. This is particularly true in the response of the engines. It has been suggested [2] that the response of the Airbus A330 MRTT's engine will not be fast enough to regulate the relative axial positions of the two aircraft. Furthermore, investigation into the bow-wave effect [14] shows the possibility of pilot-induced oscillation (PIO) due to the effect of the receiver on the tanker. This thesis will investigate a method of improving the axial response of the receiver, and of preventing PIO in the tanker.
- While in the contact position, the receiver is exposed to significant wash from the tanker. The effect of this is largely unknown and can vary dramatically based on the dimensions, separation, and configuration of the tanker and receiver aircraft. There is high certainty, however, that the receiver will experience a resultant downwash while in the contact

position [33]. This thesis will investigate the effect of the downwash on the receiver and its controllers. Furthermore, any models derived and simulations created will enable the easy inclusion of detailed interaction information if it is to become available.

- Some large aircraft, such as the Airbus A330 MRTT, are equipped with fly-by-wire systems. The systems are intended to improve the handling characteristics of the aircraft for pilots, but also include several safety features, e.g. angle of attack protection. It would be desirable for the AAR controller to operate through such a FBW system. This thesis will investigate the feasibility of controlling an Airbus A330 MRTT through its fly-by-wire system.
- Aerial refueling needs to be performed at a variety of flight points and in different trajectories. This thesis will investigate the effect of flight point and tanker parameters on the relative performance of the control system.
- While the focus of this thesis is the control of the receiver, the tanker must also be controlled. As stated in the requirements, the tanker must utilize its existing flight software. Despite this limitation, there are many possible configurations. This thesis will find a control scheme for the tanker that allows it to maintain the intended trajectory, without negatively impacting the receiver's performance.

The primary area of research of this thesis is modelling and control. To limit the scope of the thesis, less attention will be paid to the areas of aerodynamics and estimation. Furthermore, it is assumed that the reader is familiar with the traditional linear aircraft model, as derived in [34].

1.4 Document Overview

The goal of this thesis is to investigate the automatic control of the receiver aircraft during aerial refueling. The remainder of this chapter provides background information to aid the discussion of aerial refueling throughout the thesis.

Chapter 2 derives a novel non-linear aircraft model that describes the movement of the RR, and not the CG, of the aircraft. The model is linearised and decoupled to create axial, normal, and lateral state space models. A non-linear engine model is also presented.

Chapter 3 analyses the new linear models. The RR-specific models are contrasted to existing, CG-based, aircraft models by using open loop step responses and pole-zero analysis. Simplified control systems are designed to highlight the differences in closed-loop behaviour. At this point, the aircraft and actuator limits are not considered. The result of this chapter is a handy rule-of-thumb with which one can easily determine whether a specific aircraft requires an RR-specific controller. This chapter will focus primarily on the normal system, as the effect of the RR is most prevalent there.

Chapter 4 investigates the control of the tanker aircraft during aerial refueling. According to the requirements listed in Section 1.2, the tanker must be controlled using the existing hold modes and fly-by-wire system. This chapter seeks to find the optimal configuration that would aid the receiver in the refueling task. The control of the tanker on various trajectories is also

discussed. Any changes made in tanker control over the course of refueling is limited to input that a pilot could feasibly provide.

Chapter 5 presents a novel control system for the receiver aircraft during aerial refueling. Normal, axial and lateral control systems are designed for the linear RR models derived in 2. A novel high-drag configuration axial controller is proposed as a method of improving the axial performance of the system.

Chapter 6 lists detailed results from multiple non-linear simulations using the control systems designed in Chapter 5.

As part of this study, Airbus provided the researcher with the opportunity of an internship at Airbus headquarters in Toulouse. The control systems that proved promising in the Simulink simulations were then implemented on a high-fidelity simulator at Airbus. Chapter 7 presents the modelling and control of an A330 MRTT under control of its FBW system, and shows the simulation results from Airbus's high-fidelity simulator.

Chapter 8 provides a summary of the research and lists recommendations for future work.

Appendix A gives a short overview of the derivation of the standard aircraft model, as detailed in [34]. Appendices B and A.5 list DCMs used for axis transformations. Appendix C describes the non-linear simulators used, and provides details on the Simulink simulation and the high-fidelity simulator. Appendix D contains unabridged simulation results too extensive to list in the results chapter.

1.5 Reference Frames and Axis Systems

The tanker and receiver are represented as two rigid bodies moving and rotating relative to one another. The following frames and axis systems are used. The terminology and nomenclature used here are taken from [34]:

Frame of Reference A set of rigidly related points that can be used to establish distances and directions.

Inertial Frame A frame of reference that is not accelerating or rotating.

Vector An abstract geometric object that has magnitude and direction. A vector exists independently from any axis system.

Axis system A set of axes attached to a frame of reference. Vectors can be coordinated in an axis system to create a coordinate vector in \mathbb{R}^3 .

Coordinate Vector A Euclidean vector containing three values that represent the components of a vector in a given axis system.

The following frames and axis systems will be used:

Inertial Frame The inertial frame is attached to the earth. It is assumed that the earth is flat and non-rotating. The relative position of the two aircraft is the most important factor during AAR and will not be affected by these assumptions. The inertial frame is indicated by a sub- or superscript i .

Inertial Axes The inertial axes are attached to the initial frame at some convenient point on the ground. The axes are aligned as follows: the X-axis points North, the Y-axis points East and the Z-axis is orientated downward to the centre of the earth. Vectors coordinated in the inertial axes are indicated by a superscript i .

Body Frame The body frame is attached to and rotates with the body of an aircraft. The body frames of the tanker and receiver are indicated by t and r respectively.

Body Axes The body axes are attached to the body frame. The origin of the body axes is chosen as the centre of gravity of the aircraft. The axes are aligned as follows: the X-axis is chosen along the plane of symmetry, directly to the front of the aircraft. The Y-axis is positive towards the right wing. The Z-axis points down, and lies on the plane of symmetry. Vectors coordinated in the body axes of the tanker or receiver are indicated by the subscripts t and r respectively.

Aerodynamic Frame The aerodynamic frame is also attached to the body of the aircraft, but rotates according to the incoming airflow.

Aerodynamic Axes The aerodynamic axes are attached to the aerodynamic frame at the aircraft's centre of gravity. The X-axis is chosen into the oncoming air stream. The Z-axis is chosen downward and remains in the plane of symmetry of the aircraft. The Y-axis is orthogonal to the X-axis and Z-axis. The aerodynamic axes of the receiver will be indicated by a sub- or superscript of w . The angle of attack, α , and angle of sideslip, β , describe the difference between the aerodynamic and body axes.

Error Frame The error frame is positioned in space at the point where the refueling boom's tip would be, if the boom was in the zero error position. It is thus located at the desired position of the refueling receptacle and moves as the tanker moves or rotates. The frame rotates with the velocity vector of the receiver. Vectors in the error frame are indicated by a sub- or superscript e . The position and velocity errors of the RR will be expressed in this frame.

Error Axes The origin of the refueling axes is chosen behind the tanker aircraft, at the tip of the refueling boom, when it is in a zero error position. The refueling axes are aligned with the receiver's aerodynamic axes. The X-axis is chosen along the velocity vector of the receiver aircraft. The Z-axis is chosen downward, and lies on the plane of symmetry of the aircraft. The Y-axis points to the right wing and is perpendicular to the X and Z axes.

1.5.1 Notation

Table 1.1 lists the notation used in this chapter.

1.5.2 Transformation

The use of Euler angles for the attitude description of aircraft is well-established [34]. The angles ϕ, θ and ψ will refer to the Euler 3-2-1 angle roll, pitch and yaw. DCMs will be used to

Symbol	Description
\mathbf{r}_{AB}	A vector representing the position of point A relative to point B .
${}^i\dot{\mathbf{r}}_{AB}$	The derivative of the above vector in frame i .
$\mathbf{v}_{AB/i}$	The velocity of point A relative to point B , in the frame i .
$\mathbf{v}_{AB/i}^w$	The above vector coordinated in axes w .

Table 1.1: Overview of vector notation

coordinate a vector in a different axis system. The following notation will be used:

$$\mathbf{x}^a = C_{a/b}\mathbf{x}^b \quad (1.5.1)$$

where \mathbf{x}^a and \mathbf{x}^b are coordinate vectors of vector \mathbf{x} coordinated in the a and b axes respectively. $C_{a/b}$ is the direction cosine matrix that transforms a vector in b to a vector in a . The complete DCM matrices are listed in Appendix B.

1.6 Aerial Refueling

This section provides a brief introduction to aerial refueling. Section 1.6.1 investigates the mechanics of the flying boom refueling system. The degrees of freedom of the boom are described, and equations are derived to calculate boom parameters. Section 1.6.2 discusses the various flight points where AAR is performed. Section 1.6.3 briefly touches on the trajectories and flight points where aerial refueling will be simulated.

1.6.1 Flying Boom

There are currently two systems used for aerial refueling [9]. The probe-and-drogue system is used by the United States Navy and some European aircraft manufacturers. The system consists of a flexible hose that trails the tanker aircraft. A drogue (also called a basket) is attached to the hose and stabilises it. The receiver aircraft is piloted to connect a rigid probe to the drogue. This system has advantages, but is not feasible for a large receiver as the fuel flow rate is too low. Figure 1.1 shows aircraft engaged in aerial refueling using the probe-and-drogue system.



Figure 1.1: A tanker refueling a helicopter using the probe-and-drogue system [35]

The flying boom system uses a rigid boom attached to the tanker. The boom is equipped with aerodynamic surfaces that can be controlled by a boom operator in the tanker. The receiver aircraft is tasked to remain in position while the boom operator manoeuvres the boom into position and connects the boom tip to a receptacle on the receiver. Figure 1.2 shows aircraft engaged in aerial refueling using the flying boom system.



Figure 1.2: A tanker refueling a fighter aircraft using the flying boom system [36]

1.6.1.1 Mechanics

The AAR controller's performance will be judged on the deviation of the boom from the nominal position. The boom's offset from its nominal position is measured in the boom parameters which describe the three degrees of freedom of the boom, as shown in Figure 1.3.

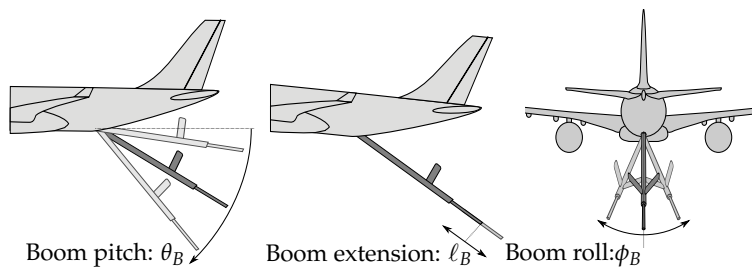


Figure 1.3: Flying boom degrees of freedom (not to scale)

The position of the boom is measured in the boom axes. The origin of the boom axes is located at the universal joint where the boom is connected to the tanker. The X-axis is positive towards the front of the aircraft, in the plane of symmetry of the aircraft. The X-axis may be inclined with respect to the X-axis of the tanker's body axes by the angle τ . In the case of the A330 MRTT, τ is three degrees. The Y-axis is positive to the right, parallel to the Y-axis in the body axes. The Z-axis is positive downward.

Boom pitch angle is defined as the angle between the boom and the X-axis of the boom axes. The nominal value is 30 degrees with permissible errors of 10 degrees in each direction. A boom pitch angle error can be induced by relative movement (especially in the normal axis) of the tanker and receiver, but also due to changes in the tanker's pitch angle.

Boom roll angle is defined as the angle between the boom and the ZX-plane of the boom axes projected onto the YZ-plane. The nominal value is 0 degrees with permissible errors of 20 degrees in each direction. Relative movement in the Y-axis or tanker roll disturbances will cause a boom roll angle error.

Boom extension is the change in the length of the boom. The nominal value is 12m with permissible errors of 2 metres in each direction. Relative movement in the X-axis is the primary cause of boom extension errors.

1.6.1.2 Boom Envelope

The boom envelopes define how far the boom can move from its nominal position. The following two envelopes are defined:

connect The receptacle must remain inside this envelope to enable the boom operator to connect the boom to the receiver's receptacle.

disconnect The disconnect envelope describes the boom's maximum permissible deflection from the nominal position. If the receptacle ever moves outside the disconnect envelope, the boom will automatically disconnect from the receptacle.

The permissible deviation for each degree of freedom is given in Table 1.2. The shapes of the envelopes are shown in Figure 1.4.

Parameter	Connect		Disconnect	
Pitch θ_b	26°	37°	20°	40°
Roll ϕ_b	-10°	10°	-20°	20°
Extension ℓ_b	15.1m	16.4m	13.9m	17.6m

Table 1.2: Rigid boom envelope definitions

To avoid cumbersome three-dimensional graphs, the results from simulations will be shown two-dimensionally. The three-dimensional volume in Figure 1.4 is complex and cannot be easily represented without losing some information. Figure 1.5 shows a side-view of the boom envelope when the roll angle is zero. The RR position will be plotted in the envelope using only boom extension and pitch angle.

Figure 1.6 shows the rear-view plot that will be used to judge the lateral performance of the control system. The X-axis and Y-axis are the roll and pitch angles of the boom respectively. Using the boom angles as the graph axes makes the envelopes appear as rectangles, even though, in space, they are not. The combination of the side- and rear-view envelope plots makes the performance of the control system clear and easy to interpret.

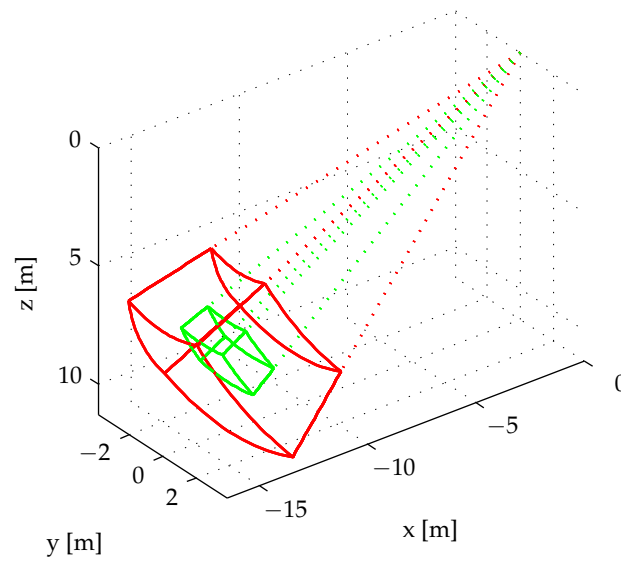


Figure 1.4: Boom envelopes in three dimensions

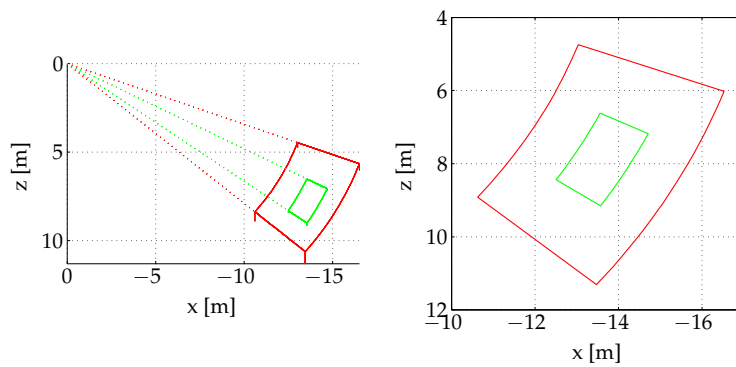


Figure 1.5: Three-dimensional and two-dimensional views of side envelope plot

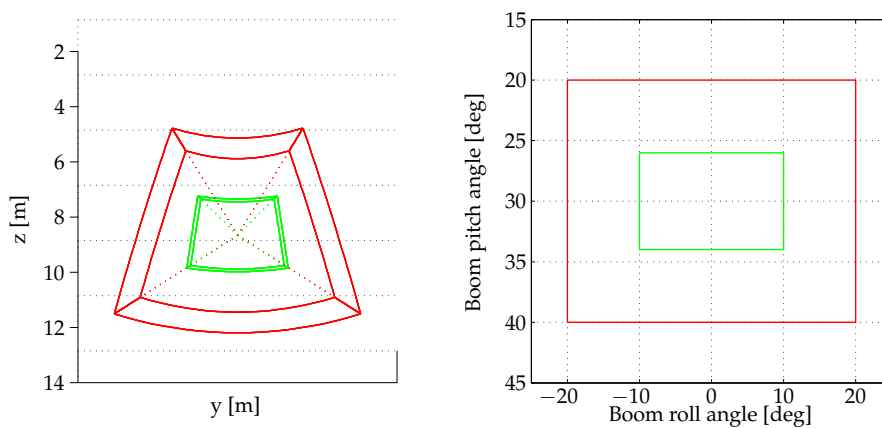


Figure 1.6: Three-dimensional and two-dimensional views of rear envelope plot

1.6.1.3 Calculation

To determine whether the receiver is successfully controlling the RR to remain inside the envelope, the boom parameters need to be calculated from the available measurements. Furthermore, the positions and velocity errors need to be calculated for use in the feedback systems. The non-linear simulation makes the velocities, rotation and position of the receiver and tanker available for these calculations. In a practical system, these quantities will not all be available and an estimator will be required. Such an estimator is investigated in [32]. For the purposes of this project, it is assumed that all required measurements are available. Consider the tanker and receiver shown in Figure 1.7.

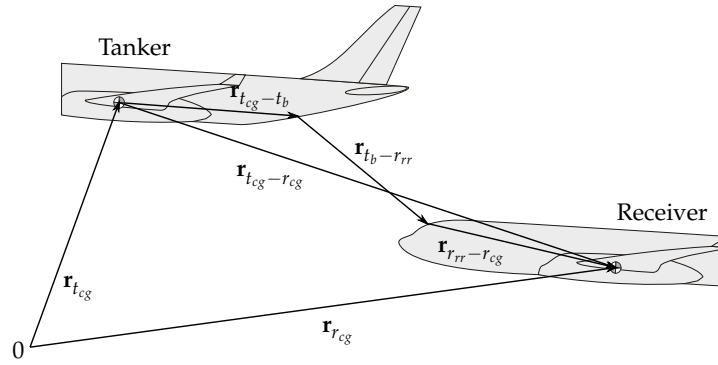


Figure 1.7: Calculating boom position

Boom Position A vector equation is constructed to describe the position of the receiver's receptacle, $r_{r_{rr}}$, relative to the boom attachment point on the tanker, r_{t_b} .

$$\begin{aligned} \mathbf{r}_{t_b-r_{rr}} &= \mathbf{r}_{t_{cg}-r_{cg}} - \mathbf{r}_{t_{cg}-t_b} - \mathbf{r}_{r_{rr}-r_{cg}} \\ &= \mathbf{r}_{r_{cg}} - \mathbf{r}_{t_{cg}} - \mathbf{r}_{t_{cg}-t_b} - \mathbf{r}_{r_{rr}-r_{cg}} \end{aligned} \quad (1.6.1)$$

In the non-linear simulations, the positions of the tanker and receiver, $\mathbf{r}_{r_{cg}}$ and $\mathbf{r}_{t_{cg}}$ respectively, are coordinated in the earth axes. The values of $\mathbf{r}_{t_{cg}-t_b}$ and $\mathbf{r}_{r_{rr}-r_{cg}}$ need to be calculated using the current CG position of the aircraft, and will be coordinated in the aircraft's body axes. DCM matrices are applied to the equation. The boom axis system will be indicated using a superscript b .

$$\begin{aligned} \mathbf{r}_{t_b-r_{rr}}^b &= C_{b/t} C_{t/i} \left[\mathbf{r}_{r_{cg}}^i - \mathbf{r}_{t_{cg}}^i - C_{i/t} \mathbf{r}_{t_{cg}-t_b}^t - C_{i/r} \mathbf{r}_{r_{rr}-r_{cg}}^r \right] \\ &= \begin{bmatrix} x_b \\ y_b \\ z_b \end{bmatrix} \end{aligned} \quad (1.6.2)$$

The RR position errors used for feedback are calculated by subtracting $\mathbf{r}_{r_{rr}-r_{cg}}$ from its nominal value, and coordinating the resulting vector in the error axes.

$$\begin{bmatrix} x_{rr} \\ y_{rr} \\ z_{rr} \end{bmatrix} = C_{e/b} \left(\mathbf{p}_{r_{rr}-r_{cg}}^b - \left(\mathbf{p}_{r_{rr}-r_{cg}}^b \right)_0 \right) \quad (1.6.3)$$

Boom Parameters The boom parameters can be calculated from $\mathbf{r}_{t_b-r_{rr}}^b$, as illustrated in Figure 1.8.

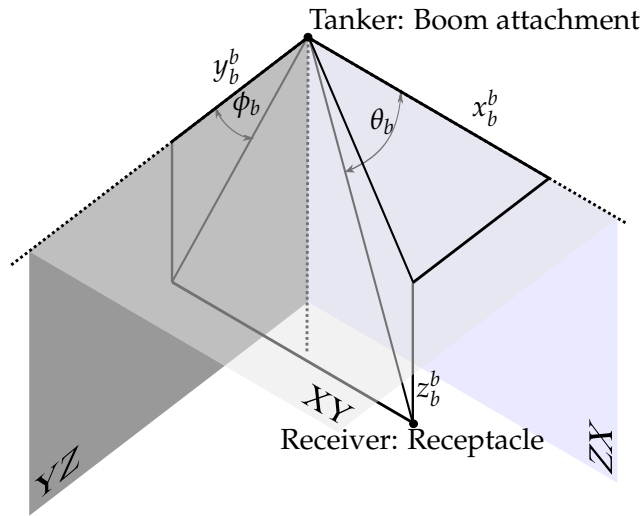


Figure 1.8: Calculating boom parameters from boom position

Equations 1.6.5 to 1.6.7 describe how the boom parameters are calculated.

$$\mathbf{r}_{t_b-r_{rr}}^b = \begin{bmatrix} x_b \\ y_b \\ z_b \end{bmatrix} \quad (1.6.4)$$

$$\theta_b = \arctan \left(\frac{\sqrt{z_b^2 + y_b^2}}{-x_b} \right) \quad (1.6.5)$$

$$\phi_b = \arctan \left(\frac{y_b}{z_b} \right) \quad (1.6.6)$$

$$\ell_b = \sqrt{z_b^2 + y_b^2 + x_b^2} \quad (1.6.7)$$

Velocities The architecture of the control system requires that the velocity errors of the refueling receptacle be used in feedback. Given that the velocities and the angular rates of the tanker and receiver are known, the RR velocity error can be calculated by deriving Equation 1.6.1 in the inertial frame.

$${}^i \dot{\mathbf{r}}_{t_b-r_{rr}} = {}^i \dot{\mathbf{r}}_{r_{cg}} - {}^i \dot{\mathbf{r}}_{t_{cg}} - {}^i \dot{\mathbf{r}}_{t_{cg}-t_b} - {}^i \dot{\mathbf{r}}_{r_{rr}-r_{cg}} \quad (1.6.8)$$

The derivatives in the inertial axes are rewritten in the body axes.

$${}^i \dot{\mathbf{r}}_{t_b-r_{rr}} = {}^i \dot{\mathbf{r}}_{0-r_{cg}} - {}^i \dot{\mathbf{r}}_{0-t_{cg}} - {}^t \dot{\mathbf{r}}_{t_{cg}-t_b} - \omega_{t/i} \times \mathbf{r}_{t_{cg}-t_b} - {}^r \dot{\mathbf{r}}_{r_{rr}-r_{cg}} - \omega_{r/i} \times \mathbf{r}_{r_{rr}-r_{cg}} \quad (1.6.9)$$

It can safely be assumed that the slow movement of the aircrafts' CGs (relative to the body axes) will not influence the dynamics of the control system. ${}^t \dot{\mathbf{r}}_{t_{cg}-t_b}$ and ${}^r \dot{\mathbf{r}}_{r_{rr}-r_{cg}}$ can thus be set to zero. This simplifies the equation to

$$\mathbf{v}_{t_b-r_{rr}/i} = \mathbf{v}_{r_{cg}/i} - \mathbf{v}_{t_{cg}/i} - \omega_{t/i} \times \mathbf{r}_{t_{cg}-t_b} - \omega_{r/i} \times \mathbf{r}_{r_{rr}-r_{cg}} \quad (1.6.10)$$

The vectors are coordinated into the appropriate axes.

$$\begin{bmatrix} u_{rr} \\ v_{rr} \\ w_{rr} \end{bmatrix} = C_{e/i} \left(\mathbf{v}_{r_{cg}/i}^i - \mathbf{v}_{t_{cg}/i}^i - C_{i/t} \omega_{t/i}^t \times \mathbf{r}_{t_{cg}-t_b}^t - C_{i/r} \omega_{r/i}^r \times \mathbf{r}_{r_{rr}-r_{cg}}^r \right) \quad (1.6.11)$$

All these calculations were implemented in Matlab Simulink; running in conjunction with the non-linear simulation described in Appendix C.

1.6.2 Flight Points

It is desirable for AAR to be performed at a wide variety of flight points and trajectories. As mentioned in Section 1.2, one of the goals of this project is to identify the effect of various flight point parameters on the performance of the control system. The following parameters combine to define a single flight point:

Receiver Mass The mass of the receiver (at the start of refueling), given in ton.

Tanker Mass The mass of the tanker (at the start of refueling), given in ton.

Calibrated Airspeed The calibrated airspeed of the tanker and receiver, given in knots.

Receiver CG Position The location of the centre of gravity of the receiver at the start of refueling, given as a percentage of the mean aerodynamic chord behind the leading edge. Written as $CG_r = 30\%$.

Tanker CG Position The location of the centre of gravity of the tanker at the start of refueling.

Flight Level The altitude of the tanker and receiver at the start of refueling, given in increments of 100ft. E.g. FL = 100 is an altitude of 10,000 ft.

Turbulence Medium or light turbulence, as defined in Section 1.6.4

Not all combinations of CG location, weight, flight level and velocity are valid. Figure 1.9 shows the valid combinations where AAR must be tested. Some simulations may be performed outside these envelopes to demonstrate certain effects, e.g. the toboggan trajectory.

1.6.3 Trajectories

This section presents four trajectories used during aerial refueling. The control and implementation of these trajectories will be covered in Chapter 5.

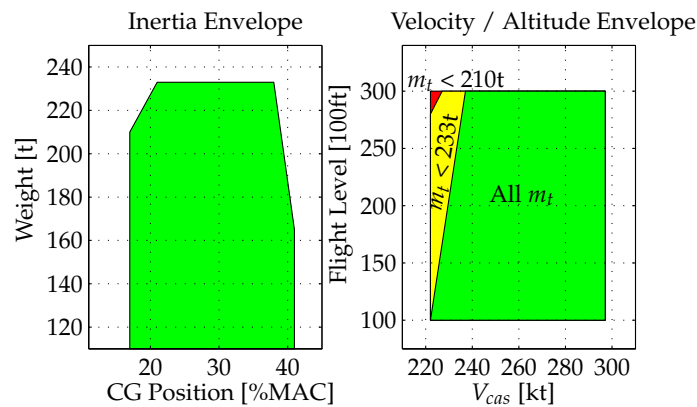


Figure 1.9: Flight envelope for AAR

1.6.3.1 Straight and Level

The simplest option is for all aerial refueling to occur during straight and level flight. However, this is not a practical solution for the refueling of a large receiver. Refueling takes a long time (more than fifteen minutes), during which time a large distance is covered. After refueling, the tanker needs to fly back to its starting position, which wastes fuel. Yet this trajectory is convenient for testing purposes, as there are no other factors complicating the control. The baseline performance of the control systems will be tested using the straight and level trajectory.

1.6.3.2 Racetrack

To prevent the tanker from moving too far from its starting location, the racetrack trajectory, illustrated in Figure 1.10, can be followed. The racetrack has two straight legs of 50 nautical miles and two 180 degree turns. The desired bank angle of these turns is 25 degrees.

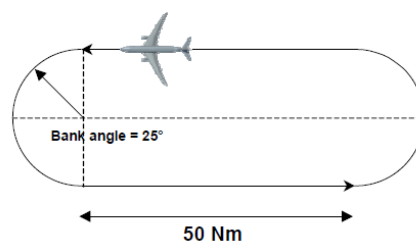


Figure 1.10: Racetrack trajectory [2]

1.6.3.3 Toboggan

At certain flight points (high speed, high mass), the engines might not have sufficient thrust to maintain the intended airspeed. This may be true for either the tanker (starting at a very high mass) or the receiver (ending at a high mass). Downwash over the receiver increases its trim thrust and further limits the flight points. In these situations, the toboggan trajectory is used [29] and has also been suggested by the project requirements [2]. A sink rate of 500 ft/min is maintained to lessen the required thrust. In a practical application, the toboggan and

racetrack trajectories need to be combined for optimal benefits, but due to limitations in scope, this will not be investigated in the current thesis.

1.6.3.4 Approach

The approach trajectory is the path followed by the receiver to reach the contact position behind the tanker. The receiver will start in the observation position illustrated in Figure 1.11.

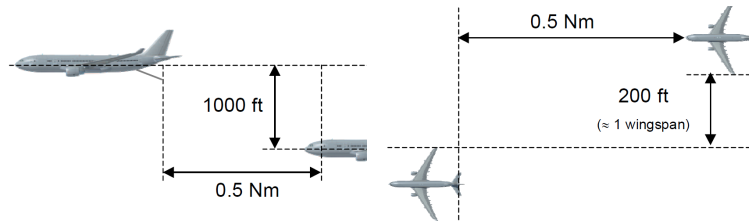


Figure 1.11: Observation position [2]

The receiver moves from the observation to the pre-contact position shown in Figure 1.12 before moving towards the contact position.

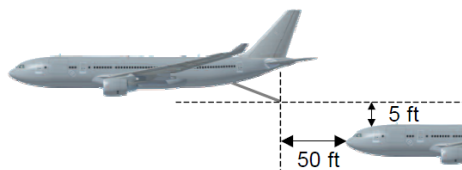


Figure 1.12: Pre-contact position [2]

1.6.4 Turbulence

During AAR, the tanker and the receiver are subjected to turbulence. Turbulence will be generated for the non-linear simulation using the MIL-STD-1797 standard model [11]. The turbulence is modelled as a field through which the tanker and receiver fly. The two aircraft experience the same turbulence, with an appropriate time delay between the tanker and receiver. Light and medium turbulence will be used.

Chapter 2

Modelling

2.1 Overview

This chapter presents the derivation of non-linear and linear models for a large receiver aircraft during automated aerial refueling (AAR). During AAR, the receiver aircraft needs to accurately maintain the position of its refueling receptacle (RR) relative to the tanker. The receiver will change orientation to generate aerodynamic forces. Figure 2.1 shows a large and a small aircraft engaged in aerial refueling.

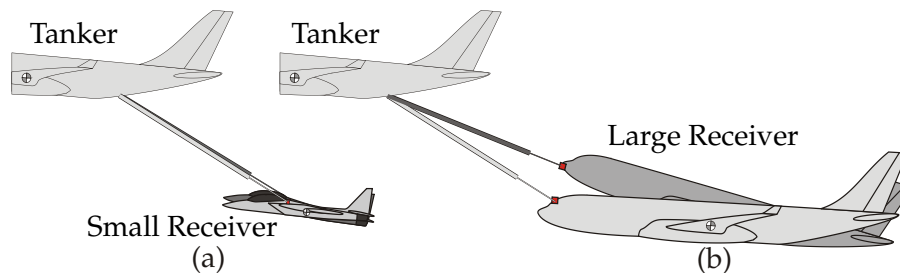


Figure 2.1: Effect of the relative distance between CG and RR

On small, fighter-sized aircraft, the refueling receptacle is close to the centre of gravity (CG). As the aircraft changes orientation, the position of the RR relative to the centre of gravity does not change significantly, and thus the refueling boom does not change orientation. It is thus possible to regulate the RR inside the required area by regulating the position of the receiver's CG relative to the tanker.

On a large aircraft, such as an Airbus A330 MRTT, the RR is located near the nose of the aircraft. When the A330 MRTT changes orientation, the displacement of the RR is much larger than in the previous case. A traditional aircraft model that tracks the movement of the aircraft CG will not capture these additional dynamics. In the non-linear simulations, which formed part of this study and which will be presented later, it is found that in medium turbulence the receiver can experience pitch angle disturbances of up to three degrees. This results in a deviation of the RR of more than one metre. This deviation represents a significant portion of the permissible movement of the RR during refueling. The permissible movement for the RR in the flying boom refueling system is shown in Chapter 1. It is proposed that these added

dynamics are significant enough to require inclusion in the linear model when automating a large aircraft for aerial refueling.

This chapter derives a novel aircraft model that describes the movement of the RR specifically, not the CG. Subsequent chapters will analyse the linear model to test the aforementioned proposition. Section 2.2 presents the refueling scenario as two rigid bodies moving and rotating in an inertial frame. Non-linear differential equations are set up for the error in the refueling receptacle's position and velocity. In Sections 2.3 and 2.4, the non-linear model is decoupled to create linear models for the longitudinal and lateral movement of the RR.

Furthermore, this chapter investigates the modelling of the tanker's effect on the receiver. While flying behind the tanker, the receiver is exposed to a flow field generated by the tanker. The goal of this thesis is not to create an accurate model describing the interaction between two Airbus A330 MRTT aircraft. Instead, Section 2.5 investigates research on the topic to determine the most likely effects. The interaction model is written in a form that simplifies its inclusion in both the linear aircraft model and non-linear simulation.

The relatively slow engine response of a large aircraft is one of the main challenges faced when automating aerial refueling. Consequently, a representative engine model is important in order to perform meaningful non-linear simulations. Airbus did not make a non-linear engine model available to Stellenbosch University, but did supply response data generated by a high-fidelity simulation. In Section 2.6, a non-linear engine model is created to match the supplied response data. This model will be used in non-linear simulation and during control design.

2.2 Non-linear Receptacle Dynamics

2.2.1 Overview

In this section, a novel set of non-linear differential equations for the movement of the refueling receptacle is derived. Initially, the equations are written for an entirely generic refueling scenario, in which the refueling receptacle position can be anywhere on the receiver. This results in a set of equations that could be adapted to any refueling scenario. Subsequently, the equations are simplified by constraining the equations to the specific location of the RR on the Airbus A330 MRTT.

The relative positions of the RR and the tanker are more important than the absolute position of the RR. Consequently, the states for the set of differential equations are chosen as the position and velocity errors of the refueling receptacle. The model will include the movement of the tanker and can thus be used for a cooperative control system controlling the tanker and receiver simultaneously. This will not be done here, as the requirements of this project do not allow changing the tanker's control system. The tanker movement will be seen as a disturbance.

Consider Figure 2.2, which illustrates the tanker and receiver in the contact position.

The figure shows three frames of reference moving relative to each other. The inertial frame, receiver body frame, and error frames are indicated by F_i , F_r and F_e respectively. Point O is fixed in the inertial frame at some convenient location. Point C is fixed in the body frame at

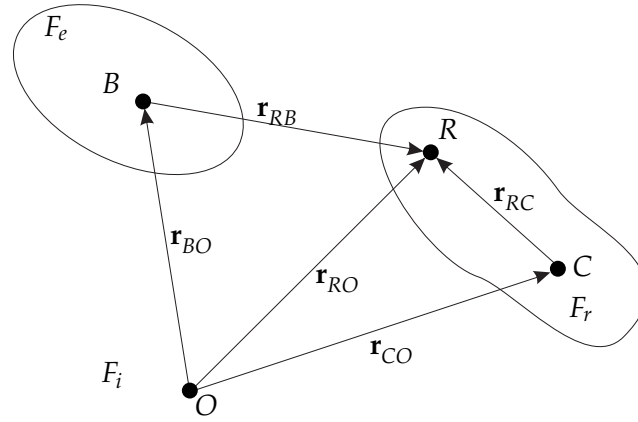


Figure 2.2: Illustration of frames of reference in the AAR scenario

the receiver's centre of gravity. Point R represents the refueling receptacle of the receiver and is fixed in the body frame, F_r . Point B is fixed in the error frame and represents the zero error position of the boom's tip, and thus the desired position of the refueling receptacle. Two vectors are defined to describe the error.

\mathbf{r}_{RB} The relative position between the desired location of the boom tip and the receptacle.

$\mathbf{v}_{RB/e}$ The relative velocity between the desired location of the boom tip and the receptacle in the error frame.

To include the error states in the linear model, the above vectors must be coordinated in an axis system. The error vectors will be coordinated in the error axes. As stated in Section 1.5, the error axes are aligned with the aerodynamic axes of the receiver. The derivatives of the vectors should thus be taken in the error frame. The error states are shown in Equation 2.2.1:

$$\mathbf{r}_{RB}^e = \begin{bmatrix} x_{rr} \\ y_{rr} \\ z_{rr} \end{bmatrix} \quad \mathbf{v}_{RB/e}^e = \begin{bmatrix} u_{rr} \\ v_{rr} \\ w_{rr} \end{bmatrix} \quad (2.2.1)$$

2.2.2 Velocity

From Figure 2.2, the position of the refueling receptacle relative to the nominal position of the boom tip can be written as

$$\mathbf{r}_{RB} = \mathbf{r}_{RO} - \mathbf{r}_{BO} = \mathbf{r}_{CO} + \mathbf{r}_{RC} - \mathbf{r}_{BO} \quad (2.2.2)$$

Note that \mathbf{r}_{RB} is the position of the refueling receptacle relative to the receiver's CG. Both sides of the equation are differentiated in the inertial frame, i .

$${}^i \dot{\mathbf{r}}_{RB} = {}^i \dot{\mathbf{r}}_{CO} + {}^i \dot{\mathbf{r}}_{RC} - {}^i \dot{\mathbf{r}}_{BO} \quad (2.2.3)$$

The derivative of \mathbf{r}_{RC} in the inertial frame cannot be easily calculated since it changes with the orientation of the receiver. It is, however, easy to find the derivative in the receiver's body frame, r . The Coriolis equation describes the relationship between derivatives taken in frames rotating relative to one another:

$$\left. \frac{d\mathbf{r}}{dt} \right|_r = \left. \frac{d\mathbf{r}}{dt} \right|_i - \boldsymbol{\omega}_{r/i} \times \mathbf{r} \quad (2.2.4)$$

Equation 2.2.4 is applied to change the derivatives of \mathbf{r}_{RB} and \mathbf{r}_{RC} to the error frame and receiver's body frame respectively.

$${}^e \dot{\mathbf{r}}_{RB} = {}^i \dot{\mathbf{r}}_{RB} - \boldsymbol{\omega}_{e/i} \times \mathbf{r}_{RB} \quad (2.2.5)$$

$${}^r \dot{\mathbf{r}}_{RC} = {}^i \dot{\mathbf{r}}_{RC} - \boldsymbol{\omega}_{r/i} \times \mathbf{r}_{RC} \quad (2.2.6)$$

where $\boldsymbol{\omega}_{e/i}$ is the rotation of the error frame relative to the inertial frame. Equations 2.2.5 and 2.2.6 are substituted into Equation 2.2.3, leading to

$${}^e \dot{\mathbf{r}}_{RB} + \boldsymbol{\omega}_{e/i} \times \mathbf{r}_{RB} = {}^i \dot{\mathbf{r}}_{CO} + {}^r \dot{\mathbf{r}}_{RC} + \boldsymbol{\omega}_{r/i} \times \mathbf{r}_{RC} - {}^i \dot{\mathbf{r}}_{BO} \quad (2.2.7)$$

The position derivatives are rewritten as velocities in the specified frames, and the terms are rearranged.

$$\mathbf{v}_{RB/e} = \mathbf{v}_{CO/i} + \mathbf{v}_{RC/r} + \boldsymbol{\omega}_{r/i} \times \mathbf{r}_{RC} - \mathbf{v}_{BO/i} - \boldsymbol{\omega}_{e/i} \times \mathbf{r}_{RB} \quad (2.2.8)$$

During the refueling of a large aircraft, the location of the centre of gravity (on the body of the aircraft) will change very slowly. Thus – in the body axes – the position of the RR relative to the CG will also change slowly. In the case of an Airbus A330 MRTT, the value will change approximately two metres over thirty minutes. The velocity term $\mathbf{v}_{RC/r}$ will thus be very small. This effect does not need to be modelled dynamically. The velocity term is removed from the equation in order to simplify further derivation. On smaller aircraft, where the fuel received forms a significant part of the aircraft inertia, this term cannot be ignored. Significant research has been performed on the modelling of these effects for smaller aircraft [16]. Equation 2.2.8 simplifies to

$$\mathbf{v}_{RB/e} = \mathbf{v}_{CO/i} - \mathbf{v}_{BO/i} + \boldsymbol{\omega}_{r/i} \times \mathbf{r}_{RC} - \boldsymbol{\omega}_{e/i} \times \mathbf{r}_{RB} \quad (2.2.9)$$

To find the derivative of the velocity error, Equation 2.2.8 is differentiated again in the inertial frame.

$$\begin{aligned} {}^i \dot{\mathbf{v}}_{RB/e} &= {}^i \dot{\mathbf{v}}_{CO/i} - {}^i \dot{\mathbf{v}}_{BO/i} \\ &\quad + {}^i \dot{\boldsymbol{\omega}}_{r/i} \times \mathbf{r}_{RC} + \boldsymbol{\omega}_{r/i} \times {}^i \dot{\mathbf{r}}_{RC} \\ &\quad - {}^i \dot{\boldsymbol{\omega}}_{e/i} \times \mathbf{r}_{RB} - \boldsymbol{\omega}_{e/i} \times {}^i \dot{\mathbf{r}}_{RB} \end{aligned} \quad (2.2.10)$$

The derivatives are converted to other frames as before,

$$\begin{aligned} {}^e \dot{\mathbf{v}}_{RB/e} + \boldsymbol{\omega}_{e/i} \times \mathbf{v}_{RB/e} &= {}^i \dot{\mathbf{v}}_{CO/i} - {}^i \dot{\mathbf{v}}_{BO/i} \\ &\quad + {}^i \dot{\boldsymbol{\omega}}_{r/i} \times \mathbf{r}_{RC} + \boldsymbol{\omega}_{r/i} \times ({}^r \dot{\mathbf{r}}_{RC} + \boldsymbol{\omega}_{r/i} \times \mathbf{r}_{RC}) \\ &\quad - {}^i \dot{\boldsymbol{\omega}}_{e/i} \times \mathbf{r}_{RB} - \boldsymbol{\omega}_{e/i} \times ({}^e \dot{\mathbf{r}}_{RB} + \boldsymbol{\omega}_{e/i} \times \mathbf{r}_{RB}) \end{aligned} \quad (2.2.11)$$

The velocity derivatives are rewritten as accelerations and the terms are rearranged. The velocities of the refueling receptacle in the body frame are removed as before.

$$\begin{aligned} {}^e \dot{\mathbf{v}}_{RB/e} &= \mathbf{a}_{CO/i} - \mathbf{a}_{BO/i} \\ &\quad + \boldsymbol{\alpha}_{r/i} \times \mathbf{r}_{RC} + \boldsymbol{\omega}_{r/i} \times \mathbf{v}_{RC/r} + \boldsymbol{\omega}_{r/i} \times \boldsymbol{\omega}_{r/i} \times \mathbf{r}_{RC} \\ &\quad - \boldsymbol{\alpha}_{e/i} \times \mathbf{r}_{RB} - 2\boldsymbol{\omega}_{e/i} \times \mathbf{v}_{RB/e} - \boldsymbol{\omega}_{e/i} \times \boldsymbol{\omega}_{e/i} \times \mathbf{r}_{RB} \end{aligned} \quad (2.2.12)$$

where $\alpha_{r/i}$ is the angular acceleration of the receiver's body frame relative to the inertial frame. Each vector is coordinated into an axis system. For each vector the most convenient axis system is chosen, and transformation matrices are included to ensure each term is coordinated in the error axes.

$$\begin{aligned} {}^e\dot{\mathbf{v}}_{RB/e} &= C_{e/i}\mathbf{a}_{CO/i}^i - C_{e/i}\mathbf{a}_{BO/i}^i \\ &+ C_{e/w}C_{w/r}(\alpha_{r/i}^r \times \mathbf{r}_{RC}^r + \omega_{r/i}^r \times \omega_{r/i}^r \times \mathbf{r}_{RC}^r) \\ &- (\alpha_{e/i}^e \times \mathbf{r}_{RB}^e + 2\omega_{e/i}^e \times \mathbf{v}_{RB/e}^e + \omega_{e/i}^e \times \omega_{e/i}^e \times \mathbf{r}_{RB}^e) \end{aligned} \quad (2.2.13)$$

Equation 2.2.13 is expanded. The term $\mathbf{a}_{CO/i}^i$ describes the acceleration of the receiver's centre of gravity in the inertial frame. All forces acting on the aircraft is contained in this term. These include gravity, thrust and actuation surfaces. The term, $\mathbf{a}_{BO/i}^i$ is the acceleration of the desired position of the receptacle. During straight and level flight this is ideally zero, but turbulence will cause the desired position to move as the tanker moves.

$$\begin{aligned} {}^e\dot{\mathbf{v}}_{RB/e} &= \frac{1}{m} \begin{bmatrix} -D \\ -S \\ -L \end{bmatrix} + C_{e/i} \begin{bmatrix} 0 \\ 0 \\ g \end{bmatrix} + C_{e/b} \frac{1}{m} \begin{bmatrix} T \\ 0 \\ 0 \end{bmatrix} - a_{B/O}^e \\ &+ C_{e/b} \left(\begin{bmatrix} \dot{P} \\ \dot{Q} \\ \dot{R} \end{bmatrix} \times \begin{bmatrix} l_x \\ l_y \\ l_z \end{bmatrix} + \begin{bmatrix} P \\ Q \\ R \end{bmatrix} \times \begin{bmatrix} P \\ Q \\ R \end{bmatrix} \times \begin{bmatrix} l_x \\ l_y \\ l_z \end{bmatrix} \right) \\ &- \left(\begin{bmatrix} \dot{P}_w \\ \dot{Q}_w \\ \dot{R}_w \end{bmatrix} \times \begin{bmatrix} x_{rr} \\ y_{rr} \\ z_{rr} \end{bmatrix} + 2 \begin{bmatrix} P_w \\ Q_w \\ R_w \end{bmatrix} \times \begin{bmatrix} u_{rr} \\ v_{rr} \\ w_{rr} \end{bmatrix} + \begin{bmatrix} P_w \\ Q_w \\ R_w \end{bmatrix} \times \begin{bmatrix} P_w \\ Q_w \\ R_w \end{bmatrix} \times \begin{bmatrix} x_{rr} \\ y_{rr} \\ z_{rr} \end{bmatrix} \right) \end{aligned} \quad (2.2.14)$$

Where l_x , l_y and l_z are the position of the RR in the body axes. Equation 2.2.14 describes the derivative of the velocity error for the refueling receptacle during aerial refueling. The novel equation includes not only the effect of aerodynamic and actuation forces on the receiver, but also the effect of the distance between the CG and RR, and the rotation of the receiver's velocity vector. The influence of the tanker's acceleration is clearly shown as well.

2.2.3 Position

The position error states are the components of the position of point R relative to B , as shown in Figure 2.2. The error vector is coordinated in the error axes. Finding the differential equation for the position states is trivial, since the velocity error is coordinated in the same axes.

$${}^e\dot{\mathbf{r}}_{RB} = \mathbf{v}_{RB/e} \quad (2.2.15)$$

The vectors are coordinated in the error axes.

$${}^e\dot{\mathbf{r}}_{RB} = \mathbf{v}_{RB/e} = \begin{bmatrix} u_{rr} \\ v_{rr} \\ w_{rr} \end{bmatrix} \quad (2.2.16)$$

2.3 Linear Longitudinal Receptacle Dynamics

The differential equations derived for the position and velocity errors are linearised in this section. The technique and nomenclature presented in [34] are followed. Since the lateral and longitudinal modes of the aircraft will be controlled separately, the equations are decoupled before linearisation, greatly reducing the complexity of the equations. Equation 2.2.14 is expanded and linearised for the longitudinal system. The model for straight and level flight is also derived here. It was found that this model is sufficiently robust to control the receiver during descending flight (toboggan trajectory) and banked flight (racetrack trajectory). It is possible to linearise the model at these trim points, to improve performance.

Equation 2.2.14 is simplified for the longitudinal system. All lateral states that do not have a steady-state component are set to zero.

$$\begin{aligned}
{}^e \dot{\mathbf{v}}_{RB/e}^e = & \left(\frac{1}{m} \begin{bmatrix} -D \\ 0 \\ -L \end{bmatrix} \right) + \begin{bmatrix} -C_\alpha S_\theta + S_\alpha C_\theta \\ 0 \\ S_\alpha S_\theta + C_\alpha C_\theta \end{bmatrix} g - a_{B/O}^e \\
& + \begin{bmatrix} C_\alpha & 0 & S_\alpha \\ 0 & 1 & 0 \\ -S_\alpha & 0 & C_\alpha \end{bmatrix} \left(\begin{bmatrix} T/m \\ 0 \\ 0 \end{bmatrix} + \begin{bmatrix} \ell_z \dot{Q} \\ 0 \\ -\ell_x \dot{Q} \end{bmatrix} + \begin{bmatrix} -\ell_x Q^2 \\ 0 \\ -\ell_z Q^2 \end{bmatrix} \right) \\
& - \left(\begin{bmatrix} \dot{Q}_w z_{rr} \\ 0 \\ -\dot{Q}_w x_{rr} \end{bmatrix} + 2 \begin{bmatrix} Q_w w_{rr} \\ 0 \\ -Q_w u_{rr} \end{bmatrix} + \begin{bmatrix} -Q_w^2 x_{rr} \\ 0 \\ -Q_w^2 z_{rr} \end{bmatrix} \right)
\end{aligned} \tag{2.3.1}$$

2.3.1 Axial Component

The axial component of the derivative of the velocity error vector, \dot{u}_{rr} , is isolated:

$$\begin{aligned}
\dot{u}_{rr} = f_{\dot{u}_{rr}}(\mathbf{X}, \mathbf{U}) = & \frac{-D}{m} \\
& + (T/m + \ell_z \dot{Q} - \ell_x Q^2) C_\alpha \\
& + (-\ell_x \dot{Q} - \ell_z Q^2) S_\alpha \\
& + (S_\alpha C_\theta - C_\alpha S_\theta) g \\
& - (\dot{Q}_w z_{rr} + 2Q_w w_{rr} - Q_w^2 x_{rr})
\end{aligned} \tag{2.3.2}$$

where \mathbf{X} and \mathbf{U} are the selected state and input vectors respectively and $f_{\dot{u}_{rr}}(\mathbf{X}, \mathbf{U})$ is the non-linear function describing \dot{u}_{rr} . The nabla operator is applied to both sides of the equation. The operator, as defined in [34], represents a row vector of partial derivatives and is introduced in detail in Appendix A. The change in the axial velocity error due to perturbations in the state

vector is

$$\begin{aligned}
\nabla_X f_{\dot{u}_{rr}} &= -\frac{1}{m} \nabla_X D \\
&+ [(T/m + \ell_z \dot{Q} - \ell_x Q^2)(-S_\alpha) + (-\ell_x \dot{Q} - \ell_z Q^2) C_\alpha] \nabla_X \alpha \\
&+ (\ell_z C_\alpha - \ell_x S_\alpha) \nabla_X \dot{Q} \\
&+ 2Q(-\ell_x C_\alpha - \ell_z S_\alpha) \nabla_X Q \\
&+ (C_\alpha C_\theta + S_\alpha S_\theta) g \nabla_X \alpha \\
&+ (-S_\alpha S_\theta - C_\alpha C_\theta) g \nabla_X \theta \\
&- \dot{Q}_w \nabla_X z_{rr} - 2Q_w \nabla_X w_{rr} + Q_w^2 \nabla_X x_{rr} \\
&- z_{rr} \nabla_X \dot{Q}_w - (2w_{rr} - 2Q_w x_{rr}) \nabla_X Q_w
\end{aligned} \tag{2.3.3}$$

The change in the axial velocity error due to perturbations in the input vector is

$$\begin{aligned}
\nabla_U f_{\dot{u}_{rr}} &= -\frac{1}{m} \nabla_U D \\
&+ \frac{C_\alpha}{m} \nabla_U T \\
&+ (\ell_z C_\alpha - \ell_x S_\alpha) \nabla_U \dot{Q} \\
&- z_{rr} \nabla_U \dot{Q}_w
\end{aligned} \tag{2.3.4}$$

Equations 2.3.3 and 2.3.4 are simplified by substituting the steady-state values. All rates and their derivatives have a steady-state value of zero. Further substitutions are made to introduce the flight path angle, γ ,

$$\nabla_X f_{\dot{u}_{rr}} = -\frac{1}{m} (\nabla_X D) - \frac{TS_\alpha}{m} (\nabla_X \alpha) + \ell_z^e (\nabla_X \dot{Q}) - g C_{\gamma+\omega} (\nabla_X \gamma) \tag{2.3.5}$$

$$\nabla_U f_{\dot{u}_{rr}} = -\frac{1}{m} (\nabla_U D) + \frac{C_\alpha}{m} (\nabla_U T) + \ell_x^e (\nabla_U \dot{Q}) \tag{2.3.6}$$

$$\ell_x^e = \ell_x \cos(\alpha_0) + \ell_z \sin(\alpha_0) \tag{2.3.7}$$

$$\ell_z^e = \ell_z \cos(\alpha_0) - \ell_x \sin(\alpha_0) \tag{2.3.8}$$

where ℓ_x^e is the axial distance between the CG and RR in the steady-state orientation of the error axes. The aerodynamic drag term, $\nabla_X D$, is expanded using the dimensional derivatives defined in Appendix A.

$$\nabla_X f_{\dot{u}_{rr}} = \frac{X_V}{m} (\nabla_X V) + \frac{X_\alpha - TS_\alpha}{m} (\nabla_X \alpha) + \ell_z^e (\nabla_X \dot{Q}) - g C_{\gamma+\omega} (\nabla_X \gamma) \tag{2.3.9}$$

$$\nabla_U f_{\dot{u}_{rr}} = \frac{X_{\delta_e}}{m} (\nabla_U \delta_e) + \frac{C_\alpha}{m} (\nabla_U T) + \ell_x^e (\nabla_U \dot{Q}) \tag{2.3.10}$$

The axial component of Equation 2.2.16 is very easy to linearise and results in

$$\nabla_X f_{\dot{x}_{rr}} = \nabla_X u_{rr} \tag{2.3.11}$$

2.3.2 Normal Component

The normal component of velocity error vector, \dot{w}_{rr} , is isolated.

$$\begin{aligned} \dot{w}_{rr} = f_{\dot{w}_{rr}}(X, U) = & -\frac{L}{m} + (S_\alpha S_\theta + C_\alpha C_\theta)g \\ & - (T/m + \ell_z \dot{Q} - \ell_x Q^2) S_\alpha \\ & - (\ell_x \dot{Q} + \ell_z Q^2) C_\alpha \\ & + (\dot{Q}_w x_{rr} + 2Q_w u_{rr} + Q_w^2 z_{rr}) \end{aligned} \quad (2.3.12)$$

The nabla operator is applied to both sides of the equation. The change in normal velocity error due to changes in the state vector is

$$\begin{aligned} \nabla_X f_{\dot{w}_{rr}} = & -\frac{1}{m} \nabla_X L \\ & - [(T/m + \ell_z \dot{Q} - \ell_x Q^2) C_\alpha - (\ell_x \dot{Q} + \ell_z Q^2) S_\alpha] \nabla_X \alpha \\ & - (\ell_z S_\alpha + \ell_x C_\alpha) \nabla_X \dot{Q} \\ & + 2Q (\ell_x S_\alpha - \ell_z C_\alpha) \nabla_X Q \\ & + (C_\alpha S_\theta - S_\alpha C_\theta) g \nabla_X \alpha \\ & + (S_\alpha C_\theta - C_\alpha S_\theta) g \nabla_X \theta \\ & + \dot{Q}_w \nabla_X x_{rr} + 2Q_w \nabla_X u_{rr} + 2Q_w^2 \nabla_X z_{rr} \\ & + x_{rr} \nabla_X \dot{Q}_w + (2u_{rr} + 2Q_w z_{rr}) \nabla_X Q_w \end{aligned} \quad (2.3.13)$$

The change in normal velocity error due to changes in the input vector is

$$\begin{aligned} \nabla_U f_{\dot{w}_{rr}} = & \frac{1}{m} \nabla_U L \\ & - \frac{S_\alpha}{m} \nabla_U T \\ & - (\ell_x C_\alpha + \ell_z S_\alpha) \nabla_U \dot{Q} \\ & + x_{rr} \nabla_U \dot{Q}_w \end{aligned} \quad (2.3.14)$$

Equations 2.3.13 and 2.3.14 are simplified as in the previous section.

$$\nabla_X f_{\dot{w}_{rr}} = -\frac{1}{m} (\nabla_X L) - \frac{TC_\alpha}{m} (\nabla_X \alpha) - \ell_e^w (\nabla_X \dot{Q}) + g S_{\theta-\alpha} (\nabla_X \gamma) \quad (2.3.15)$$

$$\nabla_U f_{\dot{w}_{rr}} = -\frac{1}{m} (\nabla_U L) - \frac{S_\alpha}{m} (\nabla_U T) - \ell_e^w (\nabla_U \dot{Q}) \quad (2.3.16)$$

Note that the term $g \sin(\theta - \alpha)$ equals zero during straight and level flight in still air. However, this term is not removed from the model. When the receiver is exposed to tanker downwash. In downwash the receiver's pitch angle will not equal its angle of attack, even during straight and level flight. The aerodynamic lift term, $\nabla_X L$, is expanded using the dimensional derivatives defined in Appendix A.

$$\begin{aligned} \nabla_X f_{\dot{w}_{rr}} = & \frac{Z_V}{m} (\nabla_X V) + \frac{Z_\alpha - TC_\alpha}{m} (\nabla_X \alpha) + \frac{Z_q}{m} (\nabla_X Q) \\ & - \ell_e^w (\nabla_X \dot{Q}) + g C_{\theta-\alpha} (\nabla_X \gamma) \end{aligned} \quad (2.3.17)$$

$$\nabla_U f_{\dot{w}_{rr}} = \frac{Z_{\delta_e}}{m} (\nabla_U \delta_e) - \frac{S_\alpha}{m} (\nabla_U T) - \ell_e^w (\nabla_U \dot{Q}) \quad (2.3.18)$$

The normal component of Equation 2.2.16 is easy to linearise and results in

$$\nabla_X f_{z_{rr}} = \nabla_X w_{rr} \quad (2.3.19)$$

2.3.3 State Space

In Appendix A, linear differential equations are given for airspeed, angle of attack, pitch rate and flight path angle. In the preceding section, linear differential equations were derived for the velocity and position error of the refueling receptacle in the longitudinal axes. This section combines the well-known dynamic equations with the novel equations to form a state-space model describing the linear longitudinal refueling receptacle dynamics. It is clear that the dynamics of u_{rr} are closely related to airspeed, and that w_{rr} is close to climb rate and thus flight path angle. Including all of these values in the state vector will lead to controllability problems. The state vector is thus chosen as

$$\mathbf{x} = \begin{bmatrix} \alpha & q & u_{rr} & w_{rr} \end{bmatrix}^T \quad (2.3.20)$$

Since airspeed and flight path angle were not chosen as states, $\nabla_X V$ and $\nabla_X \gamma$ need to be written in terms of the available states. Equation 2.2.8 describes the error states. The vectors are coordinated and expanded into Equation 2.3.21 below. All lateral states have been set to zero:

$$\begin{aligned} \begin{bmatrix} u_{rr} \\ v_{rr} \\ w_{rr} \end{bmatrix} &= \begin{bmatrix} \bar{V} \\ 0 \\ 0 \end{bmatrix} + \begin{bmatrix} C_\alpha & 0 & S_\alpha \\ * & * & * \\ -S_\alpha & 0 & C_\alpha \end{bmatrix} \begin{bmatrix} l_z Q \\ 0 \\ -l_x Q \end{bmatrix} \\ &- \begin{bmatrix} C_{\gamma-\gamma_t} & * & * \\ * & * & * \\ -S_{\gamma-\gamma_t} & * & * \end{bmatrix} \begin{bmatrix} \bar{V}_t \\ 0 \\ 0 \end{bmatrix} + \begin{bmatrix} Q_w z_{rr} \\ 0 \\ -Q_w x_{rr} \end{bmatrix} \end{aligned} \quad (2.3.21)$$

where γ_t and \bar{V}_t are the tanker's flight path angle and true airspeed. At steady state, these will match the receiver's values. Equation are extracted for u_{rr} and w_{rr} .

$$u_{rr} = \bar{V} + (C_\alpha l_z Q - S_\alpha l_x Q) - C_{\gamma-\gamma_t} \bar{V}_t \quad (2.3.22)$$

$$w_{rr} = -(S_\alpha l_z Q + C_\alpha l_x Q) + S_{\gamma-\gamma_t} \bar{V}_t \quad (2.3.23)$$

The nabla operator is applied on both sides with respect to the state vector.

$$\nabla_X u_{rr} = (\nabla_X \bar{V}) + (C_\alpha l_z - S_\alpha l_x)(\nabla_X Q) + S_{\gamma-\gamma_t} \bar{V}_t (\nabla_X \gamma) \quad (2.3.24)$$

$$\nabla_X w_{rr} = (S_\alpha l_z - C_\alpha l_x)(\nabla_X Q) + C_{\gamma-\gamma_t} \bar{V}_t (\nabla_X \gamma) \quad (2.3.25)$$

Substituting the steady-state values for the flight path angle, the equations above simplify to

$$\nabla_X u_{rr} = (\nabla_X \bar{V}) + (l_z^w)(\nabla_X Q) \quad (2.3.26)$$

$$\nabla_X w_{rr} = -(l_x^w)(\nabla_X Q) + \bar{V}_t (\nabla_X \gamma) \quad (2.3.27)$$

The equations above are solved simultaneously,

$$\nabla_X \bar{V} = \nabla_X u_{rr} + \ell_z^w (\nabla_X Q) \quad (2.3.28)$$

$$\nabla_X \gamma = \frac{1}{\bar{V}} (\nabla_X w_{rr}) + \frac{\ell_x^w}{\bar{V}} (\nabla_X Q) \quad (2.3.29)$$

Equations 2.3.28 and 2.3.29 are substituted into the linear equations for angle of attack and pitch rate from Appendix A. This results in a set of coupled linear differential equations where the velocity error of the RR is a state. Even though airspeed and flight path angle are not states, phugoid mode information has not been lost. The final linear longitudinal differential equations are:

$$\begin{aligned} \nabla_X f_{\dot{\alpha}} &= \frac{Z_\alpha - TC_\alpha}{m\bar{V}} (\nabla_X \alpha) \\ &+ \left[1 + \frac{Z_q}{m\bar{V}} - \frac{Z_V \ell_z^w}{m\bar{V}} - \frac{gS_{\theta-\alpha}}{V} \frac{\ell_x^\gamma}{\bar{V}} \right] (\nabla_X Q) \\ &+ \left[\frac{Z_V}{m\bar{V}} \right] (\nabla_X u_{rr}) \\ &+ \left[-\frac{gS_{\theta-\alpha}}{\bar{V}^2} \right] (\nabla_X w_{rr}) \end{aligned} \quad (2.3.30)$$

$$\begin{aligned} \nabla_U f_{\dot{\alpha}} &= \left[\frac{-S_\alpha}{m\bar{V}} \right] (\nabla_U T) \\ &+ \left[\frac{Z_{\delta_e}}{m\bar{V}} \right] \nabla_U \delta_e \\ &+ \left[\frac{Z_{\delta_s}}{m\bar{V}} \right] \nabla_U \delta_s \end{aligned} \quad (2.3.31)$$

$$\begin{aligned} \nabla_X f_{\dot{Q}} &= \frac{M_\alpha}{I_{yy}} (\nabla_X \alpha) \\ &+ \left[\frac{M_q}{I_{yy}} - \frac{M_V \ell_z^w}{I_{yy}} \right] (\nabla_X Q) \\ &+ \frac{M_V}{I_{yy}} (\nabla_X u_{rr}) \end{aligned} \quad (2.3.32)$$

$$\begin{aligned} \nabla_U f_{\dot{Q}} &= \left[\frac{M_{\delta_e}}{I_{yy}} \right] \nabla_U \delta_e \\ &+ \left[\frac{M_{\delta_s}}{I_{yy}} \right] \nabla_U \delta_s \end{aligned} \quad (2.3.33)$$

$$\begin{aligned}
\nabla_X f_{\dot{u}_{rr}} &= \left[\frac{X_\alpha - TS_\alpha}{m} + \frac{M_\alpha \ell_z^w}{I_{yy}} \right] (\nabla_X \alpha) \\
&+ \left[-\frac{X_V \ell_z^\gamma}{m} - \frac{g C_{\theta-\alpha} \ell_x^w}{\bar{V}} + \ell_z^w \left(\frac{M_q}{I_{yy}} - \frac{M_V \ell_z^\gamma}{I_{yy}} \right) \right] \nabla_X Q \\
&+ \left[\frac{X_V}{m} + \frac{M_V \ell_z^w}{I_{yy}} \right] \nabla_X u_{rr} \\
&+ \left[-\frac{g C_{\theta-\alpha}}{\bar{V}} \right] \nabla_X w_{rr}
\end{aligned} \tag{2.3.34}$$

$$\begin{aligned}
\nabla_U f_{\dot{u}_{rr}} &= \left[\frac{C_\alpha}{m} \right] \nabla_U T \\
&+ \left[\frac{X_{\delta_e}}{m} + \frac{M_{\delta_e} \ell_z^w}{I_{yy}} \right] \nabla_U \delta_e \\
&+ \left[\frac{X_{\delta_s}}{m} + \frac{M_{\delta_s} \ell_z^w}{I_{yy}} \right] \nabla_U \delta_s
\end{aligned} \tag{2.3.35}$$

$$\begin{aligned}
\nabla_X f_{\dot{w}_{rr}} &= \left[\frac{Z_\alpha - TC_\alpha}{m} - \frac{M_\alpha \ell_x^w}{I_{yy}} \right] (\nabla_X \alpha) \\
&+ \left[\frac{Z_q}{m} + \frac{Z_v \ell_z^w}{m} + \frac{g C_{\theta-\alpha} \ell_x^w}{\bar{V}} - \ell_x^w \left(\frac{M_q}{I_{yy}} - \frac{M_V \ell_z^\gamma}{I_{yy}} \right) \right] (\nabla_X Q) \\
&+ \left[\frac{Z_V}{m} - \frac{M_V \ell_x^w}{I_{yy}} \right] (\nabla_X u_{rr}) \\
&+ \left[\frac{g C_{\theta-\alpha}}{\bar{V}} \right] (\nabla_X w_{rr})
\end{aligned} \tag{2.3.36}$$

$$\begin{aligned}
\nabla_U f_{\dot{w}_{rr}} &= \left[\frac{-S_\alpha}{m} \right] \nabla_U T \\
&+ \left[\frac{Z_{\delta_e}}{m} - \frac{M_{\delta_e} \ell_x^w}{I_{yy}} \right] \nabla_U \delta_e \\
&+ \left[\frac{Z_{\delta_s}}{m} - \frac{M_{\delta_s} \ell_x^w}{I_{yy}} \right] \nabla_U \delta_s
\end{aligned} \tag{2.3.37}$$

The inclusion of the refueling receptacle dynamics has added several terms to the well-known longitudinal model. Some of these terms will have a significant impact on the model, while others will be negligible.

2.3.4 Longitudinal Decoupling

It is possible to decouple the longitudinal dynamics into normal and axial dynamics. The coupling between these two systems is stronger than between the longitudinal and lateral systems. Decoupling is performed here primarily to aid in reducing complexity in order to perform analysis.

2.3.4.1 Normal

The normal state and inputs vectors are chosen as

$$\mathbf{x} = \begin{bmatrix} \alpha & q & w_{rr} & z_{rr} \end{bmatrix}^T \quad \mathbf{u} = \begin{bmatrix} \delta_e & \delta_s \end{bmatrix} \tag{2.3.38}$$

The linear differential equations for the normal dynamics of the refueling point are

$$\begin{aligned} \nabla_X f_{\dot{\alpha}} &= \frac{Z_\alpha - TC_\alpha}{m\bar{V}} (\nabla_X \alpha) + \left[1 + \frac{Z_q}{m\bar{V}} \right] (\nabla_X Q) \\ &\quad - \frac{gS\gamma C_{\omega_d}}{\bar{V}^2} (\nabla_X w_{rr}) \end{aligned} \quad (2.3.39)$$

$$\nabla_U f_{\dot{\alpha}} = \left[\frac{Z_{\delta_e}}{mV_T} \right] \nabla_U \delta_e \quad (2.3.40)$$

$$\nabla_X f_{\dot{Q}} = \frac{M_\alpha}{I_{yy}} (\nabla_X \alpha) + \left[\frac{M_q}{I_{yy}} - \frac{M_V \ell_z^\gamma}{I_{yy}} \right] (\nabla_X Q) + \frac{-M_V S \omega_d}{I_{yy}} (\nabla_X w_{rr}) \quad (2.3.41)$$

$$\nabla_U f_{\dot{Q}} = \left[\frac{M_{\delta_e}}{I_{yy}} \right] \nabla_U \delta_e \quad (2.3.42)$$

$$\begin{aligned} \nabla_X f_{\dot{w}_{rr}} &= \left[\frac{Z_\alpha - TC_\alpha}{m} - \frac{M_\alpha \ell_x^w}{I_{yy}} \right] (\nabla_X \alpha) \\ &\quad + \left[\frac{Z_q}{m} - \frac{Z_v \ell_z^\gamma}{m} + \frac{gC_{\gamma+\omega_d} \ell_x^\gamma}{V_T} - \ell_x^w \left(\frac{M_q}{I_{yy}} - \frac{M_V \ell_z^\gamma}{I_{yy}} \right) \right] (\nabla_X Q) \\ &\quad + \left[-\frac{Z_V S \omega_d}{m} + \frac{gC_{\gamma+\omega_d} C_{\omega_d}}{V_T} - \frac{M_V S \omega_d \ell_x^w}{I_{yy}} \right] (\nabla_X w_{rr}) \end{aligned} \quad (2.3.43)$$

$$\nabla_U f_{\dot{w}_{rr}} = \left[\frac{Z_{\delta_e}}{m} - \frac{M_{\delta_e} \ell_x^w}{I_{yy}} \right] \nabla_U \delta_e \quad (2.3.44)$$

$$\nabla_X f_{\dot{z}_{rr}} = [1] (\nabla_X w_{rr}) \quad (2.3.45)$$

$$\nabla_U f_{\dot{z}_{rr}} = 0 \quad (2.3.46)$$

2.3.4.2 Axial

The axial state and input vectors are chosen as

$$\mathbf{x} = \begin{bmatrix} u_{rr} & x_{rr} \end{bmatrix}^T \quad \mathbf{u} = \begin{bmatrix} T \end{bmatrix} \quad (2.3.47)$$

The linear differential equations for the normal dynamics of the refueling point are

$$\nabla_X f_{\dot{u}_{rr}} = \left[\frac{X_V}{m} \right] \nabla_X u_{rr} \quad (2.3.48)$$

$$\nabla_U f_{\dot{u}_{rr}} = \left[\frac{C_\alpha}{m} \right] \nabla_U T \quad (2.3.49)$$

$$\nabla_X f_{\dot{x}_{rr}} = [1] (\nabla_X u_{rr}) \quad (2.3.50)$$

$$\nabla_U f_{\dot{x}_{rr}} = 0 \quad (2.3.51)$$

It can be seen that the normal system is essentially the short period mode approximation, as presented in [34], which has been augmented with the refueling receptacle dynamics. The axial system is simply a model of straight line movement. The information regarding the phugoid mode has been lost. The phugoid mode is a slow oscillation where energy is exchanged between velocity and altitude. The normal controller will be controlling the altitude of the aircraft with a high bandwidth. Any excitement of the phugoid mode will be damped by the controllers. Similarly, an axial controller will maintain a constant velocity.

2.4 Linear Lateral Receptacle Dynamics

Equation 2.2.14 is simplified for the lateral system. All longitudinal states that do not have steady-state values are set to zero. To prevent clutter, terms that will not have an effect on \dot{v}_{rr} are replaced by asterisks.

$$\begin{aligned}
{}^e \dot{\mathbf{v}}_{RB/i} = & \left(\frac{1}{m} \begin{bmatrix} * \\ -S \\ * \end{bmatrix} \right) + \begin{bmatrix} * \\ C_\alpha S_\beta S_\theta + C_\beta S_\phi C_\theta - S_\alpha S_\beta C_\phi C_\theta \\ * \end{bmatrix} g - a_{B/O}^e \\
& + \begin{bmatrix} C_\alpha C_\beta & S_\beta & S_\alpha C_\beta \\ -C_\alpha S_\beta & C_\beta & -S_\alpha S_\beta \\ -S_\alpha & 0 & C_\alpha \end{bmatrix} \left(\begin{bmatrix} T/m \\ 0 \\ 0 \end{bmatrix} + \begin{bmatrix} 0 \\ \dot{R}l_x - \dot{P}l_z \\ 0 \end{bmatrix} + \begin{bmatrix} -R(Rl_x - Pl_z) \\ 0 \\ P(Rl_x - Pl_z) \end{bmatrix} \right)
\end{aligned} \tag{2.4.1}$$

After multiplying the matrices, the lateral component is isolated:

$$\begin{aligned}
\dot{v}_{rr} = f_{\dot{v}_{rr}}(\mathbf{X}, \mathbf{U}) = & \frac{-S}{m} + (C_\alpha S_\beta S_\theta + C_\beta S_\phi C_\theta - S_\alpha S_\beta C_\phi C_\theta)g \\
& + C_\beta \dot{R}l_x - C_\beta \dot{P}l_z + C_\alpha C_\beta R^2 l_x - C_\alpha S_\beta RPl_z \\
& - S_\alpha S_\beta PRl_x + S_\alpha S_\beta P^2 l_z
\end{aligned} \tag{2.4.2}$$

where \mathbf{X} and \mathbf{U} are the selected state and input vectors respectively. The nabla operator is applied to both sides of the equation, and $\nabla_X S$ is expanded using the dimensional derivatives defined in Appendix A.5. The change in lateral velocity error due to the perturbations in the state vector is

$$\begin{aligned}
\nabla_X f_{\dot{v}_{rr}} = & \left[-\frac{S_\beta}{m} + (C_\alpha C_\beta S_\theta - S_\beta S_\phi C_\theta - S_\alpha C_\beta C_\phi C_\theta)g \right. \\
& - S_\beta \dot{R}l_x + S_\beta \dot{P}l_z + C_\alpha C_\beta R^2 l_x - C_\alpha C_\beta RPl_x \\
& \left. - S_\alpha C_\beta PRl_x + S_\alpha C_\beta P^2 l_z \right] \nabla_X \beta \\
& + \left[-\frac{S_P}{m} - C_\alpha S_\beta Rl_z - S_\alpha S_\beta Rl - x + 2S_\alpha S_\beta Pl_z \right] \nabla_X P \\
& + \left[-\frac{S_R}{m} + 2C_\alpha S_\beta Rl_x - C_\alpha S_\beta Pl_x - S_\alpha S_\beta Pl_x \right] \nabla_X R \\
& + [C_\beta l_x] \nabla_X \dot{R} \\
& + [-C_\beta l_z] \nabla_X \dot{P} \\
& + [C_\beta C_\phi C_\theta + S_\alpha S_\beta S_\phi C_\theta] g \nabla_X \phi
\end{aligned} \tag{2.4.3}$$

Substituting the steady-state values for straight and level flight and the equations for \dot{P} and \dot{R} ,

$$\begin{aligned}
\nabla_X f_{\dot{v}_{rr}} = & \left[-\frac{S_\beta}{m} + S_{\gamma+\omega_d} + (l_x c_4 - l_z c_3) \bar{L}_\beta + (l_x c_9 - l_z c_4) N_\beta \right] \nabla_X \beta \\
& + \left[-\frac{S_P}{m} + (l_x c_4 - l_z c_3) \bar{L}_P + (l_x c_9 - l_z c_4) N_P \right] \nabla_X P \\
& + \left[-\frac{S_R}{m} + (l_x c_4 - l_z c_3) \bar{L}_R + (l_x c_9 - l_z c_4) N_R \right] \nabla_X R \\
& + [C_\theta] g \nabla_X \phi
\end{aligned} \tag{2.4.4}$$

Similarly, the change in lateral velocity error due to change in input is

$$\begin{aligned} \nabla_U f_{\dot{v}_{rr}} = & \left[-\frac{S_{\delta_a}}{m} + (\ell_x c_4 - \ell_z c_3) \bar{L}_{\delta_a} + (\ell_x c_9 - \ell_z c_4) N_{\delta_a} \right] \nabla_X \delta_a \\ & + \left[-\frac{S_{\delta_r}}{m} + (\ell_x c_4 - \ell_z c_3) \bar{L}_{\delta_r} + (\ell_x c_9 - \ell_z c_4) N_{\delta_r} \right] \nabla_X \delta_r \end{aligned} \quad (2.4.5)$$

The lateral position error is described by,

$${}^e \dot{y}_{rr}^e = v_{rr}^e \quad (2.4.6)$$

leading to the linearised equations,

$$\nabla_X f_{\dot{y}_{rr}} = [1] \nabla_X v_{rr} \quad (2.4.7)$$

$$\nabla_U f_{\dot{y}_{rr}} = 0 \quad (2.4.8)$$

2.4.1 State Space

The equations above are combined with the linear lateral differential equations derived in Appendix A. The final linear lateral differential equations are:

$$\begin{aligned} \nabla_X f_{\dot{\beta}} = & \left[C_\alpha C_\beta \frac{-F_T}{mV_T} - \frac{S_\beta}{mV_T} + g(C_\alpha S_\beta S_\theta + C_\beta S_\phi C_\theta - S_\alpha S_\beta C_\phi C_\theta) \right] \nabla_X B \\ & + \left[S_\alpha - \frac{S_P}{mV_T} \right] \nabla_X P \\ & + \left[-C_\alpha - \frac{S_R}{mV_T} \right] \nabla_X R \\ & + \frac{g}{V_T} [C_\beta C_\phi C_\theta + S_\alpha S_\beta S_\phi C_\theta] \nabla_X \phi \end{aligned} \quad (2.4.9)$$

$$\begin{aligned} \nabla_U f_{\dot{\beta}} = & \left[\frac{-S_{\delta_a}}{mV_T} \right] \nabla_U \delta_a \\ & + \left[\frac{-S_{\delta_r}}{mV_T} \right] \nabla_U \delta_r \end{aligned} \quad (2.4.10)$$

$$\begin{aligned} \nabla_X f_{\dot{p}} = & [c_3 L_\beta + c_4 N_\beta] \nabla_X B \\ & + [c_2 Q + c_3 L_P + c_4 N_P] \nabla_X P \\ & + [c_1 Q + c_3 L_R + c_4 N_R] \nabla_X R \end{aligned} \quad (2.4.11)$$

$$\begin{aligned} \nabla_U f_{\dot{p}} = & [c_3 \bar{L}_{\delta_a} + c_4 N_{\delta_a}] \nabla_U \delta_a \\ & + [c_3 \bar{L}_{\delta_r} + c_4 N_{\delta_r}] \nabla_U \delta_r \end{aligned} \quad (2.4.12)$$

$$\begin{aligned} \nabla_X f_{\dot{R}} = & [c_4 \bar{L}_\beta + c_9 N_\beta] \nabla_X B \\ & + [c_8 Q + c_4 \bar{L}_P + c_9 N_P] \nabla_X P \\ & + [-c_2 Q + c_4 \bar{L}_R + c_9 N_R] \nabla_X R \end{aligned} \quad (2.4.13)$$

$$\begin{aligned} \nabla_U f_{\dot{R}} = & [c_4 \bar{L}_{\delta_a} + c_9 N_{\delta_a}] \nabla_U \delta_a \\ & + [c_4 \bar{L}_{\delta_r} + c_9 N_{\delta_r}] \nabla_U \delta_r \end{aligned} \quad (2.4.14)$$

$$\begin{aligned}\nabla_X f_{\dot{\phi}} &= [1] \nabla_X P \\ &+ [\tan(\theta)C_\phi] \nabla_X R\end{aligned}\quad (2.4.15)$$

$$\nabla_U f_{\dot{\phi}} = 0 \quad (2.4.16)$$

$$\begin{aligned}\nabla_X f_{\dot{y}_{rr}} &= \left[-\frac{S_\beta}{m} + S_{\gamma+\omega_d} + (\ell_x c_4 - \ell_z c_3)\bar{L}_\beta + (\ell_x c_9 - \ell_z c_4)N_\beta \right] \nabla_X \beta \\ &+ \left[-\frac{S_P}{m} + (\ell_x c_4 - \ell_z c_3)\bar{L}_P + (\ell_x c_9 - \ell_z c_4)N_P \right] \nabla_X P \\ &+ \left[-\frac{S_R}{m} + (\ell_x c_4 - \ell_z c_3)\bar{L}_R + (\ell_x c_9 - \ell_z c_4)N_R \right] \nabla_X R \\ &+ [C_\theta] g \nabla_X \phi\end{aligned}\quad (2.4.17)$$

$$(2.4.18)$$

$$\begin{aligned}\nabla_X f_{\dot{v}_{rr}} &= \left[-\frac{S_\beta}{m} + gS_{\gamma+\omega_d} + (\ell_x c_4 - \ell_z c_3)\bar{L}_\beta + (\ell_x c_9 - \ell_z c_4)N_\beta \right] \nabla_X \beta \\ &+ \left[-\frac{S_P}{m} + (\ell_x c_4 - \ell_z c_3)\bar{L}_P + (\ell_x c_9 - \ell_z c_4)N_P \right] \nabla_X P \\ &+ \left[-\frac{S_R}{m} + (\ell_x c_4 - \ell_z c_3)\bar{L}_R + (\ell_x c_9 - \ell_z c_4)N_R \right] \nabla_X R \\ &+ [C_\theta] g \nabla_X \phi\end{aligned}\quad (2.4.19)$$

$$\begin{aligned}\nabla_U f_{\dot{v}_{rr}} &= \left[-\frac{S_{\delta_a}}{m} + (\ell_x c_4 - \ell_z c_3)\bar{L}_{\delta_a} + (\ell_x c_9 - \ell_z c_4)N_{\delta_a} \right] \nabla_X \delta_a \\ &+ \left[-\frac{S_{\delta_r}}{m} + (\ell_x c_4 - \ell_z c_3)\bar{L}_{\delta_r} + (\ell_x c_9 - \ell_z c_4)N_{\delta_r} \right] \nabla_X \delta_r\end{aligned}\quad (2.4.20)$$

$$\nabla_X f_{\dot{y}_{rr}} = [1] \nabla_X v_{rr} \quad (2.4.21)$$

$$\nabla_U f_{\dot{y}_{rr}} = 0 \quad (2.4.22)$$

2.5 Tanker Downwash

During aerial refueling, the receiver flies in a flow field generated by the tanker. This flow field greatly affects the aerodynamic forces and moments experienced by the receiver. In this section, a literature study discusses the current research on modelling and understanding the interaction between the tanker and the receiver. The aim of this thesis is not to provide an accurate model or analysis of the aerodynamic effect between a tanker and receiver during AAR; however, the effects cannot be simply ignored. This section investigates various results from the literature to determine representative effects of tanker downwash on an A330 MRTT.

2.5.1 Literature Study

During aerial refueling, the tanker and the receiver must close in and remain in close contact for an extended period of time. It is well known that aircraft in close proximity influence each

other's aerodynamics, as first observed in birds flying in formation [23]. During refueling, the receiver flies in the downwash and sidewash fields of the tanker and experiences additional aerodynamic forces and moments. The receiver also has an effect on the tanker.

With the rising interest in aerial refueling, the modelling and simulation of this interaction have gained significant attention. Initially, research focused only on the effect of the tanker on the receiver. This was done for two reasons. Most receivers are small, fighter-sized aircraft which have a negligible effect on the tanker. Furthermore, initial research focused on the probe-and-drogue refueling method, where the distance between the tanker and the receiver is larger. Flight test results found that continuous actuator command was required [10] to keep the receiver in position.

As work started on the refueling of large receivers, it became clear that the effect of the receiver on the tanker also plays an important role. During various flight tests with large receivers, it was found that the tanker could experience a pilot induced oscillation (PIO) when the receiver is in the contact position. A short literature study on tanker-receiver interaction follows. This will be used as a basis from which to formulate an estimated interaction model for the A330 MRTT tanker-receiver pair.

2.5.1.1 Bloy et al.

In [4], Bloy et al. investigated the lateral dynamic stability of a large receiver during aerial refueling. The tanker's wake is represented as two horseshoe vortices. The downwash and sidewash acting on the receiver are calculated at a datum point: 2 wingspans behind, 1/4 wingspan below. The effect of the sidewash and downwash is quantified as aerodynamic derivatives, as the interference is close to linear around the datum point. It is found that the most important derivatives are the rolling moment due to bank and the rolling moment due to lateral position displacement: \bar{L}_ϕ , \bar{L}_y . The new aerodynamics derivatives are incorporated into an existing dynamic model. The lateral modes are calculated and contrasted with the free-air model. Comparisons are also made to known flight test results. The general behaviour of the system concurs with practical findings from test flights: the receiver aircraft exhibits a slow, unstable mode that the pilot can correct using mainly aileron commands.

In [6], the authors performed a similar analysis on the longitudinal dynamics of the receiver. The most important additional aerodynamic derivatives were found to be pitching moment and normal force, due to normal displacement and pitch angle perturbations: M_z , Z_z , M_θ and Z_θ . The short period mode of the receiver remained unchanged during refueling, implying that the derivative C_{m_q} was not affected by the tanker downwash. The remaining low-frequency poles could be either stable or unstable, depending on the configuration of the aircraft. The change in downwash on the wing versus on the tailplane due to a normal displacement which determine the stability. In the unstable case, constant elevator control was required to keep the receiver in position. This is in line with flight records [10].

In [8], the authors performed wind tunnel tests to simulate the effect of the tanker's wash on the lateral dynamics of the receiver. Again, the effects were found to be linear around the datum point and are presented as derivatives \bar{L}_y and \bar{L}_ϕ . A tapered tanker wing was used, and significant side force and yawing moment derivatives were measured which were not

present using a rectangular, untwisted tanker wing. Their theoretical model predicted a similar increase in these derivatives. The tanker wing wake was modelled as a flat vortex sheet, and the aerodynamic loads on the receiver were obtained using the vortex lattice method. In [5] the directional stability of a large receiver was also investigated using wind tunnel data. It was found that the sidewash on the receiver fin is the main contribution to wake effects. In the study, the theoretical results obtained from the vortex model compared favourably to the experimental results.

In another study [7] the authors presented a more accurate model of wing wake roll-up and applied it to the lateral aerodynamic interference. For the configuration investigated, the more accurate model predicted significantly higher values of rolling moment due to sideways displacement than the previous model.

In [3] Bloy et al. investigated the loss of directional stability of a KC-10 receiver when trailing a Hercules tanker. During flight tests, it was found that the receiver experiences significant loss of directional stability during steady sideslip flight (causing the fin to lie in the sidewash), as well as an increase in the aileron deflection required to maintain a bank angle. The wake roll-up model was used to estimate these effects and incorporate them into the linear model as additional derivatives.

2.5.2 Dogan et al.

In [18,39], Dogan et al. studied the aerodynamic coupling between aircraft in formation flight. Although not specifically addressing aerial refueling, their study is applicable here, and several novel techniques are presented. Each aircraft's wake was represented by two horseshoe vortices. Each aircraft experienced a non-uniform field across its aerodynamic surfaces. The non-uniform field produced by each aircraft was summed and averaged across the wing area (using a variety of averaging techniques) to obtain an effective wind and wind gradient acting at the CG of the aircraft. The effect of the vortices could thus be included in the model as a change in aerodynamic angles, $\Delta\alpha$ and $\Delta\beta$, and effective rotations, $p_{eff}, q_{eff}, r_{eff}$. The rotation would cause an aerodynamic effect, but no kinematic effects. The equivalent effect on the aerodynamic coefficients was also shown, to simplify comparisons with the wind tunnel results. The wind tunnel results followed the same trend as the theoretical results in most cases. Finally, the virtual leader concept was also introduced in this study. All aircraft in the formation were modelled relative to a virtual leading aircraft. Since the study did not deal with refueling specifically, the presented data did not represent the relative separations useful for flying boom refueling.

In [38], the same technique was used in an aerial refueling specific aircraft model, which also included Dryden turbulence and time-varying inertia. The turbulence effects were modelled separately and then added to the the wake effects. The turbulence wind gradients were not included.

In [14], the authors considered the effect of the receiver on the tanker. A simple method of modelling the bow wave effect was presented. Inviscid flow modelling around solid bodies, based on the stream functions defined with various types of singularities, was used. The flow field induced by the aircraft's volume was superimposed with the horseshoe vortices generated

by the aircraft's lift. An averaging technique was used to calculate the effects of these fields, as in previous research. The effect on the aerodynamic coefficients was shown for various receiver positions around a datum point. The point was chosen as the contact position for flying boom refueling, making this study relevant to the current project. The receiver in this study was a tailless aircraft. Furthermore, in [15], the authors approached the same problem with computational fluid dynamics (CFD) techniques, using a KC-135 tanker and a C-141B receiver. The CFD and vortex/flow-field models showed similar trends in several respects and performed much better than the vortex lattice approach, which does not include volume effects.

In [30], the authors investigated the existence and position of a so-called sweet spot behind a leading aircraft. The sweet spot is the position where the receiver expends the least amount of energy to remain. Thrust is the largest factor, but actuation energy must be considered in cases where the point is not dynamically stable. Since the flying boom refueling system dictates the position of the receiver, the current project cannot make use of the sweet spot.

2.5.3 Ryan et al.

In [33], the authors detailed the derivation of a simulation model to describe the interaction of two large aircraft engaged in aerial refueling. The flying boom refueling method was used, making the results relevant to the current project. The author used flight test results and alternative parameter identification methods to describe two separate mechanisms through which the aircraft interact.

The first mechanism described the large aerodynamic changes that both the tanker and the receiver experience as the receiver closes on the contact position. The traditional six degrees of freedom equations were expanded with additional force and moment coefficients. For example, the normal equation would be

$$m(\dot{W} - UQ + VP) = mg \cos \psi \cos \theta + \frac{1}{2}\rho V^2 (C_{M_0} + C_{M_\alpha} \alpha \dots + C_{M_{\delta e}} + \Delta C_{M_{AR}}) \quad (2.5.1)$$

where $\Delta C_{M_{AR}}$ represents the aerodynamic influence of the other aircraft.

A lookup table was created to save the values of these new aerodynamic coefficients as the receiver nears the tanker. It was not stated whether relative orientation was taken into account, or only relative position. A simulation was performed with the additional coefficients included, and the aircraft parameters (angle of attack, elevator deflections, etc.) were recorded. The simulation results were compared to flight test data and the coefficient lookup table was adjusted accordingly. This process was repeated iteratively until the simulation results closely matched the flight data. The results are differed from [14, 15] in that the aircraft remained in a valid trim position as it neared the tanker. Only two snapshots of the data were presented. It was shown that the tanker experiences a nose-down pitching moment as the receiver closes, and that the receiver experiences a restoring rolling moment for lateral displacement. These findings concur with other literature.

A mismatch was observed between the angle of attack and pitch angle for the simulation and flight test. It was found that the aircraft experienced significant downwash, causing the

velocity vector be offset from the incoming air stream. The lift vector thus reorientates to the rear, and the aircraft trims as if it is in a climb. This effect could not be quantified by simply using aerodynamic coefficients. A lookup table was created to supply appropriate downwash as a function of the aircraft separation.

The second mechanism aimed to capture the random turbulence associated with the tanker flow field. Turbulence was generated in the simulation using the NASA Dryden model. Genetic algorithms were used to find turbulence parameters that accurately describe the load factor disturbances that the receiver experienced in the flight test.

2.5.4 Downwash Modeling Overview

This section will briefly discuss how the tanker's effect on the receiver is modelled in the current project. In choosing how to represent the tanker interaction, two aspects are considered. One must be able to include the interaction in the linear aircraft model. This is necessary for an investigation into the movement of the closed loop pole positions when the system is subjected to tanker downwash. Secondly, the interaction must be easy to include in the non-linear simulation of the tanker and the receiver.

To this end, methods from two different sources in the literature are combined. The effect of the tanker on the receiver is divided into two distinct parts, each included using a different method. Firstly, the downwash significantly changes the direction of the incoming air stream. The incoming air stream is thus offset from the velocity vector, and the receiver will reach equilibrium in a different state behind the tanker than in free air. This will be termed the downwash angle, and is discussed in more detail in Section 2.5.5.

Secondly, when the aircraft deviates from its steady-state position, the downwash will change slightly. This changing downwash in turn changes the forces and moments experienced by the receiver aircraft. The effect of a perturbation from steady state will thus be different when exposed to the tanker downwash. This will be termed the downwash dynamics, which are discussed in Section 2.5.6.

2.5.5 Downwash Angle Modelling

The wash behind the tanker is turbulent, and the movement of air at any specific point is difficult to predict. However, it is clear that in the contact position, the receiver will experience a resultant downwash over all its aerodynamic surfaces [33]. This resultant downwash causes an angle between the velocity vector and the incoming air stream of the receiver. The angle will be referred to as the downwash angle, ω_d .

It is important to note that the downwash rotates the aerodynamic axes of the receiver aircraft, thereby changing the direction of the lift and drag forces. The reorientation of the large aerodynamic forces changes the steady-state trim of the receiver significantly. Consider the vector diagram shown in Figure 2.3.

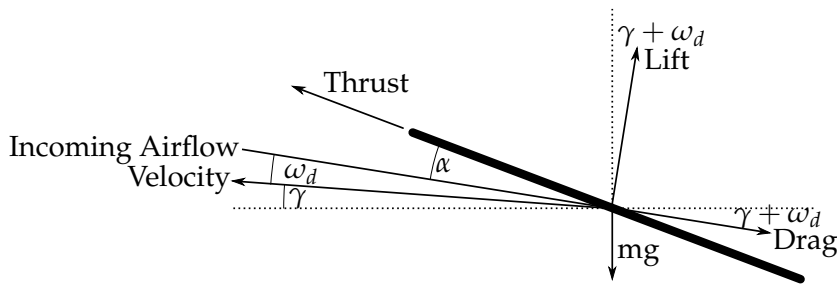


Figure 2.3: Vector diagram of receiver in tanker downwash

For the receiver to remain in equilibrium, the following equations must hold:

$$T \cos \alpha = D + mg \sin(\gamma + \omega_d) \quad (2.5.2)$$

$$L = mg \cos(\gamma + \omega_d) + T \sin \alpha \quad (2.5.3)$$

From the equations it is clear that the downwash angle, ω_d , has the same effect as the flight path angle, γ . The logical conclusion is that a receiver flying in a tanker downwash will have to be trimmed as if it is climbing. Specifically the steady-state pitch angle and thrust will be higher than during straight and level flight in still air. This matches the flight test findings in [33], where it was found that, while behind the tanker, the receiver trims "as if in a climb".

The downwash angle is included in the non-linear model as a parameter, as shown in Appendix A. When the model is linearised, any downwash angle can be selected. It is important to note that since downwash is a parameter and not a state, any dynamics introduced by a fast change in downwash are not modelled. Equations 2.5.4 and 2.5.5 illustrate how the downwash is included in the non-linear equation for angle of attack. Lateral states (yaw rate, roll rate and sideslip) have been set to zero to simplify the equations and highlight the effect of the downwash.

$$\text{Without Downwash: } \dot{\alpha} = \frac{-T \sin \alpha}{m\bar{V}} - \frac{L}{m\bar{V}} + \frac{mg}{\bar{V}} \cos \gamma + Q \quad (2.5.4)$$

$$\text{With Downwash: } \dot{\alpha} = \frac{-T \sin \alpha}{m\bar{V}} - \frac{L}{m\bar{V}} + \frac{mg}{\bar{V}} \cos(\gamma + \omega_d) + Q \quad (2.5.5)$$

The effects of the downwash angle on the linear model are limited. The angle enters the model through the gravity terms in the way that a flight path angle would. Models linearised around straight and level flight are often used for flight with several degrees of flight path angle. It will be shown later in this thesis that the inclusion of the downwash term in the linear model does not change it significantly.

Before the model can be linearised, the equilibrium point must be determined. Here the effect of the downwash is more marked. The aircraft will trim with a considerably different thrust and slightly different angle of attack. Consider the two trim cases in Table 2.1.

At some flight points, it is not possible for the receiver to remain in the contact position, since the thrust cannot meet the steady-state requirements. This will be investigated in a subsequent chapter. This method of including the downwash makes it easy to test the closed loop system robustness with regard to downwash.

Parameter	$\omega_d = 0^\circ$	$\omega_d = 3^\circ$	Unit
Angle of Attack	3.07	3.06	deg
Pitch Angle	3.07	6.06	deg
Thrust	77	166	kN

Table 2.1: Receiver trim values for different downwash angles at 250kts, 20,000ft, 175,000kg and CG at 30%

The downwash can also cause a constant pitch moment on the receiver, especially if the receiver's tailplane lies within the tanker downwash. This effect is modelled as an additional M_O in the non-linear equation. Consequently the steady-state position of the horizontal stabiliser will change. The possible effect that the changing incoming air stream has on the longitudinal aerodynamic derivatives is not considered. In summary, if one only considers the resultant downwash angle over the receiver, the effect is primarily a change in the trim point of the receiver. A small change in the dynamics of the linear model is also introduced.

Figure 2.4 illustrates the distribution of the downwash and upwash the receiver will experience. The tanker's wing tip vortices cause a resultant downwash beneath the tanker, and a resultant upwash beside the tanker.

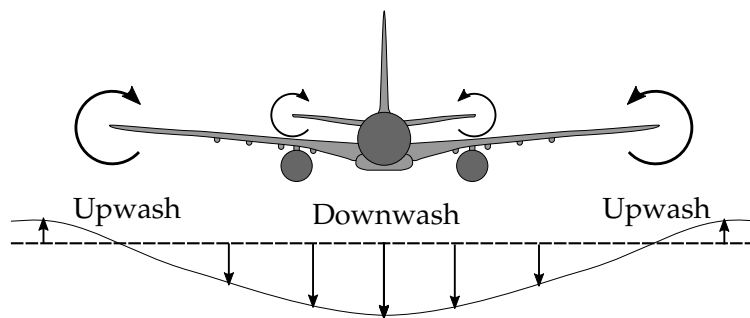


Figure 2.4: Illustration of expected downwash below and behind tanker

The receiver's position is dictated by the flying boom refueling system, and thus the receiver will experience a resultant downwash. Calculating or modelling the exact downwash that an Airbus A330MRTT receiver will experience is not the aim of this project. In various sources [13, 19, 33], a wide range of downwash angles were found. It was decided that testing the robustness of the control system to four degrees of downwash would be sufficient. The effect of downwash angle on a receiver following a tanker in a banked turn can be very complex, and is not investigated in this thesis.

2.5.6 Downwash Dynamics

The downwash angle captures the effect of the tanker when the receiver is in the nominal position behind the tanker. In this position, the lateral effects of the downwash will be minimal, since the receiver is positioned in the plane of symmetry of the tanker. Once the receiver has reached equilibrium, the effect of the downwash will be cancelled by the trim orientation and actuation of the receiver. The aircraft will experience no resultant forces or moments.

The linear aircraft model captures the behaviour of the aircraft when it is perturbed from this equilibrium, and forms the basis for much of flight control theory. However, when the receiver moves from equilibrium behind the tanker, it experiences forces and moments not predicted by the linear model. Even a small movement from the nominal position changes the downwash over the receiver significantly, thereby inducing new forces and moments. These effects will be referred to as the downwash dynamics. It has been found [8] that these dynamics are close to linear for small perturbations around the datum.

These perturbation effects are included in the linear model using additional aerodynamic derivatives that will be referred to as downwash derivatives. A typical downwash derivative is $C_{\bar{L}\psi}$, which quantifies the changing rolling moment coefficient caused by the downwash when the receiver deviates from the nominal position by yawing. It is important to note that this quantity is completely separate from the existing aerodynamic derivative $C_{\bar{L}\beta}$, which describes the aircraft's natural aerodynamic response to a sideslip angle while flying in free air. $C_{\bar{L}\beta}$ is influenced by the size and shape of the receiver's wings and fuselage. $C_{\bar{L}\psi}$ is determined not only by the receiver's wing profile, but also by the tanker's wing profile, the separation between the tanker and the receiver, and many other factors. Changes in downwash due to the position of the receiver, will be given as derivatives with respect to the receiver's CG position, e.g. the change in rolling movement coefficient due to the receiver moving in the X direction is $C_{M_{xcg}}$.

Since no accurate values exist for the downwash derivatives, they cannot be included in the linear model used to calculate feedback gains. However, estimates of the derivatives will be used during analysis to test the robustness of the designed control system. Functions were created to describe the downwash derivatives by combining the findings of all the sources presented earlier in this section. The most prominent derivatives will now be discussed.

2.5.6.1 Lift

In all cases, the receiver's lift is decreased by the presence of the tanker wake. The reduction is largest when the receiver is close to the datum position. The large reduction in lift shown in many sources will be captured by the downwash angle described previously. Using the downwash angle better captures reality than simply decreasing C_L , since the downwash angle also rotates the lift vector to the rear. The downwash derivative for lift will only capture the change as the receiver moves around the datum point. Lift is affected by X and Y deviation from the datum point, and not significantly by orientation.

Figure 2.5 shows the the curve for change in lift as the tanker moves around the datum. It can be seen that the lift will increase slightly for a positive change in the X-position, as the receiver moves forward and starts to leave the tanker downwash. $C_{L_{xcg}}$ is therefore positive.

Most literature sources agree that lift will increase for positive or negative lateral displacement as the receiver moves out of the highest downwash and into the upwash beside the tanker. The derivative $C_{\bar{L}_{ycg}}$ is zero, as shown in Figure 2.5.

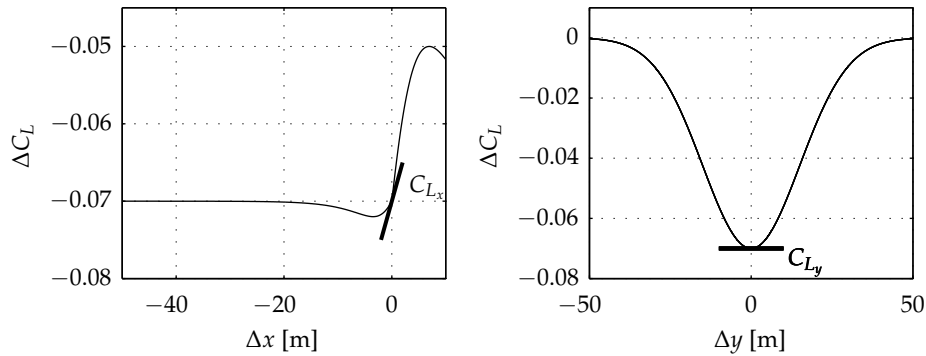


Figure 2.5: Change in the receiver's lift due to X-position and Y-position

2.5.6.2 Side Force

Due to the symmetry of the aircraft, the receiver will not experience a side force when at the datum position with zero bank angle, and yaw angle equal to the tanker's. A side force is generated as soon as the aircraft moves from the datum position. For a lateral position disturbance, the force is orientated to accelerate the aircraft further away from the datum. It has been shown in [8] that the restoring acceleration caused by the rolling moment is higher than the side force, and so the receiver will return to the datum when disturbed laterally. $C_{S_{ycg}}$ is thus negative, as shown in Figure 2.6.

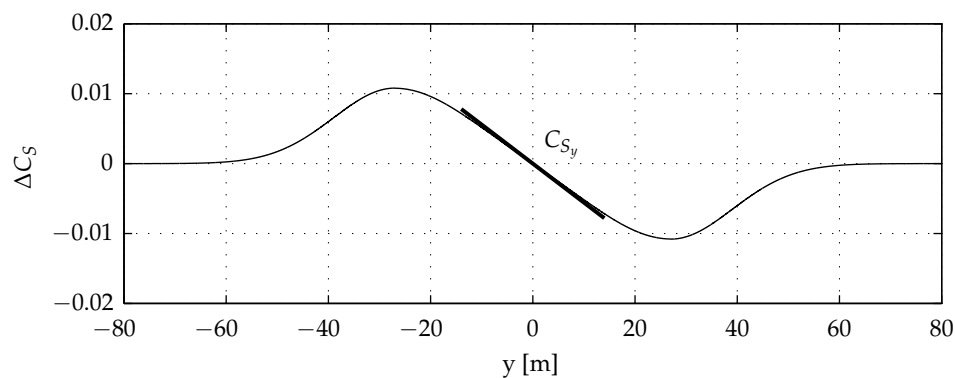


Figure 2.6: Change in the receiver's pitching moment due to change in X-position and Y-position

2.5.6.3 Pitching Moment

The receiver will experience a resultant pitching moment when positioned at the datum point. It has been shown [14] that the moment is close to constant for a large X-range behind the tanker. Close to the datum point, the moment appears to change quickly, although the sign will depend on the configuration of the aircraft. The position of the receiver's tailplane is of particular importance. For the purpose of robustness testing, a positive $C_{M_{xcg}}$ is assumed, as shown in Figure 2.7. Other perturbations do not result in a significant pitching moment.

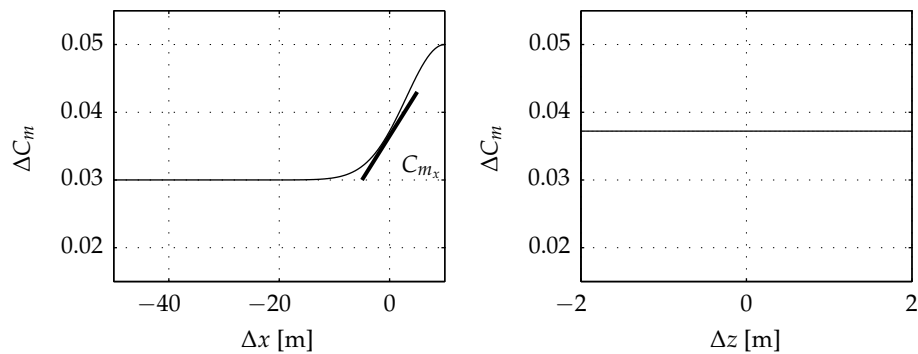


Figure 2.7: Change in the receiver's pitching moment due to change in X-position and Y-position

2.5.6.4 Rolling Moment

At the datum point, the receiver experiences no resultant rolling moment. When the receiver moves laterally from the datum point, the downwash causes a rolling moment in the direction that will accelerate the aircraft back to the datum. This is one of the largest effects and the most consistent throughout the literature. The effect is reduced for further X and Z displacement from the tanker. $C_{L_{yeg}}$ is thus negative, as shown in Figure 2.8.

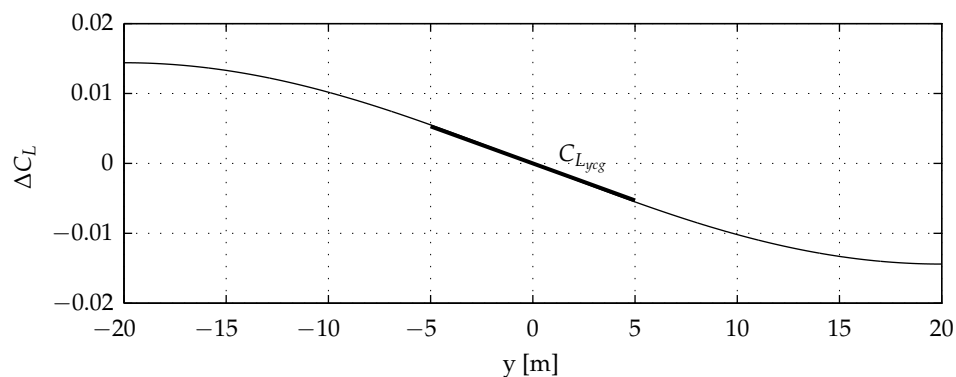


Figure 2.8: Change in the receiver's rolling moment due to change in Y-position

2.5.6.5 Yawing Moment

At the datum point, the receiver experiences no resultant yawing moment. When the receiver moves laterally from the datum point, the wake causes a yawing moment in the direction that will accelerate the aircraft back to the datum. $C_{N_{yeg}}$ is thus negative, as shown in Figure 2.9.

2.6 Engine

The relatively slow engine response of a large aircraft is one of the main challenges of AAR. It has been predicted [2] that the engine might be the single limiting factor for AAR performance.

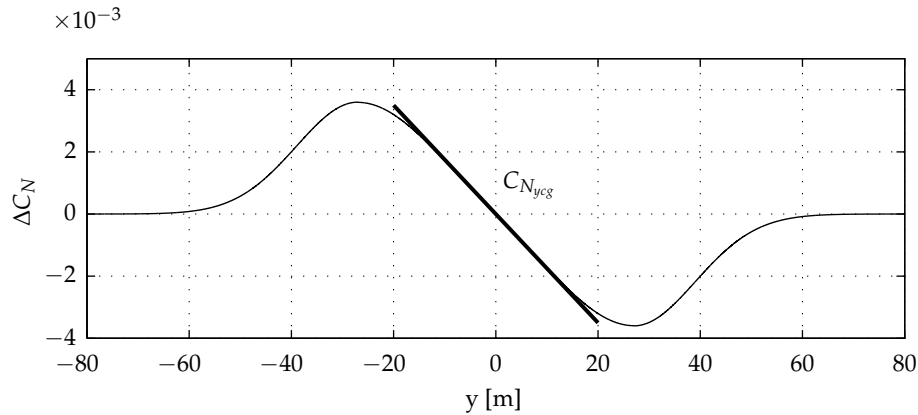


Figure 2.9: Change in the receiver's rolling moment due to change in Y-position

As such, the accurate modelling of the engine response in simulations is very important. Unfortunately, a high fidelity engine model was not available to Stellenbosch University. Airbus provided time response data for the engine at various flight points and for various engine commands. A non-linear model was created to approximate these responses and estimate the probable response at different flight points. This section will briefly describe the model. Note that, throughout this thesis, the maximum thrust of the engine is defined as the maximum thrust the auto-thrust system is allowed to command. This is less than the absolute maximum thrust the engine can achieve, for example during take-off.

2.6.1 Architecture

The engine is modelled as a second-order linear system with a complex pole pair. The thrust lever position is converted into a thrust value, and a time delay is introduced. To capture the non-linear behaviour of the engine, the first integrator of the system has a lower and an upper saturation limit. The architecture is shown in Figure 2.10.

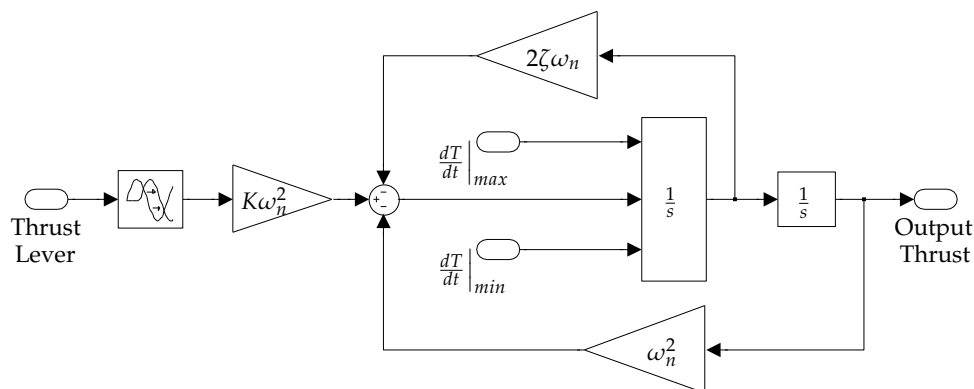


Figure 2.10: Basic architecture of the non-linear engine model

The behaviour of the engine will be dictated by the natural frequency and damping of the poles and the saturation limits. The saturation limits, effectively a rate limit on the output, are

not constant and change as a function of the current output. Figure 2.11 shows an engine response from idle to maximum thrust, and illustrates how the slew rate limits change depending on the current output.

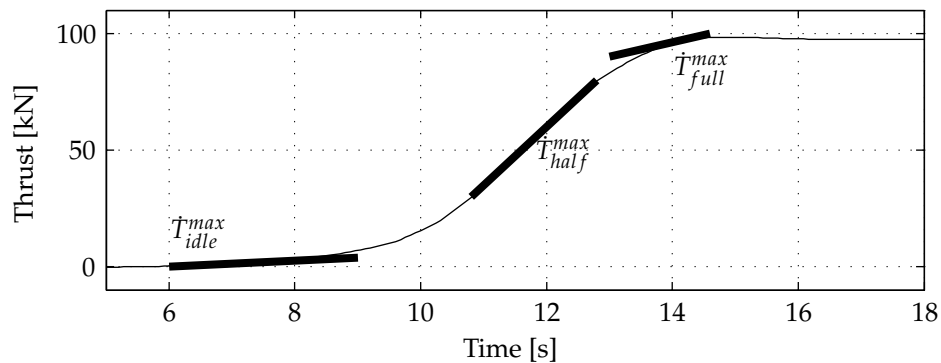


Figure 2.11: Illustration of engine slew rates

A slew-rate limit is selected at idle, half and full thrust. For most of the engine's range, the slew-rate limit \dot{T}_{half}^{max} is enforced. Between approximately 85% and 100% of output, the rising slew-rate limit is interpolated from \dot{T}_{half}^{max} to \dot{T}_{full}^{max} . Similarly, when the engine output is low, between 15% and 0%, the maximum slew rate is interpolated between \dot{T}_{half}^{max} to \dot{T}_{idle}^{max} . The same procedure is followed for the minimum slew rate. The slew rates can vary significantly across all flight points. Figure 2.12 shows the rising and falling slew rates for two flight points over the range of engine thrust as deduced from the given data.

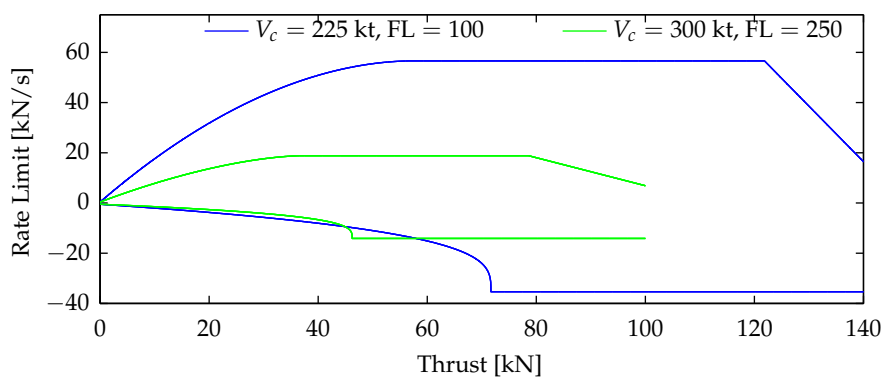


Figure 2.12: Rising and falling engine thrust slew-rate limits

The data provided by Airbus were investigated, and the engine parameters were selected at each flight point provided. Table 2.2 shows the engine parameters chosen for two flight points.

Engine data were not provided for all required flight points. A quadratic interpolation is performed using static and dynamic pressure to calculate the engine parameters at other flight points.

Parameter	$V_c = 300\text{kt}$, FL = 300	$V_c = 225\text{kt}$, FL = 100
T_{max}	81 kN	146 kN
ζ	0.7	0.49
ω_n	2.1 rad/s	1.37 rad/s
t_{delay}	0.2 s	0.2 s
\dot{T}_{idle}^{max}	0.4 kN/s	0.4 kN/s
\dot{T}_{half}^{max}	14 kN/s	45 kN/s
\dot{T}_{full}^{max}	5 kN/s	10 kN/s
\dot{T}_{full}^{min}	-10 kN/s	-34 kN/s
\dot{T}_{half}^{min}	-10 kN/s	-34 kN/s
\dot{T}_{idle}^{min}	-0.5 kN/s	-0.5 kN/s

Table 2.2: Engine parameters at two flight points

2.6.2 Responses

Comparative engine responses will now be shown at the same flight points detailed in Table 2.2. The figures will illustrate that the non-linear model follows Airbus's data closely, making it suitable for use in non-linear simulations. Furthermore, the graphs show how greatly the engine response can differ between flight points.

2.6.2.1 Small Steps

A set of engine responses was provided by Airbus, in which small steps are performed around half thrust. These are the most important responses, as they cover the region where the controllers operate. While at half thrust, the engine slew rate limits are at their fastest. Figure 2.13 shows a comparison between the model and source data at two flight points.

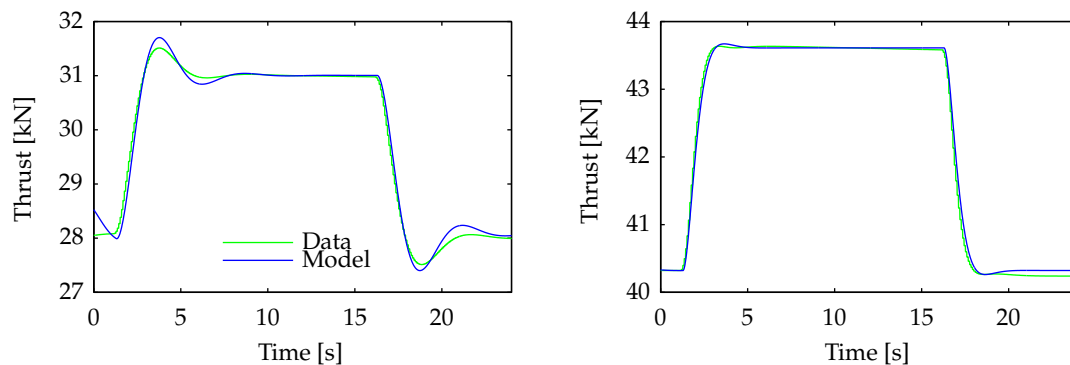


Figure 2.13: Small thrust step around steady state

2.6.2.2 Half to Full

This set of engine responses describes a step from half throttle to maximum thrust. The upper saturation value is chosen such that the simulated response matches the data. Figure 2.14 shows a comparison between the model and source data at two flight points.

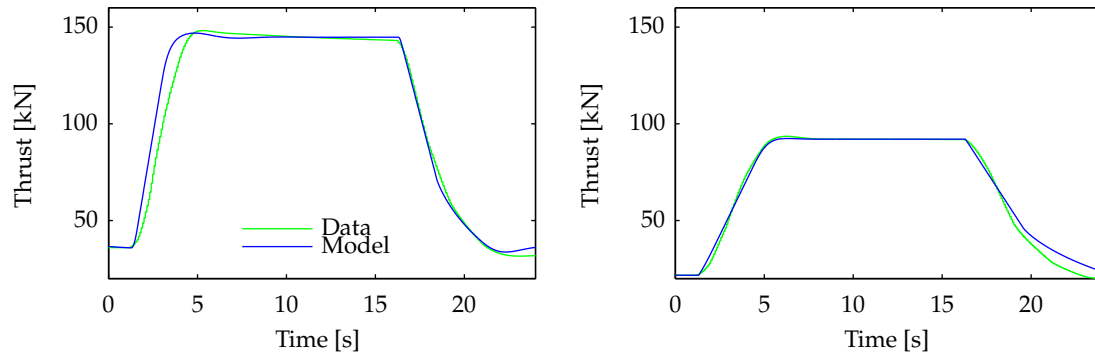


Figure 2.14: Thrust step from half to maximum thrust

2.6.2.3 Idle to Full

The final data set represents a step from engine idle to maximum thrust, and clearly shows the non-linear response around engine idle. It is important that this effect be modelled in the simulation. This ensures that the controller cannot command unrealistically low thrust values. The exact accuracy of the model is not as important, as the controller will always fail if the engine command enters this domain. This effect is simulated by lowering the upper slew rate limit at less than 15% thrust. Figure 2.15 shows a comparison between the model and source data at two flight points.

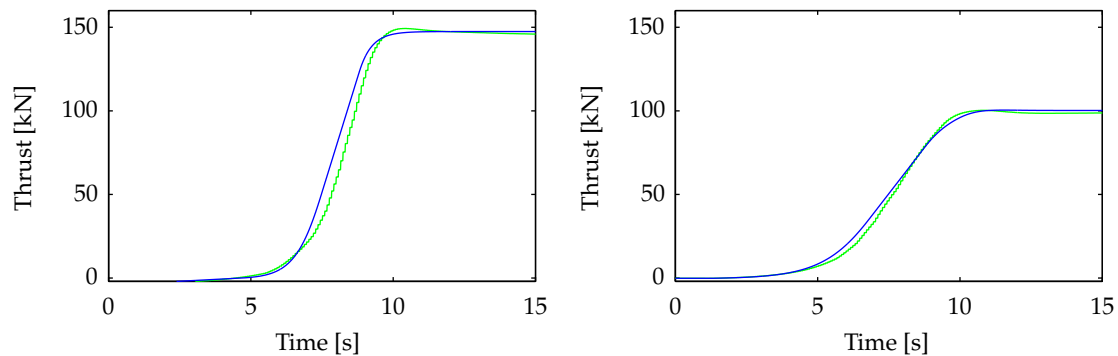


Figure 2.15: Thrust step from engine idle to maximum thrust

2.6.2.4 Reducing Thrust

It is important to note that the rising and falling thrust responses differ, further complicating linear control. The falling response is simulated in the same manner as the rising. A minimum slew rate is specified over the upper 50% of the response. This value is increased when the engine response falls below 50%.

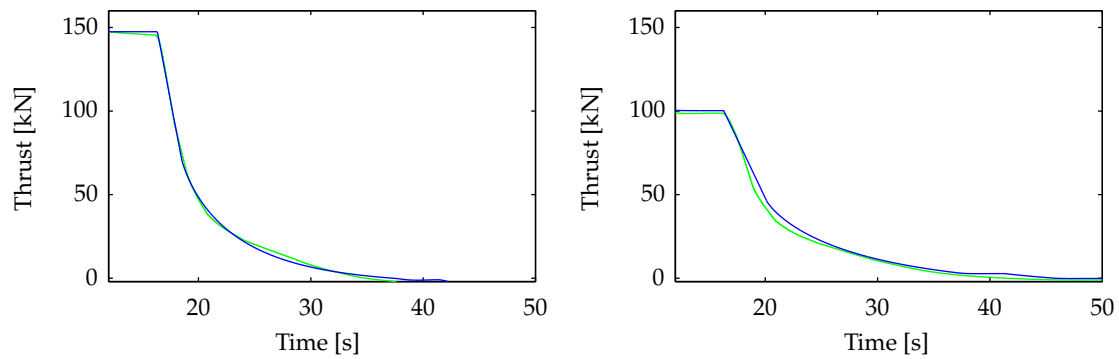


Figure 2.16: Reducing thrust from maximum to idle

2.7 Summary

This chapter presented the derivation of linear state space models describing the normal, axial and lateral movements of the RR on a receiver aircraft during aerial refueling. The traditional aircraft model was expanded to include the effect of the distance between the centre of gravity and the refueling receptacle.

From the existing research, it was found that the receiver aircraft will experience a resultant downwash in the contact position, causing it to trim as if in a climb. It was shown how this downwash can be included in the receiver's model. Other aerodynamic effects, namely the the downwash dynamics, are uncertain and require significant research to determine. While a model for these dynamics is not available, it was shown how they could be included in the receiver's model.

A non-linear engine model was created using the supplied engine response data. This model will be now used in non-linear simulations and control system design.

Chapter 3

Analysis

3.1 Overview

In the previous chapter, a linear model was derived which described the movement of the refueling receptacle on the receiver aircraft during AAR. This model differs from well-established models, which means that analysis is required. The addition of the RR dynamics represents one of the biggest challenges in automating a large receiver, as no literature exists on this topic. In this chapter, the linear model will be investigated using several techniques, including pole-zero and frequency domain analysis. The effects of the the refueling point dynamics are most easily illustrated in the normal system. The bulk of this chapter will thus be dedicated to the analysis of the normal system. In this chapter, various factors will be ignored. Among other things, the physical limits of the aircraft, actuator models and aircraft interaction are not considered. The purpose of these simplifications is to isolate the effect of the refueling receptacle dynamics. However, the limitations imposed by these effects will be taken into account when the final control systems are designed. It will be shown that the effects of the RR dynamics are more prevalent at certain flight points. To better illustrate these effects, one of these flight points will be used throughout this chapter: $V_c = 225$ kt, $FL = 300$, $m_r = 200$ t, $CG_r = 30\%$. Chapter 5 will investigate control at a variety of flight points.

It is proposed that, for a large aircraft, the inclusion of the receptacle dynamics alters the linear model sufficiently that a traditional control system will not be able to accomplish the performance required to achieve AAR. To this end, the disturbance rejection and command following performance of the new control system architectures are compared to the performance of a traditional control system.

Section 3.2 presents the analysis of the normal system. Firstly, the open loop system is investigated. The effects of the RR dynamics, downwash angle, and downwash dynamics on the system are shown. Section 3.2.3 introduces a control system that is used to investigate the closed loop effects of the RR dynamics. The architecture of the control system is discussed in Section 3.2.4 and the findings listed in Section 3.2.5. Section 3.3 gives a brief overview of the effect of the RR dynamics on the lateral system.

3.2 Normal System

Consider the state space model presented below. The model is a subsystem of the linear normal model derived in the previous chapter, where the kinematic states have been removed. The model describes the acceleration of the refueling receptacle in response to an elevator input.

$$\begin{aligned} \mathbf{x} &= \begin{bmatrix} \alpha & q \end{bmatrix}^T \\ \mathbf{u} &= \begin{bmatrix} \delta_e \end{bmatrix} \end{aligned} \quad (3.2.1)$$

$$\begin{aligned} \mathbf{y} &= \begin{bmatrix} \dot{w}_{rr} \end{bmatrix} \\ A &= \begin{bmatrix} \frac{Z_\alpha - T C_\alpha}{m V_T} & 1 + \frac{Z_q}{m V_T} \\ \frac{M_\alpha}{I_{yy}} & \frac{M_q}{I_{yy}} \end{bmatrix} \\ B &= \begin{bmatrix} \frac{Z_{\delta_e}}{m V_T} \\ \frac{M_{\delta_e}}{I_{yy}} \end{bmatrix} \end{aligned} \quad (3.2.2)$$

$$\begin{aligned} C &= \begin{bmatrix} \frac{Z_\alpha - T C_\alpha}{m} - \frac{M_\alpha \ell_x^w}{I_{yy}} & \frac{Z_q}{m} - \frac{M_q \ell_x^w}{I_{yy}} \end{bmatrix} \\ D &= \begin{bmatrix} \frac{Z_{\delta_e}}{m} - \frac{M_{\delta_e} \ell_x^w}{I_{yy}} \end{bmatrix} \end{aligned}$$

Note that if ℓ_x^w is set to zero, this model simplifies to the short period mode approximation with the normal acceleration of the CG as output. Two versions of this model are investigated. Firstly, for the CG-system, ℓ_x^w is set to zero. Secondly, a typical value for ℓ_x^w is chosen to describe the position of the receptacle on an Airbus A330 MRTT in the RR-system: approximately 23 m.

3.2.1 Poles and Zeros

Figure 3.1 shows the pole and zero positions for various values of ℓ_x^w . Since ℓ_x^w is only present in the C and D matrices, the pole positions for the CG and RR systems are the same. The CG system, where ℓ_x^w is zero, has a real positive and a real negative zero. This represents a non-minimum phase, caused by the initial downward acceleration acting on the elevator before the increased angle of attack caused an upward acceleration. When ℓ_x^w is increased, the elevator moment creates an upward acceleration at the receptacle due to the distance from the CG. As a result, the real zeros move further from the origin. At a certain point, the upward acceleration caused by the moment perfectly cancels the downward acceleration caused by the force on the elevator. This point on the aircraft experiences no immediate acceleration if the elevator is deflected. For this value of ℓ_x^w , the zeros are at positive and negative infinity.

When the distance from the CG is increased further, the zeros re-enter the s-plane as a complex pair with a negative real component. The zeros move closer to the origin as ℓ_x^w is increased. The final position shown in Figure 3.1 corresponds to the location of the receptacle on an Airbus A330 MRTT. The initial downward acceleration is clearly visible in the step responses, while the zeros are in the right half-plane. Once the zeros move into the left half-plane, it can be seen that the RR experiences an immediate upward acceleration as soon as the elevator is deflected. Zeros close to closed loop dominant poles can greatly affect the response, especially the overshoot, of a system.

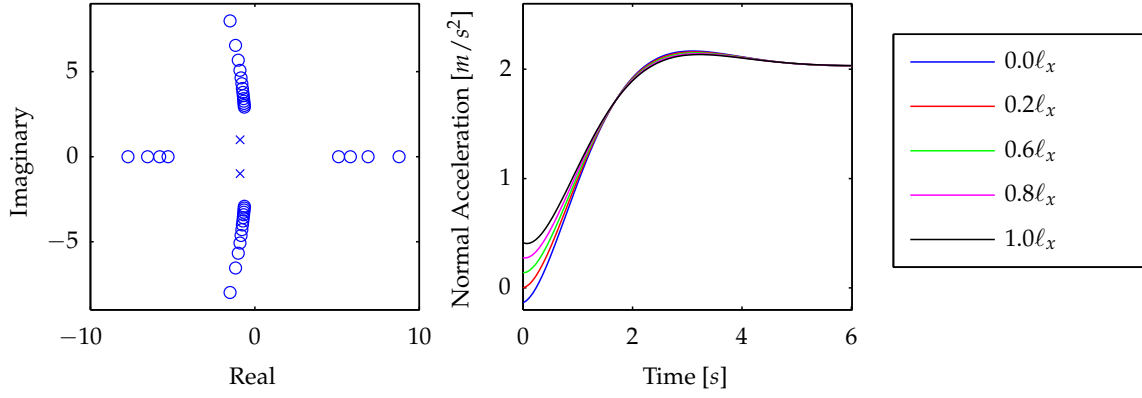


Figure 3.1: Pole and zero positions and step responses for various receptacle positions in transfer function from elevator to normal acceleration

It will be shown that the positions of the zeros play an important role when choosing design criteria for the control system. An equation for the approximate position of the zero can thus be useful for design. The movement of the zeros can be explained by calculating the system's transfer function from elevator to normal acceleration of the RR. Using the state space system shown in Equation 3.2.2, the transfer function can be found using

$$G(s) = C(sI - A)^{-1}B + D = \frac{\text{num}(s)}{\text{den}(s)} \quad (3.2.3)$$

Substituting the matrices defined in Equation 3.2.2 results in

$$G(s) = \frac{\begin{bmatrix} \frac{Z_\alpha - T_0 C_\alpha}{m} - \frac{M_\alpha \ell_x^w}{I_{yy}} & \frac{Z_q}{m} - \frac{M_q \ell_x^w}{I_{yy}} \end{bmatrix} \begin{bmatrix} s - \frac{M_q}{I_{yy}} & 1 + \frac{Z_q}{mV} \\ \frac{M_\alpha}{I_{yy}} & s - \frac{Z_\alpha - T_0 C_\alpha}{mV} \end{bmatrix} \begin{bmatrix} \frac{Z_{\delta_e}}{mV} \\ \frac{M_{\delta_e}}{I_{yy}} \end{bmatrix}}{\text{den}(s)} + \left[\frac{Z_{\delta_e}}{m} - \frac{M_{\delta_e} \ell_x^w}{I_{yy}} \right] \quad (3.2.4)$$

$$\begin{aligned} \text{num}(s) &= (I_{yy}Z_{\delta_e} - \ell_x^w m M_{\delta_e}) Vs^2 \\ &+ (M_{\delta_e} Z_q V - M_q Z_{\delta_e} V - \ell_x^w M_\alpha Z_{\delta_e} + \ell_x^w M_{\delta_e} Z_\alpha - \ell_x^w M_{\delta_e} T C_\alpha) s \\ &+ (-M_\alpha Z_{\delta_e} + M_{\delta_e} Z_\alpha - M_{\delta_e} T C_\alpha) V \end{aligned} \quad (3.2.5)$$

The numerator of the system's transfer function from elevator deflection to w_{rr} is of the form:

$$as^2 + bs + c \quad (3.2.6)$$

with the following values for the coefficients:

$$a = \ell_x^w m M_{\delta_e} V + I_{yy} Z_{\delta_e} V \quad (3.2.7)$$

$$b = \ell_x^w M_{\delta_e} (Z_\alpha - T C_\alpha) - M_q Z_{\delta_e} V + M_{\delta_e} Z_q V - \ell_x^w M_\alpha Z_{\delta_e} \quad (3.2.8)$$

$$c = M_{\delta_e} (Z_\alpha - T C_\alpha) V - M_\alpha Z_{\delta_e} V \quad (3.2.9)$$

The frequency, ω_z , and angle, θ_z , of the zeros are solved to be

$$\omega_z = \sqrt{\frac{M_{\delta_e} Z_\alpha - M_\alpha Z_{\delta_e} - M_{\delta_e} TC_\alpha}{V(I_{yy} Z_{\delta_e} - \ell_x m M_{\delta_e})}} \approx \sqrt{\frac{Z_\alpha - TC_\alpha}{m \ell_x^w}} \quad (3.2.10)$$

$$\theta_z = \arcsin \left(\frac{V(M_{\delta_e} Z_\alpha - M_\alpha Z_{\delta_e}) + \ell_x^w (M_{\delta_e} (Z_\alpha - TC_\alpha) - M_\alpha Z_{\delta_e})}{2V(I_{yy} Z_{\delta_e} - \ell_x^w m M_{\delta_e}) \sqrt{\frac{M_{\delta_e} Z_\alpha - M_\alpha Z_{\delta_e} - M_{\delta_e} TC_\alpha}{V(I_{yy} Z_{\delta_e} - \ell_x m M_{\delta_e})}}} \right) \quad (3.2.11)$$

$$\approx \arcsin \left(\sqrt{\frac{\ell_x^w m (Z_\alpha - TC_\alpha)}{4m^2 V^2}} \right)$$

Using the full values of a , b and c leads to a very unwieldy answer. To gain insight into the dominant factors that determine the zero positions, the smaller terms are excluded, leading to the approximate answers shown in the equations above. It can be seen that once ℓ_x^w becomes significant, the frequency of the zero is primarily determined by the lift force due to angle of attack, the distance from the CG to the RR, and the mass of the aircraft.

At the chosen flight points, this approximation is accurate to within 10%, as shown in Table 3.1. This approximation will not be used for design purposes, but is useful to quickly estimate the position of the RR zeros for a specific aircraft.

Flight Point		Method	Frequency	Angle [deg]
$V_C = 225\text{kts}$	FL = 300	Approximate	1.58	5.5722
$m = 225$	CG = 30%	Complete	1.69	5.7046
$V_C = 250\text{kts}$	FL = 100	Approximate	2.69	11.6539
$m = 125t$	CG = 22%	Complete	3.04	12.6503

Table 3.1: Accuracy of zeros' position approximation at two flight points

3.2.2 Downwash Angle

This section investigates the effect of a downwash angle – as defined in Section 2.5 – on the normal system. In [33], it was found that a uniform downwash does not affect the short period mode of an aircraft. Subsequently, the poles of the normal system (a short period mode approximation) will not be affected. However, adding the receptacle dynamics has moved the zeros of the normal system. These dynamics will be investigated to determine if the downwash can change the zeros' positions.

Table 3.2 shows how much the various steady-state values change when the receiver is exposed to a three degree downwash.

Consider Equations 3.2.10 and 3.2.11. Each variable in these equations will be investigated to determine how it changes in downwash.

Aerodynamic Terms The aerodynamic terms (M_{δ_e} , M_α , Z_α , etc.) will change very slightly due to a change in trim. Of all the aerodynamic derivatives, Z_α has the most dominant effect on the zeros' positions. As shown in Table 3.2, Z_α only changes by 2.3% in downwash.

Derivative	Change
θ	46%
α	-1.2%
Z_α	2.3%
T_0	107%

Table 3.2: Change in steady-state values for receiver exposed to three degree downwash

Angle of Attack Table 3.2 shows that a three degree downwash will change the angle of attack from 3.07 to 3.05 at a specific flight point. The angle of attack only affects the zeros' positions through the term $T_0 \cos(\alpha)$. For small angles, the derivative of cosine is close to 1. The small change in angle of attack will thus have a very minor effect on $\cos(\alpha)$ and consequently on the zeros' positions.

Distance to Receptacle l_x^w is the distance from the CG to the refueling receptacle in the aerodynamic axes. The change in angle of attack will change this term slightly, but will have a negligible effect on the zeros' positions.

Thrust A three degree downwash will change the steady-state thrust from 77kN to 160kN. While this represents a significant change, consider the term $Z_\alpha - T_0 \cos(\alpha)$. A typical value for Z_α is a few orders of magnitude greater than the steady-state thrust. At flight point 250kts, 20 000ft, 175 000kg, $Z_\alpha = -1.5 \times 10^7$, while $T_{ss} = 8.4 \times 10^4$. Even a major change in thrust will not cause a significant change in zeros' position.

Other Terms The mass and velocity, m and V respectively, will not change.

It was predicted from this analysis that a small downwash angle would not influence the zeros' positions significantly. This prediction is found to be accurate when Equations 3.2.10 and 3.2.11 are used to calculate the zero positions in downwash. The frequency and angle of the zeros change by only 1.6%.

3.2.3 Control System

It has been shown that the RR dynamics introduce two complex zeros in the left half-plane. The effect of the zeros on the open loop transfer function from elevator deflection to normal acceleration of the RR has been shown. While this effect might seem small, the resultant effect on the closed loop behaviour of the system can be significant. To investigate the closed loop system, a generic control system is created. This system is not intended to be a practical solution to the AAR control problem, and is only used to illustrate the effect of the zero for various bandwidth systems. The control system uses pole placement via full state feedback to achieve the following:

- Move the velocity and position poles to the desired bandwidth with optimal damping, $\zeta = 0.707$.
- Move the short period mode poles to a higher frequency (two times higher was found to be sufficient) than the kinematic poles, and damped to $\zeta = 0.707$. The kinematic pole pair is thus the more dominant pair and approximates the system bandwidth.

- Add integral control to the position, and place the integrator pole at 20% of the bandwidth frequency. Integral control is essential, since the downwash angle the receiver experiences in the contact position is unknown. The integrator must be fast enough to adjust for the changing downwash as the receiver approaches the tanker.

The augmented open loop system is,

$$\begin{aligned} \mathbf{x}' &= \begin{bmatrix} \alpha & q & w_{rr} & z_{rr} & z_{rri} \end{bmatrix}^T \\ \mathbf{u}' &= \begin{bmatrix} \delta_e \end{bmatrix} \\ \mathbf{y}' &= \begin{bmatrix} z_{rr} \end{bmatrix} \end{aligned} \quad (3.2.12)$$

$$\begin{aligned} A' &= \begin{bmatrix} & & & & 0 \\ & A & & & 0 \\ & & & & 0 \\ & & & & 0 \\ 0 & 0 & 0 & 1 & 0 \end{bmatrix} & C' &= \begin{bmatrix} C & 0 \end{bmatrix} \\ B' &= \begin{bmatrix} B & 0 \end{bmatrix}^T & D' &= 0 \end{aligned} \quad (3.2.13)$$

where z_{rri} is the integrated RR normal position error. As before, two systems are created. The RR-system is described by the equations above. The CG-system is created by removing the RR dynamics by setting ℓ_x^w and ℓ_z^w to zero. The feedback gain K is calculated such that $u = -Kx'$ places the eigenvalues of the closed loop matrix, $A'_{cl} = A' - B'K$, at the positions described above. Two responses of the closed loop system to two different disturbances will be investigated.

3.2.3.1 Tanker Tracking

The response to a tanker position disturbance is described by the following system:

$$\begin{aligned} \mathbf{x}' &= \begin{bmatrix} \alpha & q & w_{rr} & z_{rr} & z_{rri}^i \end{bmatrix}^T & B_t &= B'K \begin{bmatrix} 0 & 0 & 0 & 1 & 0 \end{bmatrix}^T \\ \mathbf{u}_t &= \begin{bmatrix} -z_t \end{bmatrix} & D_t &= \begin{bmatrix} 0 \end{bmatrix} \\ \mathbf{y} &= \begin{bmatrix} \Delta z_{rr} \end{bmatrix} \end{aligned} \quad (3.2.14)$$

$$\begin{aligned} \dot{\mathbf{x}}' &= A_{cl}\mathbf{x}' + B_t\mathbf{u}_t \\ \dot{\mathbf{y}} &= C'\mathbf{x}' + D_t\mathbf{u}_t \end{aligned} \quad (3.2.15)$$

where z_t is the normal displacement of the nominal position of the boom tip due to tanker movement, and Δz_{rr} is the movement of the refueling receptacle in response to the disturbance.

The zeros of this system are given by the solutions of Equation 3.2.16.

$$\begin{vmatrix} sI - (A' - B'K) & B_t \\ C' & 0 \end{vmatrix} = 0 \quad (3.2.16)$$

B_t is the column vector in $A' - B'K$ which corresponds to the state z_{rr} and can thus be written as,

$$B_t = (A' - B'K) \begin{bmatrix} 0 \\ 0 \\ 0 \\ 1 \\ 0 \end{bmatrix} = A' \begin{bmatrix} 0 \\ 0 \\ 0 \\ 1 \\ 0 \end{bmatrix} - B'K \begin{bmatrix} 0 \\ 0 \\ 0 \\ 1 \\ 0 \end{bmatrix} = 0 - BK_4 \quad (3.2.17)$$

The input vector B_t is therefore the elevator input vector, B' , scaled by the feedback gain for z_{rr} .

$$\begin{aligned} \begin{vmatrix} sI - A' - B'K & B'K_{w_{rr}} \\ C' & 0 \end{vmatrix} &= K_{w_{rr}} \begin{vmatrix} sI - A' - B'K & B' \\ C' & 0 \end{vmatrix} \\ &= K_{w_{rr}} \begin{vmatrix} sI - A' & B' \\ C' & 0 \end{vmatrix} \\ &= 0 \end{aligned} \quad (3.2.18)$$

Keeping in mind that adding a multiple of one column to another column does not change the determinant of a matrix, it can be deduced that this system's zeros are the same as those of the open loop system from elevator input to normal position.

3.2.3.2 Disturbance Rejection

The response to a vertical gust disturbance is modelled as a step change in angle of attack, and is described by the following system:

$$\begin{aligned} \mathbf{x}' &= \begin{bmatrix} \alpha & q & w_{rr} & z_{rr} & z_{rr}^i \end{bmatrix}^T \\ \mathbf{u}_g &= \begin{bmatrix} \Delta\alpha \end{bmatrix} \\ \mathbf{y} &= \begin{bmatrix} z_{rr} \end{bmatrix} \end{aligned} \quad (3.2.19)$$

$$\begin{aligned} B_g &= A'_{cl} \begin{bmatrix} 1 & 0 & 0 & 0 & 0 \end{bmatrix}^T \\ D_g &= \begin{bmatrix} 0 \end{bmatrix} \\ \mathbf{x}' &= A'_{cl}\mathbf{x}' + B_g\mathbf{u}_g \\ \dot{\mathbf{y}} &= C'\mathbf{x}' + D_g\mathbf{u}_g \end{aligned} \quad (3.2.20)$$

Note that B_g is equal to the first column of the closed loop matrix.

3.2.4 Architectures

The structure of the control system and feedback warrants some attention. The different architectures will be classified according to which model (RR or CG) is used to calculate the feedback gains, and whether the RR or CG position is used for feedback.

3.2.4.1 CG Model - CG Feedback

Feedback gains are calculated using the unmodified CG model, and the position of the CG is used for feedback. This architecture represents a traditional position controller where the position of the CG is regulated, and the dynamics of the refueling point are completely ignored. When used in AAR applications, it is assumed that the position of the RR relative to the CG will change very little over the course of refueling. As such, it is sufficient to control the position of the CG relative to the tanker aircraft. The CG position reference is calculated as follows:

$$z_{cg}^{cmd} = z_b - \Delta z_0 \quad (3.2.21)$$

where z_b is the current offset of the boom tip from the nominal trajectory, and Δz_0 is the normal distance between the CG and the RR in the receiver's predicted steady-state orientation. The quantities are illustrated in Figure 3.2. Note that the current orientation of the receiver is not taken into account.

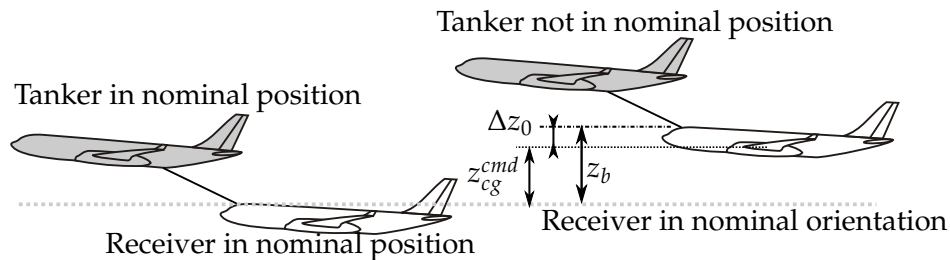


Figure 3.2: Visualisation of reference used in CG-CG architecture

3.2.4.2 CG Model - RR Feedback

Feedback gains are calculated using the unmodified CG model, but the position of the RR is used for feedback. This architecture can be seen as a naïve improvement on the CG-CG system by accounting for the change in the position of the RR relative to the CG. Since the CG model is used to calculate feedback gains, the gains are identical to those of the CG-CG system. The CG position reference is calculated as follows:

$$z_{cg}^{cmd} = z_b - \Delta z \quad (3.2.22)$$

where Δz is the instantaneous normal distance between the RR and the CG, calculated using the current orientation of the receiver, as illustrated in Figure 3.3.

The changing value of Δz is precisely the dynamics modelled by the RR model. Thus, in calculating the reference using Equation 3.2.22 the RR dynamics are included in the control loop. Since these dynamics were not considered when calculating the feedback gains, modelling errors will affect the performance of the system.

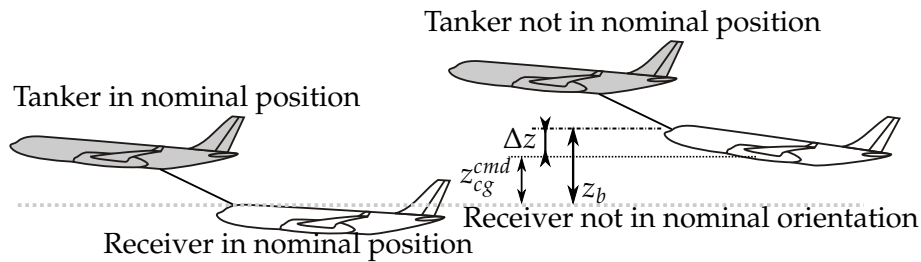


Figure 3.3: Visualisation of reference used in CG-RR architecture

3.2.4.3 RR Model - RR Feedback

Feedback gains are calculated using the modified RR model, and the position error of the RR is used for feedback. A new control system is calculated taking the left half-plane zeros into account. The position error of the RR is measured or estimated and used for feedback. A new controller and estimator are thus required. The RR reference is calculated as follows:

$$z_{rr}^{cmd} = z_b \quad (3.2.23)$$

Since the model describes the movement of the RR and not the CG, the distance between the CG and RR does not need to be included in the reference calculation.

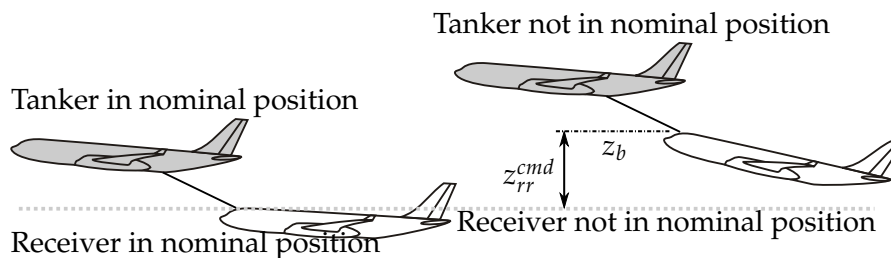


Figure 3.4: Visualisation of reference used in RR-RR architecture.

The goal of investigating these three architectures is to find out in which situation a certain scheme is acceptable. The order in which the models were presented represents increasing deviation from a standard station keeping controller architecture. It is thus desirable to select the simplest architecture required for a specific aircraft. It will be shown that this largely depends on the required closed loop bandwidth of the control system and the position of the RR zeros.

3.2.5 Results

The systems are investigated at four bandwidths. The dominant (slower) poles are placed at 50%, 80%, 100% and 120% of the natural frequency of the zeros. The gains are applied to a model that contains the CG and RR kinematic states. While only the applicable states are used for feedback, it is important to investigate the movement of the CG and the RR.

3.2.5.1 CG Model - CG Feedback

The system's response to a position command step is shown in Figure 3.5. As expected, the CG system's rise time decreases as the bandwidth is increased. The RR system shows a dis-

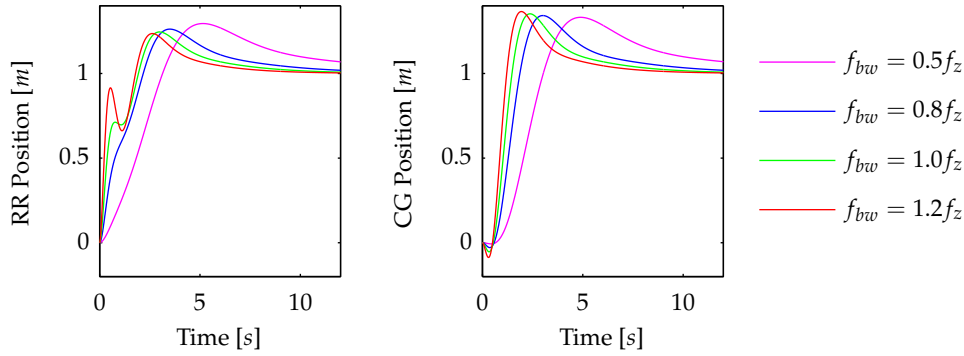


Figure 3.5: CG Model - CG Feedback: Time response of the RR and the CG to a CG position step command

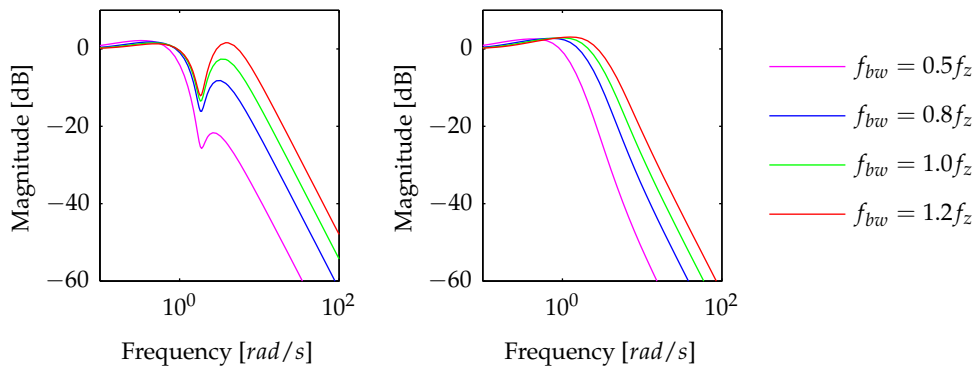


Figure 3.6: CG Model - CG Feedback: Frequency response of the CG and the RR to a CG position command

rupted response at higher bandwidths. This occurs when the bandwidth of the system nears and passes the RR zeros. In addition to the added oscillation, the RR system shows a slower peak time than the CG system with the same pole positions. This indicates that the attainable bandwidth of the RR system could be limited by the presence of the zeros.

Figure 3.6 shows the frequency response of the CG-CG system's command tracking. It can be seen that the notch created by the left half-plane zeros enters the passband as the bandwidth increases.

Figures 3.7 and 3.8 show the frequency and time responses respectively to a vertical gust disturbance. The plots show perfect rejection of steady-state disturbances at the CG. The RR shows poor rejection of low-frequency disturbances. This makes intuitive sense, as the aircraft will change orientation to combat the disturbance, thereby changing the position of the RR relative to the CG. The term Δz will thus change, but is considered to be constant when calculating the CG reference, as shown in Equation 3.2.21. Any constant offset from the calculated steady-state orientation will therefore result in an error.

This architecture completely ignores the dynamics of the RR, which is a valid assumption that will result in minimal errors if:

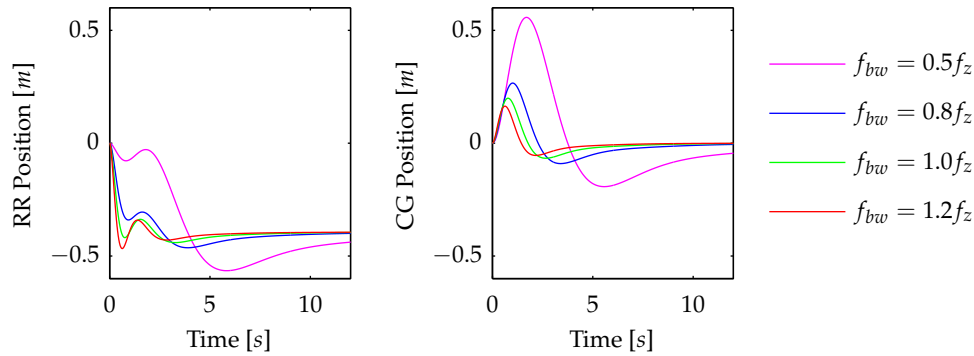


Figure 3.7: CG Model - CG Feedback: Time response of the CG and the RR to a downwash step disturbance

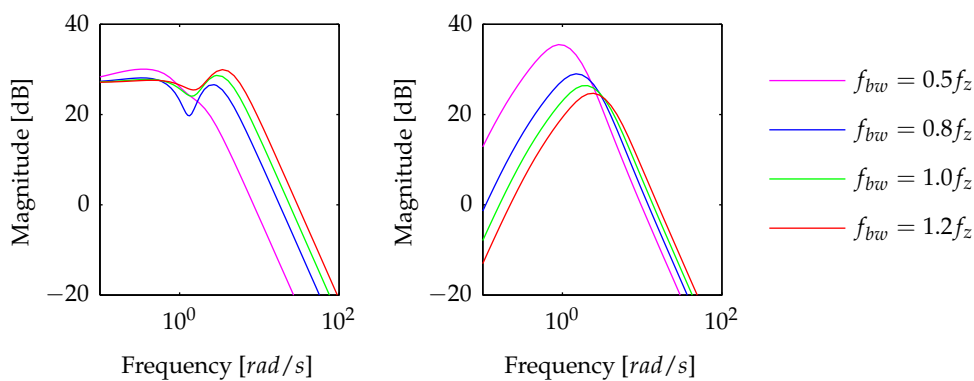


Figure 3.8: CG Model - CG Feedback: Frequency response of the CG and the RR to a downwash disturbance

- The bandwidth of the system is significantly lower than the frequency of the zeros. As seen in the graphs, the zeros start to affect the response when the bandwidth passes 80% of the zeros' frequency. Using Equation 3.2.10, one can easily approximate the position of any aircraft's RP zeros and determine whether further investigation into RP dynamics is warranted for that specific aircraft. Small- and medium-sized aircraft will have high-frequency zeros and can readily use this architecture.
- The expected error caused by the constant offset in orientation due to disturbances is small. Most aircraft that meet the first requirement will also meet this requirement, since the distance to the RP will be short.

3.2.5.2 CG Model - RR Feedback

The CR-RR architecture was proposed as a way of improving the steady-state error of the RR when the receiver is subjected to a constant disturbance. The disturbance Bode plots in Figure 3.9 show that this has been achieved. Compared to Figure 3.8, the RR, and not the CG, has perfect rejection of steady-state disturbances.

As mentioned earlier, the architecture includes the RR dynamics without modelling them. The consequence of this is clearly visible in the step responses shown in Figure 3.10. The step

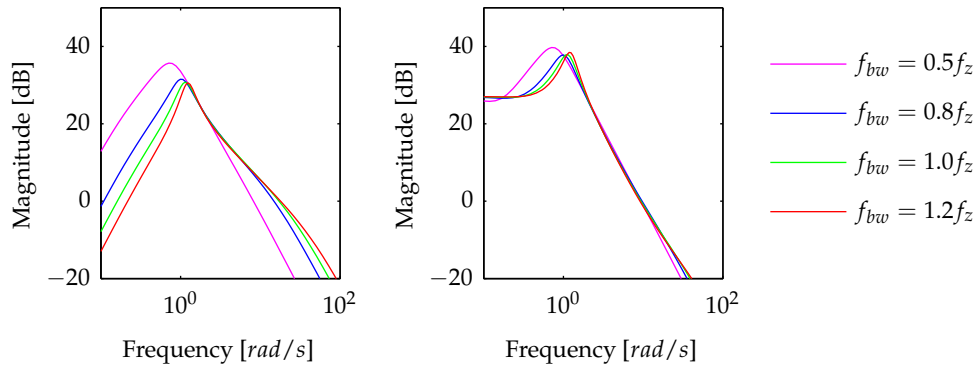


Figure 3.9: CG Model - RR Feedback: Frequency response of the CG and the RR to a downwash step disturbance

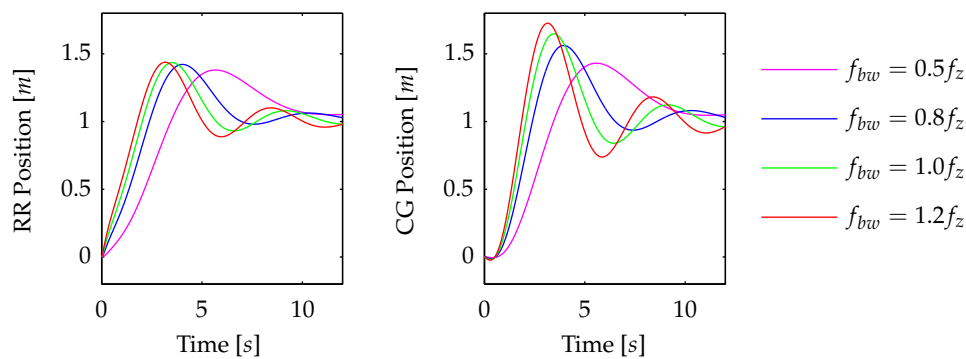


Figure 3.10: CG Model - RR Feedback: Step response of the CG and the RR to a step command response shows that the poles have moved to positions with significantly less damping.

This architecture will offer an improvement over the CG-CG system and introduce minimal errors if:

- The system bandwidth is significantly lower than the RP zeros. Lower-frequency zeros will place impracticable limitations on the attainable system bandwidth.
- The expected change in the steady-state orientation of the aircraft introduces large changes in the normal distance between the CG and the RR.

Considering the effect of ℓ_x on the frequency of the RR zeros (Equation 3.2.10), it is unlikely that the two conditions listed above would both be true for a given aircraft.

A large distance between the CG and the RR introduces significant complexity to the AAR problem. Simply using the instantaneous orientation to determine a desired CG position does not adequately address this complexity.

3.2.5.3 RR Model - RR Feedback

The problems mentioned above necessitate that an RR-specific model be derived. New feedback gains are calculated using the model derived in the previous section. The RR dynamics are thus included in the control loop and considered when calculating the feedback gains.

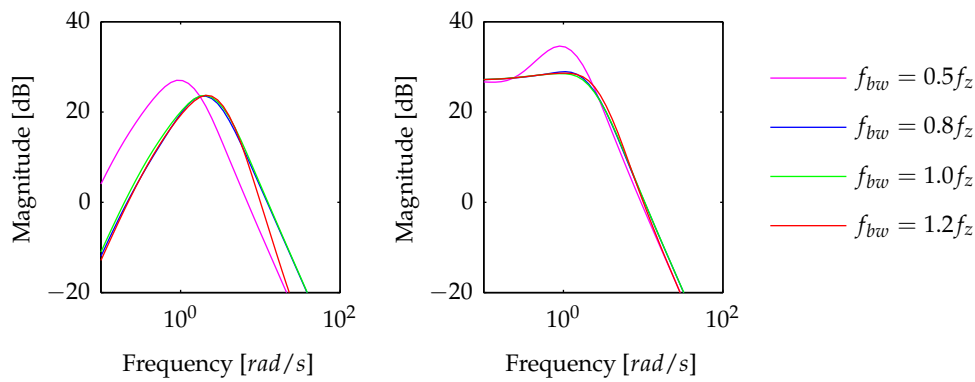


Figure 3.11: RR Model - RR Feedback: Frequency response of the CG and the RR to a downwash disturbance

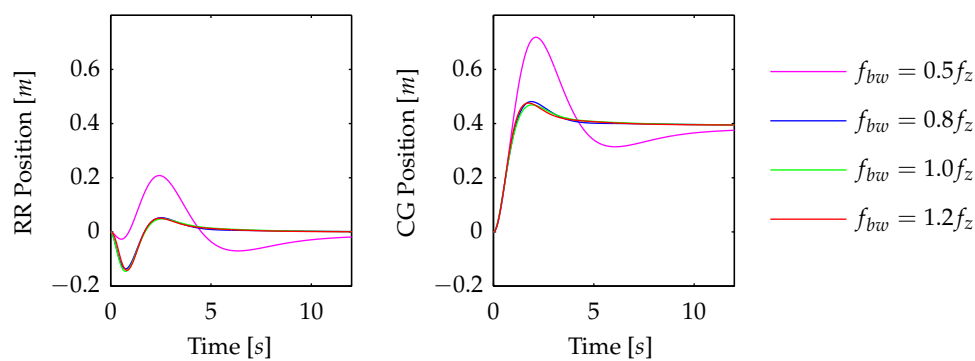


Figure 3.12: RR Model - RR Feedback: Time response of the CG and the RR to a downwash step disturbance

Figure 3.11 shows the disturbance rejection Bode plot for this architecture. It can be seen that in this case the RR, and not the CG, has perfect rejection of low-frequency disturbances.

Figure 3.12 shows the time response to a downwash step. Note that the position of the RR settles back to zero, in contrast to Figure 3.12, where the CG settles back to zero. Furthermore, the degradation due to modelling errors, present in the CG-RR system, is not visible here. The RR-RR system will thus have an advantage over the CG-CG system if the receiver is exposed to an unknown downwash angle.

The response to a position step command is shown in Figure 3.13. The distortion of the RR response is still visible in the higher-bandwidth systems. It is clear that, even with the RR-RR architecture, the bandwidth of the system cannot be increased past the frequency of the zeros.

This architecture needs to be used if:

- The aircraft is large enough for a change in orientation to result in a fairly large displacement of the RR relative to the CG.
- Large low-frequency disturbances are expected.

The inclusion of the RR dynamics in the model has removed the steady-state errors, but does not remove the limitation the zeros place on the attainable bandwidth. It is clear that for the

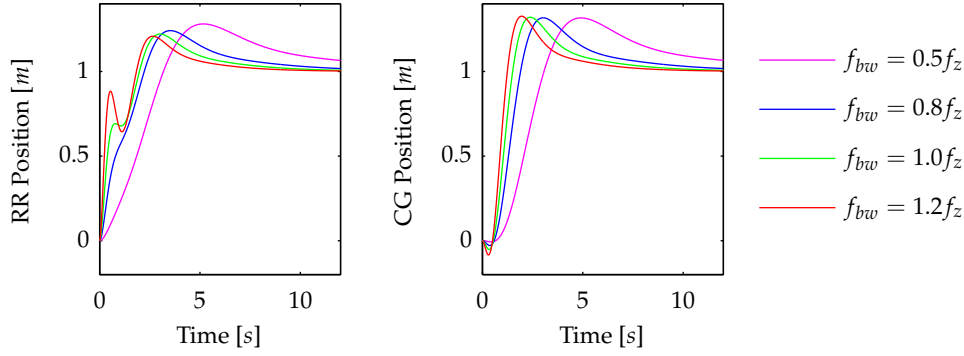


Figure 3.13: RR Model - RR Feedback: Step response of the CG and the RR to a step command

Airbus A330 MRTT, the RR-RR architecture must be used.

3.3 Lateral

Consider the state space model presented below. The model describes the change in lateral velocity error (lateral acceleration) of the refueling receptacle in response to aileron and rudder inputs.

$$\begin{aligned} \mathbf{x} &= \begin{bmatrix} \beta & p & q & \phi \end{bmatrix} \\ \mathbf{u} &= \begin{bmatrix} \delta_a \\ \delta_r \end{bmatrix} \\ \mathbf{y} &= \begin{bmatrix} \dot{v}_{rr} \end{bmatrix} \end{aligned} \quad (3.3.1)$$

$$\begin{aligned} \mathbf{A} &= \begin{bmatrix} \frac{-C_\alpha F_T}{m\bar{V}} & S_\alpha - \frac{S_p}{m\bar{V}} & -C_\alpha - \frac{S_R}{m\bar{V}} & \frac{gC_\theta}{V_T} \\ c_3\bar{L}_\beta + c_4N_\beta & c_3\bar{L}_p + c_4N_p & c_3\bar{L}_R + c_4N_R & 0 \\ c_4\bar{L}_\beta + c_9N_\beta & c_4\bar{L}_p + c_9N_p & c_4\bar{L}_R + c_9N_R & 0 \\ 0 & 1 & \tan(\theta) & 0 \end{bmatrix} \\ \mathbf{B} &= \begin{bmatrix} \frac{-\bar{S}_{\delta_a}}{m\bar{V}} & \frac{-\bar{S}_{\delta_r}}{m\bar{V}} \\ c_3\bar{L}_{\delta_a} + c_4N_{\delta_a} & c_4\bar{L}_{\delta_a} + c_9N_{\delta_a} \\ c_3\bar{L}_{\delta_r} + c_4N_{\delta_r} & c_4\bar{L}_{\delta_r} + c_9N_{\delta_r} \\ 0 & 0 \end{bmatrix} \\ \mathbf{C} &= \begin{bmatrix} -\frac{\bar{S}_\beta}{m} + gS_{\gamma+\omega_d} + l_x(c_4\bar{L}_\beta + c_9N_\beta) - l_z(c_3\bar{L}_\beta + c_4N_\beta) \\ -\frac{\bar{S}_p}{m} + gS_{\gamma+\omega_d} + l_x(c_4\bar{L}_p + c_9N_p) - l_z(c_3\bar{L}_p + c_4N_p) \\ -\frac{\bar{S}_R}{m} + gS_{\gamma+\omega_d} + l_x(c_4\bar{L}_R + c_9N_R) - l_z(c_3\bar{L}_R + c_4N_R) \\ gC_\theta \end{bmatrix}^T \\ \mathbf{D} &= \begin{bmatrix} -\frac{\bar{S}_{\delta_a}}{m} + l_x(c_4\bar{L}_{\delta_a} + c_9N_{\delta_a}) - l_z(c_3\bar{L}_{\delta_a} + c_4N_{\delta_a}) \\ -\frac{\bar{S}_{\delta_r}}{m} + l_x(c_4\bar{L}_{\delta_r} + c_9N_{\delta_r}) - l_z(c_3\bar{L}_{\delta_r} + c_4N_{\delta_r}) \end{bmatrix}^T \end{aligned} \quad (3.3.2)$$

Similar to the normal dynamics, the lateral dynamics of the refueling point can differ significantly from those of the centre of gravity. In this section, the effect of the distance to the refueling point on the lateral system will be analysed to aid in the eventual control design. As

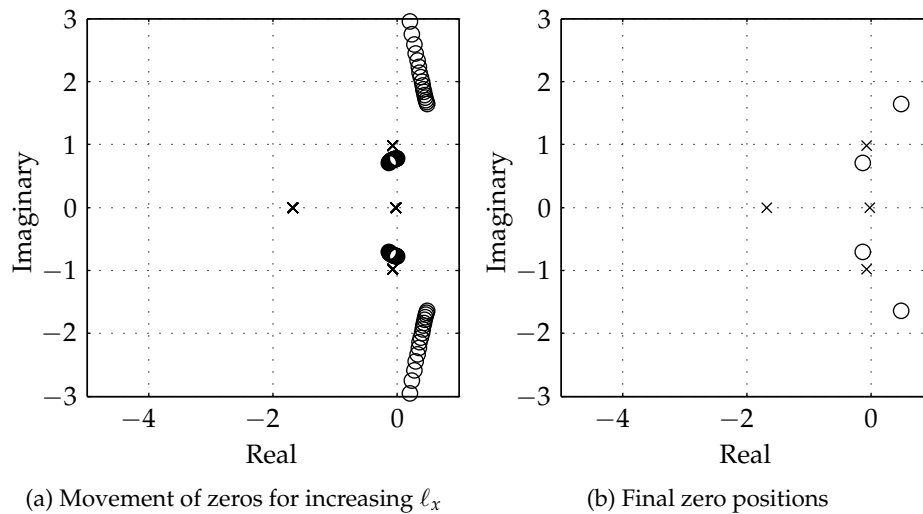


Figure 3.14: Poles and zeros of system from aileron input to lateral acceleration of RR

before, two models will be investigated: a CG model where l_x^w and l_z^w are set to zero, and an RR model where the distances for an Airbus A330 MRTT are used.

3.3.1 Zeros

Since zeros are specific to a certain input and output, the aileron and rudder inputs will be investigated separately. Figure 3.14 shows the poles and zeros of the transfer function from aileron deflection to lateral position for various refueling receptacle positions.

There are four zeros present in the transfer function. Two zeros are positioned close to the Dutch roll mode zeros. In the CG model, there is a pair of relatively high-frequency zeros in the left half-plane. As the receptacle moves forward and upward, the frequency of the zeros decreases and the zeros move to the right half-plane. Figure 3.15 shows the poles and zeros of the transfer function from rudder deflection to lateral position for various refueling receptacle positions.

The rudder system also contains four zeros. As the receptacle moves forward from the centre of gravity, a pair of zeros close to the Dutch roll mode poles move around said poles. A much larger change is seen in the other two zeros' positions. The CG system has real positive and negative zeros, indicating non-minimum phase behaviour. This is due to the initial negative acceleration caused by the rudder deflection before the increased sideslip causes a positive lateral acceleration. Similar to the zeros in the normal system, the zeros move toward positive and negative infinity before becoming a pair of complex zeros in the left half-plane.

3.3.2 Closed Loop

The effect of the zeros on the closed loop system is investigated. As before, a control system is created to control the linear lateral model. Non-linearities and practical limitations are not considered. LQR is used to create the control system. Building on the results of the previous section, the RP-RP architecture will be used. Two different weighting schemes were trialed and

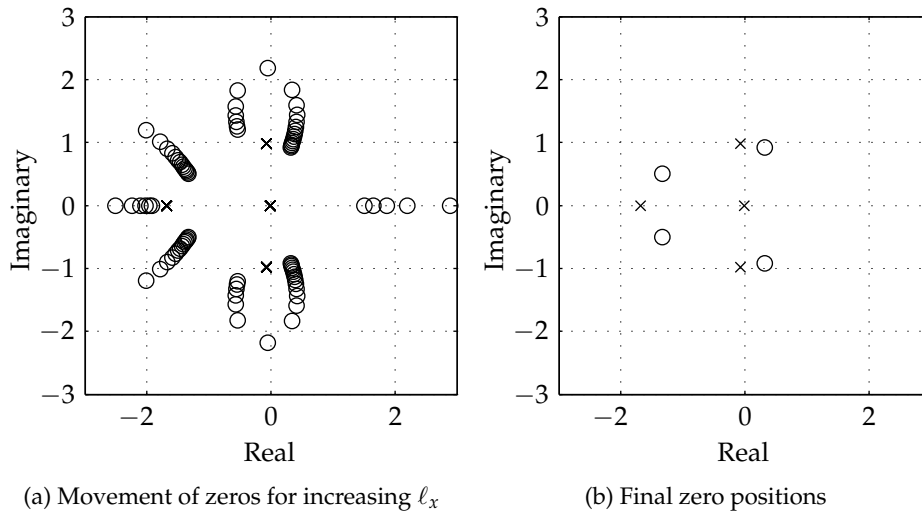


Figure 3.15: Poles and zeros of system from rudder input to lateral acceleration of RR

are shown in Table 3.3. The weightings were chosen to encourage LQR to use either roll-to-turn or yaw-to-turn exclusively.

State	Roll to Turn	Yaw to Turn
β	5	0.1
p	0.1	1
r	1	0.1
ϕ	0.1	5
v_{rr}	0.5	0.5
y_{rr}	0.2	0.2
y_{rri}	0.1	0.1
δ_a	0.01	0.1
δ_r	0.1	0.01

Table 3.3: LQR state weightings used for analysis of lateral RR-system

Figures 3.16 and 3.17 show the RR and CG responses to a lateral RR position step command for the two weighting schemes.

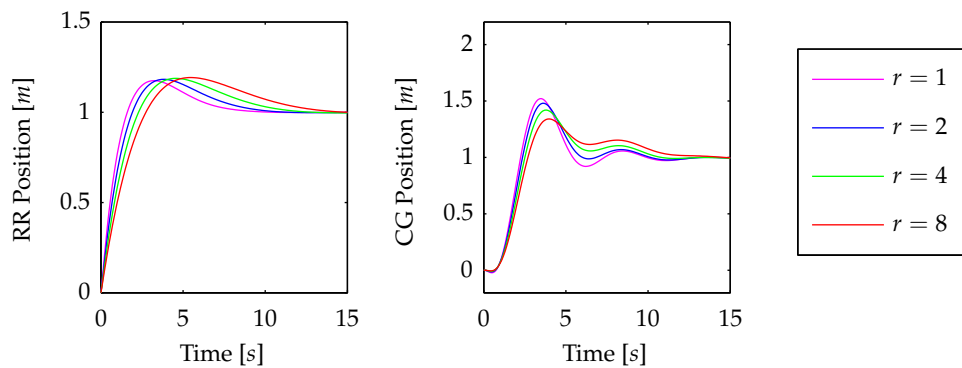


Figure 3.16: Response of the CG and the RR to a lateral step command using primarily bank-to-turn

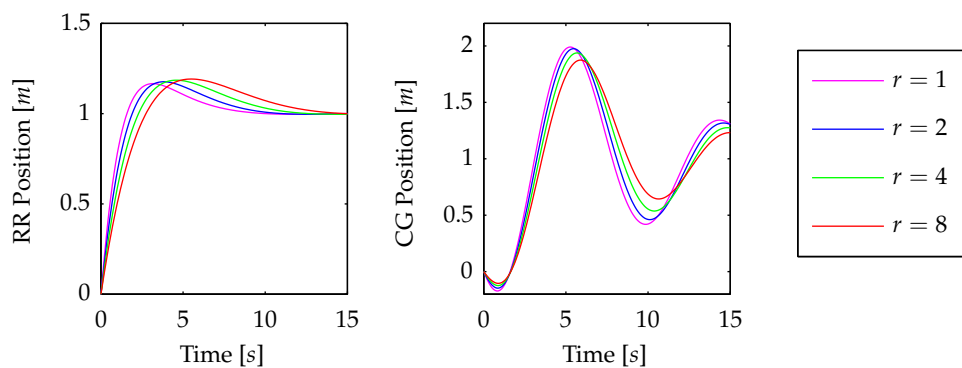


Figure 3.17: Response of the CG and the RR to a lateral step command using primarily skid-to-turn

The responses show that using primarily skid-to-turn results in a poorly damped response for the CG. This is due to the yawing of the aircraft and the distance between the CG and the RR. In Section 5.2.2, it will be shown that LQR places poles close to the RR zeros to improve the response of the RR kinematics. Care must be taken not to cause too much oscillation at the CG. The bank-to-turn response shows less CG movement since $l_z < l_x$. The optimal solution will be a combination of the two responses, and will be investigated in Chapter 5.

3.4 Summary

This chapter presented a comprehensive analysis of a linear aircraft model with refueling receptacle dynamics added. It was found that the inclusion of the RR dynamics introduces a pair of complex zeros in the left half-plane of the normal system. The zeros limit the attainable closed loop bandwidth. It was shown that to achieve good rejection of low-frequency disturbances, the position of the RR and not the CG must be used for feedback. Furthermore, to prevent modelling errors, the RR dynamics must be included in the linear model when calculating feedback gains. This was referred to as the RR-RR control architecture, in contrast to the traditional CG-CG architecture. These findings apply primarily to large receiver aircraft. A set

of equations was also derived for the approximate RR zero position. Using this equation, a designer can quickly establish whether a specific aircraft requires an RR-specific controller, or not. Finally, The effect of the RR dynamics on the lateral system was also shown. This analysis forms one of the major contributions of this thesis.

Chapter 4

Tanker Control

4.1 Overview

As stated in the requirements in Section 1.2, the tanker must not use an AAR-specific control system. It is the task of the receiver to follow the tanker. This section will investigate the control options available to the tanker and find the best configuration for use during AAR. Recorded data from the tanker will be shown to illustrate the path that the receiver's RR needs to follow.

The tanker is controlled by two sets of control loops. The inner loop is the Airbus FBW (fly-by-wire) system, which abstracts the actuators to convenient inputs such as roll rate and normal acceleration. The outer loop is a collection of lower-bandwidth hold modes that provide inputs to the FBW system. The internal structure of the hold modes was not made available and thus cannot be analysed. Several control schemes were trialled in non-linear simulations; the controllers that resulted in the best performance are presented here.

The general philosophy in the control of the tanker is to apply the minimum control needed to prevent the tanker from moving too far from the trajectory or straying from the flight point. Since the tanker and receiver are exposed to the same turbulence, any aggressive control inputs from the tanker will increase, not decrease, the receiver's workload.

Sections 4.2, 4.4 and 4.5.2 investigate the normal, lateral and axial control of the tanker respectively. Section 4.5 presents the control scheme implemented to command the tanker to fly the racetrack trajectory.

4.2 Normal Control

The normal FBW system maintains the normal acceleration of the tanker to the commanded value. The hold mode maintains a constant flight-path angle by commanding normal acceleration. Altitude is not controlled; if the tanker is disturbed during straight and level flight, it will return to the commanded flight-path angle, and not the initial altitude. If the altitude is allowed to increase or decrease too much, it could be problematic, since the linear model calculated for the receiver would become inaccurate.

For aerial refueling on the straight and level trajectory, the flight-path angle is commanded to zero. When using the toboggan trajectory, a flight path angle is calculated that would result in a sink rate of 500ft/min.

Figure 4.1 shows the Z-offset (relative to initial altitude) and velocity (in inertial axes) of the tanker's CG when exposed to medium turbulence at the flight point: $FL = 100$, $V_c = 200kt$, $m_t = 125t$.

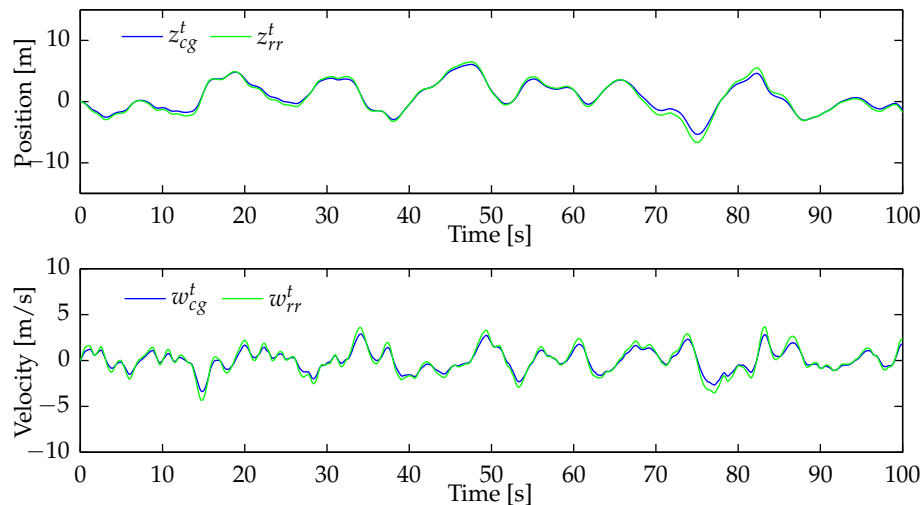


Figure 4.1: Change in Z position and velocity of tanker CG and desired receiver RR position for tanker exposed to medium turbulence

The figure also shows the altitude and normal velocity of the nominal position of the boom tip, calculated using equations from Section 1.6.1. The nominal position of the boom tip will be the commanded position of the receiver's RR. Note that the deviation of the boom tip can exceed the movement of the CG by up to 1 m. Considering the size of the connect envelope, it becomes clear that the orientation of the tanker must be taken into account when controlling the receiver.

4.3 Lateral Control

The lateral FBW system maintains the commanded sideslip angle and roll rate. The hold modes maintain a constant heading and sideslip angle by providing input to the FBW system. It was found that the heading hold mode is not required. In light and medium turbulence, the tanker will maintain its approximate heading if it maintains a zero bank angle. If the tanker were to move too far off course, the tanker's pilot could correct this with minor commands that would not impact the AAR controller's performance.

Figure 4.2 shows the Y-position and velocity (in earth axes) of the tanker's CG when exposed to medium turbulence at the flight point: $FL = 100$, $V_c = 200kt$, $m_t = 125t$. The figure also shows the Y-position and Y-velocity of the desired position of the receiver's RR, calculated using equations from Section 1.6.1.

Since the East position deviates far from the original position, the difference between the tanker CG and desired receiver RR positions cannot be seen in Figure 4.2. Figure 4.3 shows

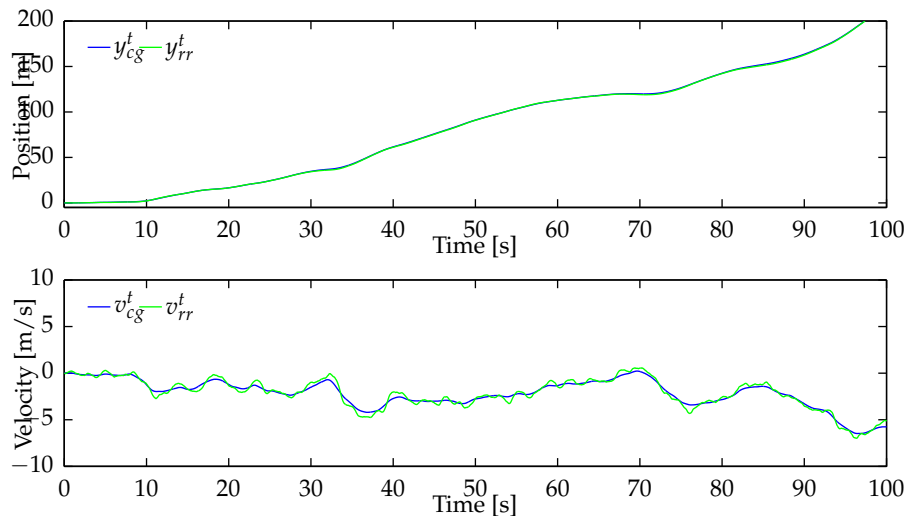


Figure 4.2: Change in East position and velocity of tanker CG and desired receiver RR position for tanker exposed to medium turbulence

the difference between these two quantities. Note that the difference can be as high as 0.5m, a significant portion of the width of the connect envelope.

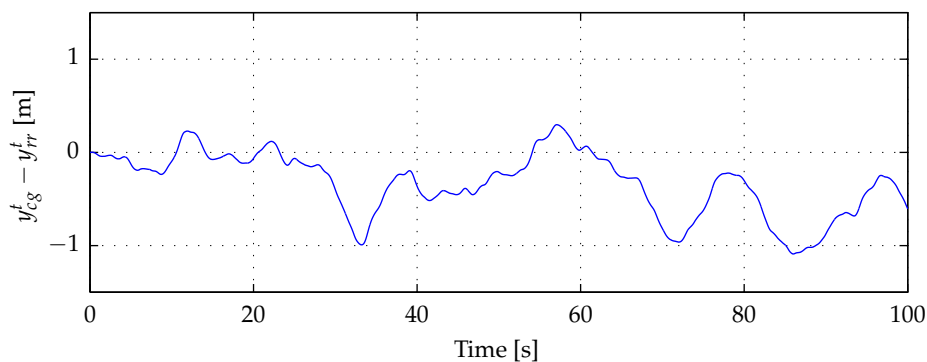


Figure 4.3: Difference in East position of tanker CG and desired receiver RR position for tanker exposed to medium turbulence

4.4 Axial Control

The Airbus A330 MRTT is equipped with an auto-thrust system to maintain the commanded airspeed. As with the hold modes, the internal structure of the auto-thrust system was not made available. The bandwidth of the auto-thrust (as with the other hold modes) is too low to be used to control the receiver aircraft. While the normal and lateral hold modes are needed to prevent the tanker from deviating too far from the intended trajectory, the use of the auto-thrust is not required. A tanker with a constant throttle position will maintain a relatively constant airspeed - if the change of mass due to fuel transfer is ignored. A pilot can provide the slow change required as the tanker changes mass over the course of refueling.

Through non-linear simulations, it was found that the axial control of the receiver encounters difficulty when following a tanker with auto-thrust engaged. Such a receiver has to match the thrust actuation of the tanker while also correcting relative errors. This saturated the slew rate of the engine model, and consequently the RR could not be regulated inside the disconnect envelope. A rudimentary implementation of the bow-wave effect in the non-linear simulation further worsened performance, as the tanker's auto-thrust responds to the bow-wave. This caused oscillation, since the two axial control systems coupled [2].

The tanker's axial actuation is thus simply a constant throttle setting. A slight adjustment is made in a banked turn, as will be discussed in the next section. Figure 4.4 shows the ground speed of the tanker flying in turbulent conditions with a constant throttle setting.

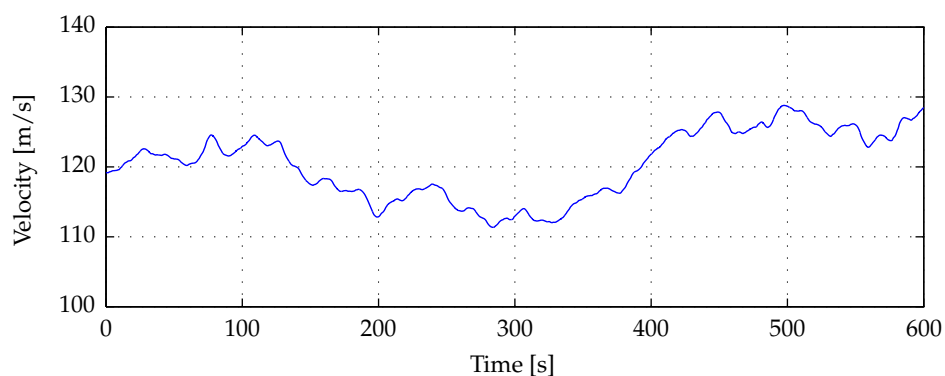


Figure 4.4: Ground speed of tanker when exposed to medium turbulence with constant throttle position at flight point $FL = 100$, $V_c = 200kt$, $m_t = 125t$

4.5 Racetrack Trajectory

4.5.1 Normal Control

No adjustments are required to the tanker's normal control when flying a banked turn. The FBW and hold mode will increase the angle of attack sufficiently to maintain the desired flight-path angle.

4.5.2 Lateral Control

The hold modes for lateral control of the tanker need to be adjusted to fly a racetrack trajectory. The trajectory is divided into four segments, as illustrated in Figure 4.5.

Segment 1: Bank-angle hold 0 degrees

Segment 2: Bank-angle hold +25 degrees

Segment 3: Bank-angle hold 0 degrees

Segment 4: Bank-angle hold +25 degrees

The exact shape of the racetrack is not critically important, as long as the aircraft remain close to their original locations. Consequently, to keep the tanker's control input simple, the tanker will not attempt to turn exactly 180 degrees at each turn.

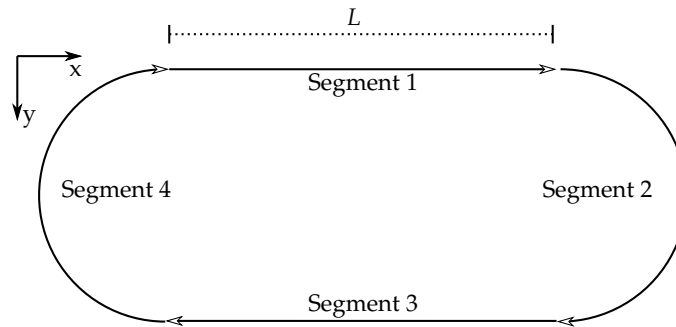


Figure 4.5: Racetrack trajectory segments

As stated in the requirements in Section 1.2, the control of the tanker must be as simple as possible. The tanker is banked by supplying a deflection of the lateral stick over 10 seconds. This input can easily be supplied by a pilot. Figure 4.6 shows the tanker's bank angle response when entering a turn.

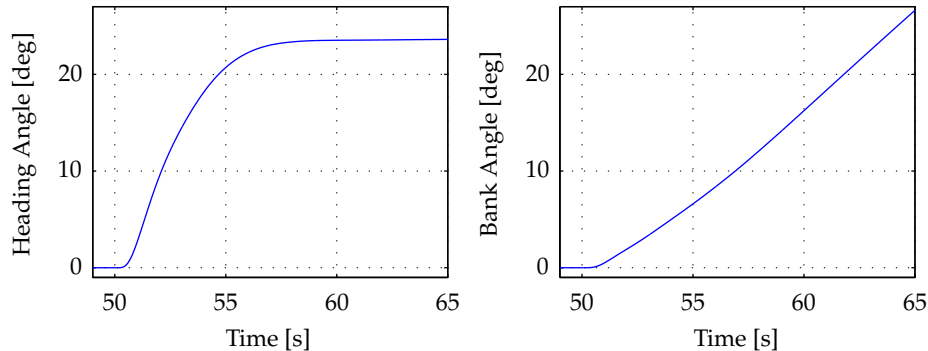


Figure 4.6: Bank and heading angle of tanker entering banked turn

The transitions between the segments are triggered at the following conditions:

- 1 → 2 X position reaches side length, L .
- 2 → 3 Heading angle is 160 deg.
- 1 → 2 X position reaches 0.
- 2 → 3 Heading angle is -20 deg.

Through simulation it was found that when the bank angle is reduced from 25 degrees, the tanker turns approximately another 20 degrees. By changing segment 20 degrees before the desired heading angle, excessive overshoot in the heading angle is prevented. The result is

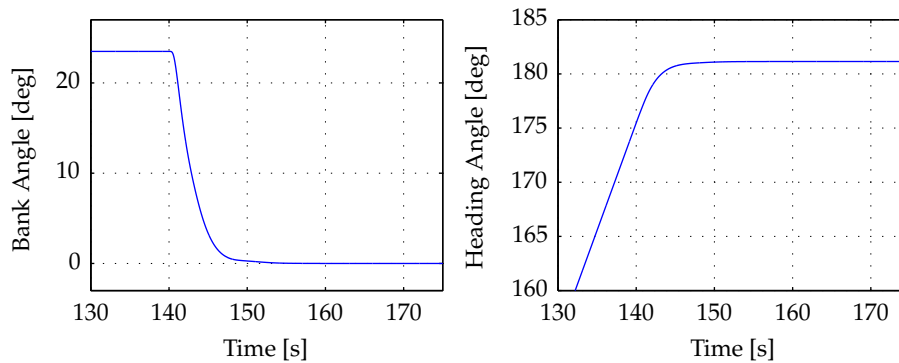


Figure 4.7: Bank and heading angle of tanker leaving banked turn

a trajectory close to a perfect racetrack, which can be slowly adjusted by the tanker pilot, if desired. The bank and heading angle of a tanker leaving a banked turn are shown in Figure 4.7

4.5.3 Axial Control

While in banked turn flight, the normal FBW system commands a higher angle of attack to maintain the commanded flight-path angle. The increased angle of attack causes an increase in drag that will slow the aircraft, since auto-thrust is not engaged. Ultimately, this will cause the tanker to start losing altitude. Figure 4.8 shows the altitude and ground speed of a tanker over the course of a 180 degree turn with a constant throttle setting. The change in airspeed will cause the receiver's linear model to become inaccurate. In extreme cases, on the edge of the speed and mass envelope, it can cause the tanker or receiver to leave the permissible envelope.

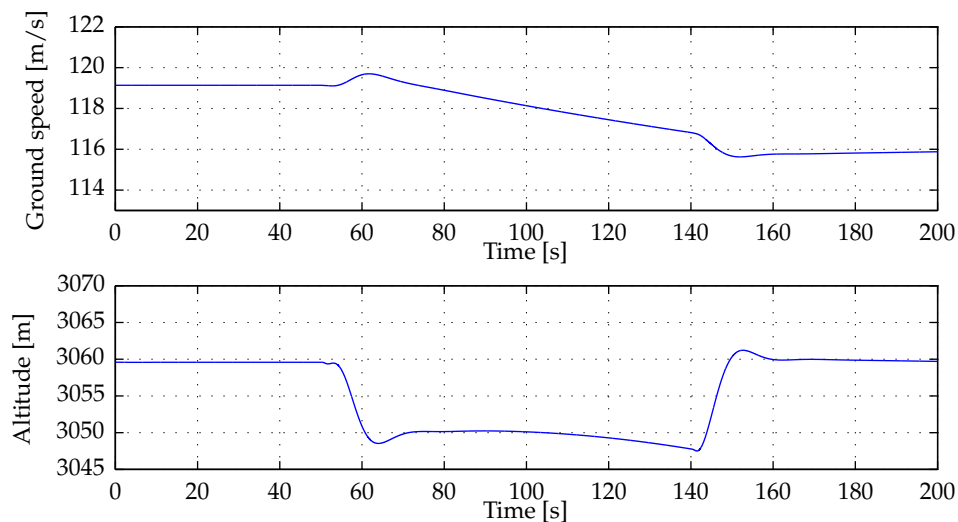


Figure 4.8: Ground speed and altitude of tanker over course of banked turn without increasing thrust

To prevent the change in airspeed, the thrust is increased manually. To minimize the additional complexity to the receiver's command, the thrust must be increased gradually over time. For a given flight point, the required increase in thrust is calculated and commanded

over 20 seconds from the start of the segment. The thrust is also reduced over a period of 20 seconds when returning to a straight and level segment. Figure 4.9 shows the ground speed and altitude of the tanker with this change included.

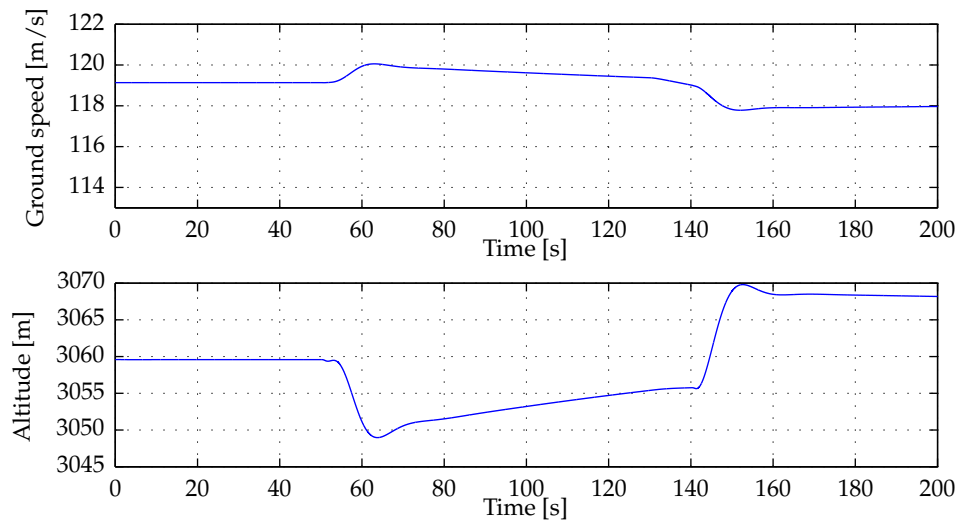


Figure 4.9: Ground speed and altitude of tanker over course of banked turn when increasing thrust

The figures show that there is still some change in ground speed and altitude. These errors are not significantly greater than the changes due to turbulence, and can be followed by the receiver.

4.6 Summary

When performing AAR, control of the tanker and the control of the receiver are equally important. The requirements of this project stated that the receiver must be equipped with AAR-specific controllers, while the tanker must use the existing flight software on the Airbus A330 MRTT. Despite these restrictions, there are still many ways to configure the tanker's control. Some options (e.g. using the auto-thrust system) can dramatically increase the workload of the receiver or make successful AAR impossible.

Through numerous non-linear simulations, an optimal tanker control strategy was found. The use of hold modes is combined with small inputs that can feasibly be provided by the tanker's pilot. The control strategy allows the tanker to follow the intended trajectory (straight and level, toboggan or racetrack) in light or medium turbulence. The findings presented in this chapter are of practical use for future researchers and address one of the secondary research objectives of this thesis.

Chapter 5

Receiver Control

5.1 Overview

This chapter details the feedback control of the receiver aircraft used to achieve AAR, using the linear models derived in Chapter 2. Designing controllers capable of performing AAR of a large receiver is the primary research objective of this thesis.

A novel normal RR controller is presented. The controller specifically addresses the presence of the RR dynamics. Two axial controllers are discussed: a controller that uses only thrust for actuation, and a novel high-drag controller using a drag virtual actuator. The high-drag controller allows accurate axial regulation of the RR position, despite the relatively slow response of the large receiver's engines. In addition, lateral control is performed using optimal control. These three controllers address the specific challenges when automating the aerial refueling of a large receiver, namely the RR dynamics and the slow engine response. To the author's knowledge this is the first time such controllers are presented. While the control of a receiver aircraft in racetrack trajectory has been presented before, this is the first time it is performed using a large receiver.

For the purposes of illustrating the behaviour of the control systems, limited linear and non-linear simulation results will be shown in this chapter. The complete non-linear simulation results can be found in Chapter 6. Section 5.2, immediately below, discusses the normal controller, while Sections 5.3 and 5.4 present the two axial controllers. The lateral control system is dealt with in Section 5.5. Section 5.6 investigates the changes required to the control system to allow the receiver to follow the tanker while flying the racetrack trajectory.

5.2 Normal

In Section 2.2, a linear model for the normal dynamics of the refueling receptacle was derived. In Section 3.2, it was shown that the receptacle dynamics introduce two zeros in the left half-plane of the traditional normal dynamics of an aircraft. When the closed loop bandwidth approaches the zeros' frequency, additional oscillation is observed in the receptacle's response. This effectively limits the bandwidth of the closed loop system to be lower than the zeros' frequency. Additionally, it was shown that for large aircraft experiencing uncertain downwash angles and low-frequency disturbances, the RR-RR architecture must be used.

Various practical factors were ignored in order to analyse the closed loop RR system. In this section, a control scheme is presented, using the RR-RR architecture, to control an Airbus A330 MRTT across a variety of flight points. Actuator models and other limitations will be considered here. In Section 5.2.1, a controller is described that is capable of performing AAR at most flight points. Section 5.2.2 investigates whether it is possible to practically increase the closed loop frequency past the bound imposed by the presence of the RR zeros.

5.2.1 Receptacle-Specific Control

The normal state-space model used for control is given by Equations 5.2.1 and 5.2.2.

$$\begin{aligned}
 \mathbf{x} &= \begin{bmatrix} \alpha & q & w_{rp} & z_{rr} & z_{rri} \end{bmatrix}^T \\
 \mathbf{u} &= \begin{bmatrix} \delta_e \end{bmatrix} \\
 \mathbf{y} &= \begin{bmatrix} z_{rr} \end{bmatrix}
 \end{aligned} \tag{5.2.1}$$

$$\begin{aligned}
 \mathbf{A} &= \begin{bmatrix} \frac{Z_\alpha - T C_\alpha}{mV} & 1 + \frac{Z_q}{mV} & 0 & 0 & 0 \\ \frac{M_\alpha}{I_{yy}} & \frac{M_q}{I_{yy}} & 0 & 0 & 0 \\ \frac{Z_\alpha - T C_\alpha}{m} - \frac{M_\alpha \ell_x^w}{I_{yy}} & \frac{Z_q}{m} - \frac{M_q \ell_x^w}{I_{yy}} & 0 & 0 & 0 \\ 0 & 0 & 1 & 0 & 0 \\ 0 & 0 & 0 & 0 & 1 \end{bmatrix} & \mathbf{C} = \begin{bmatrix} 0 & 0 & 0 & 1 & 0 \end{bmatrix} \\
 \mathbf{B} &= \begin{bmatrix} \frac{Z_{\delta_e}}{mV} & \frac{M_{\delta_e}}{I_{yy}} & 0 & 0 & 0 \end{bmatrix}^T & \mathbf{D} = 0
 \end{aligned} \tag{5.2.2}$$

As before, pole placement is used to control the normal RR system. The valid area to place closed loop poles is determined by many factors. For example, the disturbance rejection criteria place a lower bound on the closed loop bandwidth. Actuator, load factor and comfort considerations enforce an upper bound. In the RR system, the position of the left half-plane zeros imposes an equally important restriction on the position of the closed loop poles. If these limits are ignored, poor performance or instability occurs at certain flight points.

Since the zero positions vary for different flight points, the closed loop pole positions need to be specifically chosen at each flight point. It was found that specifying pole positions relative to the zeros ensures similar performance across the flight domain. Suitable positions were determined experimentally:

- The short period modes are placed at 80% of the zeros' frequency, with 0.707 damping ratio.
- The kinematic (dominant) poles are placed at 65% of the zeros' frequency with 0.8 damping ratio. At most flight points, this position ensures a sufficient closed loop bandwidth to regulate the RR inside the disconnect envelope for light and medium turbulence. The poles are placed far enough from the zeros that the response is not affected.
- The integrator pole is moved to 20% of the zeros' frequency.

Figure 5.1 shows the response of the system above to a normal position step command at three flight points. The flight points were chosen with a high, low and average zero frequency and are detailed below.

$$\omega_z = 1.81 \quad V_c = 225 \text{ kt, FL} = 300, m_r = 225,000 \text{ kg}$$

$$\omega_z = 2.59 \quad V_c = 300 \text{ kt, FL} = 300, m_r = 225,000 \text{ kg}$$

$$\omega_z = 3.59 \quad V_c = 300 \text{ kt, FL} = 300, m_r = 125,000 \text{ kg}$$

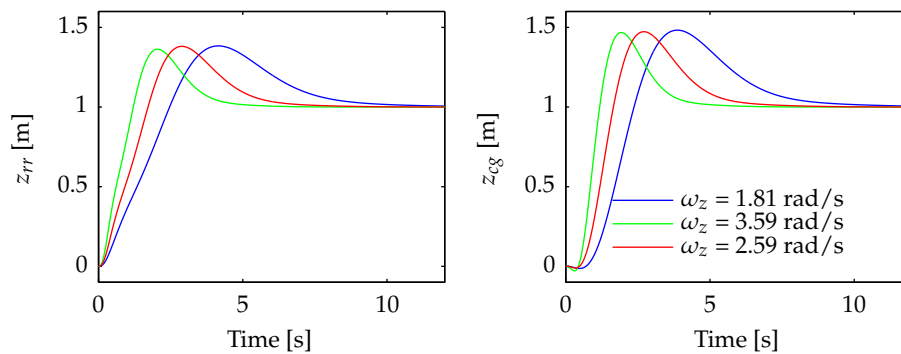


Figure 5.1: RR and CG response to a position step command

It can be seen in Figure 5.1 that the characteristics of the response are the same at all three flight points. This is important when one considers how much the zero frequency can change over flight points. Consider Figure 5.2, where the poles are placed at constant positions for all three flight points. At the flight point with the lowest zero frequency, there is additional oscillation present in the RR's response.

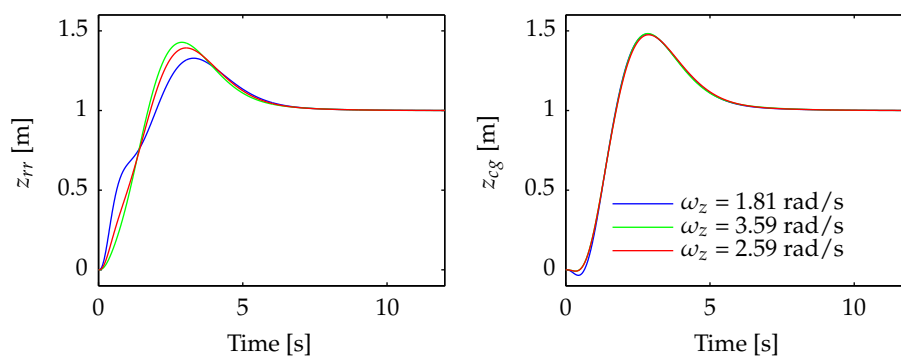


Figure 5.2: RR and CG response to a position step command at various flight points using constant closed loop pole positions

5.2.1.1 Linear Simulation

A more detailed simulation is performed at each of the flight points. A full non-linear simulation is performed of a tanker flying at the chosen altitude and speed in medium turbulence. The receiver is simulated using the linear state-space normal model, with the non-linear elevator model included in the loop. The recorded tanker position and velocity are used as commands. The goal of this simulation is to highlight the performance of the normal control system while using representative actuator models and command inputs.

Figures 5.3 to 5.5 shows the performance of the control scheme described above at flight points with varying zero frequencies. It can be seen that the normal errors are smaller than two metre. The performance of the system will be slightly better in the full non-linear simulation, as the receiver will be affected by the same turbulence as the tanker.

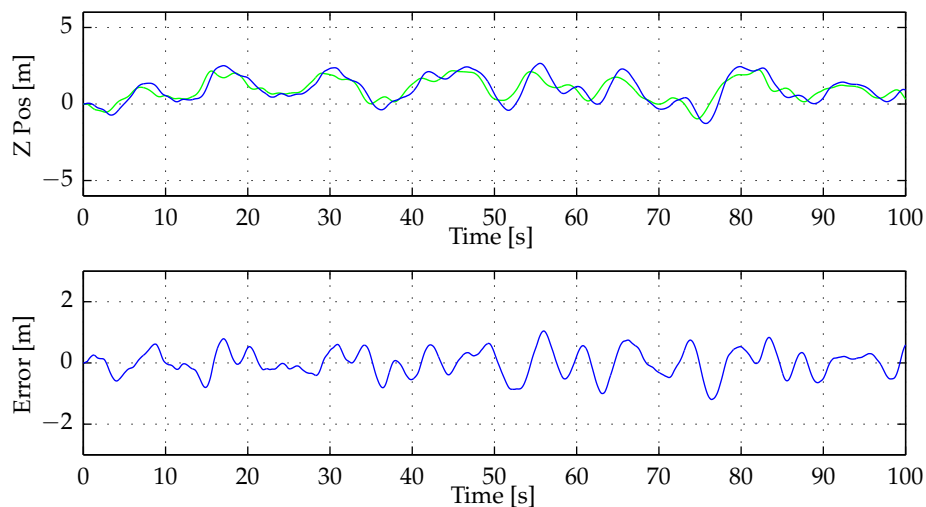


Figure 5.3: RR command, position and error in medium turbulence with zero frequency of 1.65 rad/s

5.2.2 Compensating for Receptacle Dynamics

If the bandwidth of the control systems described in the previous section is increased, the effect of the RR zeros will become visible in the response. As shown in Section 3.2, the RR dynamics influence the response when the closed loop bandwidth passes 80% of the zeros' frequency. This section will investigate possible methods of increasing the bandwidth past this point. Two methods are investigated to improve the response: cancelling receptacle dynamics, and LQR.

5.2.2.1 Cancelling Receptacle Dynamics

The RR response can be improved by placing the faster pole pair (henceforth referred to as the cancelling poles) at the zeros' position. This completely eliminates the effect of the zeros. The closed loop response of the RR is determined solely by the remaining poles. Figure 5.6 shows

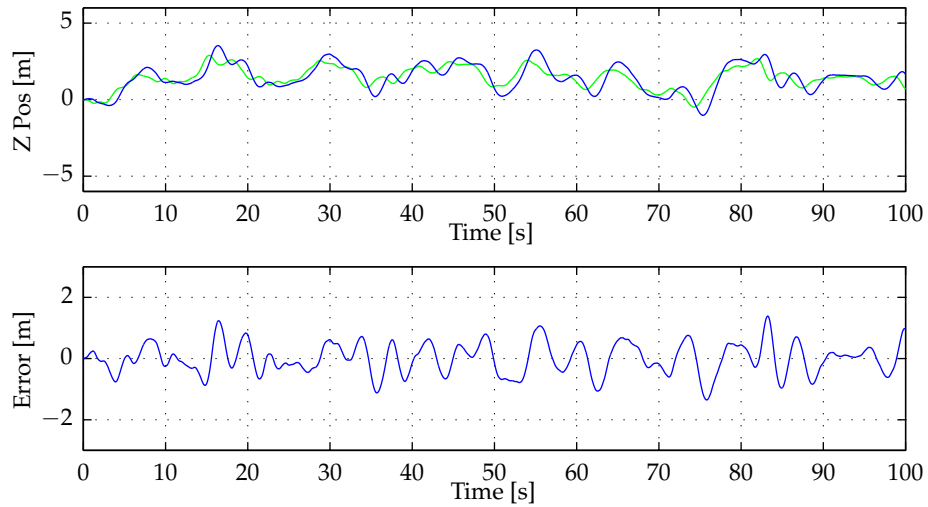


Figure 5.4: RR command, position and error in medium turbulence with zero frequency of 2.62 rad/s

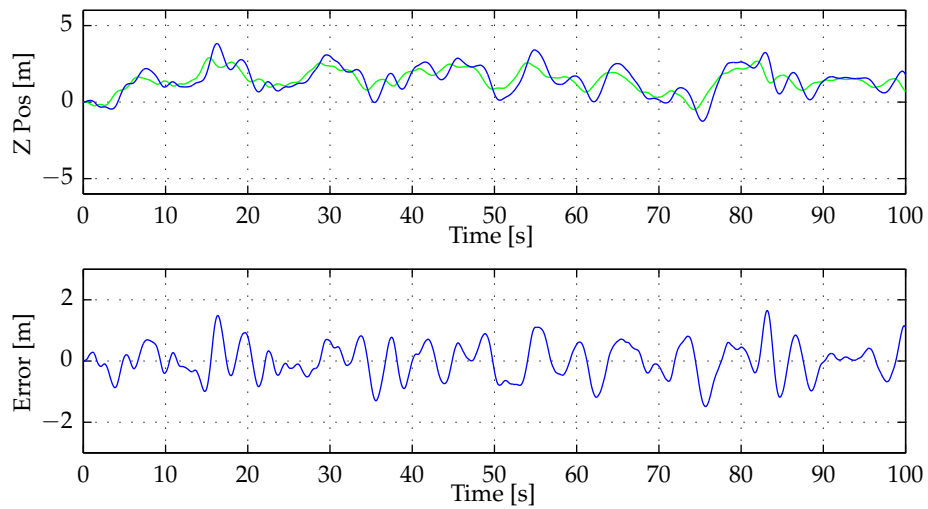


Figure 5.5: RR command, position and error in medium turbulence with zero frequency of 3.57 rad/s

the step response of the system when the zeros are cancelled. The graph shows a considerable improvement in the RR's response when cancelling the zero (b) over the previously described control design, (a).

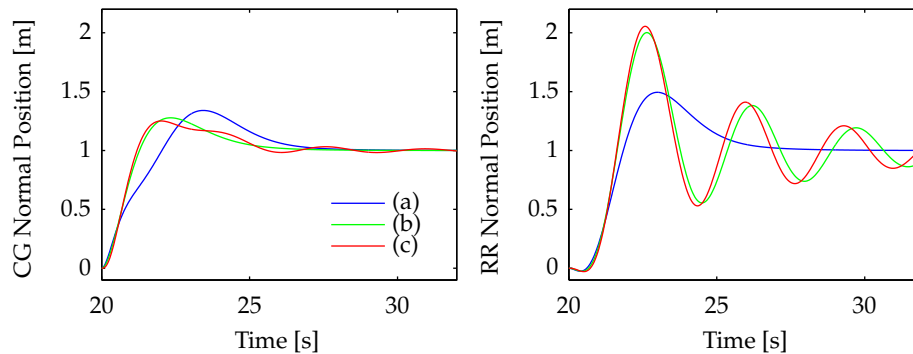


Figure 5.6: RR and CG response to a step command. (a) Unmodified control scheme. (b) Cancelling zero, without elevator model. (c) Cancelling zero with elevator model included

There are two significant problems with this method. Firstly, the RR response depends on the zero being cancelled perfectly, which is not practical. When the elevator model is included, shown as graph (c) in Figure 5.6, the response starts degrading. Secondly, the CG system's response is very poorly damped. The zeros are not present in the CG system, but the pole positions are the same as in the RR system, causing the poorly damped poles to dominate the CG response. This would place undesired strain on the aircraft. Both problems are addressed by placing the cancelling poles at the same frequency as the zeros, but with slightly more damping. Figure 5.7 shows the response of the CG and the RR for a closed loop system, where the cancelling poles are placed 15 degrees off the zeros.

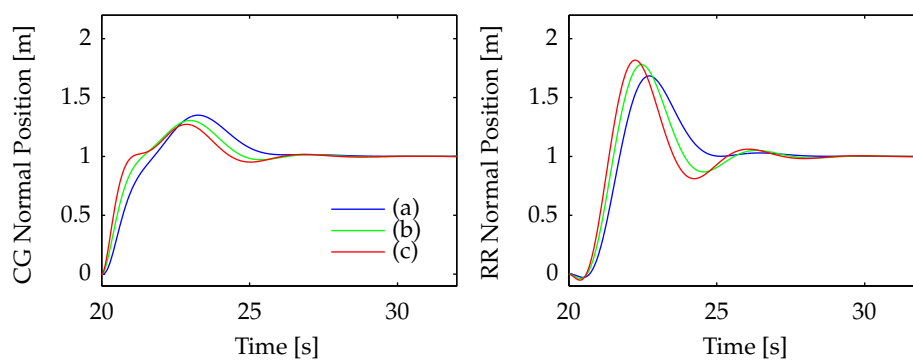


Figure 5.7: RR and CG response to a step command with 15 degree separation between zero and cancelling pole for various closed loop bandwidths. (a) Unmodified control scheme (b) Cancelling zero, without elevator model (c) Cancelling zero with elevator model included

The CG response has improved significantly. The RR response has deteriorated from Figure 5.6, but does not show a shorter rise time compared to Figure 5.2. Once the closed loop bandwidth passes the zero's frequency, the settling time of the RR system does not improve

significantly. This method can thus not mitigate the bandwidth limit imposed by the zeros, but is successful in improving the RR response when the bandwidth is chosen close (80% to 100%) to the zero's frequency. This method only needs to be used if the closed loop bandwidth must approach the zero frequency to meet performance requirements.

5.2.2.2 Optimal Control

Optimal gains are calculated using LQR, and the closed loop response of the system is investigated. The aim is to establish whether LQR can provide a solution to increase the bandwidth of a system with low-frequency zeros. For the initial investigation, the state weightings are

$$Q = \text{diag}\left(\begin{bmatrix} 10 & 10 & 0.01r & 0.2r & 0.001 \end{bmatrix}\right) \quad (5.2.3)$$

$$R = 10 \quad (5.2.4)$$

where 'diag' is a function that creates a matrix with the argument on the diagonal and zeros elsewhere. Parameter r is changed to create a more or less aggressive system. Figure 5.8 shows the pole positions of the closed loop system for various values of r . It is clear that LQR results in the same strategy described in the previous section when the RR states are heavily weighted. A complex pole pair is placed close to the RR zeros to cancel their effect. The CG response shows the same oscillation found in the pole-placement section, as shown in Figure 5.9.

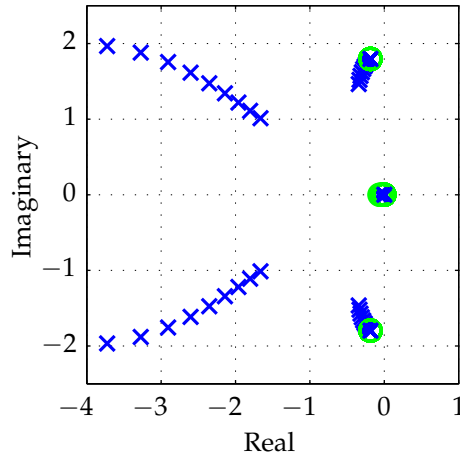


Figure 5.8: Closed loop pole positions for values of r in range 0.1 to 10. (Increasing zero frequencies correspond to higher r values.)

In an attempt to lessen the oscillation of the CG, the velocity of the CG must be assigned a weight in the cost function. In Equation 5.2.3, the weighting matrix is a diagonal matrix. By including off-diagonal entries in the weighting matrix, the product of two states can be assigned a weight. Consider the state vector x' , the weighting matrix Q' and the cost J' of

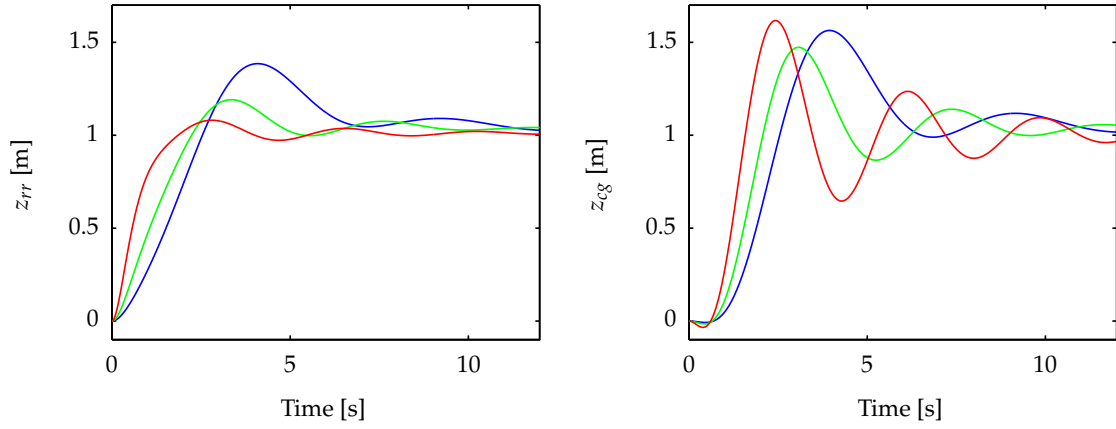


Figure 5.9: RR and CG reponse to position command step for values of r in range 0.1 to 10. (Decreasing rise times correspond to higher r values.)

an augmented system that contains the normal velocity of the CG as a state.

$$J' = \mathbf{x}'^T \mathbf{Q}' \mathbf{x}'$$

$$J' = \begin{bmatrix} \alpha \\ q \\ w_{rp} \\ z_{rr} \\ z_{rri} \\ w_{cg} \end{bmatrix}^T \begin{bmatrix} k_\alpha & 0 & 0 & 0 & 0 & 0 \\ 0 & k_q & 0 & 0 & 0 & 0 \\ 0 & 0 & k_{z_{rr}} & 0 & 0 & 0 \\ 0 & 0 & 0 & k_{w_{rr}} & 0 & 0 \\ 0 & 0 & 0 & 0 & k_{z_{rri}} & 0 \\ 0 & 0 & 0 & 0 & 0 & k_{w_{cg}} \end{bmatrix} \begin{bmatrix} \alpha \\ q \\ w_{rp} \\ z_{rr} \\ z_{rri} \\ w_{cg} \end{bmatrix} \quad (5.2.5)$$

The matrices are multiplied to form an equation for the desired cost, K' .

$$J' = k_\alpha \alpha^2 + k_q q^2 + k_{w_{rr}} w_{rr}^2 + k_{z_{rr}} z_{rr}^2 + k_{z_{rri}} (z_{rri})^2 + k_{w_{cg}} w_{cg}^2 \quad (5.2.6)$$

$$(5.2.7)$$

A substitution is made to write w_{cg} in terms of w_{rr} and q , since $w_{cg} \approx w_{rr} + \ell_x q$. The terms are regrouped.

$$\begin{aligned} J' &= k_\alpha \alpha^2 + k_q q^2 + k_{w_{rr}} w_{rr}^2 + k_{z_{rr}} z_{rr}^2 + k_{z_{rri}} (z_{rri})^2 + k_{w_{cg}} (w_{rr} + \ell_x q)^2 \\ &= k_\alpha \alpha^2 + k_q q^2 + k_{w_{rr}} w_{rr}^2 + k_{z_{rr}} z_{rr}^2 + k_{z_{rri}} (z_{rri})^2 \\ &\quad + k_{w_{cg}} w_{rr}^2 + 2k_{w_{cg}} w_{rr} \ell_x q + k_{w_{cg}} \ell_x^2 q^2 \\ &= k_\alpha \alpha^2 + (k_q + k_{w_{cg}} \ell_x^2) q^2 + (k_{w_{rr}} + k_{w_{cg}}) w_{rr}^2 + k_{z_{rr}} z_{rr}^2 + k_{z_{rri}} (z_{rri})^2 + 2k_{w_{cg}} \ell_x w_{rr} q \end{aligned} \quad (5.2.8)$$

The desired cost, J' , can now be written using the original state vector \mathbf{x} .

$$J' = \mathbf{x}^T \mathbf{Q} \mathbf{x}$$

$$J' = \begin{bmatrix} \alpha \\ q \\ w_{rp} \\ z_{rr} \\ z_{rr}^i \end{bmatrix}^T \begin{bmatrix} k_\alpha & 0 & 0 & 0 & 0 \\ 0 & k_q + k_{w_{cg}} \ell_x^2 & k_{w_{cg}} \ell_x & 0 & 0 \\ 0 & k_{w_{cg}} \ell_x & k_{w_{rr}} + k_{w_{cg}} & 0 & 0 \\ 0 & 0 & 0 & k_{z_{rr}} & 0 \\ 0 & 0 & 0 & 0 & k_{z_{rr}^i} \end{bmatrix} \begin{bmatrix} \alpha \\ q \\ w_{rp} \\ z_{rr} \\ z_{rr}^i \end{bmatrix} \quad (5.2.9)$$

The equation shows that the CG velocity can be included in the cost function even though it is not present as a state. The velocity of the CG is weighted as a multiple of the RR velocity's weight: $k_{w_{cg}} = 10k_{w_{rr}}$. Figure 5.10 shows the step responses for a system including these off-diagonal weightings. The pole positions for these closed loop systems are shown in Figure 5.11.

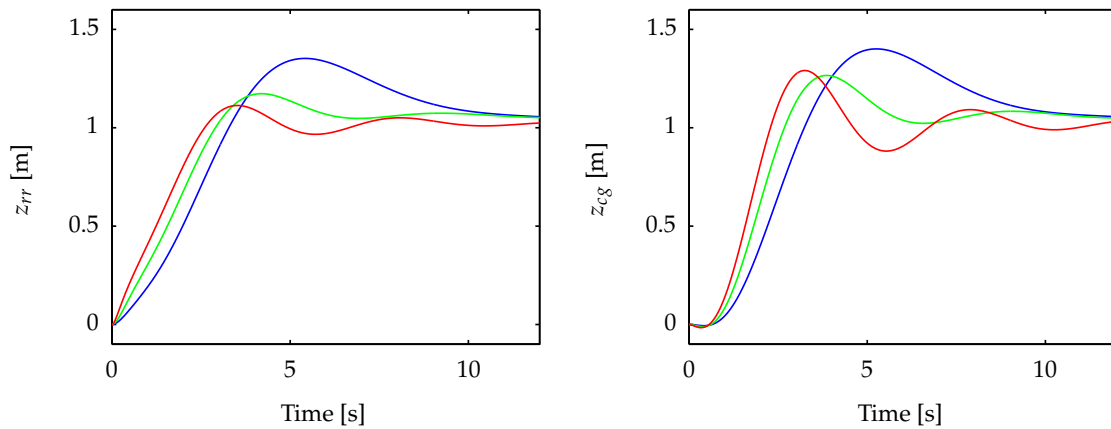


Figure 5.10: RR and CG response to position command step for values of r in range 0.1 to 10 when assigning a weight to the CG velocity

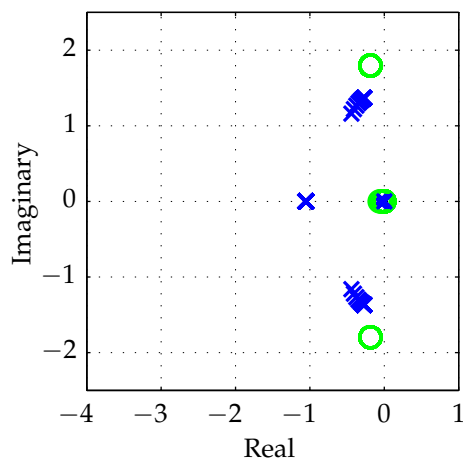


Figure 5.11: RR and CG response to position command step for values of r in range 0.1 to 10 when assigning a weight to the CG velocity

The resultant pole positions move in a similar manner to that proposed in the previous section. This illustrates that the solution presented in the previous section is the optimal method for balancing the response of the RR and the CG system when controlling a receiver aircraft during aerial refueling. The use of LQR holds several benefits, but cannot increase the system bandwidth past the RR zeros.

5.2.3 Summary

The architecture of the normal controller is shown in Figure 5.12.

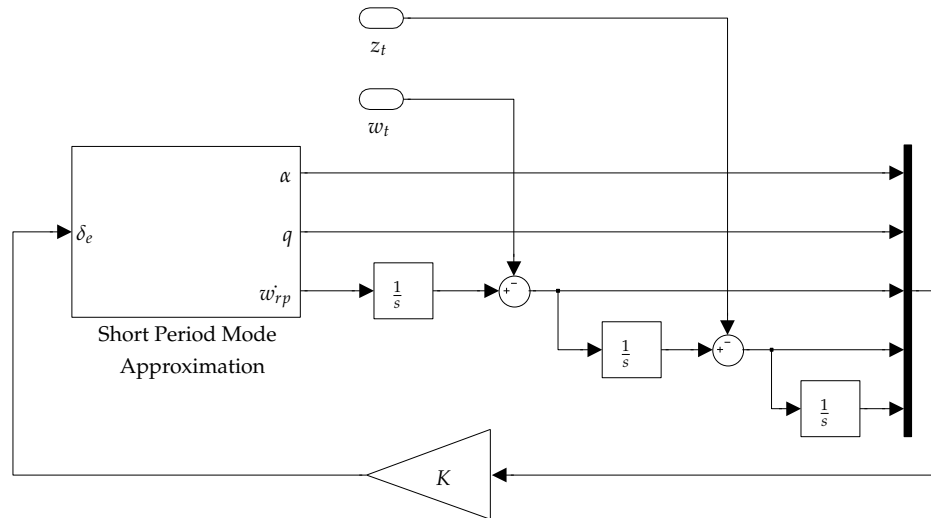


Figure 5.12: Block diagram for normal receptacle controller

Gains are calculated using pole placement, with the following criteria being followed to choose the pole positions. The boundaries for the different schemes were determined experimentally.

- If the zero frequency is relatively high, $w_z > 2.6$ rad/s:
 - Place short period mode poles at 2 rad/s with 0.7 damping ratio.
 - Place kinematic poles at 1.8 rad/s with 0.9 damping ratio
 - Place integrator poles at 1.3 rad/s
- If the zero frequency is relatively low, $w_z < 2.0$ rad/s:
 - Place short period mode poles at the zeros' frequency with 15 degrees more damping.
 - Place kinematic poles at 90% of the frequency of the short period mode poles with 0.9 damping ratio.
 - Place integrator poles at 60% of the zeros' frequency.
- In all other cases:
 - Place short period mode poles at 80% of the zeros' frequency with 0.7 damping ratio.
 - Place kinematic poles at 70% of the frequency of the short period mode poles with 0.9 damping ratio.
 - Place integrator poles at 50% of the zeros' frequency.

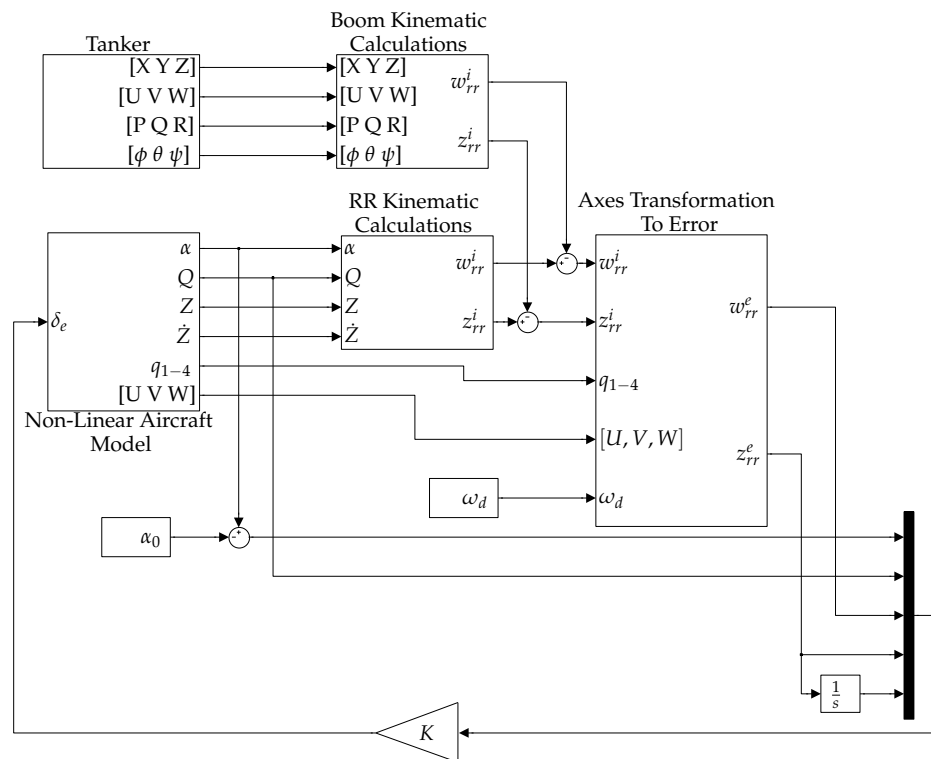


Figure 5.13: Block diagram of controller implementation in non-linear simulation

Figure 5.13 shows how the normal control system is incorporated into the non-linear simulation.

This section presented the derivation of a controller to regulate the normal position of a large aircraft's refueling receptacle. One of the secondary research objectives of this thesis is to achieve AAR across a wide variety of flight points. To achieve this, the RR zeros' frequency is used to determine suitable pole positions at each flight point. Furthermore, the control scheme is slightly adapted for flight points with the highest and lowest zero frequencies. For flight points with low-frequency zeros, a novel method was presented which allows a slight increase in bandwidth without causing additional oscillation in the RR's response.

5.3 Axial: Thrust Only

In Chapter 2, a linear model for the axial dynamics was derived. In Section 2.6, it was shown that the response of the engines is highly non-linear. The axial control system is designed to minimize the effect of the non-linear thrust by ensuring that the thrust command does not change quickly.

It is important to note that the engine thrust will not change over its full available range, shown in Figure 2.15 in Section 2.6, during aerial refueling. The thrust actuation will be limited to small changes around the trim settings, as shown in Figure 2.13. As such, the small command response of the engine is investigated to determine the slew rate limits. Even though the response resembles a first-order response, it is not. The engine thrust changes at a limited slew rate until it reaches the commanded value.

Franklin and Powell [22] outlines a method for choosing LQR weightings. It is suggested that each weighting be chosen as the squared reciprocal of the desired maximum deviation for the state. The axial linear model is augmented to include the thrust as a state and the derivative of thrust as input. The augmented system is

$$x = \begin{bmatrix} v_{rr} & x & x_{rri} & T \end{bmatrix}^T \quad (5.3.1)$$

$$u = \begin{bmatrix} \delta \dot{T} \end{bmatrix}$$

$$\dot{x} = \begin{bmatrix} \frac{X_V}{m} & 0 & 0 & \frac{X_T \cos(\alpha_0)}{m} \\ 0 & 1 & 0 & 0 \\ 0 & 0 & 1 & 0 \\ 0 & 0 & 0 & 0 \end{bmatrix} x + \begin{bmatrix} 0 \\ 0 \\ 0 \\ 1 \end{bmatrix} u \quad (5.3.2)$$

At each flight point, the thrust model is investigated to determine the maximum slew rate, \dot{T}_{max} . Furthermore, for each flight point a maximum desired thrust deviation, ΔT_{max} , is calculated. This indicates the point where the engine approaches idle or full thrust, and nonlinearities increase. If the engine is allowed to enter this state, the controller will not be able to recover and keep the receiver in the connect envelope. Figure 5.14 illustrates how these quantities are defined. These values are readily available at each flight point, as they were calculated when creating the engine model. Unique weightings are chosen for each flight point.

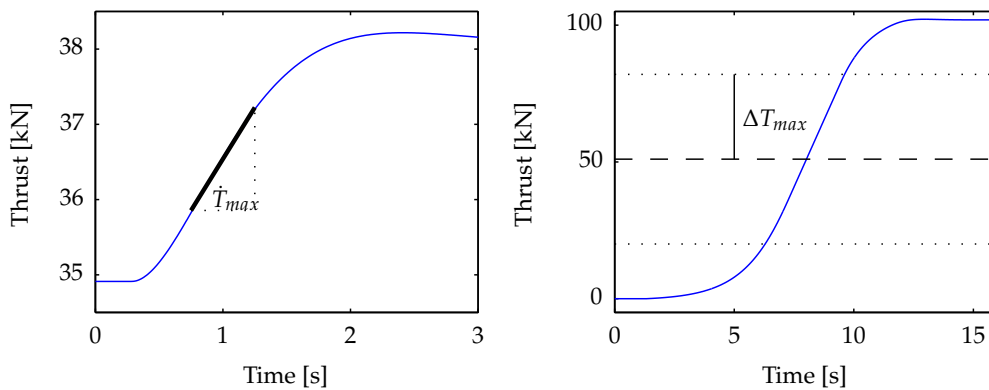


Figure 5.14: Illustration detailing \dot{T}_{max} and ΔT_{max}

The weightings are calculated using the maximum deviations listed in Table 5.1.

State	Max Deviation	Input	Max Deviation
v_{rr}	0.2 m/s	$\delta_{\dot{T}}$	\dot{T}_{max} N/s
x_{rr}	1 m		
x_{rri}	0.01 m.s		
T	ΔT_{max} m.s		

Table 5.1: Max deviations for axial LQR control system

The block diagram for the closed loop system is shown in Figure 5.15. It was found that this method of controlling the axial position of the refueling receptacle is not suitable for medium turbulence conditions. The thrust cannot change quickly enough to regulate the RR in the connect envelope.

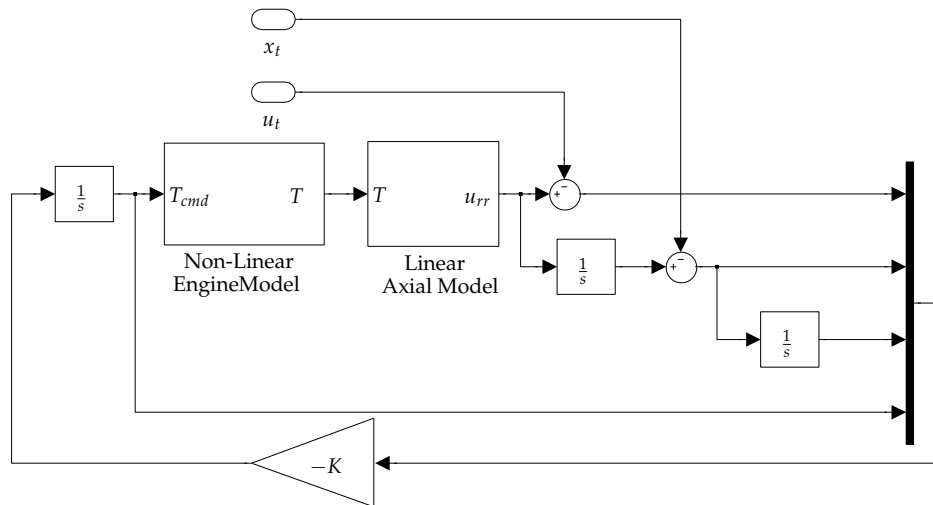


Figure 5.15: Simplified block diagram of axial system

5.4 Axial: High-Drag Configuration

5.4.1 Overview

In Section 5.3, a controller was designed for the linear axial system derived in Chapter 2. The bandwidth of the controller is limited by the slow slew rate of the engines. The high-drag configuration is presented here as a means of improving the response of the axial system. In [1], induced drag is used to provide high-bandwidth axial control. The angle of attack is adjusted to quickly change the drag of the aircraft. It was found that, even though this degraded the performance of the normal control system, it led to an overall improvement in terms of boom parameters. The high-drag configuration seeks to improve on this system by adding the use of spoilers. The spoilers are used to adjust the lift of the wings to negate the effect of the change in angle of attack. The result is a virtual actuator, δ_d , which creates drag without a large impact

on the normal system. To allow the actuator to create positive and negative axial forces, the spoiler must be able to deflect in both directions. The receiver is thus trimmed with a spoiler deflection and more steady-state drag, i.e. in a high-drag configuration.

5.4.2 Modeling

To create a model for the the drag virtual actuator, the aircraft is trimmed in the nonlinear simulation at the desired flight point with various spoiler deflections. At each spoiler position, the steady-state drag, angle of attack and horizontal tailplane position are recorded, as illustrated in Figure 5.16.

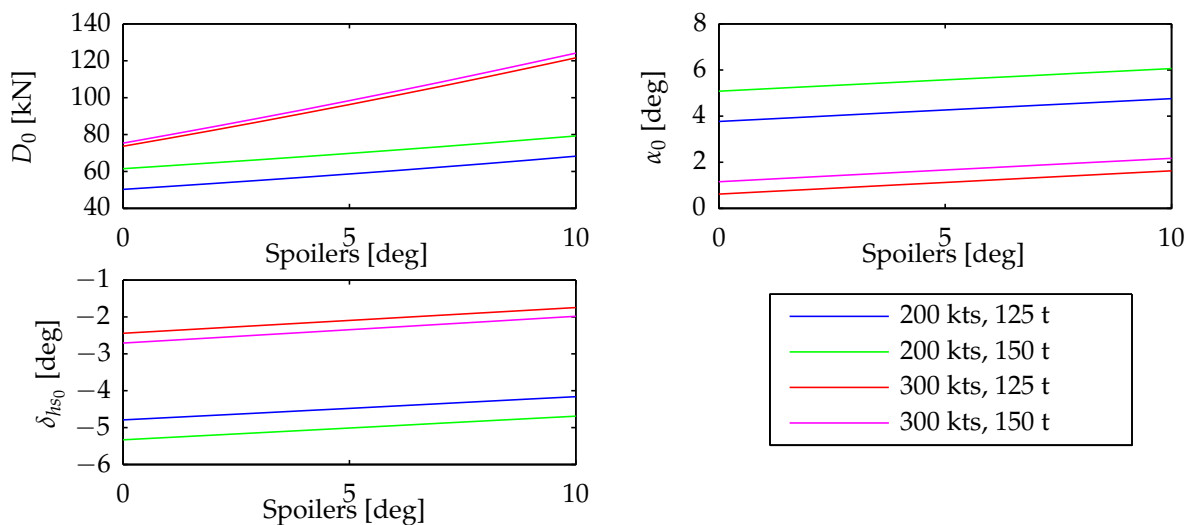


Figure 5.16: Steady-state parameters for various spoiler deflections

For a specific flight point, a steady-state spoiler deflection, δ_{s_0} , is chosen where the steady-state thrust is increased, but not close to the maximum allowable level. At most flight points, five degrees of spoiler deflection is used. More detail on different flight points is given in Section 5.4.5. Lookup tables are created where spoiler deflection maps to steady-state values for angle of attack and horizontal tailplane deflection. The drag virtual actuator is a combination of three commands:

- The spoiler deflection is changed from its steady-state value. $\delta_s = \delta_{s_0} + \delta_d$
- The steady-state angle-of-attack used in the normal system is changed. The new value is selected from the lookup tables. $\alpha_{cmd} = \alpha_{cmd_0} + f_\alpha(\delta_s)$
- The position of the horizontal tailplane is changed. The new value is selected from the lookup tables. $\delta_h = \alpha_{h_0} + f_{\delta_h}(\delta_s)$

The normal control system quickly settles the aircraft at the new trim point. The changed drag will create a net axial force on the aircraft. The control system is designed to have a bandwidth slower than the normal system. This ensures that the normal control system can reject the disturbances caused by the induced-drag virtual actuator. The change in drag is equal to the

change in steady-state thrust seen in Figure 5.16, $\Delta D = f_D(\delta_s) - D_0$. The control derivative for the drag virtual actuator, X_{δ_d} , is equal to the slope of the thrust graph.

5.4.3 Control

LQR is used to calculate feedback gains. The permissible slew rate of the drag virtual actuator is limited to the slew rate of the spoilers. The current command to the drag virtual actuator is thus added as a state, and the derivative of the actuator is used as input.

The range of the drag virtual actuator is limited, while the range of thrust is relatively wide. Any steady-state actuation of the drag virtual actuator is thus not desirable, as it will the limit range in one direction. The thrust must be used to supply any steady-state – and low-frequency – actuation needed in the axial system. To that end, the actuation of the drag virtual actuator is integrated and filtered by a low-pass filter. The integrator and filter states, δ_{di} and δdf respectively, are augmented to the linear model. Figure 5.17 shows the basic architecture of this control system.

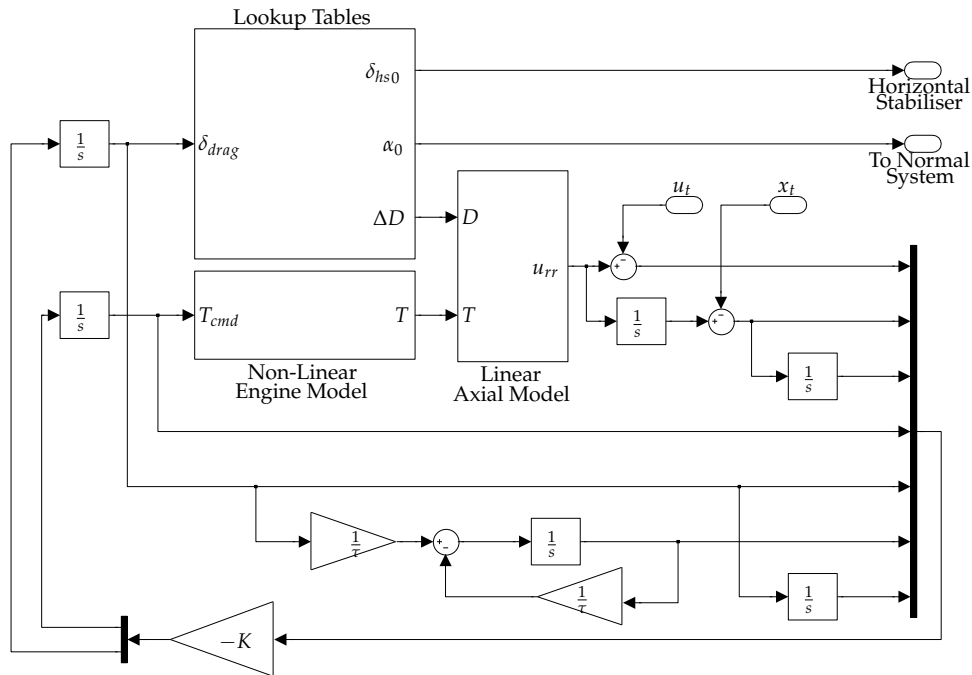


Figure 5.17: Block diagram of high-drag axial system

The linear model does not contain the dynamics induced by the spoilers, as the normal states are required for this. The effect of the drag virtual actuator is modelled as a change in drag. The dynamics of the spoilers are considered a disturbance to be rejected by the normal system. The augmented linear state space model is

$$x = \begin{bmatrix} V & x & x_{int} & T & \delta_d & \delta_{df} & \delta_{di} \end{bmatrix}^T \quad (5.4.1)$$

$$u = \begin{bmatrix} \dot{T} & \dot{\delta}_d \end{bmatrix}^T$$

$$\dot{x} = \begin{bmatrix} X_V & 0 & 0 & 0 & X_{\delta_d} & 0 & 0 \\ 1 & 0 & 0 & 0 & 0 & 0 & 0 \\ 0 & 1 & 0 & 0 & 0 & 0 & 0 \\ 0 & 0 & 0 & 0 & 0 & 0 & 0 \\ 0 & 0 & 0 & 0 & 0 & 0 & 0 \\ 0 & 0 & 0 & 0 & \frac{1}{\tau} & -\frac{1}{\tau} & 0 \\ 0 & 0 & 0 & 0 & 1 & 0 & 0 \end{bmatrix} x + \begin{bmatrix} 0 & 0 \\ 0 & 0 \\ 0 & 0 \\ 0 & 0 \\ 1 & 0 \\ 0 & 1 \\ 0 & 0 \\ 0 & 0 \end{bmatrix} u \quad (5.4.2)$$

The augmented system allows the control designer to determine how the actuators are used to control the axial errors. By weighting the derivative of the spoiler command, the speed with which the spoiler is varied can be limited. The time constant of the first-order low-pass filter and the weighting of its output are selected such that the spoilers are predominantly used for higher-frequency actuation. The integrated spoiler command is assigned a weight in order to ensure that a constant axial disturbance is compensated for by using solely thrust. Each weighting is chosen as the reciprocal of the desired maximum deviation of the state (or input) from its steady-state value. Table 5.2 shows the maximum deviation chosen for each state and a rationalisation for the chosen value. The filter time constant was chosen as three seconds. This will result in the filter reaching the input value in 15 seconds which is sufficient time for the engine to respond.

State	Max	Unit	Explanation
u_{rp}	0.2	m/s	Velocity causing RR to leave boom envelope in 10s
x_{rp}	2	m	Distance from middle to edge of the boom envelope
x_{rp-i}	100	m.s	No physical significance
T	ΔT_{max}	kN	Linear region of thrust response
δ_{sp}	5	deg	Available spoiler deflection from trim value
δ_{sp-f}	5	deg	Available spoiler deflection from trim value
δ_{sp-i}	75	deg	Spoiler is fully deflected for 15 s
\dot{T}	\dot{T}_{max}	kN/s	Max slew rate of engine
$\dot{\delta}_{sp}$	30	deg/s	Max slew rate of spoiler actuator

Table 5.2: Maximum deflections for axial system LQR

Figure 5.18 shows the response of the high-drag axial system to a position step command at flight point: $FL = 200$, $V_c = 260$ kt, $m_r = 175$ t, $CG_r = 30\%$. The commanded thrust and spoiler deflections are also shown.

Note that the step is achieved by using almost exclusively the drag virtual actuator. The thrust actuation is a few newton, which is negligible. By contrast, the system's response to a velocity step command is shown in Figure 5.19.

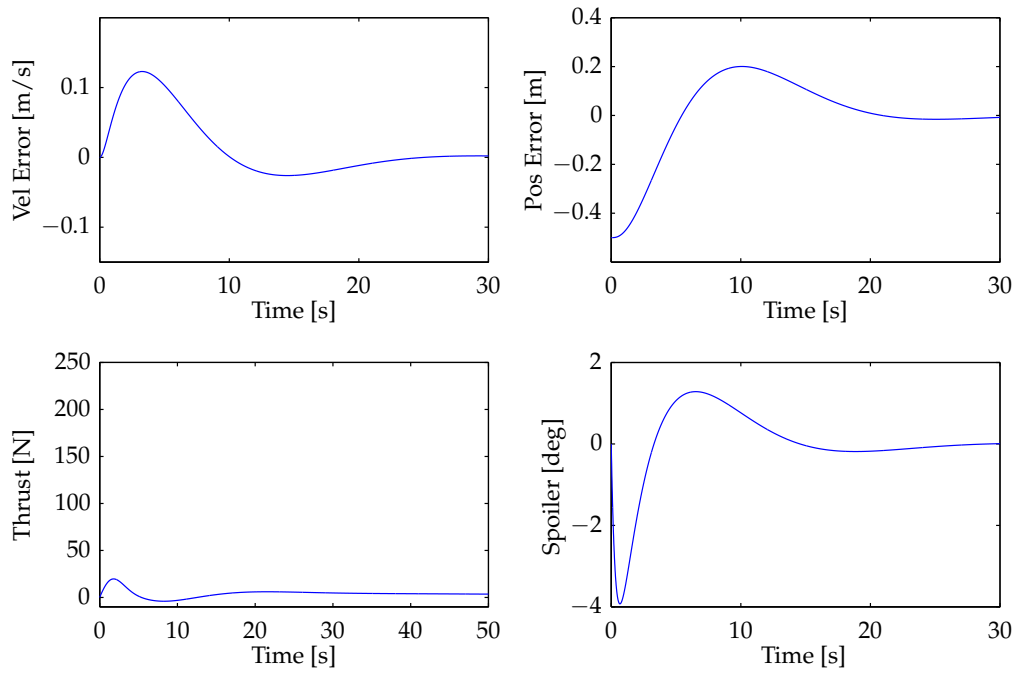


Figure 5.18: High-drag axial system actuator response to a 0.5 m position disturbance

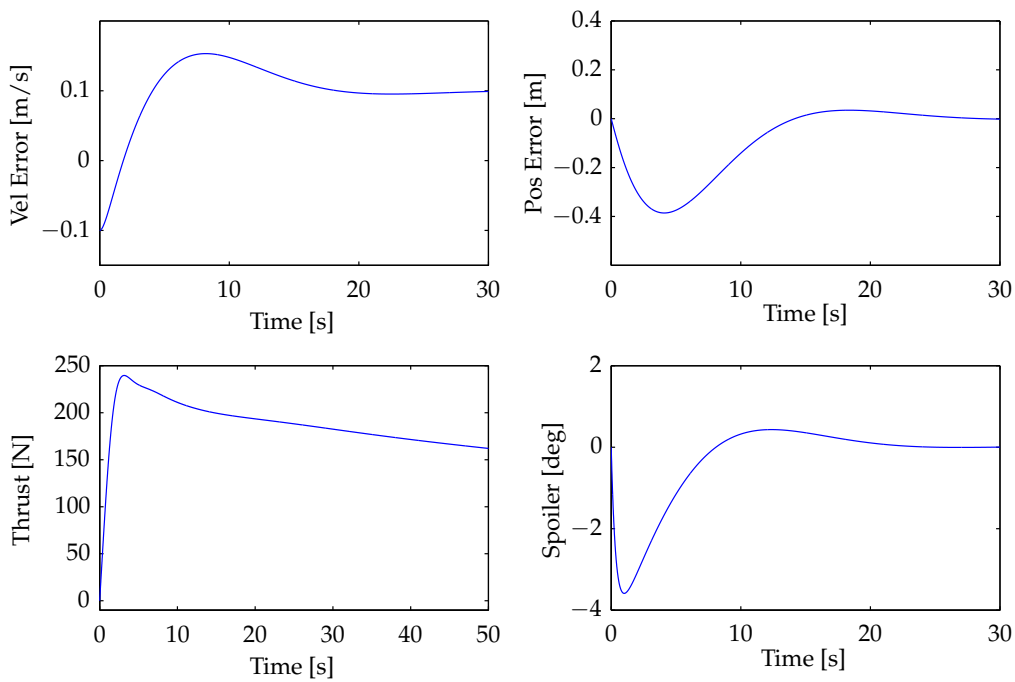


Figure 5.19: High-drag axial system response to a 0.1 m/s velocity disturbance

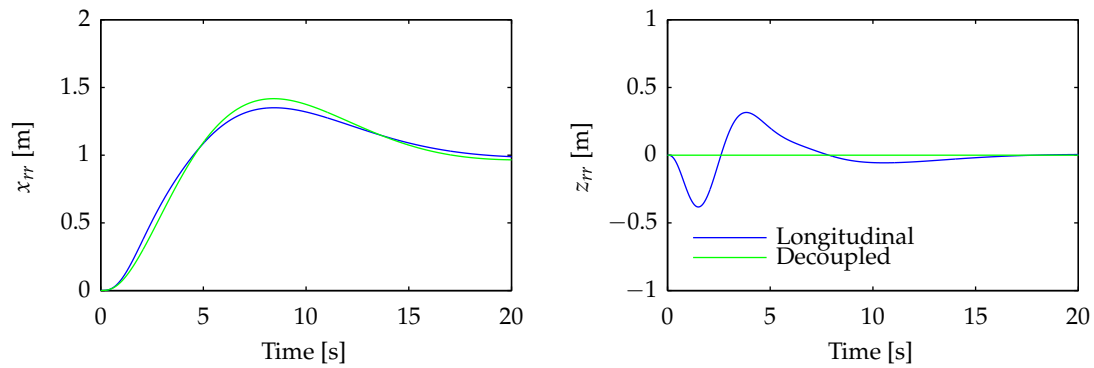


Figure 5.20: X- and Z-position response to an axial position step of the longitudinal system controlled by decoupled controllers

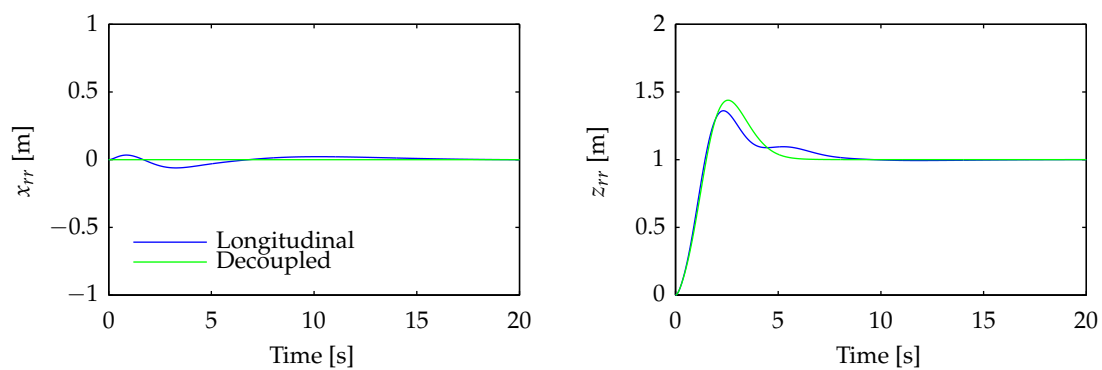


Figure 5.21: X- and Z-position response to a normal position step of the longitudinal system controlled by decoupled controllers

a downwash angle from the tanker already increases the state-state thrust requirement for the receiver.

Table 5.3 lists the steady-state thrust at various flight points with different steady-state spoiler actuations and downwash angles. In each case, the steady-state thrust is given as a percentage of the maximum thrust available. In Chapter 2, it was shown that the tanker's response enters a non-linear region when it approaches 80% of the maximum thrust. In order to use the high-drag configuration, it was judged that the trim thrust should not exceed 60% of the maximum available thrust per engine.

Note that maximum thrust here refers to CLB thrust, that is, the maximum available thrust during cruise. The engine can produce more thrust, as used during take-off and go-around, but it is infeasible to trim the aircraft with such a high thrust. It can be seen that at some flight points (high altitude, heavy receiver) the high-drag axial control scheme is not feasible. At this point, the toboggan trajectory, introduced in Chapter 1, becomes relevant. Table 5.4 shows the steady-state thrust values for various configurations when trimmed in a toboggan trajectory with a sink rate of 500ft/min. Some flight points which could not use the high-drag configuration for straight and level flight can do so when using the toboggan trajectory.

FL	V_c [kt]	m [t]	T_{max} [kN]	$(\frac{T_0}{T_{max}})_{\delta_{sp}=3^\circ}$	$(\frac{T_0}{T_{max}})_{\delta_{sp}=5^\circ}$	$(\frac{T_0}{T_{max}})_{\delta_{sp}=7^\circ}$
100	200	175	144	28%	29%	30%
100	200	200	144	33%	34%	36%
100	200	225	144	39%	40%	41%
100	300	175	142	35%	38%	41%
100	300	200	142	36%	39%	43%
100	300	225	142	39%	43%	45%
300	200	175	82	50%	52%	54%
300	200	200	82	60%	62%	64%
300	200	225	82	72%	74%	76%
300	300	175	81	61%	66%	72%
300	300	200	81	66%	71%	79%
300	300	225	81	77%	81%	98%

Table 5.3: Steady-state thrust at various flight points in high-drag configuration

FL	V_c [kt]	m [t]	T_{max} [kN]	$(\frac{T_0}{T_{max}})_{\delta_{sp}=3^\circ}$	$(\frac{T_0}{T_{max}})_{\delta_{sp}=5^\circ}$	$(\frac{T_0}{T_{max}})_{\delta_{sp}=7^\circ}$
300	200	175	82	34%	36%	37%
300	200	200	82	42%	44%	45%
300	200	225	82	51%	53%	55%
300	300	175	81	49%	55%	61%
300	300	200	81	53%	59%	66%
300	300	225	81	63%	66%	83%

Table 5.4: Steady-state thrust at various flight points in high-drag configuration and toboggan trajectory

5.4.5.1 Summary

Section 5.4 presented a novel high-drag axial controller that allows a large receiver aircraft to accurately regulate the axial position of its refueling receptacle, despite the relatively slow response of its engines. It was found that, due to the effect of tanker downwash, the high-drag controller cannot be used at all flight points. The use of the toboggan trajectory was then presented as a method of reducing the required steady state thrust, thereby allowing the high-drag controller to be used at more flight points.

This controller provides a contribution to the field by improving upon the induced-drag axial controller in [2], and addresses one of the primary research objectives for this thesis.

5.5 Lateral

The lateral controller will use LQR to control the lateral subsystem of the receiver dynamics. The lateral system will not be analysed in the same depth as the normal system. However, it must be noted that the controller is still a unique contribution to the field, as it is specifically designed to take the RR dynamics into account, and uses the RR-RR architecture.

The linear lateral state-space model, derived in Section 2.4, is augmented here to include the integrated lateral position error.

$$\begin{aligned} \mathbf{x} &= \begin{bmatrix} \beta & p & r & \phi & v_{rr} & y_{rr} & y_{rri} \end{bmatrix} \\ \mathbf{u} &= \begin{bmatrix} \delta_a & \delta_r \end{bmatrix} \end{aligned} \quad (5.5.1)$$

The LQR state and input weightings are chosen using the maximum deflection methods described in [22]. The chosen maximum deviations are listed in Table 5.5.

State	Max Deviation	Input	Max Deviation
β	5 deg	δ_a	10 deg
p	10 deg/s	δ_r	10 deg
r	10 deg/s		
ϕ	5 deg		
v_{rr}	0.5 m/s		
y_{rri}	10 m		

Table 5.5: Maximum deviation for lateral LQR controller

The primary aim of the controller is to maintain the position of the receptacle relative to the tanker. To this end, the commanded values for the lateral states are not calculated to follow the intended trajectory, but to follow the tanker. If the receiver were to attempt to maintain a zero roll angle, it would only move to correct the error once the tanker had moved from the intended trajectory. This could result in the receiver banking in the wrong direction, as illustrated in Figure 5.22.

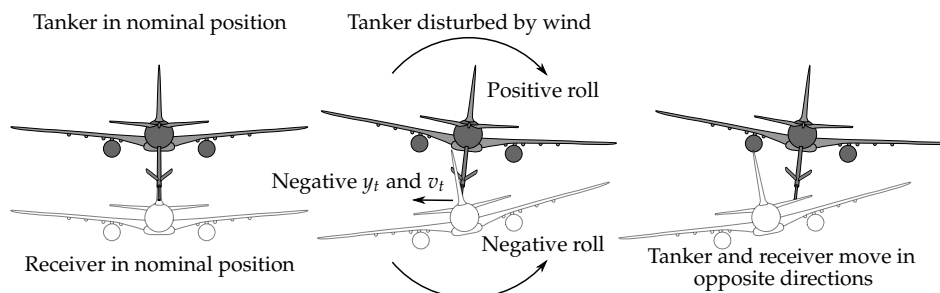


Figure 5.22: Tanker and receiver when tanker is disturbed by lateral wind

Consider the scenario where the tanker is disturbed by a lateral gust. For simplicity, the effect of the gust on the receiver is not considered here. The tanker is perturbed from its nominal position to have a positive roll rate. Due to the location of the boom on the tanker and

the normal distance of the boom tip from the tanker’s centre of gravity, the nominal position of the boom tip moves in the negative Y-direction. Immediately, the receiver would thus try to move the refueling receptacle in the negative Y-direction. To achieve this, the controller will command a negative roll rate for the receiver. The tanker and receiver now have opposing bank angles and will start to accelerate in opposite directions.

To improve the control system’s response in this scenario, the tanker’s bank angle is fed forward as a command to the lateral system. This ensures that the receiver does not roll in the opposite direction to the tanker when disturbed by a gust. Furthermore, as shown in Table 5.5, the permissible deviation of the rudder actuation and angle of side-slip is relatively large. This allows the controller to use side-slip to correct small lateral errors. The control structure of the lateral controller is shown in Figure 5.23.

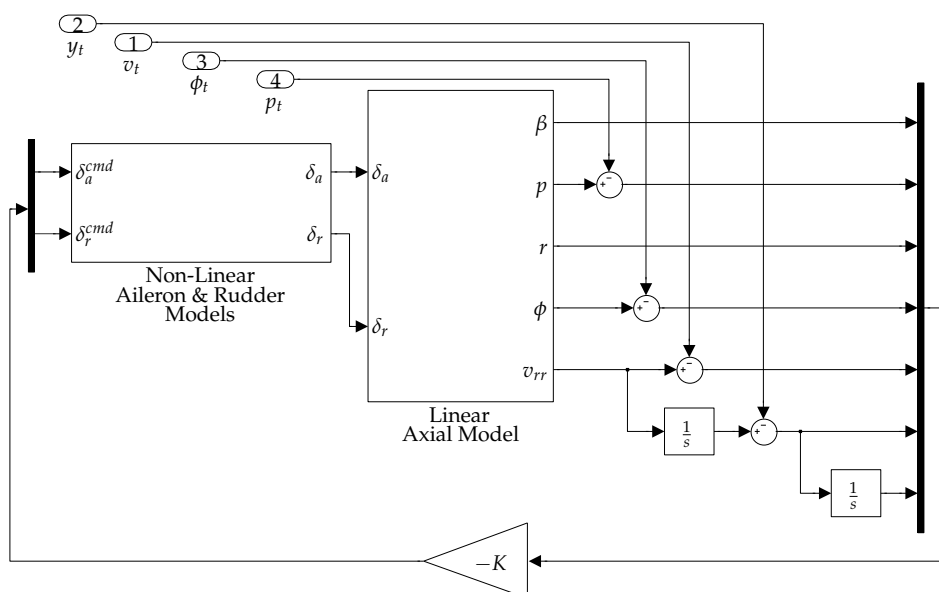


Figure 5.23: Block diagram of lateral system

Figure 5.24 shows the linear system’s response to a position step command at various flight points. Note that the actuator dynamics have been included in this simulation. The flight points chosen are:

- $m_r = 125000\text{kg}$, $V_c = 225\text{kts}$, $\text{FL}=300$
- $m_r = 225000\text{kg}$, $V_c = 225\text{kts}$, $\text{FL}=300$
- $m_r = 125000\text{kg}$, $V_c = 300\text{kts}$, $\text{FL}=300$
- $m_r = 225000\text{kg}$, $V_c = 300\text{kts}$, $\text{FL}=300$

The response of the RR shows the same characteristic effect of complex zeros as the normal system at higher bandwidth. It shows that the lateral system is also limited by the presence of the zeros shown in Section 3.3. Increasing the weighting on the RR states does not significantly

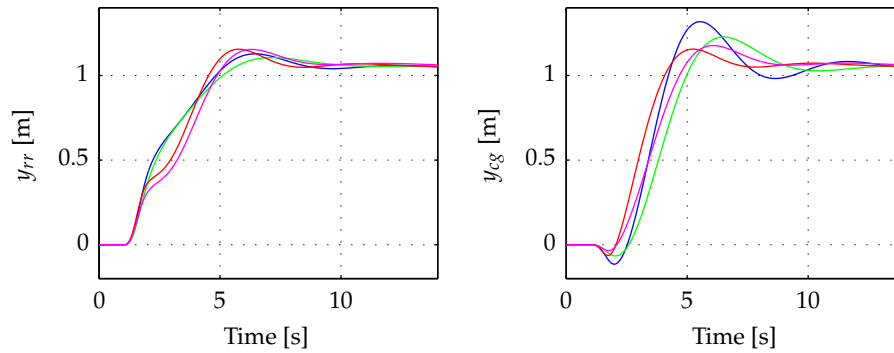


Figure 5.24: RR and CG response to a lateral RR position step command at four flight points

improve performance. If the weightings are increased too far, the effect of the actuator non-linear model will cause instability. Figures 5.25, 5.26 and 5.27 show the lateral system tracking a tanker in light turbulence. These are short linear simulations, performed as an initial test of the system. Non-linear simulations, with longer simulation durations, are presented in Chapter 6.

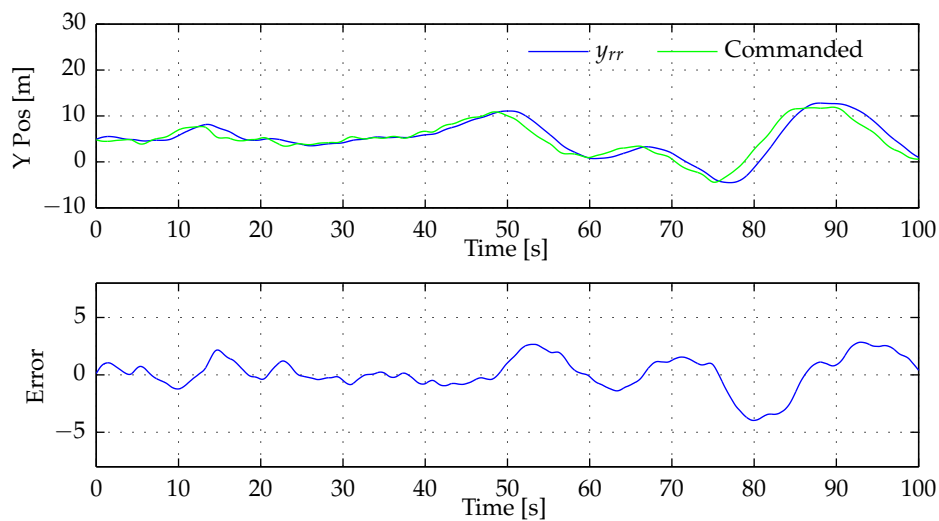


Figure 5.25: RR command, position and error in light turbulence at $V_c = 300$ kt, FL = 300 and $m_r = 225$ t

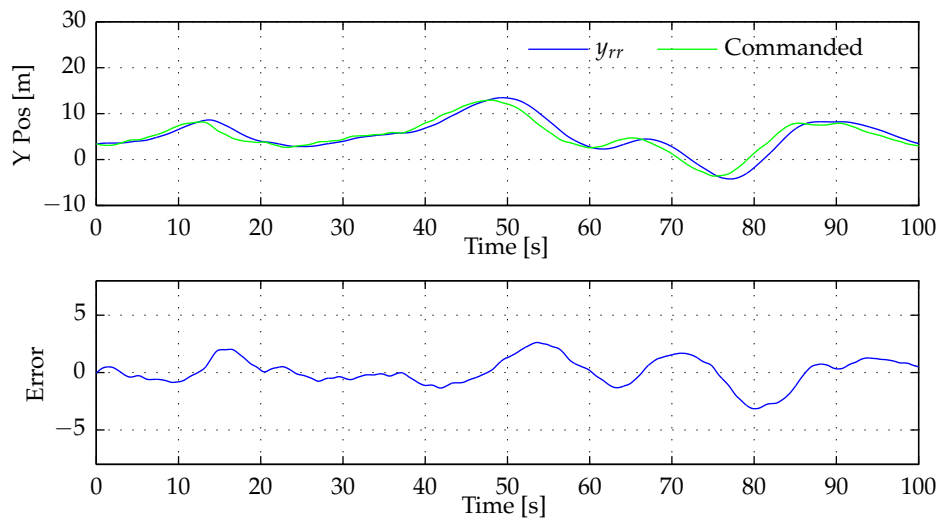


Figure 5.26: RR command, position and error in light turbulence at $V_c = 225$ kt, $FL = 300$ and $m_r = 225$ t

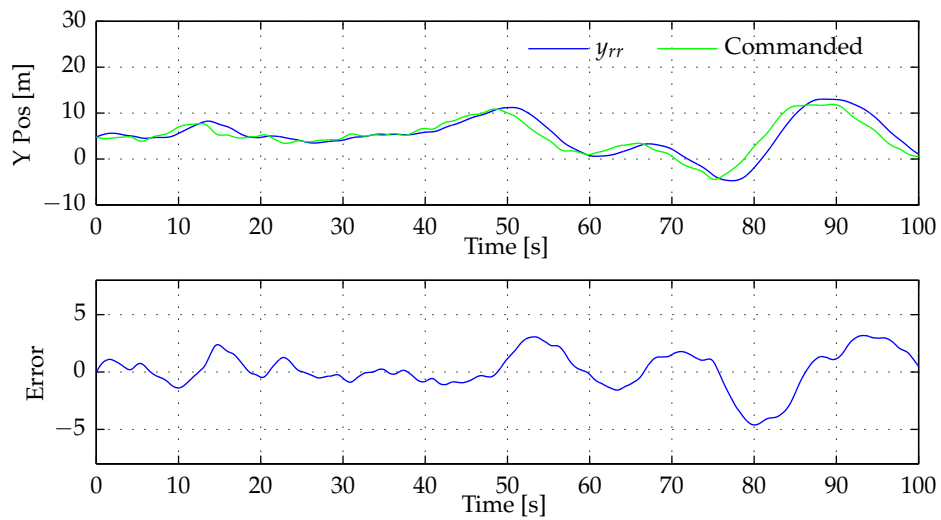


Figure 5.27: RR command, position and error in light turbulence at $V_c = 300$ kt, $FL = 300$ and $m = 125$ t

5.6 Banked Turn

In Section 1.6.3, it was argued that the racetrack trajectory is essential to make aerial refueling of a large receiver practically viable. To fly a racetrack trajectory, the tanker and the receiver must fly a banked turn while the receiver remains connected to the tanker. This section will investigate whether the receiver's control systems need to be adjusted to achieve AAR using the racetrack trajectory, which is one of the secondary research objectives of this thesis.

5.6.1 Normal

The normal system is robust for sizeable changes in the linear model due to bank angle, and is able to maintain control while the receiver is banked at 25 degrees. The system bandwidth is high enough to quickly supply the increased angle-of-attack required when banking. The addition of the integrated normal position error to the normal control system ensures that the steady-state error will be zero.

It is possible to increase the commanded angle-of-attack when entering the turn, although this was found to produce only a negligible improvement in performance.

5.6.2 Lateral

It was found that the receiver's lateral system could not reliably respond fast enough to follow the tanker into a banked turn. As stated in the requirements in Section 1.2, the tanker is not allowed to communicate directly with the receiver. The tanker is thus not allowed to signal when the banked turn will begin.

To increase the speed of the receiver's response to a rolling tanker, the tanker's roll rate is provided as a command to the receiver. The receiver's control system will thus attempt to track the roll rate, and not only the roll angle, as before.

This control scheme relies on the availability (with acceptable delay) of the relative roll rate between the tanker and the receiver. Estimating the relative roll rate could be a difficult task for the sensors and estimator.

5.6.3 Axial

The axial control system does not need to be changed for the racetrack trajectory.

5.7 Summary

This chapter presented a set of controllers capable of regulating the position of a large receiver aircraft's refueling receptacle. The controllers are novel in that they take the RR dynamics (caused by the distance between the CG and the RR) into account, and thus offer a unique contribution to the field. Developing these controllers formed the primary research objective of the current project.

Over the course of the project, a controller was also tested which controls the complete longitudinal system, without decoupling normal and axial dynamics. The performance in this case was slightly better than that of the decoupled normal and axial controllers. It was decided,

however, to focus primarily on the decoupled controllers for this thesis. This was done so that the normal RR dynamics and the high-drag configuration could be focussed on individually. Limited simulation results of the coupled longitudinal controller will be shown in Chapter 6. A similar controller is used to control receiver through the FBW system in Chapter 7.

Chapter 6

Results

6.1 Overview

This chapter will present comprehensive non-linear simulation results for the controllers discussed in Chapter 5. The controllers are verified over a wide range of flight points. One of the secondary research objectives of this thesis is to ascertain the effect of all flight point parameters on the controllers' performance, and this Chapter 6 seeks to address this objective.

In Section 6.2, the results from a large number of flight points will be shown at straight and level flight in light turbulence. Section 6.3 highlights the impact of various parameters (e.g. tanker weight, CG-location, high-drag configuration) on the performance of the system. Section 6.4 presents non-linear simulation results to show the efficacy of the high-drag configuration, whereas Section 6.5 covers the performance of the system in the racetrack, toboggan, and approach trajectories.

It was found that medium turbulence taxes the control system, making it difficult to quantify differences in performance. For example, without the high-drag configuration, the receiver seldom manages to regulate the RR inside the disconnect envelope. As such, non-linear simulations intended to compare different control schemes, flight points or trajectories will all be performed in light turbulence. Section 6.6 presents non-linear simulation results performed with medium turbulence.

Unless stated otherwise, the high-drag axial controller, normal controller described in section 5.2.3 and LQR lateral controller is used. The envelope plots, described in section 1.6.1 are used extensively to show and compare control system performance. To reduce visual clutter, repeated axis labels have been removed.

6.2 Light Turbulence

This section presents a large number of simulations performed in light turbulence. Simulations were performed at a large number of flight points, so as to cover the complete mass and altitude envelope, as stated in the project requirements. Simulations were performed at all combinations of the following flight-point parameters:

Flight Level 100, 200, 300

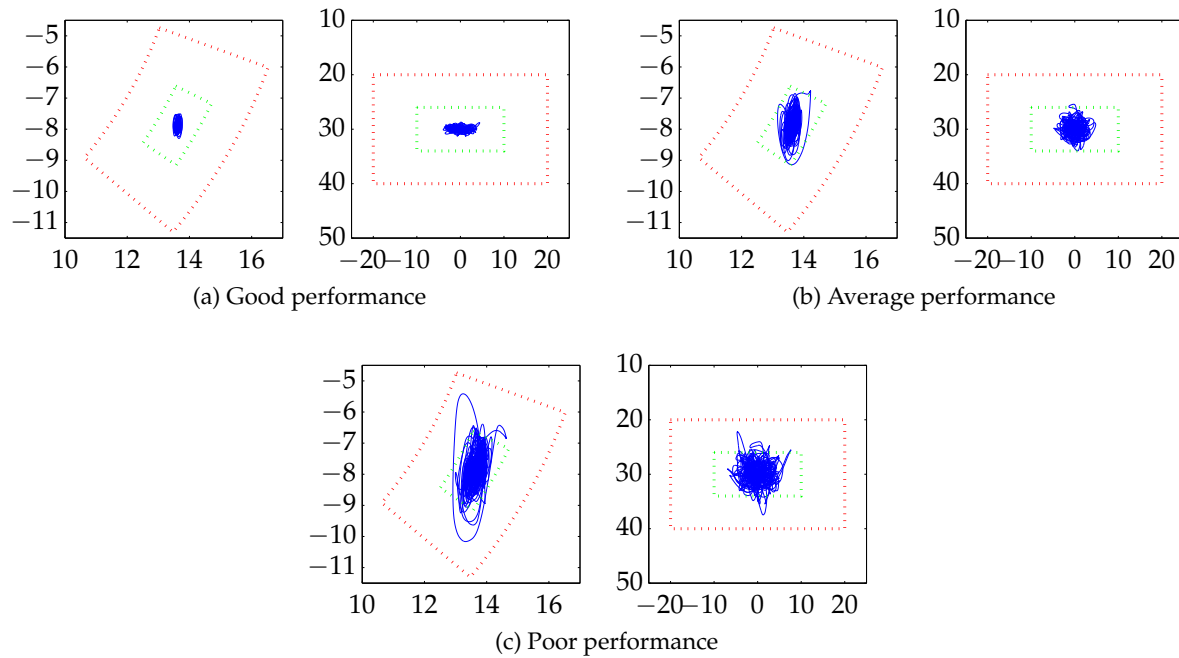


Figure 6.1: Good, average and poor performance at various flight points in light turbulence

Calibrated Airspeed 225kt, 250kt, 275kt, 300kt

Receiver Mass 125t, 150t, 175t, 200t, 225t

Receiver CG 23%, 30%, 37%

Tanker Mass 175t

Tanker and Receiver CG 30%

It would be impractical to list the results from all 180 simulations in this chapter. Instead, the results of three simulation performed in light turbulence are presented here, which each represents a category of relative performance: good, average, and poor. The chosen flight points are:

Good FL=300, $V_c = 275$, $m_r = 125t$, $CG_r = 30\%$

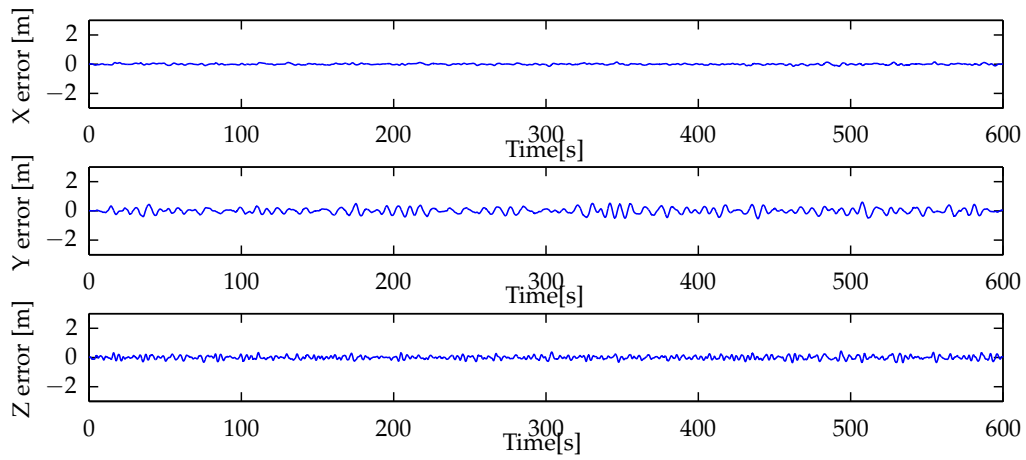
Average FL=200, $V_c = 225$, $m_r = 200t$, $CG_r = 23\%$

Poor FL=100, $V_c = 250$, $m_r = 225t$, $CG_r = 30\%$

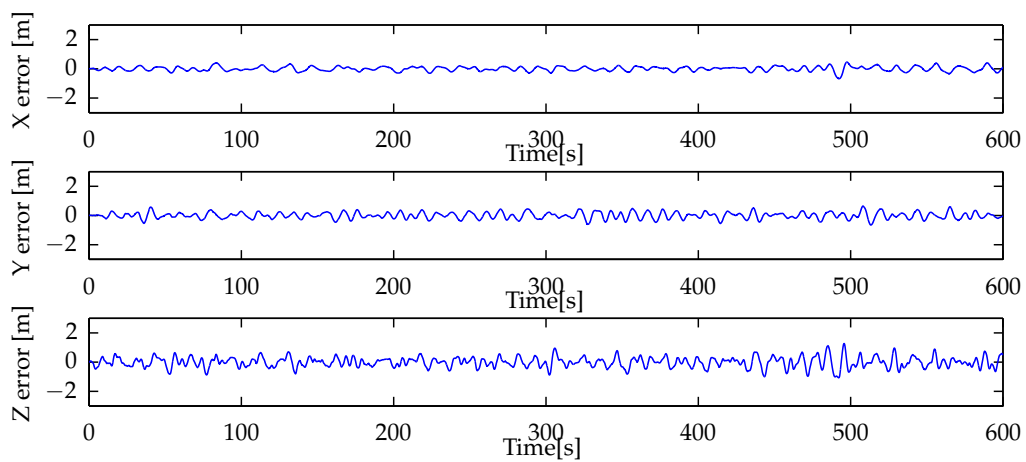
Figure 6.1 shows the location of the RR in the boom envelope over the course of the simulations.

Figures 6.2 (a) to (c) shows the X,Y and Z errors of the RR over the course of the simulation.

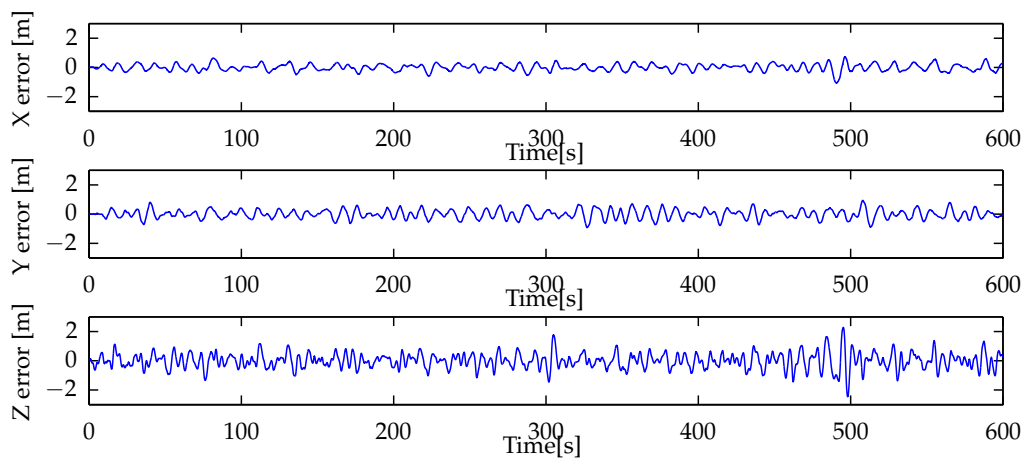
The results clearly show that the control system successfully regulates the RR inside the disconnect envelope over the complete extent of the simulation. Furthermore, at most flight points, the RR also remains inside the connect envelope for long periods of time. This allows the boom operator time to connect the boom to the RR. The results of all of the simulations can be found in Table D.1 in Appendix D.



(a) (a) Good performance



(b) (b) Average performance



(c) (c) Poor performance

Figure 6.2: Good, average and poor performance at various flight points in light turbulence

6.3 Flight-Point Parameters

One of the requirements of the project, as listed in Section 1.2, is to establish which flight-point parameters increase or decrease the difficulty of the refueling control problem. This section will investigate several simulations that vary from a baseline by only one parameter. The following flight point is used as said baseline:

Flight Level 200

Calibrated Airspeed 260kt

Receiver Mass 175t

Tanker Mass 175t

Tanker and Receiver CG 30%

The standard deviation of the boom-parameter errors over the course of the simulation will be used to quantify the relative performance of the control system. The performance of the controller at the baseline flight point is shown in Figure 6.3.

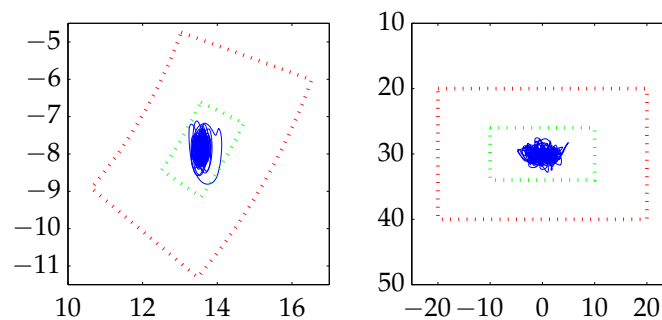


Figure 6.3: Control system performance at baseline flight point

6.3.1 Calibrated Airspeed

The calibrated airspeed is changed to 225 kts and 300 kts respectively. Table 6.1 summarises the results of the simulations.

Parameter	Slower	Baseline Flight Point	Faster
Boom Length	0.16 m (+3.8%)	0.15 m	0.14 m (-3.0%)
Boom Pitch	1.1 deg (+35%)	0.81 deg	0.81 deg (+0.0%)
Boom Roll	1.5 deg (-5%)	1.60 deg	1.5deg (-2.0%)

Table 6.1: Standard deviation of boom-parameter errors over course of refueling simulation for different calibrated airspeeds

The results show that it is more difficult for the receiver to maintain the normal position of the RR at lower airspeeds. This is likely due to the increased effectiveness of the control surfaces at higher airspeeds. Equation 3.2.10 shows that Z_α affects the frequency of the RR

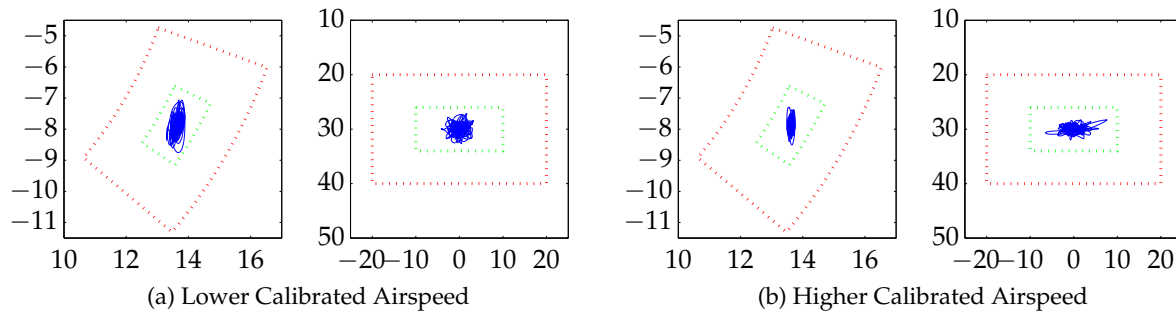


Figure 6.4: Simulation results for receivers with different airspeed in light turbulence

zeros. A higher dynamic pressure thus increases the frequency of the zeros and subsequently the bandwidth of the normal system. The lateral performance does not change significantly with airspeed. Figures 6.4 (a) and (b) show the position of the RR in the boom envelopes at the slower and faster flight points.

6.3.2 Flight Level

Various flight level values were selected, and non-linear simulations were performed. Table 6.2 summarises the results of the simulations.

Parameter	FL = 100	FL = 150	FL = 175	FL = 200
Boom Length	0.17 [m] (52%)	0.14 [m] (21%)	0.11 [m] (0%)	0.10 [m] (-7%)
Boom Pitch	1.21 [deg] (97%)	0.74 [deg] (21%)	0.61 [deg] (0%)	0.59 [deg] (-4%)
Boom Roll	1.88 [deg] (41%)	1.56 [deg] (17%)	1.33 [deg] (0%)	1.25 [deg] (-6%)
Parameter	FL = 225	FL = 250	FL = 300	
Boom Length	0.10 [m] (-10%)	0.10 [m] (-11%)	0.14 [m] (25%)	
Boom Pitch	0.59 [deg] (-4%)	0.65 [deg] (5%)	0.84 [deg] (37%)	
Boom Roll	1.26 [deg] (-6%)	1.26 [deg] (-6%)	1.31 [deg] (-2%)	

Table 6.2: Standard deviation of boom parameters over course of refueling simulation for different flight levels

The results show that the system performs best at a flight level between 200 and 225. Performance falls drops towards lower flight levels, due to the increase in turbulence supplied by the MIL-STD-1797 model [11]. Axial and normal performance suffer at higher altitudes, due to the smaller available thrust range, as shown in Section 2.6. Lateral performance remains slightly better at higher altitudes, since it is not heavily affected by the thrust limitations.

6.3.3 Tanker Mass

The tanker mass is changed to 125 t and 225 t respectively. Table 6.3 summarises the results of the simulations.

The system performs significantly better when following a heavy tanker. This is likely as a result of the decreased effect of turbulence on the tanker with higher inertia.

Parameter	Light Tanker	Baseline Tanker	Heavy Tanker
Boom Length	0.13 m (-9.4%)	0.15 m	0.08 m (-47%)
Boom Pitch	0.87 deg (+10%)	0.79 deg	0.54 deg (-31%)
Boom Roll	1.5 deg (-4.3%)	1.60 deg	1.4 deg (-13%)

Table 6.3: Standard deviation of boom parameters over course of refueling simulation for different tanker masses

6.3.4 Tanker CG Position

The tanker's CG position is changed to 23% and 37% respectively Table 6.4 summarises the results of the simulations.

Parameter	Fore Tanker CG	Baseline Tanker	Aft Tanker CG
Boom Length	0.15 m (+0.5%)	0.15 m	0.17 m (+14%)
Boom Pitch	0.77 deg (-2.0%)	0.79 deg	0.86 deg (+9.3%)
Boom Roll	1.5 deg (-6.0%)	1.6 deg	1.65 deg (+2.6%)

Table 6.4: Standard deviation of boom parameters over course of refueling simulation for different tanker CG locations

The boom length regulation is negatively impacted by a CG that is located either far forward or far rearward. The boom pitch is also negatively impacted, which leads to the conclusion that the X-direction regulation is affected overall. The roll parameter shows a slight improvement for a tanker CG that is located further aft from the leading edge. The recorded tanker data shows changes to the characteristics of the RR commands. Moving the tanker CG location fore or aft results in increases in the standard deviation of the nominal boom tip position of 12% and 7% respectively. This implies that the receiver needs to move the RR further to remain inside the boom envelope. The conclusion can be drawn that a tanker CG position at either extreme (fore or aft) leads to a more difficult command for the receiver to track.

6.3.5 Receiver Mass

The receiver mass is changed to 125 t and 225 t. Table 6.5 summarises the results of the simulations.

Parameter	Light Receiver	Baseline Receiver	Heavy Receiver
Boom Length	0.10 m (-4.6%)	0.11 m	0.14 m (+30%)
Boom Pitch	0.51 deg (-13%)	0.59 deg	0.83 deg (+41%)
Boom Roll	1.11 deg (-11%)	1.25 deg	1.35 deg (+7.7%)

Table 6.5: Standard deviation of boom parameters over course of refueling simulation for different receiver masses

Performance is reduced when receiver weight is increased. This is likely caused by the increased inertia of the receiver, which lowers the bandwidth of the closed loop system. This, in turn, reduces the receiver's ability to track the tanker as it is disturbed by turbulence. Figures

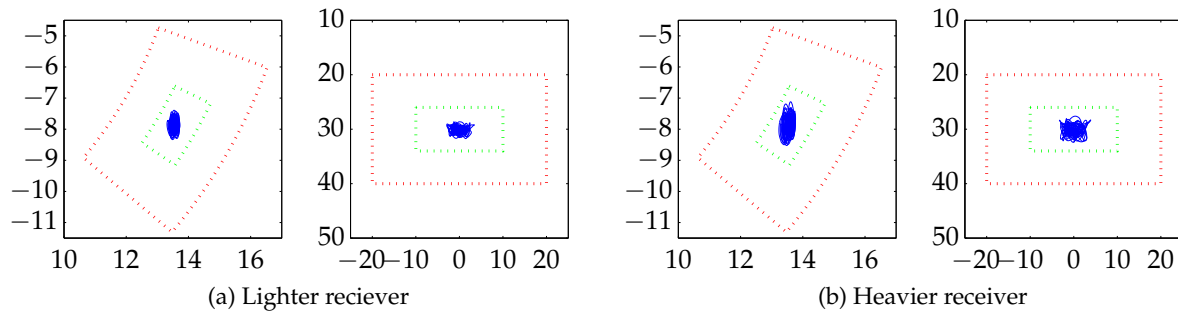


Figure 6.5: Simulation results for receivers with mass in light turbulence

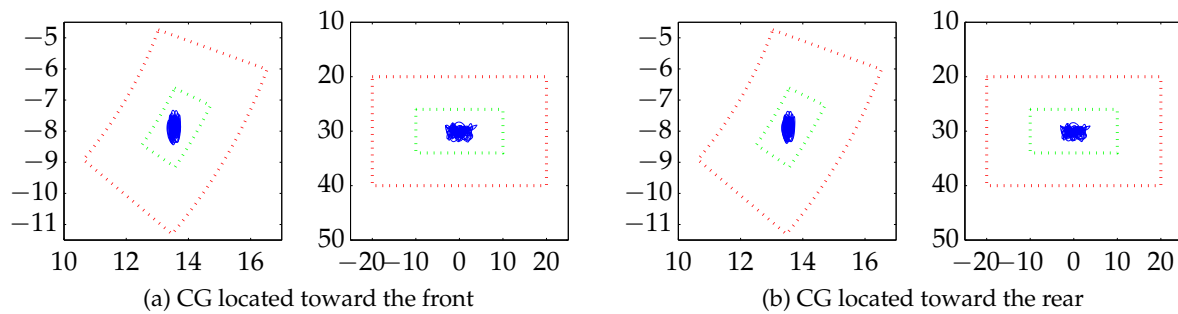


Figure 6.6: Simulation results for receivers with varying CG location

6.5 (a) and (b) show the position of the RR in the boom envelopes for a lighter and a heavier receiver.

6.3.6 Receiver CG

The receiver's CG position is changed to 23% and 37% respectively. Table 6.6 summarises the results of the simulations.

Parameter	Fore Receiver CG	Baseline Receiver	Aft Receiver CG
Boom Length	0.16 m (+5.2%)	0.15 m	0.15 m (-3.0%)
Boom Pitch	0.85 deg (+5.1%)	0.81 deg	0.82 deg (+1.0%)
Boom Roll	1.6 deg (+3.5%)	1.60 deg	1.57 deg (-1.9%)

Table 6.6: Change in boom parameters when changing receiver CG location

The results show a slight decrease in performance when the receiver's CG is located closer to the leading edge. The reduction is not significant. Figures 6.6 (a) and (b) show the position of the RR in the boom envelopes for receivers with different CG positions.

6.3.7 Downwash

The simulation is performed using downwash angles between 0° and 4° . Table 6.7 summarises the results.

Parameter	0° Downwash	1° Downwash	2° Downwash	3° Downwash	4° Downwash
Boom Length	0.15 [m] (0%)	0.14 [m] (-8%)	0.13 [m] (-13%)	0.13 [m] (-13%)	0.20 [m] (29%)
Boom Pitch	0.81 [deg] (0%)	0.82 [deg] (1%)	0.84 [deg] (4%)	0.87 [deg] (8%)	0.93 [deg] (14%)
Boom Roll	1.60 [deg] (0%)	1.59 [deg] (-1%)	1.58 [deg] (-1%)	1.56 [deg] (-2%)	1.55 [deg] (-3%)

Table 6.7: Change in boom parameters when changing downwash angles

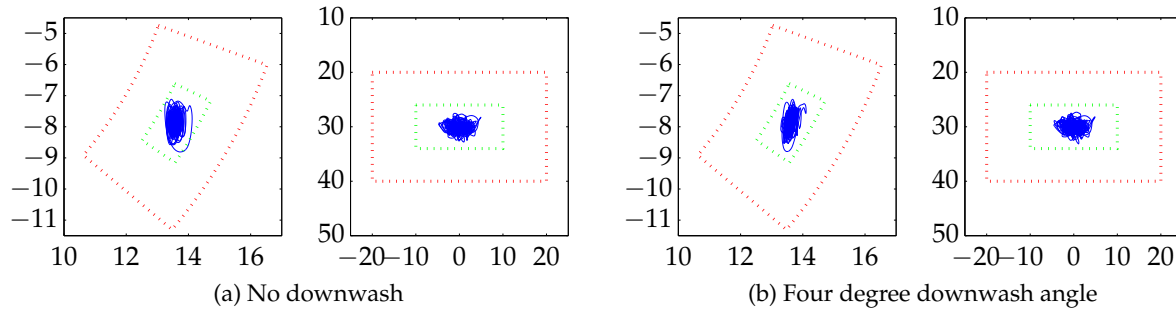


Figure 6.7: Simulation results for receivers experiencing different downwash angles

The results show that the regulation of the boom length and pitch angle worsens when the receiver is exposed to a downwash. Lateral performance, on the other hand, is not significantly impacted. Figures 6.7 (a) and (b) show the boom envelope plots for a receiver experiencing two different downwash angles.

Figure 6.8 shows the receiver's commanded thrust over the course of a simulation for receivers exposed to different downwash angles. It is clear that the receiver which experiences the downwash has significantly higher thrust values, as it trims as if in a climb.

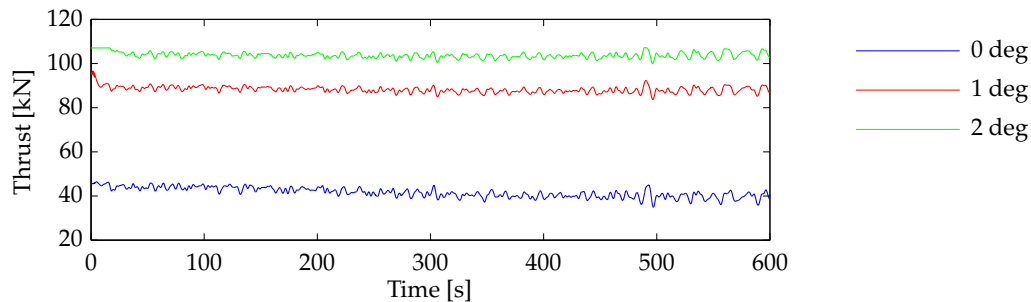


Figure 6.8: Commanded thrust over the course of simulation for different downwash angles

6.4 High-Drag Configuration

In Section 5.4, the high-drag configuration was presented as a method of improving the axial controller. This section will present non-linear simulation results to illustrate the effectiveness of this control scheme. A simulation is performed in light turbulence, with the receiver starting in the contact position, at all combinations of the following flight-point parameters:

Flight Level 100, 300

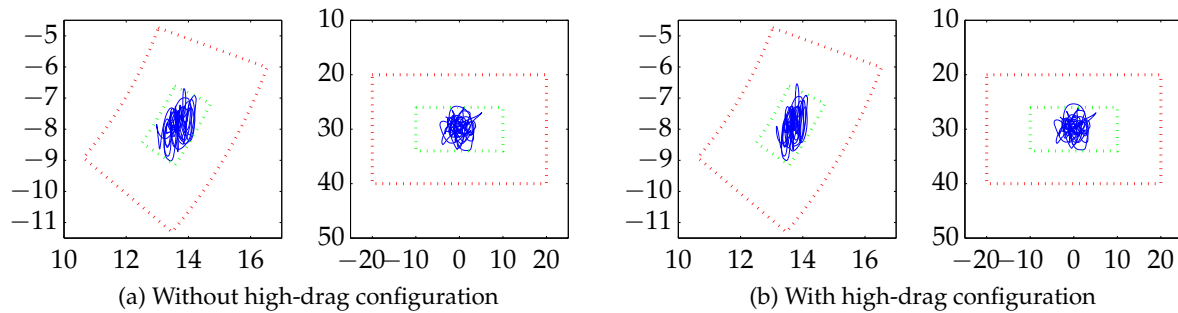


Figure 6.9: Simulation results for receivers with and without high-drag configuration at flight point: $FL = 100$, $V_c = 250$ kt, $m_r = 225$ t, $m_t = 175$ t

Calibrated Airspeed 250kt, 300kt

Receiver Mass 125t, 225t

Tanker Mass 175t

Tanker and Receiver CG 30%

The simulation is performed using the straight and level trajectory and without tanker downwash. Graphs will be used to compare performance at a single flight point. Numerical data will be shown at other flight points.

Figures 6.9 (a) and (b) show the envelope plot for receivers with and without the high-drag configuration. Qualitatively, it is noticeable that the axial performance of the system employing the high-drag configuration is better. The standard deviation of the X-error and Z-error of the RR are 0.34 m and 0.41 m respectively when using only thrust. When using the high-drag configuration, the standard deviation is 0.26 m and 0.42 m. In accordance with the design specifications, the axial performance of the controller has improved significantly, while the normal performance has degraded slightly. However, the errors in the boom parameters are of more importance than X-position and Z-position errors. The standard deviations of the boom length and the boom pitch angle are 0.29 m and 1.6 degrees respectively when using only thrust. These improves to 0.25 m and 1.5 degrees when using the high-drag configuration. The boom pitch angle is calculated as a combination of X and Z position, and the large improvement of the X-position negates the slight loss in Z-position performance. In terms of boom parameters, the high-drag configuration delivers the best performance.

Figure 6.10 shows the thrust and spoiler actuation over the course of the simulation. The deviation in thrust is less when the high-drag configuration is used. The standard deviations of the thrust (per engine) are 6.5 kN and 4.7 kN for the thrust-only system and the high-drag configuration respectively. The mean thrust is higher when using the high-drag configuration, as expected, and increases from 54 kN to 62 kN (per engine) when the high-drag configuration is used. It has therefore been shown that, at this flight point, the high-drag configuration delivers much better axial performance and smaller thrust variation at the cost of a higher mean thrust. Table 6.8 lists the quantities discussed here at other flight points.

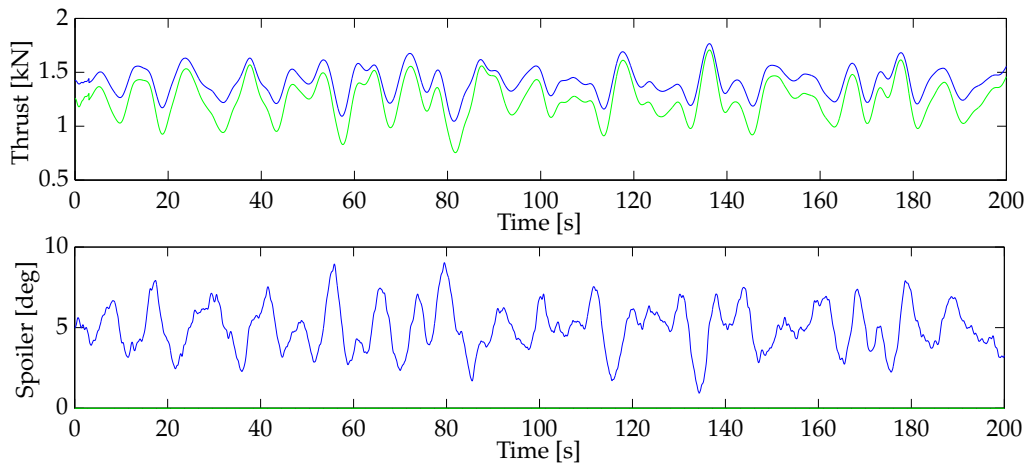


Figure 6.10: Thrust and spoiler actuation with and without high-drag configuration

Flight Point			σ_{ℓ_b} [m]		σ_{θ_b} [deg]		σ_T [kN]		\bar{T} [kN]	
FL	V_c	m_r	A	B	A	B	A	B	A	B
300	300	225	0.18	0.20	0.83	1.08	2.19	1.39	63.85	72.03
100	250	125	0.23	0.16	0.92	0.83	5.40	3.20	30.85	36.14
100	250	225	0.22	0.20	1.63	1.58	7.04	5.15	48.18	54.67
100	300	125	0.19	0.11	0.70	0.66	3.73	1.03	38.50	50.40
100	300	225	0.20	0.14	1.12	1.02	4.23	1.98	49.47	60.44
300	250	125	0.31	0.15	0.73	0.47	1.86	1.40	32.61	40.11
300	250	225	-	0.21	-	0.67	-	3.45	62.98	67.36
300	300	125	0.10	0.06	0.38	0.35	0.80	0.23	38.00	48.28
300	300	225	0.18	0.20	0.83	1.08	2.19	1.39	63.85	72.03

Table 6.8: Standard deviation of boom parameters and thrust, and mean thrust for thrust-only system (A) and high-drag configuration (B)

6.5 Trajectories

6.5.1 Racetrack Trajectory

The racetrack trajectory allows for the refueling process to take a long time, without the tanker and receiver moving too far from their starting positions. This section will investigate the non-linear simulation results of a tanker and receiver flying a racetrack trajectory. Specific attention is paid to the controller's performance during turn-in and during the banked segment. Simulations will be performed at the following flight points: $FL = 200$, $V_c = 260kt$, $m_r = 175t$, $CG_r = 30\%$. Figure 6.11 shows the performance of the controller over the entire racetrack.

Figure 6.12 shows the path flown by the tanker and the receiver. The straight leg of the racetrack was shortened from the definition in Section 1.6.3 to shorten simulation time. Due to the simplified tanker control, the shape is not a perfect racetrack.

Different colours are used to identify the different stages of the racetrack trajectory. Figure 6.13 shows the envelope plots for the individual stages. The lateral performance appears good across all stages. During turn-in and turn-out, the axial regulation exhibits slightly worse performance. This is due to the tanker's very simplistic axial control, which causes it to change

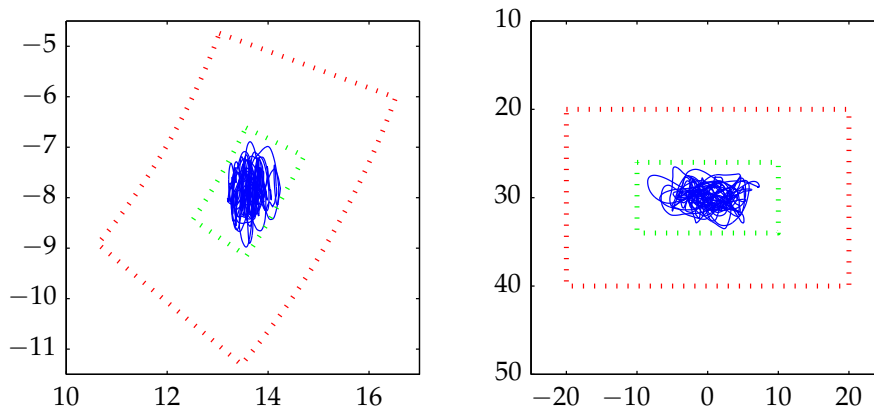


Figure 6.11: Control system performance in light turbulence during racetrack trajectory

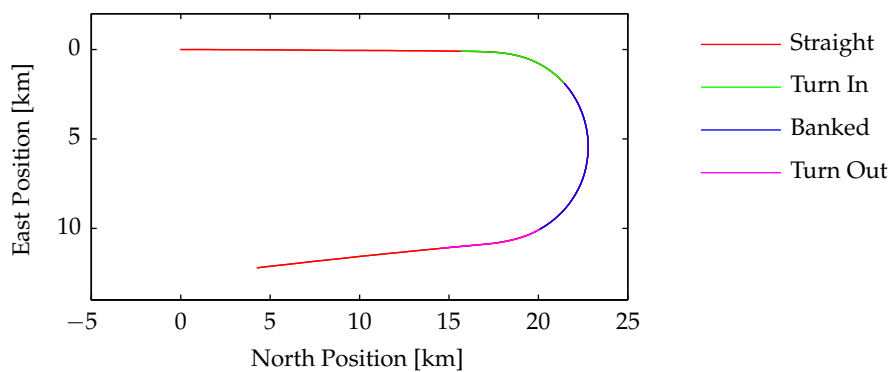


Figure 6.12: Path flown by tanker and receiver during racetrack trajectory

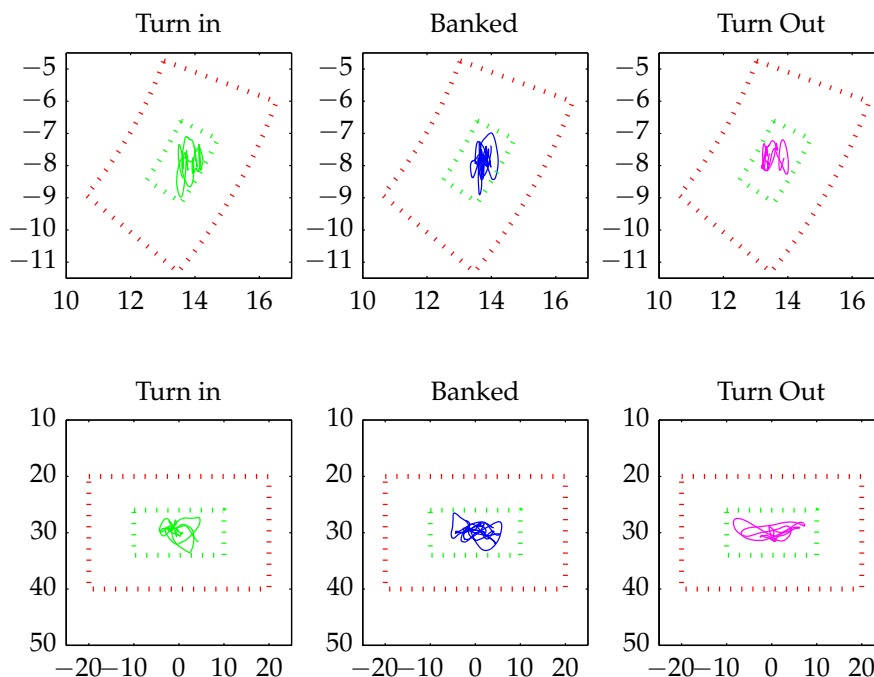


Figure 6.13: Control system performance in light turbulence during stages of racetrack trajectory

airspeed and altitude during turn-in and turn-out.

6.5.2 Toboggan Trajectory

The toboggan trajectory is intended to make refueling possible at flight points where either the receiver, or the tanker or both do not have adequate available thrust. A simulation is performed at flight point: $V_c = 225kt$, $FL = 300$, $m_r = 260t$. At this flight point, the receiver needs a very large angle of attack due to its low speed and high mass. This leads to more drag and subsequently a higher steady-state thrust. The problem is exacerbated by the use of the high-drag configuration. Figure 6.14 shows the envelope plot of the controller attempting to regulate the receiver in light turbulence.

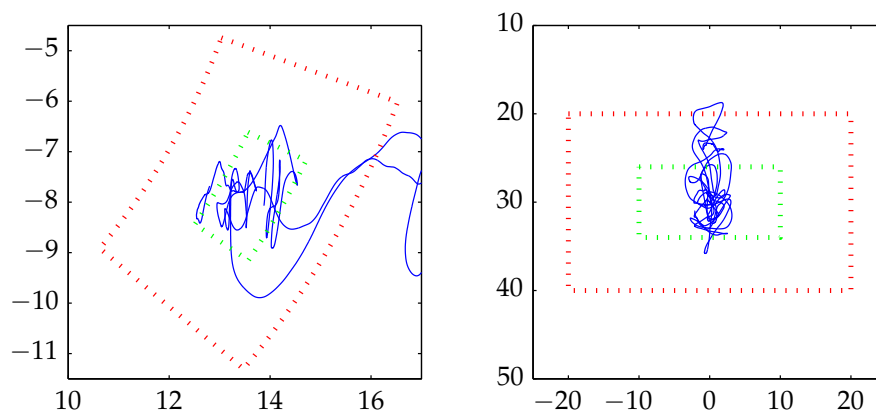


Figure 6.14: Control system performance in light turbulence during straight and level flight with high steady-state thrust requirement

The graph shows that the controller is unable to maintain the required airspeed. Figure 6.15 shows the results of a simulation with the same initial flight point parameters, but using the toboggan trajectory descending at 500ft/min.

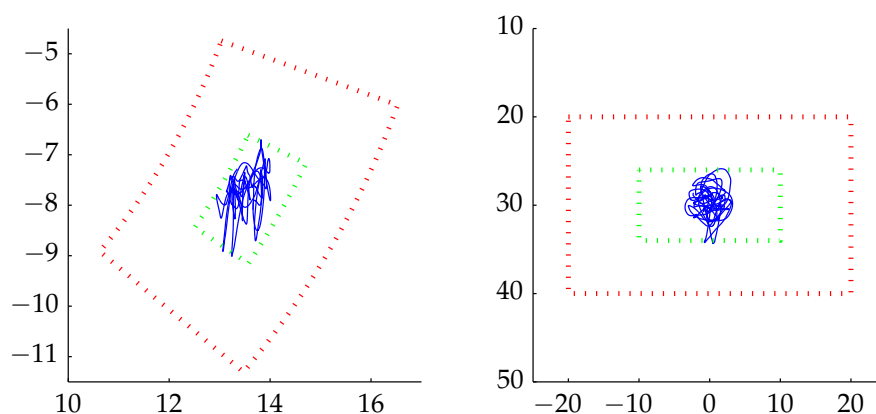


Figure 6.15: Control system performance in light turbulence during toboggan trajectory with high steady-state thrust requirement

The graphs shows that the controller successfully regulates the position of the RR. The effect of the toboggan trajectory is clearly visible when comparing the thrust actuation of the two simulations, as shown in Figure 6.16. The thrust of the receiver flying straight saturates at the maximum permissible level, preventing it from maintaining the required airspeed. The receiver following the toboggan trajectory has a lower steady-state thrust, and thus has the headroom to supply the additional thrust required for control.

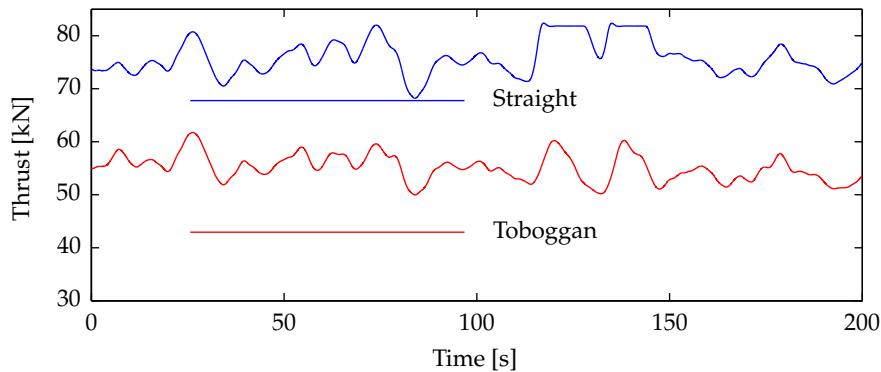


Figure 6.16: Thrust command comparison between straight and level flight and toboggan trajectory

6.5.3 Approach Trajectory

The receiver follows the approach trajectory, as defined in section 1.6.3, to reach the contact position. Figure 6.17 shows the North, East, and Down distances between the tanker and the receiver.

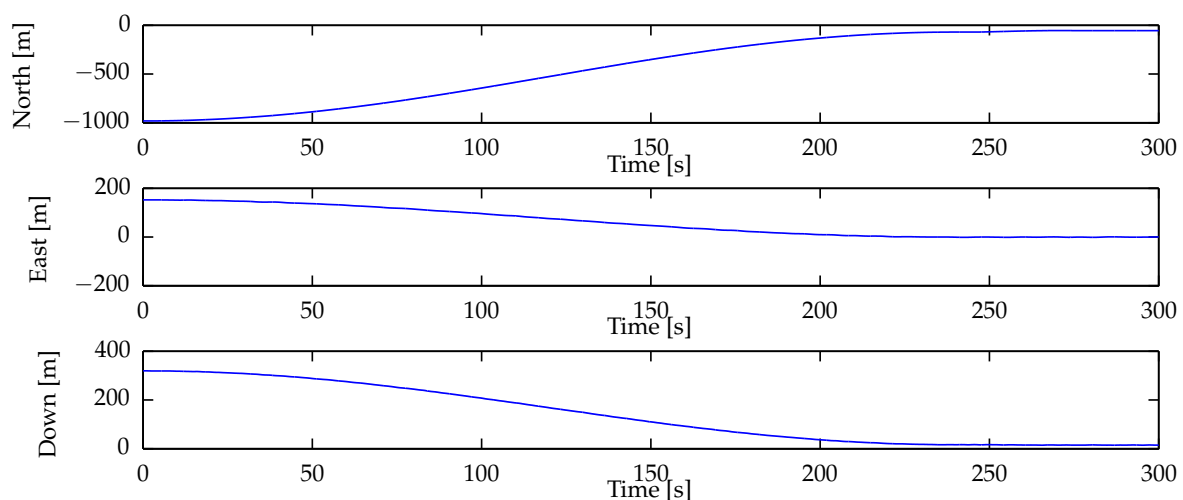


Figure 6.17: North, East and Down separation between tanker and receiver CGs during approach.

Figure 6.18 shows the RR entering the connect envelope as the receiver moves from the pre-contact position to the contact position. The controller successfully controls the receiver throughout approach and does not overshoot or come dangerously close to the tanker.

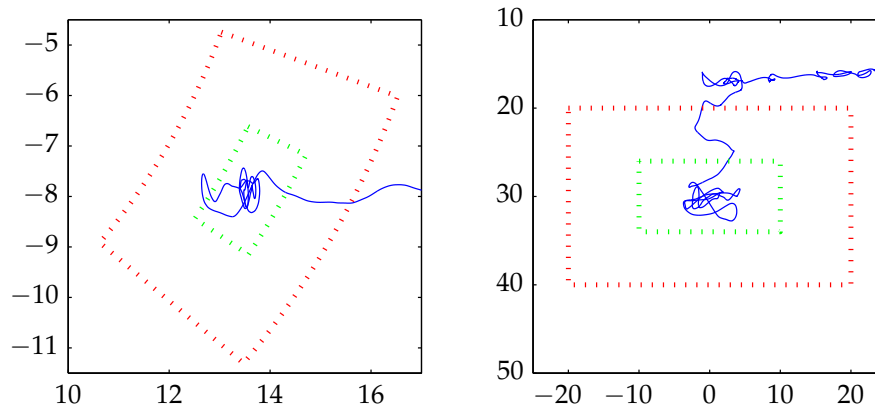


Figure 6.18: Location of RR in boom envelope as receiver transitions from pre-contact to contact position

6.6 Medium Turbulence

This section will investigate the controller's ability to regulate the RR to remain inside the disconnect envelope at various flight points. It was found that medium turbulence taxes the control system to the point where actuators can easily saturate. As such, non-linear simulations will be performed using the straight and level trajectory to focus on the effect of the turbulence. Simulations are performed at all combinations of the following flight-point parameters:

Flight Level 100, 200, 300

Calibrated Airspeed 225kt, 250kt, 275kt, 300kt

Receiver Mass 125t, 150t, 175t, 200t, 225t

Receiver CG 23%, 30%, 37%

Tanker Mass 175t

Tanker and Receiver CG 30%

The simulation results show that the controller successfully regulates the RR inside the disconnect envelope at some, but not all flight points. In contrast to light turbulence, automated refueling in medium turbulence is feasible at significantly fewer flight points. When simulating AAR in medium turbulence, the RR occasionally moves outside the disconnect envelope. If AAR were to be performed in the real world, this would result in the boom immediately disconnecting, and the receiver retreating to the observation position. This receiver behaviour was not included in the simulation. Instead, the simulation is continued as the controller attempts to return the RR to the nominal boom tip position. Consequently, the simulation results

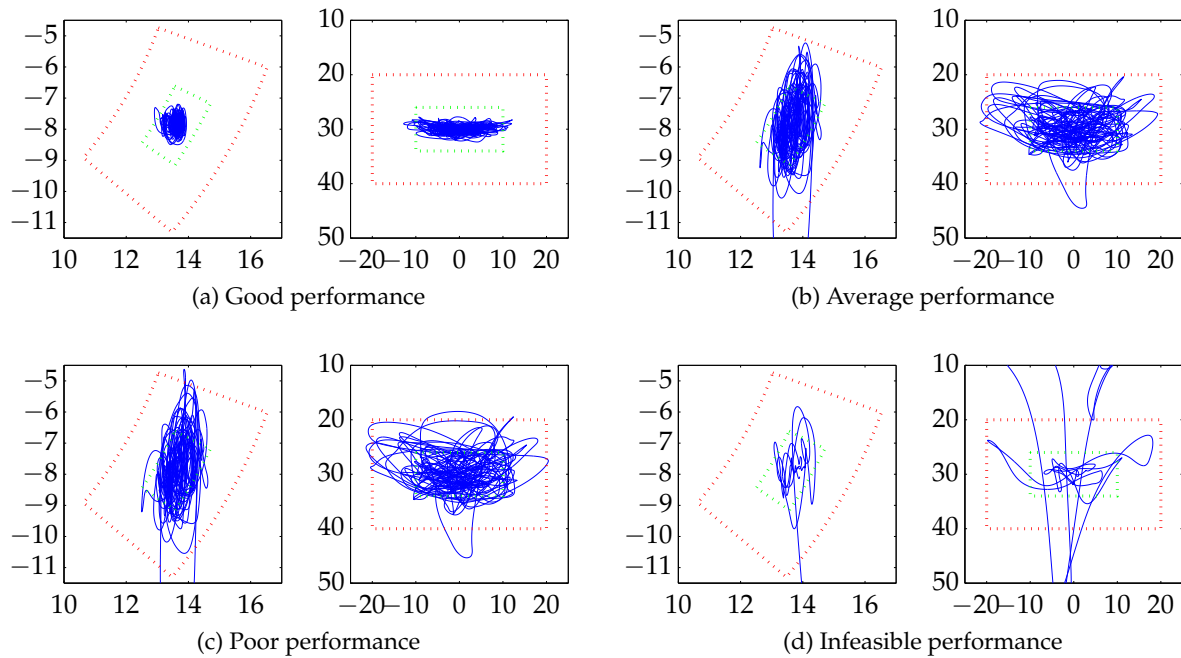


Figure 6.19: Good, average, poor and infeasible performance at various flight points in medium turbulence

can be used to determine the relative performance of the controller at different flight points, even if AAR was not successful.

Table D.2 in Appendix D lists all the flight points at which the controller succeeded as well as the standard deviations of the boom parameter errors at those flight points. Detailed results from four flight points, namely with good, average, poor and unfeasible performance, will be shown here.

Good FL = 300, $V_c = 275$, $m_r = 125t$, $CG_r = 30\%$

Average FL = 100, $V_c = 225$, $m_r = 125t$, $CG_r = 30\%$

Poor FL = 200, $V_c = 225$, $m_r = 225t$, $CG_r = 30\%$

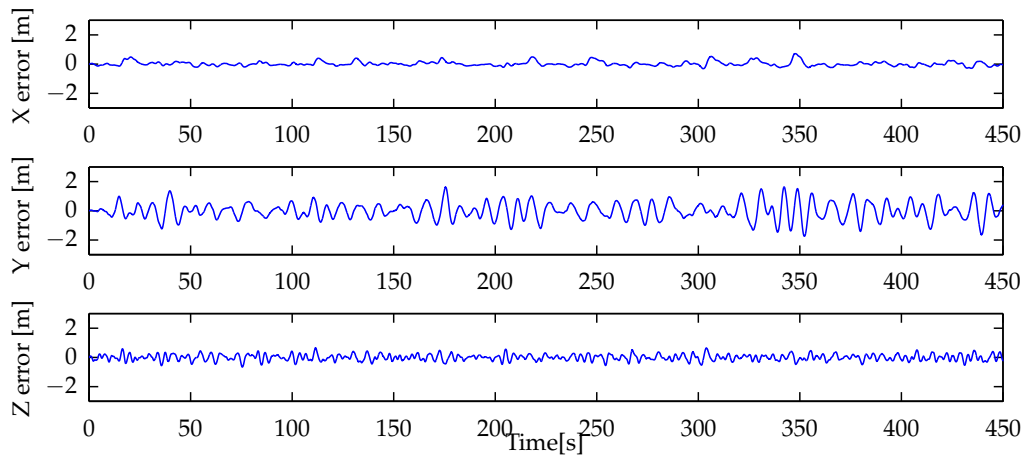
Infeasible

Figures 6.19 (a) to (c) show the location of the RR in the boom envelope over the course of the simulations.

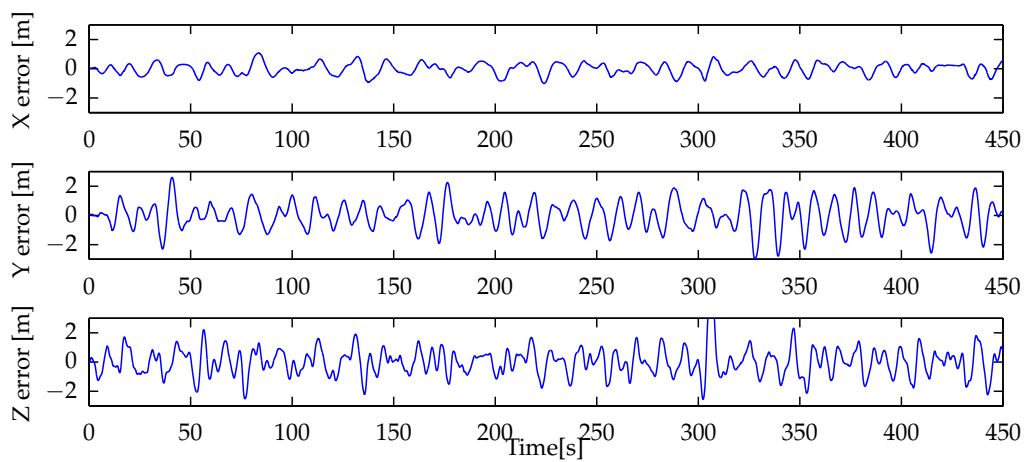
Figures 6.20 and 6.21 show the X,Y and Z-errors of the RR over the course of the simulations.

Figure 6.19 (a) shows that, at flight points with “good” performance, the control system is able to regulate the RR well inside the disconnect envelope. In fact, the RR remains inside the smaller connect envelope for the majority of the simulation.

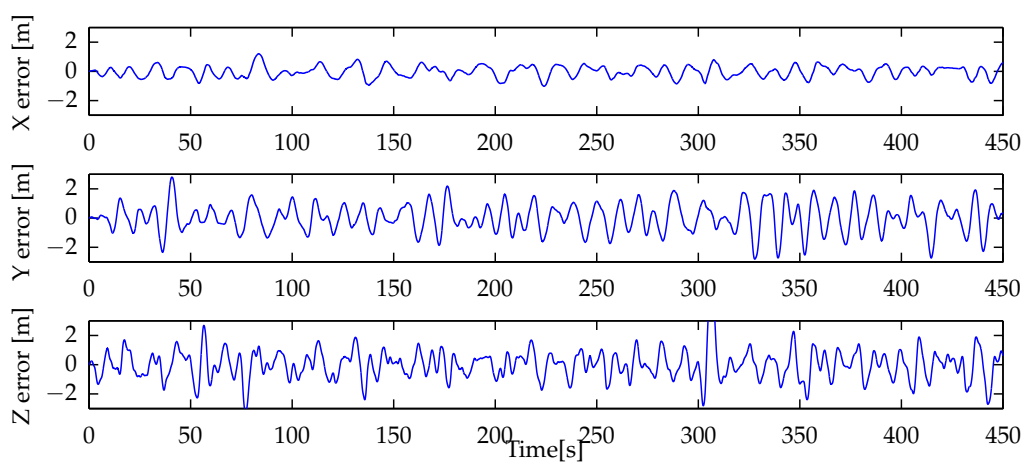
At most flight points, termed to have “average” performance, the RR moves across the extent of the disconnect envelope, as shown in Figure 6.19 (b). At these flight points, it would be more difficult for the boom operator to connect the boom to the receiver, as the RR regularly



(a) Good performance



(b) Average performance



(c) Poor performance

Figure 6.20: Good, average, poor and infeasible performance at various flight points in medium turbulence

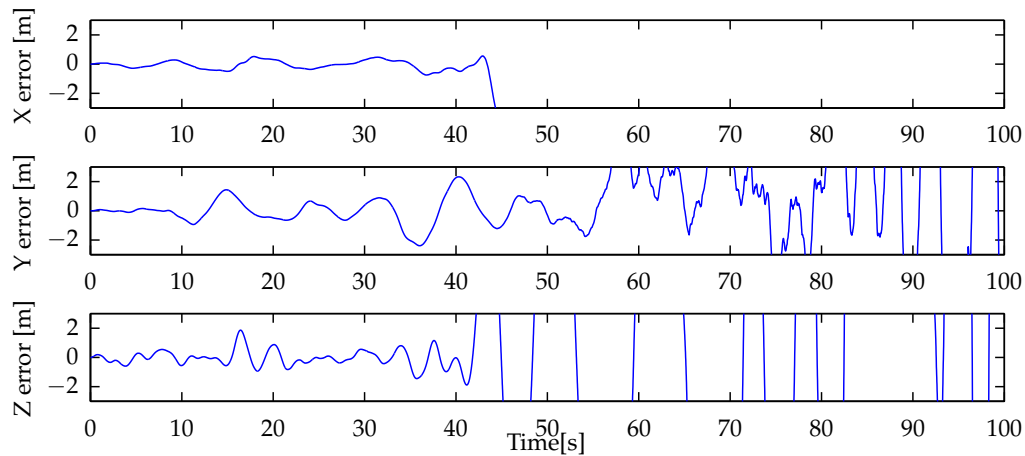


Figure 6.21: Infeasible control system performance in medium turbulence

leaves the connect envelope. Once the boom is connect, however, refueling can be completed, since the RR never moves outside the disconnect envelope.

At flight points with “poor” performance, as illustrated in Figure 6.19 (c) the RR regularly strays outside the disconnect envelope. It was found that the limiting factor at these flight points was the actuator limits implemented in the Simulink simulation. The actuator limits in the Simulink simulation represent conservative limits, and there is room for them to be expanded. Simulations performed with increased actuator limits allowed the controller to regulate the RR inside the disconnect envelope over the whole simulation at some of these flight points. In Section 6.8, it will be shown that when using Airbus’s high-fidelity simulator, the controller succeeds at some of these flight points.

At other flight points, as shown in Figure 6.19 (c), the RR continuously strays outside the disconnect envelope and AAR is infeasible. Achieving AAR at these flight points – even with an improved control system and increased actuator limits – is unlikely. At infeasible flight points, the control system does not have the control authority to reach the required closed loop bandwidth. The most common limiting factor appears to be the availability of thrust as evidenced by the large X error shown in Figure 6.21.

Table D.2 in Appendix D lists the performance of the control system at all flight points. The performance of the control system is quantified by the standard deviations of the boom parameter errors. Further, each flight points is marked as having good, average, poor or infeasible performance.

6.7 Downwash Dynamics

In Chapter 2, the downwash dynamics were presented. The downwash dynamics captures the effect of the changing tanker downwash when the receiver moves from the nominal position. The downwash dynamics can be included into a model as additional aerodynamic derivatives. From available literature, it was found that the most prominent downwash derivatives are: $C_{L_{xcg}}$, $C_{M_{xcg}}$, $C_{S_{ycg}}$, $C_{\bar{L}_{ycg}}$, $C_{N_{ycg}}$. Since the values of these derivatives are not known, they were

not included in the non-linear simulations discussed throughout this chapter. Instead, the effect of each derivative on the closed loop system will be investigated in turn using non-linear simulations. For the simulation results presented in this section, the magnitude of the downwash derivatives were chosen such that the effect is clearly visible. The real values can potentially be much higher or lower. The signs of the derivatives were chosen to match data taken from the literature discussed in Section 2.5.6.

6.7.1 Axial Displacement

In this section, the receiver is perturbed from the nominal position in the X direction. The effect of the changing tanker downwash is captured by the downwash derivatives $C_{L_{xcg}}$ and $C_{M_{xcg}}$. The X and Z position errors of the RR are investigated to judge the effect of the additional derivative on the control system's performance. Figure 6.22 shows control system's response to an initial -1 m X error if the downwash derivative $C_{L_{xcg}}$ is included in the simulation.

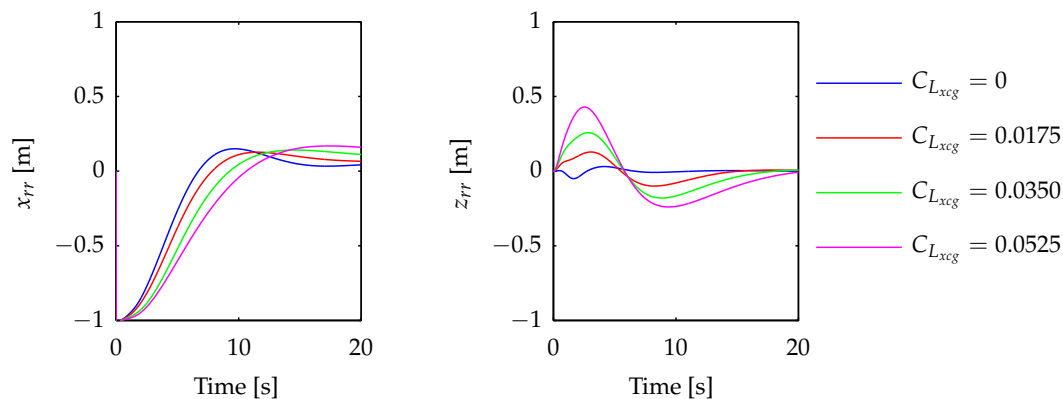


Figure 6.22: Effect of $C_{L_{xcg}}$ on closed loop normal and axial system

As shown in Section 2.5.6, it is expected that $C_{L_{xcg}}$ would be positive. This results in lift decreasing when the receiver moves too far to the rear. The responses show that the inclusion of the downwash derivative greatly increases the coupling between the normal and axial control system. This is to be expected, as an axial displacement is causing a normal force. The damping of the axial response has increased. The expected value of $C_{L_{xcg}}$ is 0.0035, much less than the values shown in the figure. The control system is robust enough to withstand the expected $C_{L_{xcg}}$.

Figure 6.23 shows control system's response to an initial -1 m X error if the downwash derivative $C_{M_{xcg}}$ is included in the simulation.

As shown in Section 2.5.6, it is expected that $C_{M_{xcg}}$ would be positive. This results in a nose down moment when the receiver moves to the rear. As in the previous example the coupling between the axial and normal systems has increased. The damping of the axial system is slightly decreased. The expected value of $C_{M_{xcg}}$ is 0.0015. At this value, the coupling between the normal and axial system is significantly increased, and control system performance is neg-

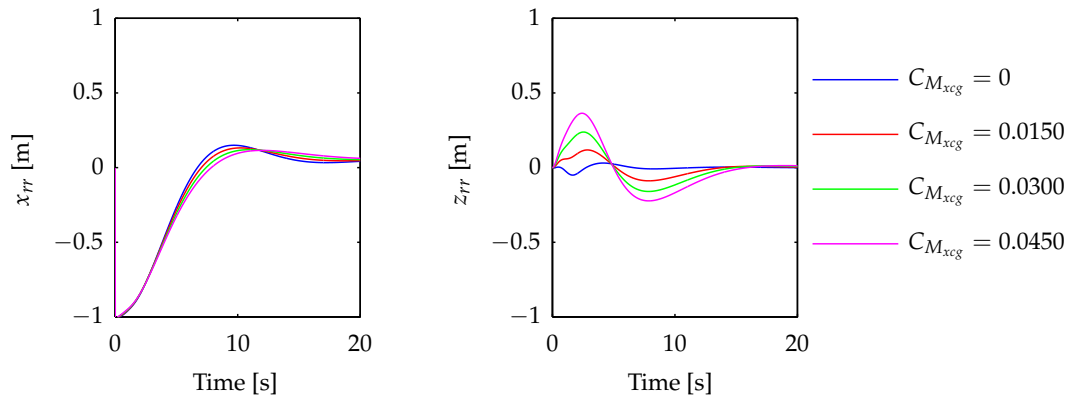


Figure 6.23: Effect of $C_{M_{xcg}}$ on closed loop normal and axial system

actively impacted. While the control system is robust enough to withstand the expected $C_{M_{xcg}}$, the loss in performance can cause AAR to become infeasible at certain flight points.

6.7.2 Lateral Displacement

In this section, the receiver is perturbed from its nominal position in the Y direction. The effect of the changing tanker downwash is captured by the downwash derivatives $C_{S_{ycg}}$, $C_{\bar{L}_{ycg}}$, and $C_{N_{ycg}}$. The Y position error of the RR is investigated to judge the impact of the derivatives on the control system's performance.

Figure 6.24 shows control system's response to an initial -1 m Y error if the downwash derivative $C_{S_{ycg}}$ is included in the simulation.

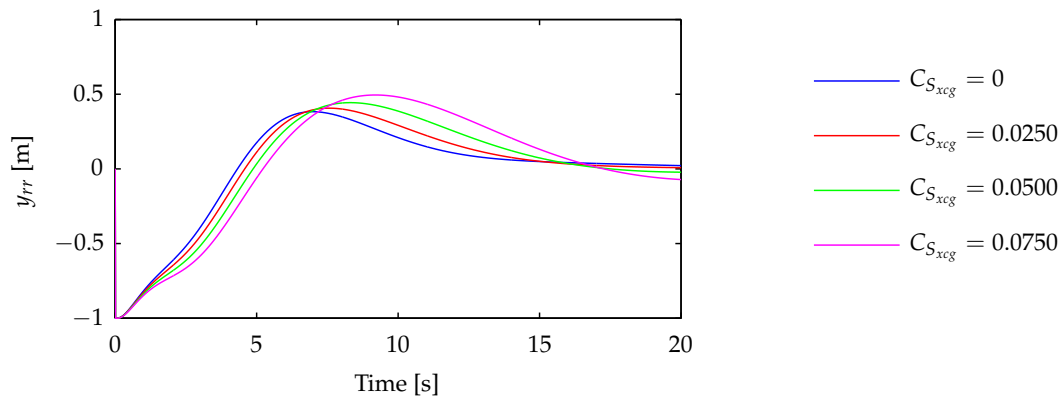


Figure 6.24: Effect of $C_{S_{ycg}}$ on closed loop normal and axial system

As shown in Section 2.5.6, it is expected that $C_{S_{ycg}}$ would be negative. The result is a force that drives the receiver further away from the nominal position once it is perturbed in the Y direction. The figure shows an increase in rise time and a reduction in damping. If the derivative is increased further, the control system is not able to return the receiver to the nominal position. The expected value of $C_{S_{ycg}}$ is -0.00075. This is much smaller and the control system is robust

enough withstand this modeling error. Furthermore, if all downwash derivatives are included, the negative $C_{\bar{L}_{ycg}}$ will aid in returning the receiver to the nominal position.

Figure 6.25 shows control system's response to an initial -1 m Y error if the downwash derivative $C_{\bar{L}_{ycg}}$ is included in the simulation.

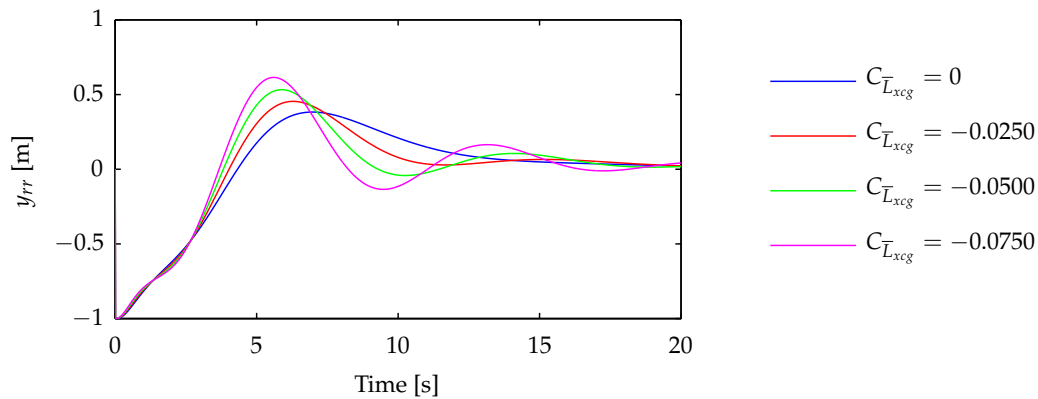


Figure 6.25: Effect of $C_{\bar{L}_{ycg}}$ on closed loop normal and axial system

As shown in Section 2.5.6, it expected that $C_{\bar{L}_{xcg}}$ would be negative. This results in a rolling motion that will return the receiver to the nominal position if is perturbed in the Y direction. The response shows a decrease in rise time and damping as $C_{\bar{L}_{xcg}}$ increases in magnitude. The expected value of $C_{\bar{L}_{xcg}}$ is -0.0016. The control system is robust enough to withstand this expected value.

Figure 6.24 shows control system's response to an initial -1 m Y error if the downwash derivative $C_{N_{ycg}}$ is included in the simulation.

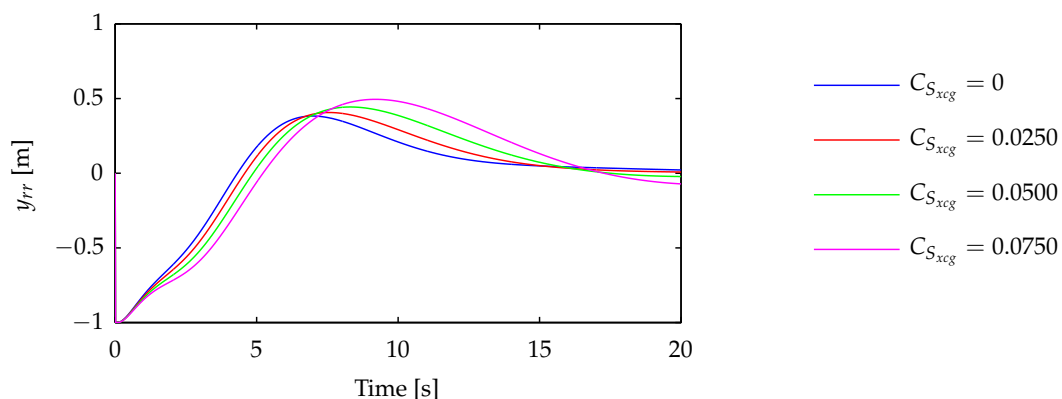


Figure 6.26: Effect of $C_{N_{ycg}}$ on closed loop normal and axial system

As shown in Section 2.5.6, it expected that $C_{N_{ycg}}$ would be negative. This results in a yawing motion that will return the receiver to the nominal position if is perturbed in the Y direction. The response shows that the inclusion of the derivative has increased the speed of the response,

as expected, but has also decreased the damping. The expected value of $C_{N_{y\dot{c}g}}$ is -0.00025 . This is much smaller and the control system is robust enough withstand this modeling error.

6.7.3 Summary

In Section 2.5.6, available literature was investigated to find representative value for the downwash derivatives. Through non-linear simulations, it was shown that the control systems derived in Chapter 5 are robust enough to withstand the inclusion of these derivatives, though performance does suffer. The effect of the derivatives are minimized by the fact that the high-bandwidth controllers keep the position errors small. The real values of these derivatives, for a Airbus A330 MRTT tanker and receiver could possibly vary significantly from values tested here.

6.8 High-Fidelity Simulator Verification

As part of this project, the researcher performed an internship at Airbus's headquarters in Toulouse, France. The goal of the internship was to implement the newly designed control systems on a high-fidelity simulator, and present the results to Airbus employees. This section will give a brief overview of this simulator and the results obtained.

6.9 Simulator

The high-fidelity simulator is a better representation of an Airbus A330 MRTT than the Simulink simulator used throughout this thesis. The high-fidelity simulator is used by Airbus internally for the development of flight control software. The simulator executes on a server, but can be controlled from a local PC over a network. The simulator contains:

- Accurate aerodynamics model of the aircraft.
- Accurate non-linear actuator models.
- Accurate non-linear engine models.
- Realistic actuator models.
- Realistic sensor models, including noise and delays.
- The FBW and hold mode flight software that run on an Airbus A330 MRTT.
- The same turbulence model implemented in the Simulink simulation.
- A component that sends input to a Matlab Simulink model running on the local PC at each time step. The output of this model is fed back into the simulation.

As before, the tanker is simulated first, and its position and orientation are recorded and saved on the local PC. The receiver's AAR control system is implemented on the local PC in Simulink. For all receiver states used in feedback (angular rates, aerodynamic angles, etc.), the output of the sensor models was used. This means that the accuracy and delays are representative of those in a real aircraft.

The tanker and receiver's relative states (relative position and orientation) were calculated on the local PC using the same techniques as before. This means that the relative states' accuracy and delays are not representative yet; more research is required in this area.

6.10 Results

The results of the high-fidelity simulations were very promising. The control system performed slightly better in the high-fidelity simulator compared to the Simulink simulation. Refueling in medium turbulence was possible at more flight points. This is a vital research outcome, as it validated the modelling and control performed in the preceding chapters. The high-fidelity results also show that the Simulink simulation does provide meaningful results.

Unfortunately, the author only had access to the high-fidelity simulator for the duration of the internship. Certain elements of the model (such as downwash and toboggan trajectory) were not included when the high-fidelity simulations were performed. The derivation of the linear model and controller structure has also changed slightly since the completion of the internship. It was thus decided not to use the high-fidelity results in the majority of this chapter, as these results do not accurately represent the modelling and control presented in this thesis.

A small selection of high-fidelity simulation results will now be shown. Note that while the modelling and controller gain selection differ slightly in these simulations, the most important factors – the inclusion of RR-dynamics, RR-RR controller architecture and high-drag configuration – are still present. Banked turn flight was also successfully validated in the high-fidelity simulator. Figures 6.27 (a) to (c) show the location of the RR in the boom envelope over the course of the simulations at the following three flight points.

Good FL = 300, $V_c = 275\text{kt}$, $m_r = 150\text{t}$, $CG_r = 30\%$

Average FL = 300, $V_c = 225\text{kt}$, $m_r = 125\text{t}$, $CG_r = 30\%$

Poor FL = 100, $V_c = 250\text{kt}$, $m_r = 225\text{t}$, $CG_r = 30\%$

Figures 6.28 to (a) to (c) show the X,Y and Z-errors of the RR over the course of the simulation.

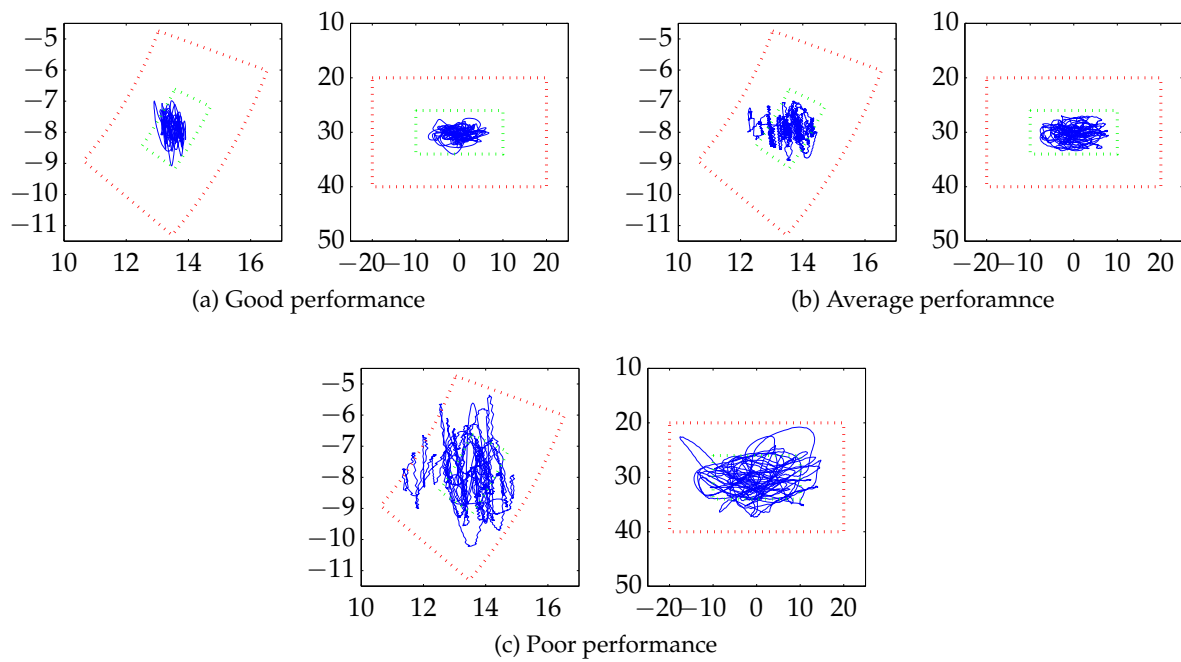
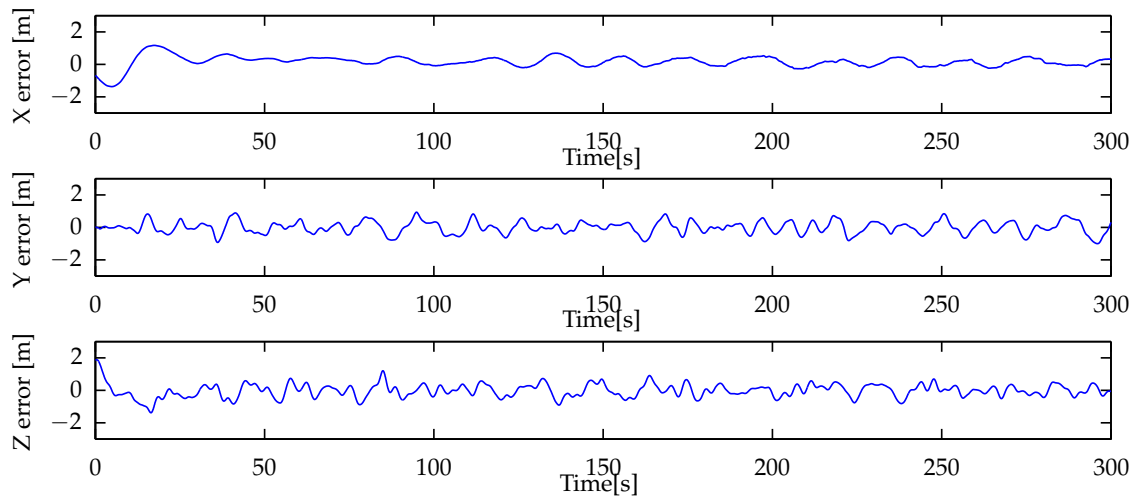
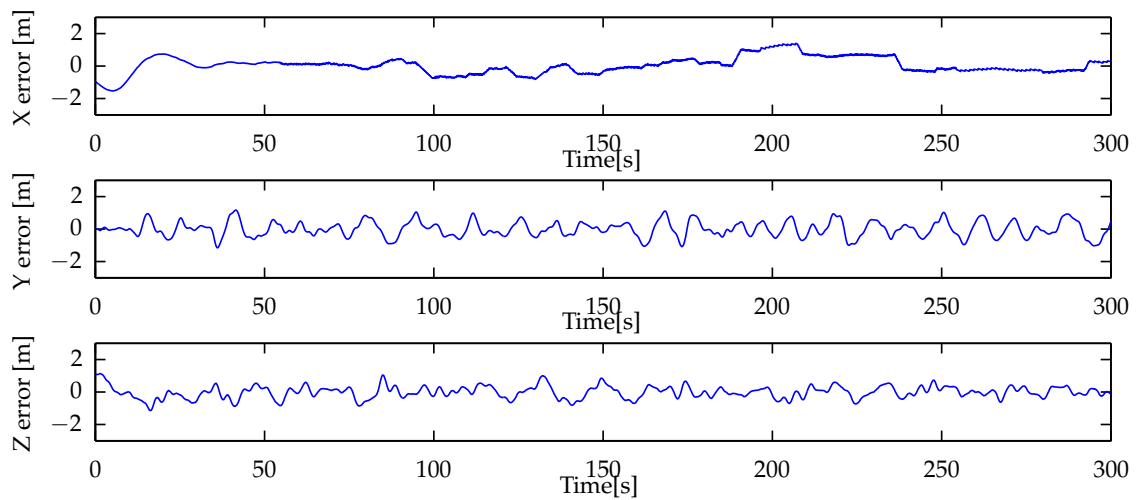


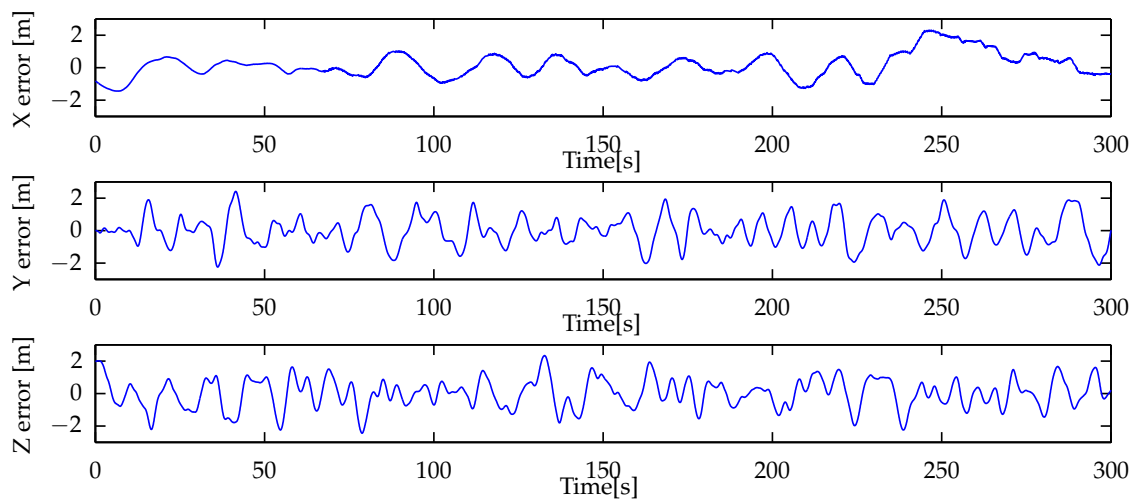
Figure 6.27: Good, average and poor performance at various flight points in medium turbulence using high-fidelity simulator



(a) Good performance



(b) Average performance



(c) Poor performance

Figure 6.28: Good, average and poor performance at various flight points in medium turbulence using high-fidelity simulator

Chapter 7

Fly-by-Wire

7.1 Overview

All modern Airbus aircraft are equipped with a fly-by-wire system. The fly-by-wire is a partial control system that breaks the direct link between the pilot and the actuation surfaces. The pilot's stick inputs provide reference inputs that the fly-by-wire control system then follows. The goal is to make all Airbus models have similar handling characteristics. Several protection rules are also incorporated into the fly-by-wire system. It is desirable for the AAR controller to work through the FBW system, as this will reduce the number of systems that need to be duplicated, tested and certified again. One of the secondary research objectives of this project is to investigate the feasibility of controlling the receiver aircraft through the fly-by-wire system.

This chapter presents the investigation into achieving AAR through the FBW system. Note that the goal of this chapter is not to discuss the design of the FBW system. The FBW system is discussed in detail in [20]. Section 7.2 presents the structure of the Airbus FBW system, and shows how the FBW controller was added to the RR-dynamics model derived in Chapter 2. Section 7.3 discusses the control of the receiver through the FBW system. Results from high-fidelity simulations are shown in Section 7.4.

7.2 Modeling

This section will investigate a simplified version of the normal manual control laws that Airbus supplied to Stellenbosch University in the form of a Matlab Simulink model. The FBW system is referred to as the normal laws, as these control laws are applied while the aircraft is in the normal flight envelope. While the Simulink model does not contain most of the protection subsystems, it is accurate as long as the aircraft remains inside the intended flight envelope. It is acceptable to slightly change some elements of the FBW system, but this should ideally be kept to a minimum. Alternate FBW laws exist, but will not be considered here.

By introducing the FBW system, the number of controllers and models is increased. To prevent confusion, the terms are defined below.

RR Dynamics Model The open loop natural dynamics model describing the movement of the aircraft and the RR, as derived in Chapter 2.

AAR Controller The control system designed in Chapter 5 to regulate the RR dynamics model.

FBW Model A linear model of the FBW system.

Normal Law Model A model of the aircraft that is being controlled by the FBW model, i.e. a linear model with longitudinal stick, lateral stick and pedal inputs.

FBW Controller A control system designed to control the normal law model.

7.2.1 Longitudinal FBW System

The longitudinal FBW system receives a longitudinal stick input, δ_Q , and translates it to a normal specific acceleration command. The commanded acceleration is achieved by actuating the elevator and horizontal tailplane. The acceleration will be expressed as a load factor, in g , and is positive in the negative Z-direction, i.e. upwards.

7.2.1.1 Architecture

Figure 7.1 shows how the manual laws convert a longitudinal stick deflection, δ_Q , into a commanded normal load factor, N_{Z_c} .

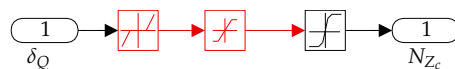


Figure 7.1: Normal FBW system: input state

The dead-zone non-linearity is present to prevent very small or accidental stick deflections from resulting in actuation changes. The saturation block merely limits the total permissible load factor command which the pilot can supply. These blocks are not required when the manual control laws are being driven by an outer loop controller, and are therefore removed. The removed blocks are shown in red. If these blocks cannot be removed, it is possible to compensate for them by deforming the input signal. Note that these blocks do not represent the protection modes implemented into the FBW-system. Figure 7.2 shows the calculation of the normal specific acceleration. The input is the normal load factor at the IRS of the aircraft. The IRS is located in front of the CG, but not as far forward as the refueling receptacle. The component of the normal load factor that opposes gravity and the centripetal acceleration present in a banked turn is removed. The output, ΔN_z , is the specific acceleration, which will cause a change in the flight path of the aircraft.

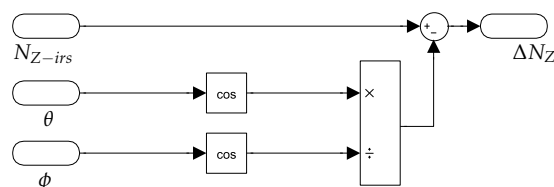


Figure 7.2: Normal FBW system: load factor calculation

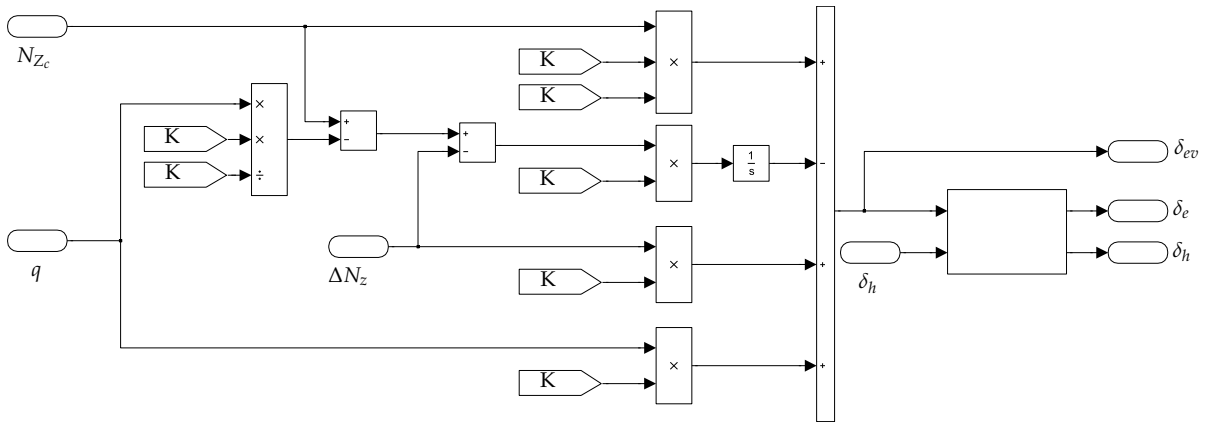


Figure 7.3: Normal FBW system

Figure 7.3 shows the calculation of the feedback signal for the normal load factor controller. Simplifying the block diagram shown in the figure, the effective elevator deflection δ_{ev} can be calculated as follows:

$$\delta_{ev} = K_{N_{z_c}} N_{z_c} + K_{N_z} N_z + K_q q + K_{N_{z_i}} N_{z_i} + K_{q_i} q_i \quad (7.2.1)$$

where N_{z_i} and q_i are the integrated load factor error, and integrated pitch rate respectively. At the flight points considered in this thesis, K_{q_i} is zero. The gains are retrieved from a lookup table, and change depending on aircraft mass and dynamic air pressure. Figure 7.4 shows the output stage for the manual control laws that converts the effective elevator deflection to an elevator and horizontal stabiliser deflection. A relatively slow first-order response filters any constant elevator deflection to the horizontal stabiliser. The gains are chosen in such a way that the combined pitching moment of the elevator and horizontal stabiliser is equal to the effective elevator pitching moment. Consequently, this stage does not need to be modelled.

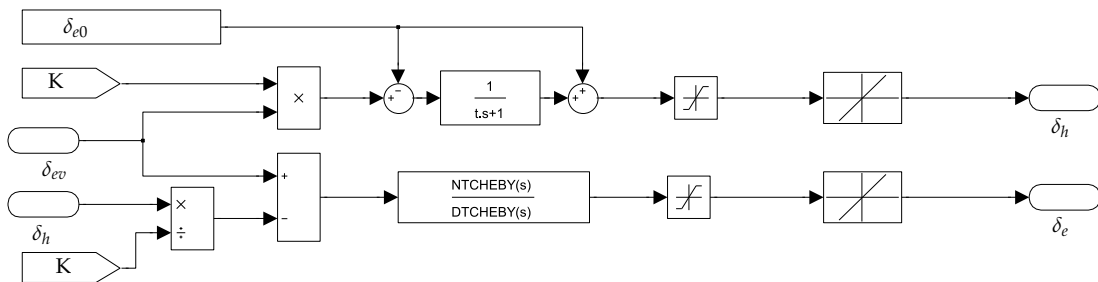


Figure 7.4: Normal FBW system - output

The Chebyshev filter on the output of the elevator, which is present for safety reasons [1], must be considered. The inclusion of this filter is one of the main reasons why the specification requires control through fly-by-wire. One of the aims of the investigation is to ascertain whether AAR is possible with this filter in place.

7.2.1.2 State Space

A state-space model is constructed to represent the normal FBW system. The states and matrices are

$$\begin{aligned}\mathbf{x}_{fbw} &= \begin{bmatrix} N_{zi} & F_1 & F_2 \end{bmatrix}^T \\ \mathbf{u}_{fbw}^1 &= \begin{bmatrix} N_z & q \end{bmatrix}^T \\ \mathbf{u}_{fbw}^2 &= \begin{bmatrix} \delta_q \end{bmatrix} \\ \mathbf{y}_{fbw} &= \begin{bmatrix} \delta_e \end{bmatrix} \\ \dot{\mathbf{x}}_{fbw} &= A_{fbw}\mathbf{x}_{fbw} + B_{fbw}^1\mathbf{u}_{fbw}^1 + B_{fbw}^2\mathbf{u}_{fbw}^2\end{aligned}\quad (7.2.2)$$

where F_1 and F_2 are the states of the Chebyshev filter. The state space system is

$$\begin{aligned}\dot{\mathbf{x}}_{fbw} &= \begin{bmatrix} 0 & K_{N_{zi}} & 0 \\ 0 & K_{f11} & K_{f12} \\ 0 & K_{f21} & K_{f22} \end{bmatrix} \mathbf{x}_{fbw} + \begin{bmatrix} 1 & 0 \\ K_{N_z} & K_q \\ 0 & 0 \end{bmatrix} \mathbf{u}_{fbw}^1 + \begin{bmatrix} -1 \\ K_{N_{zc}} \\ 0 \end{bmatrix} \mathbf{u}_{fbw}^2 \\ \begin{bmatrix} \delta_e \end{bmatrix} &= \begin{bmatrix} 0 & 0 & 1 \end{bmatrix} \mathbf{x}_{fbw}\end{aligned}\quad (7.2.3)$$

The dynamics state space model derived in Section 2.3.3 is changed to have an output vector containing the pitch rate, q , and the normal acceleration at the IRS, N_z . The IRS is located slightly in front of the leading edge of the wing. The dynamics state space now has the following structure:

$$\begin{aligned}\mathbf{x}_{dyn} &= \begin{bmatrix} \alpha & q & u_{rr} & w_{rr} \end{bmatrix}^T \\ \mathbf{u}_{dyn} &= \begin{bmatrix} T & \delta_e & \delta_s \end{bmatrix}^T \\ \mathbf{y}_{dyn} &= \begin{bmatrix} q & N_z \end{bmatrix}^T\end{aligned}\quad (7.2.4)$$

$$\dot{\mathbf{x}}_{dyn} = A_{dyn}\mathbf{x}_{dyn} + \begin{bmatrix} B_T & B_{\delta_e} & B_{\delta_s} \end{bmatrix} \mathbf{u}_{dyn}\quad (7.2.5)$$

$$\begin{aligned}\mathbf{y}_{dyn} &= C_{dyn}\mathbf{x}_{dyn} + \begin{bmatrix} D_T & D_{\delta_e} & D_{\delta_s} \end{bmatrix} \mathbf{u}_{dyn} \\ C_{dyn} &= \begin{bmatrix} 0 & 1 & 0 & 0 \\ \frac{Z_\alpha}{mg} - \frac{\ell_{x-irs}M_\alpha}{I_{yy}g} & -\frac{\ell_{x-irs}M_q}{I_{yy}g} & \frac{Z_V}{mg} & 0 \end{bmatrix} \\ D_{\delta_e} &= \begin{bmatrix} 0 & \frac{Z_{\delta_e}}{mg} - \frac{\ell_{x-irs}M_{\delta_e}}{I_{yy}g} \end{bmatrix}^T \\ D_T &= \begin{bmatrix} 0 & \sin(\alpha_0)/g \end{bmatrix}^T\end{aligned}\quad (7.2.6)$$

The aircraft dynamics and normal FBW system can be combined into a single system with states and outputs:

$$\begin{aligned}\mathbf{x}_{fbw-cl} &= \begin{bmatrix} \alpha & q & u_{rr} & w_{rr} & N_{zi} & F_{s1} & F_{s2} \end{bmatrix}^T \\ \mathbf{u}_{fbw-cl} &= \begin{bmatrix} T & \delta_s & \delta_q \end{bmatrix}^T\end{aligned}\quad (7.2.7)$$

The matrices of this combined system are:

$$\begin{aligned}\dot{\mathbf{x}}_{fbw-cl} &= \begin{bmatrix} A & B_{\delta_e}C_{fbw} \\ B_{fbw}^1C_{dyn} & A_{fbw} + B_{fbw}^1D_{\delta_e}C_{fbw} \end{bmatrix} \mathbf{x}_{fbw-cl} \\ &+ \begin{bmatrix} B_T & B_{\delta_s} & \mathbf{0} \\ B_{fbw}^1D_T & B_{fbw}^1D_{\delta_s} & B_{fbw}^2 \end{bmatrix} \mathbf{u}_{fbw-cl}\end{aligned}\quad (7.2.8)$$

The position error and integrated position error states are augmented before the FBW system is controlled.

$$\begin{aligned} \mathbf{x}_{fbw-cl} &= \left[\alpha \quad q \quad u_{rr} \quad x_{rr} \quad x_{rri} \quad w_{rr} \quad z_{rr} \quad z_{rri} \quad N_{Zi} \quad F_1 \quad F_2 \right]^T \\ \mathbf{u}_{fbw-cl} &= \left[T \quad \delta_s \quad \delta_q \right]^T \end{aligned} \quad (7.2.9)$$

This system will be referred to as the normal law longitudinal model. Figure 7.5 compares the pole and zero positions of the longitudinal system and the normal law longitudinal system. The fly-by-wire system introduces another integral pole close to the origin, the integrated load

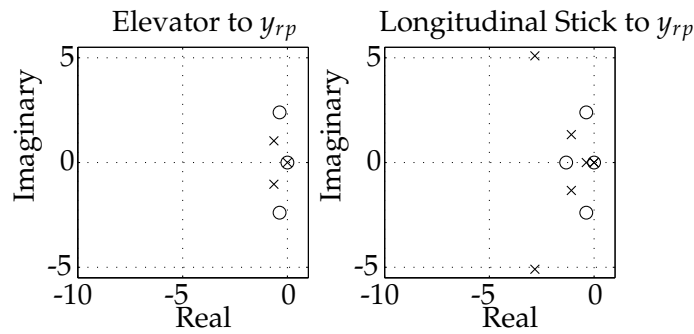


Figure 7.5: Change in longitudinal pole and zero positions when fly-by-wire system is engaged

factor error, and the filter poles. It is important to note that the RR zeros are still present and have not changed position.

7.2.2 Lateral FBW System

The lateral FBW system receives two inputs from the pilot: lateral stick, δ_p , and pedals, δ_R . The lateral stick is used to control the rolling motion of the aircraft by following a banked angle command. The pedal input commands sideslip angle. Both inputs actuate the rudder, ailerons and spoilers.

7.2.2.1 Architecture

Figure 7.6 shows the input stage for the lateral fly-by-wire. Both inputs are passed through non-linear blocks, similar to the longitudinal signals. Once again these will be removed, as shown in red. The commanded roll angle is a combination of instantaneous and integrated lateral stick deflection.

The integrated component makes sense for a FBW system flown by a pilot. The pilot can maintain a banked turn with zero stick deflection. However, it is not convenient for an automatic control system, because another state will be added to the system unnecessarily. The integrated component of ϕ_{cmd} is thus removed for the purposes of automatic control through FBW. The removed blocks are shown in red. The gain from lateral stick deflection, δ_p , to commanded roll angle, ϕ_{cmd} , is K_{δ_p} . The side-slip command is simply equal to the pedal deflection scaled by a constant factor. Figure 7.7 shows the architecture of the lateral stick FBW system.

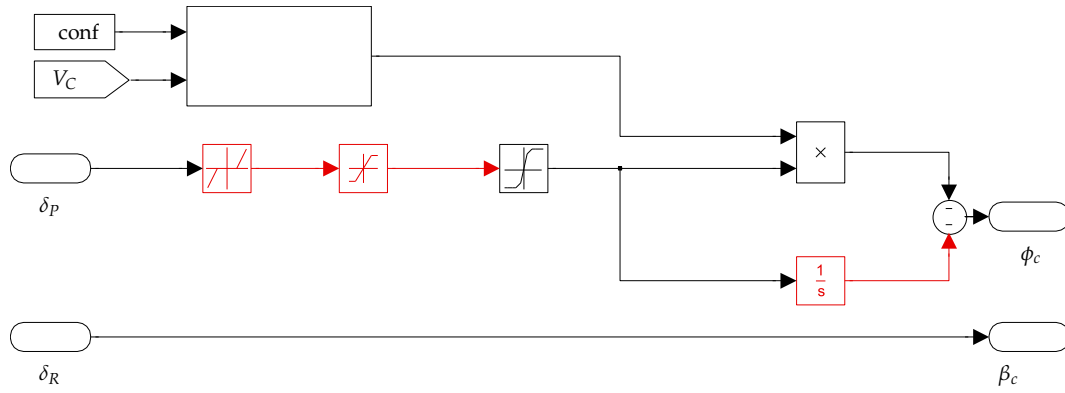


Figure 7.6: Lateral FBW system - input

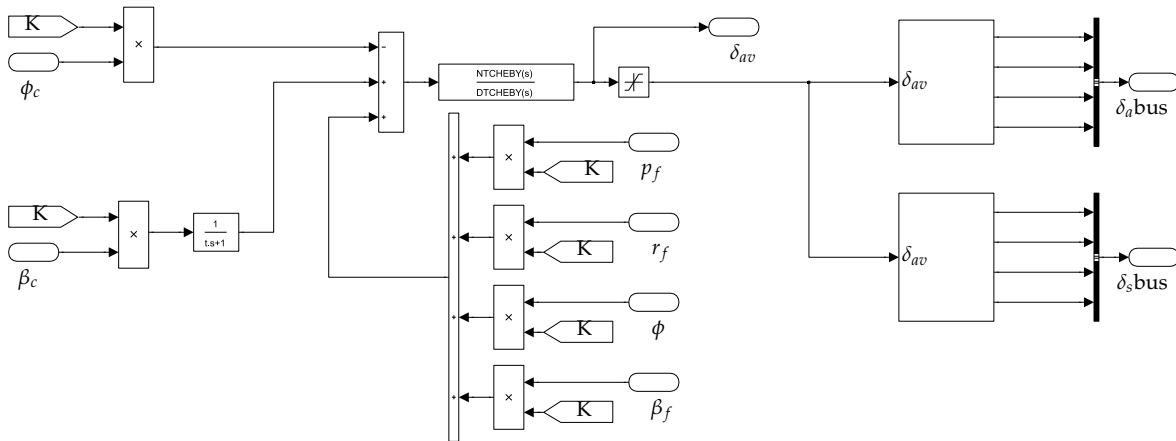


Figure 7.7: Lateral FBW system - lateral stick (roll)

The lateral stick FBW system also contains a Chebyshev filter. The output of the filter is a virtual aileron command, δ_{av} . The FBW system commands a combination of spoilers (reducing lift on one wing) and ailerons to provide a more effective rolling moment than when using only ailerons. New control derivatives are derived for the virtual aileron command, e.g. $C_{L_{\delta_{av}}}$. The virtual aileron deflection is given by:

$$\delta_{av} = K_{\phi}^a \phi - K_{\phi_c}^a \phi_c + K_{\beta}^a \beta - K_{\beta_c f}^a \beta_c f + K_p^a p_f + K_r^a r_f \quad (7.2.10)$$

where the addition of an f in the subscript indicates that the state is filtered before the gain is applied, and K_x^a refers to the feedback gain from state x to virtual aileron. All the filters are of the first order. Note that the gains applied to the bank angle and commanded bank angle are not equal.

$$K_{\phi}^a \phi - K_{\phi_c}^a \phi_c \neq K(\phi - \phi_c) \quad (7.2.11)$$

There will thus be a steady state aileron actuation when the aircraft reaches the commanded bank angle. The same is true for the side-slip gains. The gains have been calculated such that these steady state actuations maintain the commanded orientation.

Figure 7.8 shows the architecture of the pedal FBW system.

The rudder deflection is given by:

$$\delta_r = K_{\delta_r} (K_{\phi}^r \phi - K_{\phi_c f}^r \phi_c f + K_{\beta}^r \beta - K_{\beta_c}^r \beta_c + K_p^r p_f + K_r^r r_f) \quad (7.2.12)$$

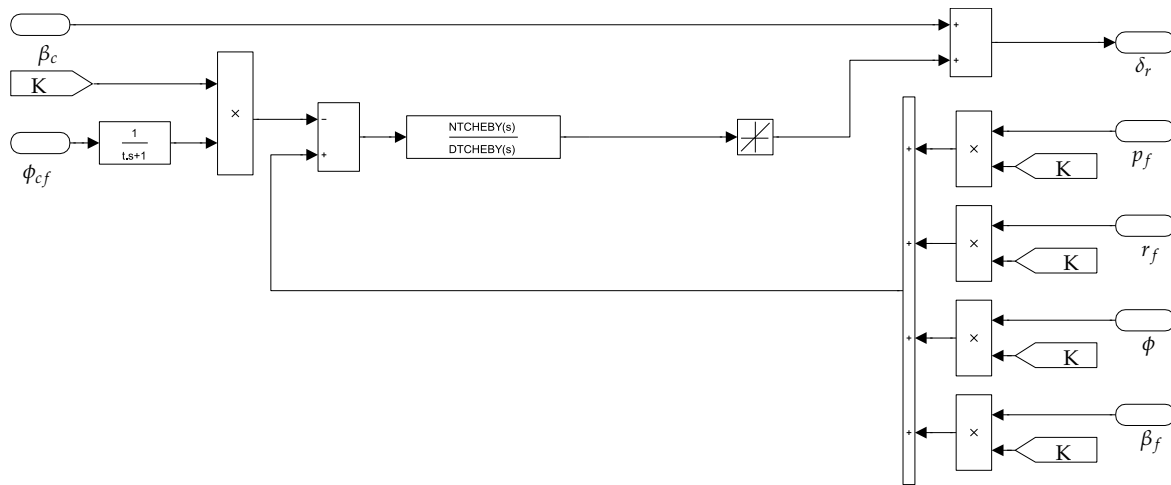


Figure 7.8: Lateral FBW system - pedal (sideslip)

where K_x^r refers to the feedback gain for state x , and K_{δ_r} is the linear gain of the final block in Figure 7.8. Equations 7.2.10 and 7.2.12 show that both the lateral stick and the pedal inputs result in actuations of the aileron and the rudder. This architecture simplifies the control of the aircraft for the pilot. For example, when the pilot commands a roll angle, the ailerons cause a small yawing moment as well. Without FBW, the pilots would have to correct this. With the FBW system, however, the rudder is also deflected slightly to cancel the yawing moment. It was found that this limits the ability of the controller to command individual actuators, and ultimately leads to slightly higher actuations of especially the rudder.

7.2.2.2 State Space

The lateral FBW system is written as a state space model with the following state, input and output vectors:

$$\begin{aligned}
 \mathbf{x}_{fbw} &= \left[\beta_f \quad p_f \quad r_f \quad \phi_{cf} \quad \beta_{cf} \quad f_{a1} \quad f_{a2} \quad f_{r1} \quad f_{r2} \right]^T \\
 \mathbf{u}_{fbw}^1 &= \left[\beta \quad p \quad r \quad \phi \right]^T \\
 \mathbf{u}_{fbw}^2 &= \left[\delta_P \quad \delta_R \right]^T \\
 \mathbf{y}_{fbw} &= \left[\delta_{av} \quad \delta_r \right]^T
 \end{aligned} \tag{7.2.13}$$

where δ_p is the lateral stick input and δ_r is the pedal input. The state space representation of the lateral FBW system is

$$\dot{\mathbf{x}}_{fbw} = \begin{bmatrix} -\frac{1}{\tau_\beta} & 0 & 0 & 0 & 0 & 0 & 0 & 0 & 0 \\ 0 & -\frac{1}{\tau_p} & 0 & 0 & 0 & 0 & 0 & 0 & 0 \\ 0 & 0 & -\frac{1}{\tau_r} & 0 & 0 & 0 & 0 & 0 & 0 \\ 0 & 0 & 0 & -\frac{1}{\tau_{\phi_c}} & 0 & 0 & 0 & 0 & 0 \\ 0 & 0 & 0 & 0 & -\frac{1}{\tau_{\beta_c}} & 0 & 0 & 0 & 0 \\ 0 & K_p^a & K_r^a & 0 & K_\beta^a & K_{f11} & K_{f12} & 0 & 0 \\ 0 & 0 & 0 & 0 & 0 & K_{f21} & K_{f22} & 0 & 0 \\ 0 & K_p^r & K_r^r & K_{\phi_c}^r & 0 & 0 & 0 & K_{f11} & K_{f12} \\ 0 & 0 & 0 & 0 & 0 & 0 & 0 & K_{f21} & K_{f22} \end{bmatrix} \mathbf{x}_{fbw} \quad (7.2.14)$$

$$+ \begin{bmatrix} \frac{1}{\tau_\beta} & 0 & 0 & 0 \\ 0 & \frac{1}{\tau_p} & 0 & 0 \\ 0 & 0 & \frac{1}{\tau_r} & 0 \\ 0 & 0 & 0 & 0 \\ 0 & 0 & 0 & 0 \\ K_\beta^a & 0 & 0 & K_{\phi_c}^a \\ 0 & 0 & 0 & 0 \\ K_\beta^r & 0 & 0 & 0 \\ 0 & 0 & 0 & 0 \end{bmatrix} \mathbf{u}_{fbw}^1 + \begin{bmatrix} 0 & 0 \\ 0 & 0 \\ \frac{K}{\tau_{\phi_c}} K_{\delta_p} & 0 \\ 0 & \frac{K_{\delta_r}}{\tau_{\beta_c}} \\ K_{\phi_c}^a K_{\delta_p} & 0 \\ 0 & 0 \\ 0 & 0 \\ 0 & 0 \\ 0 & 0 \end{bmatrix} \mathbf{u}_{fbw}^2 \quad (7.2.15)$$

$$\mathbf{y}_{fbw} = \begin{bmatrix} 0 & 0 & 0 & 0 & 0 & 0 & 1 & 0 & 0 \\ 0 & 0 & 0 & 0 & 0 & 0 & 0 & 0 & K \end{bmatrix} \mathbf{x}_{fbw} \quad (7.2.16)$$

$$+ \begin{bmatrix} 0 & 0 & 0 \\ 0 & 0 & 0 \\ 0 & 0 & 0 \end{bmatrix} \mathbf{u}_{fbw}^1 + \begin{bmatrix} 0 & 0 \\ 0 & K_{\delta_r} \end{bmatrix} \mathbf{u}_{fbw}^2 \quad (7.2.17)$$

The lateral dynamics state space model, derived in Section 2.3.3, is changed to contain an output vector containing the sideslip, roll rate, yaw rate and roll angle. The lateral dynamics state space model now has the following structure:

$$\begin{aligned} \mathbf{x}_{dyn} &= \begin{bmatrix} \beta & p & r & \phi & v_{rr} & y_{rr} & y_{rri} \end{bmatrix}^T \\ \mathbf{u}_{dyn} &= \begin{bmatrix} \delta_{av} & \delta_r \end{bmatrix}^T \\ \mathbf{y}_{dyn} &= \begin{bmatrix} \beta & p & r & \phi \end{bmatrix}^T \\ \dot{\mathbf{x}}_{dyn} &= A_{dyn} \mathbf{x}_{dyn} + B_{dyn} \mathbf{u}_{dyn} \\ \mathbf{y}_{dyn} &= C_{dyn} \mathbf{x}_{dyn} \end{aligned} \quad (7.2.18)$$

The lateral aircraft dynamics and lateral FBW system is combined into a single system with states and outputs

$$\begin{aligned} \mathbf{x}_{fbw-cl} &= \begin{bmatrix} \beta & p & r & \phi & v_{rr} & y_{rr} & y_{rri} & \beta_f & p_f & r_f & \phi_{cf} & \beta_{cf} & f_{a1} & f_{a2} & f_{r1} & f_{r2} \end{bmatrix}^T \\ \mathbf{u}_{fbw-cl} &= \begin{bmatrix} \delta_p & \delta_r \end{bmatrix}^T \end{aligned} \quad (7.2.19)$$

The matrices of the combined system are

$$\begin{aligned} \dot{\mathbf{x}}_{fbw-cl} = & \begin{bmatrix} A_{dyn} & BC_{fbw} \\ B_{fbw}^1 C_{dyn} & A_{fbw} \end{bmatrix} \mathbf{x}_{fbw-cl} \\ & + \begin{bmatrix} B_{dyn} D_{fbw} \\ B_{fbw}^2 \end{bmatrix} \mathbf{u}_{fbw-cl} \end{aligned} \quad (7.2.20)$$

This system will be referred to as the normal law lateral system. The resulting system poles and zeros are shown in Figures 7.9 and 7.10. It is clear that some of the filter poles are significantly higher in frequency than the possible final bandwidth of the control system.

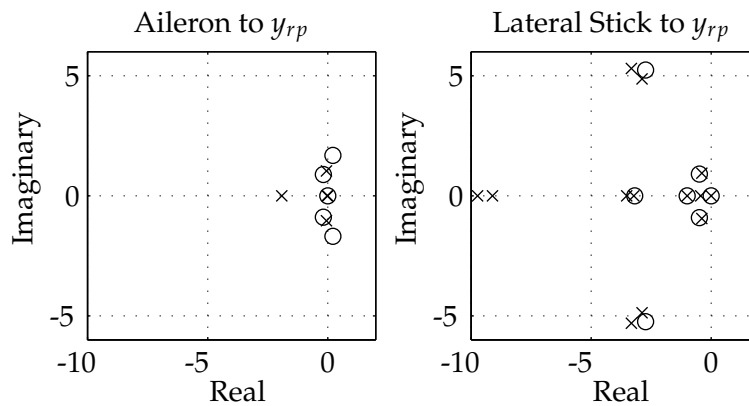


Figure 7.9: Comparison between pole and zero positions between aileron and lateral stick inputs

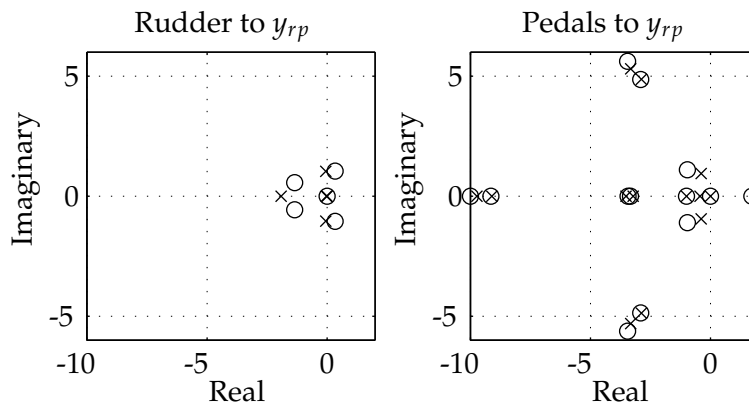


Figure 7.10: Comparison between pole and zero positions between rudder and pedal inputs

7.3 Control

This section will present the controllers designed to control the receiver aircraft using the FBW system. Controlling an aircraft through the FBW system presents some challenges which are elaborated on below.

- The Chebyshev filters applied to the command signal for each actuator limit the control system's ability to command actuations.
- Modelling the complete FBW system introduces a large number of states due to several filters and integrated states.
- The non-linearities included in the input state of the FBW system are not conducive to automatic control.
- The mixing from lateral stick and pedal inputs to aileron and rudder actuation prevent the FBW controller from actuating the rudder and aileron independently.

7.3.1 Longitudinal Normal Law Model

The addition of the FBW states has increased the number of states in the system. LQR will be used as an easy way to determine whether it is feasible to control the receiver aircraft through the FBW system. In the preceding chapters, it was shown that the high-drag configuration improved the axial performance of the control system. The high-drag configuration is also used to control the longitudinal FBW system. Since the normal and axial dynamics have not been decoupled, the creation of the drag virtual actuator is not required.

If the system is controlled using the model described in Equation 7.3.1, LQR will not limit the speed at which the spoilers and thrust are actuated. As before, the model is augmented to include the thrust and spoiler actuation as states, with the derivatives of the actuators as inputs.

$$\begin{aligned} \mathbf{x}_{fbw-cl} &= \left[\alpha \quad q \quad u_{rr} \quad x_{rr} \quad x_{rri} \quad w_{rr} \quad z_{rr} \quad z_{rri} \quad N_{zi} \quad F_{s1} \quad F_{s2} \quad T \quad \delta_s \quad \delta_{si} \quad \delta_{sf} \right]^T \\ \mathbf{u}_{fbw-cl} &= \left[\dot{T} \quad \dot{\delta}_s \quad \dot{\delta}_q \right]^T \end{aligned} \quad (7.3.1)$$

By choosing the weightings of \dot{T} and $\dot{\delta}_s$ appropriately, the designer can prevent LQR from commanding fast-changing actuation of the thrust and the spoilers. The maximum deviation method is used again to determine the state weightings.

7.3.2 Lateral Normal Law Model

As before, LQR will be used to control the longitudinal FBW system. It was found that some of the filters applied to the states in the FBW system are of such a high bandwidth that they do not significantly affect the system. Non-linear simulations were conducted with the filters both included and excluded from the controller. The filters did not seem to have an influence on the performance. The Chebyshev output filters, however, need to remain in the model. The maximum deviation method is used again to determine the state weightings.

7.4 Results

During the internship at Airbus, the FBW controller was verified on the high fidelity simulator (as presented in Section 6.8). In the high fidelity simulator, the FBW system is implemented using the real flight code. As such, the author could not easily make changes to the FBW system.

The changes discussed in Section 7.2 were implemented by an Airbus employee assisting the author. Apart from these changes, the FBW controller verification was performed as discussed in Section 6.8.

High fidelity simulations were performed at the following flight points:

Flight Level 100, 200, 300

Calibrated Airspeed 225kt, 250kt, 275kt, 300kt

Receiver Mass 150t, 175t, 200t, 225t

Receiver CG 25%, 30%, 35%

Tanker Mass 150t

Tanker and Receiver CG 25%

Figures 7.11 to 7.13 show the location of the RR in the boom envelope over the course of the simulations at the following three flight points:

Good FL = 300, $V_c = 275\text{kt}$, $m_r = 150\text{t}$, $\text{CG}_r = 30\%$

Average FL = 300, $V_c = 225\text{kt}$, $m_r = 125\text{t}$, $\text{CG}_r = 30\%$

Poor FL = 100, $V_c = 250\text{kt}$, $m_r = 225\text{t}$, $\text{CG}_r = 30\%$

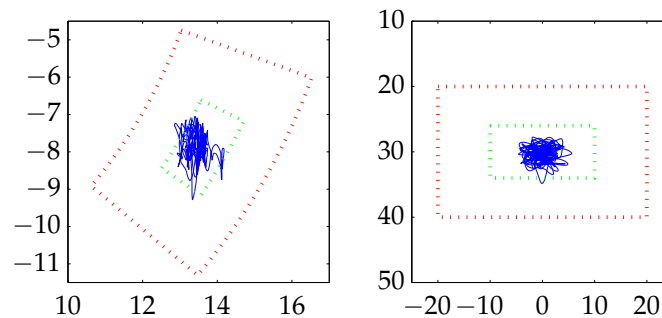


Figure 7.11: Good control system performance in medium turbulence in high-fidelity simulator

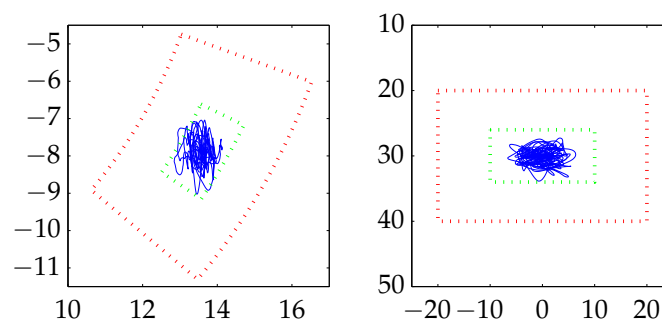


Figure 7.12: Average control system performance in medium turbulence in high-fidelity simulator

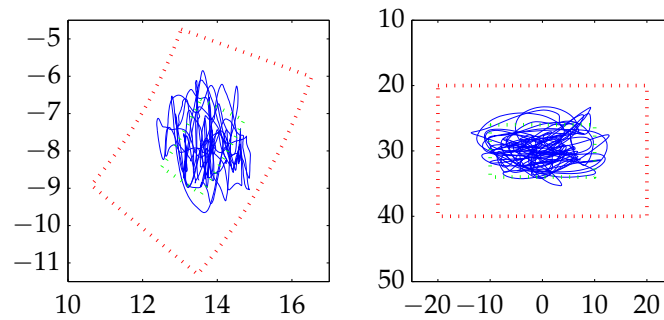


Figure 7.13: Poor control system performance in medium turbulence in high-fidelity simulator

Figures 7.14 to 7.16 show the X,Y and Z errors of the RR over the course of the simulation.

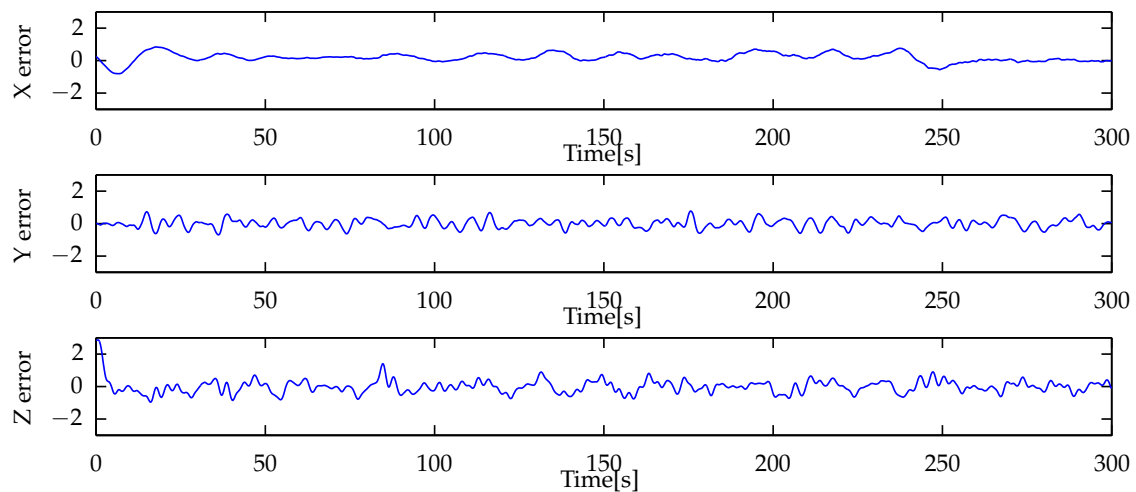


Figure 7.14: Good control system performance in medium turbulence in high-fidelity simulator

7.5 Summary

The results from high-fidelity simulations are promising, and show that controlling the receiver through the FBW system is feasible. Numerous simulations and design variations resulted in the following findings:

- To achieve the required closed loop bandwidth to enable AAR in medium turbulence, the Chebyshev filters must be included in the linear model. In the high-fidelity simulator, the filter states were not available for feedback and an estimator had to be implemented. If the filters are not included, modelling errors degrade the controller's performance.
- The non-linearities in the input stages of the FBW-system need to be removed, or compensated for, to enable automatic control. Furthermore, the integral component in the

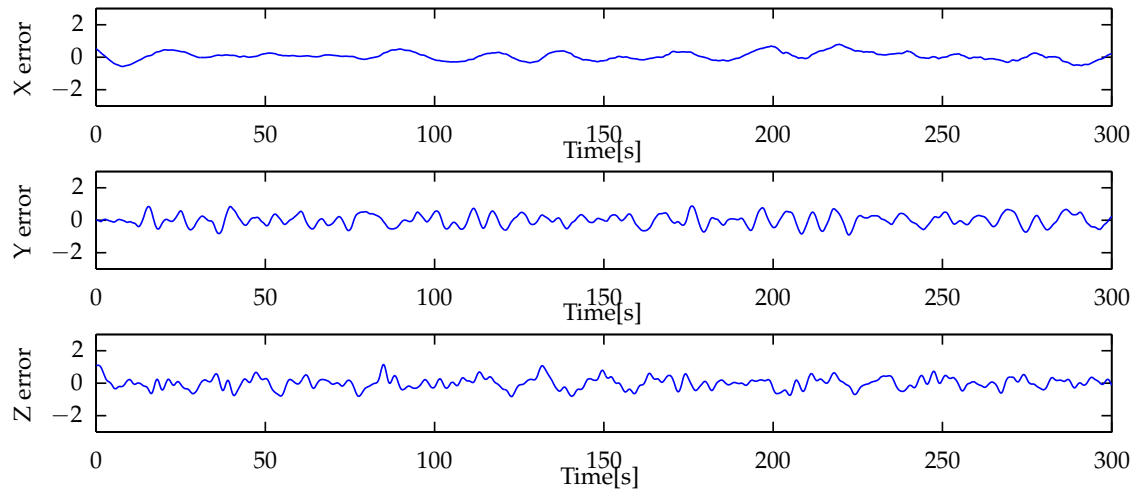


Figure 7.15: Average control system performance in medium turbulence in high-fidelity simulator

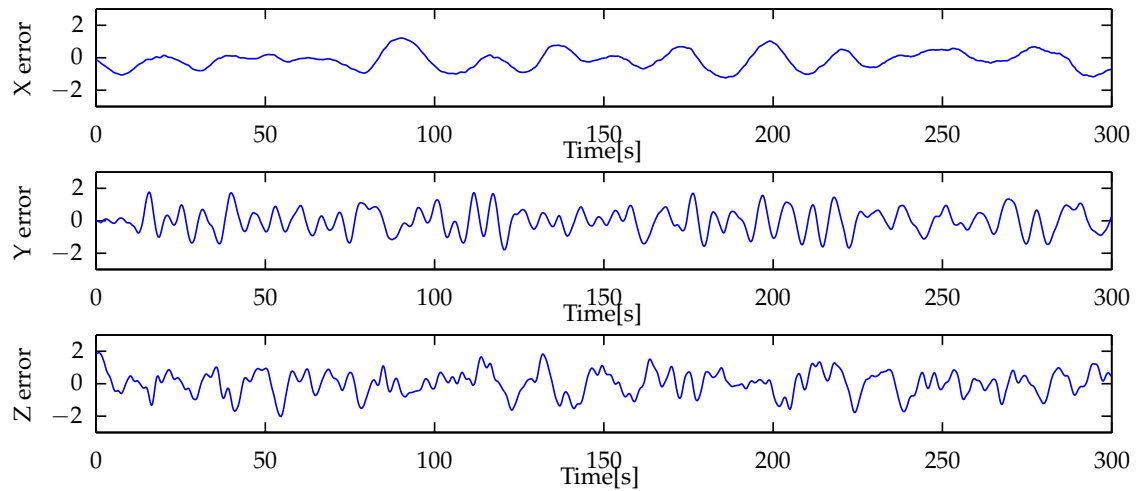


Figure 7.16: Poor control system performance in medium turbulence in high-fidelity simulator

calculation of the commanded bank angle, as shown in Figure 7.6, must be removed to enable automatic control.

- The mixing from lateral stick and pedal inputs to aileron and rudder actuation results in higher rudder actuation compared to the AAR controller. The increase can be avoided by removing the feed-forward path from lateral stick to rudder actuation, as shown in Figure 7.8, but this is not required.

In addition to this contribution, these results further verify the RR-RR controller architecture and the high-drag configuration control.

Chapter 8

Conclusion and Recommendations

8.1 Summary

A control system was presented that is capable of controlling a large receiver aircraft (Airbus A330 MRTT) through all phases of aerial refueling in light and medium turbulence. The design started with the derivation of a non-linear model describing the movement of the refueling receptacle (RR) of the receiver aircraft. This is in contrast to traditional aircraft models which describe the movement of the centre of gravity (CG). The non-linear model was linearised for straight and level flight, and decoupled into a longitudinal and lateral model. The longitudinal model was further decoupled into an axial and a normal model. The possible effects of the tanker on the receiver was investigated using the available literature. The linear models were adapted to contain the resultant downwash angle that the receiver experiences in the contact position. The model also allows the inclusion of the dynamic effect of the downwash through additional derivatives. This was performed only during analysis of the model, and not during control or verification, as accurate data were not available.

In Chapter 3, the linear models were analysed to identify the effect of the distance between the CG and the RR, primarily focusing on the normal system. It was found that the distance moves the positive and negative real zeros present in the transfer function from elevator to normal acceleration to form a complex pair in the left half-plane. The effect of the RR zeros on the closed loop response was investigated. It was found that the zeros place a limit on the attainable closed loop bandwidth of the system. Different control architectures were investigated, and it was found that including the RR dynamics in the model and feedback loop is essential for large aircraft. An equation was derived describing the approximate frequency of an aircraft's RR zeros.

Chapter 4 investigated the control of the tanker aircraft during aerial refueling. The requirements of the project stated that the flight software of the tanker must not be customized. A pilot should be able to provide the required input using existing fly-by-wire (FBW) systems and autopilot hold modes. Through numerous non-linear simulations, an optimal tanker control strategy was found.

Chapter 5 presented the control of the receiver aircraft. The control system for the normal model was designed using pole placement. A control scheme was presented which ensures similar performance across all flight points. At flight points with very low-frequency RR zeros,

a method of compensating for the RR dynamics was introduced. An axial controller that uses only engine thrust was presented, but found to be inadequate for axial control in medium turbulence. A novel axial control system was introduced which utilises a high-drag configuration and a drag virtual actuator to improve the axial response. The lateral system was controlled using optimal control (LQR).

Chapter 6 listed the results from non-linear simulations using a Matlab Simulink model provided by Airbus. The control system's performance was presented in light and medium turbulence. The effects of various parameters (velocity, downwash, tanker mass, etc.) were shown. The control system's performance in the approach, toboggan and racetrack trajectories was also shown. Lastly, selected results were presented from simulations performed using a high-fidelity simulator at Airbus's headquarters.

Chapter 7 presented a simplified version of the Airbus A330 MRTT's fly-by-wire system. The system was linearised and augmented to the linear longitudinal and lateral dynamics. Some changes were made to the FBW system to make it more suited to automatic control. Optimal control was used to control the longitudinal and lateral models. High-fidelity simulation results were presented as verification of the FBW control system.

8.2 Contributions to the Field

To the best of the author's knowledge, this study has made the following contributions to the field of automatic control of aircraft engaged in aerial refueling:

- Non-linear and linear aircraft models describing the movement of the refueling receptacle, not the centre of gravity.
- Showing through analysis that the RR dynamics introduce a complex pair of zeros in the left half-plane of the normal system which limits the attainable closed loop bandwidth.
- Showing through analysis that, once an aircraft becomes large enough, the RR dynamics must be taken into account in order to achieve acceptable performance.
- A journal article has been published on the modelling and control of the normal RR dynamics [25].
- Investigating the implications of trimming a large receiver aircraft in tanker downwash.
- A control strategy to control tanker aircraft during aerial refueling using the existing, certified flight software.
- A novel set of control systems which control the RR specifically.
- A novel high-drag configuration axial controller to account for the slow engine response of a large receiver aircraft.
- Adapting the control system to allow the receiver to remain connected to the tanker throughout a racetrack trajectory.
- Investigating the feasibility of controlling a large aircraft through an existing fly-by-wire system.

- Comprehensive verification of control system performance over a wide range of flight points on two different non-linear simulators.
- An evaluation of non-linear simulation results to establish the effect of various flight-point parameters on control system performance.

8.3 Suggestions for Future Work

This thesis focused on the control of the receiver aircraft. Several aspects of aerial refueling still need to be investigated before the system can be implemented in practice. These aspects are listed below.

- It was assumed in this thesis that accurate state estimates are available. The estimation of the relative position, orientation and rotation of the tanker and receiver is critical if AAR is to be achieved. The use of visual methods of estimation is being investigated [32].
- In the current system, a single set of feedback gains was used throughout the simulation. In reality, some flight-point parameters will change over time. The receiver's and tanker's mass will change as fuel is transferred. The flight level will also change over the course of the toboggan trajectory. These changes will occur slowly, and gain scheduling can be implemented to account for the changes. Gain scheduling can also be used during banked-turn flight to use feedback gains that are calculated using a model linearised for banked flight.
- While the interaction between the tanker and receiver was addressed in this thesis, much more work is required. An in-depth aerodynamic analysis needs to be performed for the specific combination of aircraft used in aerial refueling.
- In this thesis, the flight software of the tanker was not changed. However, an AAR-specific controller could be designed for the tanker. The same principles that were applied to the RR controller could be applied here. The tanker's controller could be designed to control the position of the nominal boom tip, not its CG. While the values for l_x and l_z will change, much of the receiver's controller design will still apply.
- Implementing cooperative control, where the tanker and receiver are both equipped with AAR-specific controllers, would be a very interesting problem and could greatly improve the system's performance.

Appendices

Appendix A

Model Derivation

A.1 Non-linear Equations

This chapter presents a brief overview of the linearisation of the non-linear dynamic equations of an aircraft. The non-linear equations are taken from [34]:

$$\dot{V} = \frac{T}{m}C_\alpha C_\beta - D + g_1 \quad (\text{A.1.1})$$

$$\dot{\beta} = -\frac{T}{mV_T}C_\alpha S_\beta - \frac{S}{mV_T} + mg_2 - (RC_\alpha - PS_\alpha) \quad (\text{A.1.2})$$

$$\dot{\alpha} = -\frac{T}{mV} \frac{S_\alpha}{C_\beta} - \frac{L}{mVC_\beta} + \frac{g_3}{VC_\beta} + \frac{Q \cos \beta - PS_\alpha - RS_\alpha}{C_\beta} \quad (\text{A.1.3})$$

$$\dot{P} = (c_1R + c_2P)Q + c_3\bar{L} + c_4N \quad (\text{A.1.4})$$

$$\dot{Q} = c_5PR - c_6(P^2 - R^2) + c_7M \quad (\text{A.1.5})$$

$$\dot{R} = (c_8P - c_2R)Q + c_4L + c_9N \quad (\text{A.1.6})$$

$$\dot{\phi} = P + \tan \theta(QS_\phi + RC_\phi) \quad (\text{A.1.7})$$

$$\dot{\theta} = QC_\phi - RS_\phi \quad (\text{A.1.8})$$

$$\dot{\psi} = (QS_\phi + RC_\phi)/C_\theta \quad (\text{A.1.9})$$

with g_1 to g_2 being the components of the gravity vector in the aerodynamic axes,

$$g_1 = C_\alpha S_\beta S_\theta + C_\beta S_\phi C_\theta - S_\alpha S_\beta C_\phi C_\theta \quad (\text{A.1.10})$$

$$g_2 = C_\alpha S_\beta S_\theta + C_\beta S_\phi C_\theta - S_\alpha S_\beta C_\phi C_\theta \quad (\text{A.1.11})$$

$$g_3 = S_\alpha S_\theta \quad (\text{A.1.12})$$

$$(\text{A.1.13})$$

and c_1 to c_9 being moment of inertia terms

$$c_1 = \frac{(I_{yy} - I_{zz})I_{zz} - I_{xz}^2}{I_{xx}I_{zz} - I_{xz}^2} \quad (\text{A.1.14})$$

$$c_3 = \frac{I_{zz}}{I_{xx}I_{zz} - I_{xz}^2} \quad (\text{A.1.15})$$

$$c_4 = \frac{I_{xz}}{I_{xx}I_{zz} - I_{xz}^2} \quad (\text{A.1.16})$$

$$c_9 = \frac{I_{xx}}{I_{xx}I_{zz} - I_{xz}^2} \quad (\text{A.1.17})$$

$$(\text{A.1.18})$$

The set of equations above can be written as

$$\dot{\mathbf{X}} = \mathbf{f}(\mathbf{X}, \mathbf{U}) \quad (\text{A.1.19})$$

where $\mathbf{X} = [V \ \beta \ \alpha \ P \ Q \ R \ \phi \ \theta \ \psi]^T$ is the state vector and $\mathbf{U} = [T \ \delta_e \ \delta_s \ \delta_a \ \delta_r]^T$ is the input vector. $\mathbf{f}(\mathbf{X}, \mathbf{U})$ is a row vector containing the non-linear functions above.

$$\dot{\mathbf{X}} = \mathbf{f}(\mathbf{X}, \mathbf{U}) = \begin{bmatrix} f_V(\mathbf{X}, \mathbf{U}) \\ f_\beta(\mathbf{X}, \mathbf{U}) \\ \dots \\ f_\psi(\mathbf{X}, \mathbf{U}) \end{bmatrix} \quad (\text{A.1.20})$$

The nabla operator is used to simplify the derivation of the linear equation. $\nabla_X Y$ is a row vector of partial derivatives of Y with respect to each entry in \mathbf{X} . The first-order Taylor series expansion of $f_\alpha(\mathbf{X}, \mathbf{U})$ can be written as

$$\begin{aligned} \dot{\alpha} &= f_{\dot{\alpha}}(\mathbf{X}_0, \mathbf{U}_0) + (\nabla_X f_{\dot{\alpha}}) \partial \mathbf{X} \\ &= 0 + \begin{bmatrix} \frac{\partial f_{\dot{\alpha}}}{\partial V} & \frac{\partial f_{\dot{\alpha}}}{\partial \beta} & \dots \end{bmatrix} \begin{bmatrix} \partial V \\ \partial \beta \\ \dots \end{bmatrix} \end{aligned} \quad (\text{A.1.21})$$

where \mathbf{X}_0 and \mathbf{U}_0 are the steady state state and input vectors respectively. Note that the nabla operator applied to a variable in the state vector, e.g. $\nabla_X V$, is simply a row vector with 1 at the entry that corresponds to the position of V in the state vector. The complete system can thus be written as

$$\dot{\mathbf{x}} = A\mathbf{x} + B\mathbf{u} \quad (\text{A.1.22})$$

$$\dot{\mathbf{x}} = \begin{bmatrix} \nabla_X f_V \\ \nabla_X f_\beta \\ \nabla_X f_{\dot{\alpha}} \\ \dots \end{bmatrix} \mathbf{x} + \begin{bmatrix} \nabla_U f_V \\ \nabla_U f_\beta \\ \nabla_U f_{\dot{\alpha}} \\ \dots \end{bmatrix} \mathbf{u} \quad (\text{A.1.23})$$

A.2 Aerodynamic Forces

The expansions of the partial derivatives of the aerodynamic forces are shown below. The dimensional derivatives used are defined in an upcoming section. No information on the effect

of $\dot{\alpha}$ was available. As such, no derivatives with regard to $\dot{\alpha}$ are included in the model.

$$\nabla_X L = -Z_v \nabla_X V - Z_\alpha \nabla_X \alpha - Z_q \nabla_X Q \quad (\text{A.2.1})$$

$$\nabla_U L = -Z_{\delta_e} \nabla_U \delta_e - Z_{\delta_s} \nabla_U \delta_s \quad (\text{A.2.2})$$

$$\nabla_X S = -C_\beta \nabla_X \beta - C_P \nabla_X P - C_R \nabla_X R \quad (\text{A.2.3})$$

$$\nabla_U S = -C_{\delta_a} \nabla_U \delta_a - C_{\delta_r} \nabla_U \delta_r \quad (\text{A.2.4})$$

$$\nabla_X D = -X_v \nabla_X V - X_\alpha \nabla_X \alpha - X_q \nabla_X Q \quad (\text{A.2.5})$$

$$\nabla_U D = -X_{\delta_e} \nabla_U \delta_e - X_{\delta_s} \nabla_U \delta_s \quad (\text{A.2.6})$$

$$\nabla_X L = L_\beta \nabla_X \beta + L_P \nabla_X P + L_R \nabla_X R \quad (\text{A.2.7})$$

$$\nabla_U L = L_{\delta_a} \nabla_U \delta_a + L_{\delta_r} \nabla_U \delta_r \quad (\text{A.2.8})$$

$$\nabla_X M = M_v \nabla_X V + M_\alpha \nabla_X \alpha + M_q \nabla_X Q \quad (\text{A.2.9})$$

$$\nabla_U M = M_{\delta_e} \nabla_U \delta_e + M_{\delta_s} \nabla_U \delta_s \quad (\text{A.2.10})$$

$$\nabla_X N = N_\beta \nabla_X \beta + N_P \nabla_X P + N_R \nabla_X R \quad (\text{A.2.11})$$

$$\nabla_U N = N_{\delta_a} \nabla_U \delta_a + N_{\delta_r} \nabla_U \delta_r \quad (\text{A.2.12})$$

A.3 Longitudinal Model

The nabla operator is applied to each of the differential equations.

$$\begin{aligned} \nabla_X f_{\dot{V}} &= -\frac{T}{m} S_\alpha C_\beta (\nabla_X \alpha) - (\nabla_X D) \\ &\quad + g(S_\alpha C_\beta S_\theta + C_\alpha C_\beta C_\phi C_\theta) (\nabla_X \alpha) \\ &\quad + (-C_\alpha C_\beta C_\theta - S_\beta S_\phi S_\theta - S_\alpha S_\beta C_\phi S_\theta) (\nabla_X \theta) \end{aligned} \quad (\text{A.3.1})$$

$$\begin{aligned} \nabla_X f_{\dot{\alpha}} &= \frac{T}{mV} \frac{C_\alpha}{C_\beta} (\nabla_X L) - \frac{1}{mVC_\beta} (\nabla_X L) \\ &\quad - \frac{g}{VC_\beta} (C_\alpha C_\theta - S_\alpha C_\phi C_\theta) (\nabla_X \alpha) \\ &\quad + \frac{g}{VC_\beta} (S_\alpha C_\theta - C_\alpha C_\phi S_\theta) (\nabla_X \theta) \\ &\quad + 1(\nabla_X Q) - R \frac{C_\alpha}{C_\beta} (\nabla_X \alpha) \end{aligned} \quad (\text{A.3.2})$$

$$\nabla_X f_{\dot{Q}} = \frac{1}{I_{yy}} \nabla_X M \quad (\text{A.3.3})$$

A.3.1 Straight and Level Flight

The linear longitudinal equations are simplified by substituting the steady state value for wings level flight. The aerodynamic terms are expanded using the definitions given in the previous

section.

$$\nabla_X f_{\dot{V}} = \frac{X_v}{m} (\nabla_X V) + \frac{X_\alpha - TS_\alpha}{m} (\nabla_X \alpha) - gC_{\theta-\alpha} (\nabla_X \gamma) \quad (\text{A.3.4})$$

$$\begin{aligned} \nabla_X f_{\dot{\alpha}} &= \frac{Z_v}{mV} (\nabla_X V) + \frac{Z_\alpha - TC_\alpha}{mV} (\nabla_X \alpha) \\ &\quad + \left(1 + \frac{Z_q}{mV}\right) (\nabla_X Q) - \frac{gS_{\theta-\alpha}}{V} (\nabla_X \gamma) \end{aligned} \quad (\text{A.3.5})$$

$$\nabla_X f_{\dot{Q}} = \frac{M_v}{I_{yy}} (\nabla_X V) + \frac{M_q}{I_{yy}} (\nabla_X Q) \quad (\text{A.3.6})$$

$$\nabla_U f_{\dot{V}} = \frac{C_\alpha}{m} (\nabla_U T) + \frac{X_{\delta_e}}{m} (\nabla_U \delta_e) + \frac{X_{\delta_s}}{m} (\nabla_U \delta_s) \quad (\text{A.3.7})$$

$$\nabla_U f_{\dot{\alpha}} = -\frac{S_\alpha}{mV} (\nabla_U T) + \frac{Z_{\delta_e}}{mV} (\nabla_X \delta_e) + \frac{Z_{\delta_s}}{mV} (\nabla_X \delta_s) \quad (\text{A.3.8})$$

$$\nabla_U f_{\dot{Q}} = \frac{M_{\delta_e}}{I_{yy}} (\nabla_X \delta_e) + \frac{M_{\delta_s}}{I_{yy}} (\nabla_X \delta_s) \quad (\text{A.3.9})$$

A.4 Lateral Model

The nabla operator is applied to each of the differential equations.

$$\begin{aligned} \nabla_X f_{\dot{\beta}} &= \left[C_\alpha C_\beta \frac{-F_T}{mV_T} - \frac{S_\beta}{mV_T} + g(C_\alpha S_\beta S_\theta + C_\beta S_\phi C_\theta - S_\alpha S_\beta C_\phi C_\theta) \right] \nabla_X B \\ &\quad + \left[S_\alpha - \frac{S_P}{mV_T} \right] \nabla_X P \\ &\quad + \left[-C_\alpha - \frac{S_R}{mV_T} \right] \nabla_X R \\ &\quad + \frac{g}{V_T} [C_\beta C_\phi C_\theta + S_\alpha S_\beta S_\phi C_\theta] \nabla_X \phi \end{aligned} \quad (\text{A.4.1})$$

$$\begin{aligned} \nabla_U f_{\dot{\beta}} &= \left[\frac{-S_{\delta_a}}{mV_T} \right] \nabla_U \delta_a \\ &\quad + \left[\frac{-S_{\delta_r}}{mV_T} \right] \nabla_U \delta_r \end{aligned} \quad (\text{A.4.2})$$

$$\begin{aligned} \nabla_X f_{\dot{P}} &= [c_3 L_\beta + c_4 N_\beta] \nabla_X B \\ &\quad + [c_2 Q + c_3 L_P + c_4 N_P] \nabla_X P \\ &\quad + [c_1 Q + c_3 L_R + c_4 N_R] \nabla_X R \end{aligned} \quad (\text{A.4.3})$$

$$\begin{aligned} \nabla_U f_{\dot{P}} &= [c_3 L_{\delta_a} + c_4 N_{\delta_a}] \nabla_U \delta_a \\ &\quad + [c_3 L_{\delta_r} + c_4 N_{\delta_r}] \nabla_U \delta_r \end{aligned} \quad (\text{A.4.4})$$

$$\begin{aligned} \nabla_X f_{\dot{R}} &= [c_4 L_\beta + c_9 N_\beta] \nabla_X B \\ &\quad + [c_8 Q + c_4 L_P + c_9 N_P] \nabla_X P \\ &\quad + [-c_2 Q + c_4 L_R + c_9 N_R] \nabla_X R \end{aligned} \quad (\text{A.4.5})$$

$$\begin{aligned} \nabla_U f_{\dot{R}} &= [c_4 L_{\delta_a} + c_9 N_{\delta_a}] \nabla_U \delta_a \\ &\quad + [c_4 L_{\delta_r} + c_9 N_{\delta_r}] \nabla_U \delta_r \end{aligned} \quad (\text{A.4.6})$$

$$\begin{aligned}\nabla_X f_{\dot{\phi}} &= [1] \nabla_X P \\ &+ [\tan(\theta)C_{\phi}] \nabla_X R\end{aligned}\tag{A.4.7}$$

$$\nabla_U f_{\dot{\phi}} = 0\tag{A.4.8}$$

A.5 Aerodynamic Derivatives

To populate the linear equations derived in the previous section, the aerodynamic derivatives are required. In practical applications, the aerodynamics derivatives would be determined by flight and wind tunnel tests. However, the Matlab Simulink model (as described in Appendix C.1) was the only information available to the author. Consequently, the aerodynamic derivatives were extracted from the Simulink Model. In the model, the aerodynamic coefficients are calculated by a compiled S-function of which the source was not available. Separate S-Functions are used for the longitudinal and lateral coefficients:

$$C_D = f_D(\mathbf{x})\tag{A.5.1}$$

$$C_L = f_L(\mathbf{x})\tag{A.5.2}$$

$$C_S = f_S(\mathbf{x})\tag{A.5.3}$$

$$C_{\bar{L}} = f_{\bar{L}}(\mathbf{x})\tag{A.5.4}$$

$$C_M = f_M(\mathbf{x})\tag{A.5.5}$$

$$C_N = f_N(\mathbf{x})\tag{A.5.6}$$

$$\mathbf{x} = \left[\text{Mach} \quad \alpha \quad \beta \quad p \quad q \quad r \dots \right]\tag{A.5.7}$$

Each derivative was calculated in turn by perturbing a single variable around its steady state value. For example,

$$\frac{\partial C_L}{\partial \alpha} = \frac{f_D(\mathbf{x}_0) + \Delta \mathbf{x} - f_D(\mathbf{x}_0 - \Delta \mathbf{x})}{2\Delta \alpha}\tag{A.5.8}$$

$$\mathbf{x} = \left[0 \quad \Delta \alpha \quad 0 \quad 0 \quad 0 \quad 0 \dots \right]\tag{A.5.9}$$

Different perturbation values were chosen for each variable. The equations below show how the non-dimensional derivatives (e.g. $C_{L_{\alpha}}$) and dimensional derivatives (e.g. Z_{α}) were calculated.

$$\begin{aligned}
X_V &= -\frac{qS}{mV_e}(2C_{D_e} + C_{D_v}) & C_{D_v} &= V_e \frac{\partial C_D}{\partial V} \\
X_\alpha &= -\frac{qS}{m}(C_{D_\alpha}) & C_{D_\alpha} &= \frac{\partial C_D}{\partial \alpha} \\
Z_V &= -\frac{qS}{mV_e}(2C_{L_e} + C_{L_v}) & C_{L_v} &= V_e \frac{\partial C_L}{\partial V} \\
Z_\alpha &= -\frac{qS}{m}(C_{L_\alpha}) & C_{L_\alpha} &= \frac{\partial C_L}{\partial \alpha} \\
Z_q &= -\frac{qS}{m} \frac{c}{2V_e}(C_{L_q}) & C_{L_q} &= \frac{2V_e}{c} \frac{\partial C_L}{\partial q} \\
M_V &= -\frac{qSc}{V_e I_{yy}}(C_{M_e} + C_{M_v}) & C_{M_v} &= V_e \frac{\partial C_M}{\partial V} \\
M_\alpha &= -\frac{qSc}{I_{yy}}(C_{M_\alpha}) & C_{M_\alpha} &= \frac{\partial C_M}{\partial \alpha} \\
M_q &= -\frac{qSc}{I_{yy}} \frac{c}{2V_e}(C_{M_q}) & C_{M_q} &= \frac{2V_e}{c} \frac{\partial C_M}{\partial q}
\end{aligned}$$

$$\begin{aligned}
X_{\delta_e} &= -\frac{qS}{m}(C_{D_{\delta_e}}) & C_{D_{\delta_e}} &= \frac{\partial C_D}{\partial \delta_e} \\
X_{\delta_{sp}} &= -\frac{qS}{m}(C_{D_{\delta_{sp}}}) & C_{D_{\delta_{sp}}} &= \frac{\partial C_D}{\partial \delta_{sp}} \\
X_{\delta_t} &= \frac{1}{m} \frac{\partial F_T}{\partial \delta_r} \\
Z_{\delta_e} &= -\frac{qS}{m}(C_{L_{\delta_e}}) & C_{D_{\delta_e}} &= \frac{\partial C_L}{\partial \delta_e} \\
Z_{\delta_{sp}} &= -\frac{qS}{m}(C_{L_{\delta_{sp}}}) & C_{D_{\delta_{sp}}} &= \frac{\partial C_L}{\partial \delta_{sp}} \\
M_{\delta_e} &= -\frac{qS}{m}(C_{M_{\delta_e}}) & C_{M_{\delta_e}} &= \frac{\partial C_M}{\partial \delta_e} \\
M_{\delta_{sp}} &= -\frac{qS}{m}(C_{M_{\delta_{sp}}}) & C_{M_{\delta_{sp}}} &= \frac{\partial C_M}{\partial \delta_{sp}}
\end{aligned}$$

A.6 Model Verification

Throughout the development of the AAR system, models were checked and verified whenever possible. At the start of the project, actuator step responses were simulated and sent to Airbus for verification. Later, during the internship, the results from the high-fidelity simulator were compared to those from the Matlab Simulink model.

The linear receptacle models were verified against the Simulink simulation. Doublet inputs were used to compare the linear and non-linear models. The verification process was repeated for the linear FBW models. During the internship at Airbus, the author has access to Airbus's internal tool for generating linear models. These linear models were also used to verify the linear receptacle models.

Appendix B

Axes System Transformations

B.1 Body Axes

The orientation of the aircraft body relative to the inertial axes is described using the Euler 3-2-1 angles: roll, pitch and yaw.

$$C_{b/i} = C_{\phi,\theta,\psi} = \begin{bmatrix} C_\theta C_\psi & C_\theta S_\psi & -S_\theta \\ -C_\phi S_\psi + S_\phi S_\theta C_\psi & C_\phi C_\psi + S_\phi S_\theta S_\psi & S_\phi C_\theta \\ S_\phi S_\psi + C_\phi S_\theta C_\psi & -S_\phi C_\psi + C_\phi S_\theta S_\psi & C_\phi C_\theta \end{bmatrix} \quad (\text{B.1.1})$$

B.1.1 Aerodynamic Axes & Error Axes

The orientation of the aerodynamic axes is described in two ways. The angle of attack, α , and sideslip angle, β , describe the direction of the velocity vector relative to the aircraft's body.

$$C_{w/b} = C_{0,\beta,-\alpha} = \begin{bmatrix} C_\alpha C_\beta & S_\beta & S_\alpha C_\beta \\ -C_\alpha S_\beta & C_\beta & -S_\alpha S_\beta \\ -S_\alpha & 0 & C_\alpha \end{bmatrix} \quad (\text{B.1.2})$$

The two direction cosine matrices (DCM) defined above can be combined to provide a DCM from the inertial to aerodynamic axes. To limit the number of terms in the matrix, some assumptions are made. This DCM will only be used to include the effect of gravity, so only the third column of the DCM is required. The other columns will not be shown. Furthermore, the angle of sideslip is assumed to be zero, as this is the case for all the linear models.

$$\begin{aligned} C_{w/i} = C_{w/b} C_{b/i} &= \begin{bmatrix} C_\alpha C_\beta & S_\beta & S_\alpha C_\beta \\ -C_\alpha S_\beta & C_\beta & -S_\alpha S_\beta \\ -S_\alpha & 0 & C_\alpha \end{bmatrix} \begin{bmatrix} * & * & -S_\theta \\ * & * & S_\phi C_\theta \\ * & * & C_\phi C_\theta \end{bmatrix} \\ &= \begin{bmatrix} * & * & -C_\alpha C_\beta S_\theta + S_\beta S_\phi C_\theta + S_\alpha C_\beta C_\phi C_\theta \\ * & * & C_\alpha S_\beta S_\theta + C_\beta S_\phi C_\theta - S_\alpha S_\beta C_\phi C_\theta \\ * & * & S_\alpha S_\theta + C_\alpha C_\phi C_\theta \end{bmatrix} \end{aligned} \quad (\text{B.1.3})$$

Appendix C

Simulation Setup

Throughout this thesis, a non-linear simulation was used to verify the performance of control systems. At the start of this project, Airbus provided a Matlab Simulink model of the Airbus A330 MRTT. This model expanded to create the full aerial refueling simulation. This appendix will give a brief overview of the non-linear aerial refueling simulation environment.

C.1 Airbus A330 MRTT Model

The aircraft is simulated in a fixed time step (0.01s steps) simulation. The various components of the simulation will now be discussed.

C.1.1 Initialisation Scripts

Several Matlab scripts were used to initialize the simulation. The scripts perform the following tasks:

1. Define the following aircraft and flight-point parameters: mass, calibrated airspeed, flight level, CG location.
2. Define the FBW settings, stick inputs and hold-mode settings. These are defined over time and can thus change over the course of the simulation.
3. Calculate other quantities using the given parameters: moments of inertia, Mach number, etc.
4. Trim the aircraft using an iterative solver to determine trim values for angle of attack, actuator position, etc.
5. Calculate initial values for all integrators (including 6DOF) and filters in the simulation. Retrieve FBW feedback gains from lookup tables.

After these scripts have been executed, the Simulink model can be run. These scripts were expanded over the course of the project to include new functionalities:

- Trimming the aircraft in downwash

- Trimming the aircraft for a constant sink rate to perform the toboggan trajectory
- Trimming the aircraft in the high-drag configuration
- Providing the required input for the tanker to fly the racetrack trajectory
- Ability to offset receiver in order to start simulation in the contact or observation position

C.1.2 Aerodynamic Calculations

The aerodynamics block uses two Matlab S-Functions to calculate the aerodynamic coefficients. The inputs are: Mach number, angle of attack, angle of sideslip, aircraft rates and actuator positions. The outputs are aerodynamic force coefficients in the aerodynamic axes, and moment coefficients in the body axes.

C.1.3 Aircraft Kinematics

The kinematics block contains a six degree of freedom block tracks the position, rotation and orientation of the aircraft. The aerodynamic coefficients are converted to forces and moments, and transformed to the body axes. The aerodynamic forces and moments are combined with forces and moments provided by the engines and gravity. The aircraft's orientation is stored as quaternions, but converted to Euler angles for use elsewhere in the simulation.

C.1.4 Sensor Model

The model contains a very simplistic sensor model. The values from the kinematics block are filtered by a first-order filter.

C.1.5 Actuator Model

Each actuator is modelled as its individual control surfaces, e.g. the spoilers are modelled as eight moving surfaces. For each control surface, the commanded value is passed through a first-order filter, saturation and a slew-rate limit. The filter and saturation values differ for each control surface.

The original simulation contained a very simplistic engine model consisting of a slow first-order filter. This was replaced by the non-linear engine model described in Section 2.6.

C.1.6 Fly-by-wire System

The fly-by-wire system described in Section 7.2 is implemented as a Simulink block diagram receiving inputs from the sensor model and providing input to the actuator model.

C.1.7 Hold Modes

The hold modes are implemented as Matlab S-Functions receiving inputs from the sensor model and providing input to the fly-by-wire model.

C.2 Aerial Refueling Simulation

The aerial refueling simulation used the A330 MRTT model to simulate both the tanker and the receiver aircraft. The following components were added to the model.

C.2.1 Control Scripts

The modelling and control discussed throughout this thesis were implemented in the control scripts. The scripts used the trim information to query the aerodynamic S-functions and find the linear aerodynamic derivatives. The linear models were calculated and used to find the feedback gains.

C.2.2 AAR System

The AAR system was added to the Simulink model used to simulate the receiver. The system loads recorded tanker data from file to calculate the relative position and velocity of the tanker and receiver. The boom and error calculations detailed in Section 1.6.1 were implemented in this system. A variable delay was applied to the error signals to enable robustness testing.

The turbulence data (recorded during the tanker simulation) was delayed before being applied to the receiver. The control system discussed in Chapter 5 was implemented as Simulink block diagrams. The AAR system block provided inputs for the actuator or the FBW system.

C.2.3 Simulation Process

The following process was followed:

1. Parameters are entered to define a list of flight points where refueling will be simulated. Values are set up for the following parameters, and all combinations are simulated:
 - a) Calibrated airspeed and flight level
 - b) Tanker mass CG location
 - c) Receiver mass and CG location
 - d) Downwash angle
 - e) Turbulence level: light or medium
 - f) Trajectory: straight and level, racetrack or toboggan
 - g) Axial control scheme: thrust only or high drag
2. The initialisation scripts (as described in the previous section) are run for the tanker aircraft.
3. The tanker is simulated; several parameters (including the turbulence) are saved to a file.
4. The initialisation scripts are run for the receiver aircraft.
5. The control scripts are run to calculate the feedback gains.
6. The receiver model (with the AAR system added) is simulated.

7. The results are saved to file and analysed.

Appendix D

Unabridged Results

This appendix lists the tables and figures containing verbose non-linear simulation results that would clutter the main body of the document.

Table D.1: Boom parameters during straight and level flight in light turbulence

FL	V_c	m_r	CG _r	σ_{ℓ_b}	σ_{θ_b}	σ_{ϕ_b}	Performance
100	225	125	23%	0.17	0.89	1.80	Poor
100	225	125	30%	0.16	0.93	1.85	Poor
100	225	125	38%	0.15	0.92	1.88	Poor
100	225	150	23%	0.17	1.26	1.94	Poor
100	225	150	30%	0.17	1.24	1.99	Poor
100	225	150	38%	0.16	1.06	2.00	Poor
100	225	175	23%	0.18	1.43	2.05	Poor
100	225	175	30%	0.17	1.43	2.09	Poor
100	225	175	38%	0.17	1.42	2.10	Poor
100	225	200	23%	0.18	1.60	2.15	Poor
100	225	200	30%	0.18	1.60	2.17	Poor
100	225	200	38%	0.18	1.61	2.18	Poor
100	225	225	23%	0.19	1.76	2.23	Poor
100	225	225	38%	0.19	1.77	2.24	Poor
100	250	125	23%	0.16	0.83	1.87	Poor
100	250	125	30%	0.16	0.83	1.84	Average
100	250	125	38%	0.16	0.84	1.80	Poor
100	250	150	23%	0.17	0.96	2.00	Poor
100	250	150	30%	0.16	1.00	1.95	Poor
100	250	150	38%	0.16	1.03	1.93	Poor
100	250	175	23%	0.18	1.34	2.10	Poor
100	250	175	30%	0.18	1.30	2.02	Poor
100	250	175	38%	0.18	1.31	2.02	Poor
100	250	200	23%	0.19	1.46	2.16	Poor
100	250	200	30%	0.19	1.45	2.05	Poor
100	250	200	38%	0.19	1.40	2.09	Poor
100	250	225	23%	0.20	1.58	2.19	Poor
100	250	225	30%	0.20	1.58	2.06	Poor
100	250	225	38%	0.20	1.59	2.15	Poor
100	275	125	23%	0.14	0.74	1.78	Average
100	275	125	30%	0.14	0.74	1.76	Average
100	275	125	38%	0.14	0.76	1.74	Average
100	275	150	23%	0.16	0.87	1.93	Poor
100	275	150	30%	0.16	0.88	1.91	Poor
100	275	150	38%	0.16	0.87	1.88	Poor
100	275	175	23%	0.15	0.89	2.05	Poor

Table D.1: Boom parameters during straight and level flight in light turbulence

FL	V_c	m_r	CG _r	σ_{ℓ_b}	σ_{θ_b}	σ_{ϕ_b}	Performance
100	275	175	30%	0.15	0.90	2.01	Poor
100	275	175	38%	0.15	0.94	1.98	Poor
100	275	200	23%	0.16	1.12	2.13	Poor
100	275	200	30%	0.15	1.06	2.09	Poor
100	275	200	38%	0.15	1.08	2.04	Poor
100	275	225	23%	0.19	1.43	2.21	Poor
100	275	225	30%	0.18	1.37	2.16	Poor
100	275	225	38%	0.17	1.23	2.09	Poor
100	300	125	23%	0.11	0.66	1.69	Average
100	300	125	30%	0.11	0.66	1.65	Average
100	300	125	38%	0.11	0.67	1.62	Average
100	300	150	23%	0.13	0.81	1.83	Average
100	300	150	30%	0.13	0.81	1.79	Average
100	300	150	38%	0.13	0.82	1.76	Average
100	300	175	23%	0.16	0.95	1.95	Poor
100	300	175	30%	0.16	0.97	1.91	Poor
100	300	175	38%	0.16	0.98	1.87	Poor
100	300	200	23%	0.16	0.99	2.04	Poor
100	300	200	30%	0.15	0.96	2.00	Poor
100	300	200	38%	0.15	0.95	1.95	Poor
100	300	225	23%	0.15	1.06	2.11	Poor
100	300	225	30%	0.14	1.02	2.06	Poor
100	300	225	38%	0.14	1.04	2.02	Poor
200	225	125	23%	0.10	0.52	1.23	Good
200	225	125	30%	0.10	0.51	1.21	Good
200	225	125	38%	0.10	0.47	1.20	Good
200	225	150	23%	0.12	0.81	1.32	Average
200	225	150	30%	0.12	0.80	1.30	Good
200	225	150	38%	0.11	0.73	1.28	Good
200	225	175	23%	0.13	0.95	1.39	Average
200	225	175	30%	0.13	0.95	1.36	Average
200	225	175	38%	0.13	0.94	1.33	Average
200	225	200	23%	0.14	1.06	1.45	Average
200	225	200	30%	0.14	1.07	1.41	Average
200	225	200	38%	0.14	1.06	1.36	Average
200	225	225	23%	0.14	1.16	1.49	Poor
200	225	225	30%	0.14	1.17	1.45	Average
200	225	225	38%	0.14	1.17	1.37	Average
200	250	125	23%	0.12	0.60	1.22	Good
200	250	125	30%	0.12	0.61	1.18	Good
200	250	125	38%	0.12	0.62	1.16	Good
200	250	150	23%	0.11	0.61	1.32	Good
200	250	150	30%	0.11	0.60	1.28	Good
200	250	150	38%	0.11	0.59	1.25	Good
200	250	175	23%	0.13	0.71	1.40	Average
200	250	175	30%	0.13	0.69	1.35	Average
200	250	175	38%	0.12	0.63	1.32	Good
200	250	200	23%	0.15	0.84	1.47	Average
200	250	200	30%	0.15	0.83	1.42	Average
200	250	200	38%	0.14	0.82	1.39	Average
200	250	225	23%	0.15	0.91	1.51	Poor
200	250	225	30%	0.15	0.91	1.46	Average
200	250	225	38%	0.15	0.91	1.43	Average
200	275	125	23%	0.08	0.46	1.12	Good
200	275	125	30%	0.08	0.46	1.10	Good
200	275	125	38%	0.07	0.46	1.07	Good
200	275	150	23%	0.09	0.55	1.21	Good
200	275	150	30%	0.09	0.56	1.19	Good

Table D.1: Boom parameters during straight and level flight in light turbulence

FL	V_c	m_r	CG _r	σ_{ℓ_b}	σ_{θ_b}	σ_{ϕ_b}	Performance
200	275	150	38%	0.09	0.57	1.16	Good
200	275	175	23%	0.10	0.65	1.29	Good
200	275	175	30%	0.09	0.65	1.26	Good
200	275	175	38%	0.09	0.61	1.23	Good
200	275	200	23%	0.11	0.79	1.35	Average
200	275	200	30%	0.10	0.75	1.32	Good
200	275	200	38%	0.09	0.69	1.29	Good
200	275	225	23%	0.12	0.84	1.41	Average
200	275	225	30%	0.12	0.84	1.38	Average
200	275	225	38%	0.12	0.83	1.34	Average
200	300	125	23%	0.07	0.39	1.11	Good
200	300	125	30%	0.07	0.39	1.10	Good
200	300	125	38%	0.07	0.40	1.09	Good
200	300	150	23%	0.08	0.48	1.20	Good
200	300	150	30%	0.08	0.48	1.19	Good
200	300	150	38%	0.08	0.49	1.18	Good
200	300	175	23%	0.09	0.56	1.28	Good
200	300	175	30%	0.09	0.56	1.27	Good
200	300	175	38%	0.09	0.57	1.25	Good
200	300	200	23%	0.10	0.74	1.35	Good
200	300	200	30%	0.10	0.71	1.33	Good
200	300	200	38%	0.10	0.68	1.31	Good
200	300	225	23%	0.11	0.86	1.41	Average
200	300	225	30%	0.11	0.86	1.39	Average
200	300	225	38%	0.10	0.79	1.36	Good
300	225	125	23%	0.09	0.55	1.29	Good
300	225	125	30%	0.08	0.55	1.25	Good
300	225	125	38%	0.08	0.52	1.22	Good
300	225	150	23%	0.12	0.66	1.38	Good
300	225	150	30%	0.12	0.66	1.35	Good
300	225	150	38%	0.12	0.65	1.31	Good
300	225	175	23%	0.13	0.76	1.44	Average
300	225	175	30%	0.13	0.76	1.40	Average
300	225	175	38%	0.13	0.76	1.37	Average
300	225	200	23%	0.14	0.84	1.48	Average
300	225	200	30%	0.14	0.84	1.44	Average
300	225	225	30%	0.15	0.90	1.48	Average
300	225	225	38%	0.15	0.90	1.44	Average
300	250	125	23%	0.15	0.46	1.26	Good
300	250	125	30%	0.15	0.47	1.25	Good
300	250	125	38%	0.15	0.48	1.25	Good
300	250	150	23%	0.17	0.59	1.35	Average
300	250	150	30%	0.17	0.56	1.33	Average
300	250	150	38%	0.17	0.56	1.33	Average
300	250	175	23%	0.19	0.85	1.42	Poor
300	250	175	30%	0.21	0.93	1.40	Poor
300	250	175	38%	0.16	0.81	1.39	Average
300	250	200	23%	0.16	0.54	1.45	Average
300	250	200	30%	0.16	0.54	1.43	Average
300	250	200	38%	0.16	0.55	1.43	Average
300	250	225	23%	0.20	0.65	1.48	Average
300	250	225	30%	0.21	0.67	1.45	Average
300	250	225	38%	0.23	0.69	1.44	Average
300	275	125	23%	0.06	0.37	1.19	Good
300	275	125	30%	0.06	0.37	1.20	Good
300	275	125	38%	0.06	0.36	1.20	Good
300	275	150	23%	0.06	0.40	1.29	Good
300	275	150	30%	0.06	0.39	1.30	Good

Table D.1: Boom parameters during straight and level flight in light turbulence

FL	V_c	m_r	CG _r	σ_{ℓ_b}	σ_{θ_b}	σ_{ϕ_b}	Performance
300	275	150	38%	0.06	0.39	1.30	Good
300	275	175	23%	0.15	0.88	1.39	Average
300	275	175	30%	0.14	0.81	1.40	Average
300	275	175	38%	0.13	0.73	1.39	Average
300	275	200	23%	1.07	2.18	1.48	Poor
300	275	200	38%	0.16	0.80	1.48	Average
300	275	225	23%	0.11	0.57	1.57	Good
300	275	225	30%	0.12	0.63	1.57	Average
300	275	225	38%	0.11	0.59	1.56	Good
300	300	125	23%	0.06	0.36	2.07	Good
300	300	125	30%	0.06	0.35	2.11	Good
300	300	125	38%	0.06	0.35	2.14	Good
300	300	150	23%	0.06	0.40	2.23	Average
300	300	150	30%	0.06	0.40	2.26	Average
300	300	150	38%	0.06	0.40	2.29	Good
300	300	175	23%	0.06	0.40	2.35	Good
300	300	175	30%	0.06	0.40	2.37	Good
300	300	175	38%	0.06	0.42	2.40	Average
300	300	200	23%	0.14	0.77	2.45	Poor
300	300	200	30%	0.13	0.72	2.46	Average
300	300	200	38%	0.12	0.65	2.48	Average
300	300	225	23%	0.49	1.43	2.53	Poor
300	300	225	30%	0.20	1.08	2.51	Poor
300	300	225	38%	0.24	1.10	2.55	Poor

Table D.2: Boom parameters during straight and level flight in medium turbulence

FL	V_c	m_r	CG _r	σ_{ℓ_b}	σ_{θ_b}	σ_{ϕ_b}	Performance
100	225	125	23%	0.52	2.09	6.04	Poor
100	225	125	30%	0.53	2.21	6.20	Poor
100	225	125	37%	-	-	-	Infeasible
100	225	150	23%	0.55	2.87	6.90	Poor
100	225	150	30%	0.53	2.78	7.03	Poor
100	225	150	37%	0.49	2.50	7.09	Poor
100	225	175	23%	0.56	3.50	7.69	Poor
100	225	175	30%	0.55	3.43	7.79	Poor
100	225	175	37%	0.52	3.21	7.83	Poor
100	225	200	23%	0.59	4.15	8.44	Poor
100	225	200	30%	0.58	4.09	8.49	Poor
100	225	200	37%	0.56	3.98	8.52	Poor
100	225	225	23%	0.65	4.88	9.14	Poor
100	225	225	30%	-	-	-	Infeasible
100	225	225	37%	-	-	-	Infeasible
100	250	125	23%	-	-	-	Infeasible
100	250	125	30%	-	-	-	Infeasible
100	250	125	37%	-	-	-	Infeasible
100	250	150	23%	0.40	2.16	6.74	Poor
100	250	150	30%	-	-	-	Infeasible
100	250	150	37%	-	-	-	Infeasible
100	250	175	23%	0.57	3.54	7.36	Poor
100	250	175	30%	0.53	3.30	7.29	Poor
100	250	175	37%	-	-	-	Infeasible
100	250	200	23%	0.67	4.45	7.95	Poor
100	250	200	30%	0.65	4.32	7.82	Poor
100	250	200	37%	0.59	3.83	7.82	Poor

Table D.2: Boom parameters during straight and level flight in medium turbulence

FL	V_c	m_r	CG _r	σ_{ℓ_b}	σ_{θ_b}	σ_{ϕ_b}	Performance
100	250	225	23%	-	-	-	Infeasible
100	250	225	30%	0.66	4.67	8.16	Poor
100	250	225	37%	0.65	4.55	8.32	Poor
100	275	125	23%	-	-	-	Infeasible
100	275	125	30%	-	-	-	Infeasible
100	275	125	37%	-	-	-	Infeasible
100	275	150	23%	-	-	-	Infeasible
100	275	150	30%	-	-	-	Infeasible
100	275	150	37%	-	-	-	Infeasible
100	275	175	23%	-	-	-	Infeasible
100	275	175	30%	-	-	-	Infeasible
100	275	175	37%	-	-	-	Infeasible
100	275	200	23%	0.55	3.45	7.65	Poor
100	275	200	30%	0.54	3.46	7.54	Poor
100	275	200	37%	-	-	-	Infeasible
100	275	225	23%	0.68	4.61	8.07	Poor
100	275	225	30%	-	-	-	Infeasible
100	275	225	37%	-	-	-	Infeasible
100	300	125	23%	-	-	-	Infeasible
100	300	125	30%	-	-	-	Infeasible
100	300	125	37%	-	-	-	Infeasible
100	300	150	23%	-	-	-	Infeasible
100	300	150	30%	-	-	-	Infeasible
100	300	150	37%	-	-	-	Infeasible
100	300	175	23%	-	-	-	Infeasible
100	300	175	30%	-	-	-	Infeasible
100	300	175	37%	-	-	-	Infeasible
100	300	200	23%	-	-	-	Infeasible
100	300	200	30%	-	-	-	Infeasible
100	300	200	37%	-	-	-	Infeasible
100	300	225	23%	-	-	-	Infeasible
100	300	225	30%	-	-	-	Infeasible
100	300	225	37%	-	-	-	Infeasible
200	225	125	23%	0.27	1.41	4.99	Average
200	225	125	30%	0.27	1.45	4.92	Average
200	225	125	37%	0.28	1.57	4.88	Average
200	225	150	23%	0.32	2.09	5.51	Average
200	225	150	30%	0.31	2.02	5.42	Average
200	225	150	37%	0.29	1.80	5.38	Average
200	225	175	23%	0.37	2.63	5.96	Poor
200	225	175	30%	0.36	2.57	5.85	Poor
200	225	175	37%	0.34	2.45	5.82	Poor
200	225	200	23%	0.42	3.12	6.36	Poor
200	225	200	30%	0.41	3.08	6.24	Poor
200	225	200	37%	0.40	2.99	6.22	Poor
200	225	225	23%	0.47	3.61	6.68	Poor
200	225	225	30%	0.46	3.58	6.59	Poor
200	225	225	37%	0.45	3.52	6.59	Poor
200	250	125	23%	-	-	-	Infeasible
200	250	125	30%	-	-	-	Infeasible
200	250	125	37%	-	-	-	Infeasible
200	250	150	23%	-	-	-	Infeasible
200	250	150	30%	-	-	-	Infeasible
200	250	150	37%	-	-	-	Infeasible
200	250	175	23%	0.34	2.00	5.94	Average
200	250	175	30%	0.33	1.96	5.80	Average
200	250	175	37%	0.31	1.85	5.69	Average
200	250	200	23%	0.39	2.41	6.37	Poor

Table D.2: Boom parameters during straight and level flight in medium turbulence

FL	V_c	m_r	CG _r	σ_{ℓ_b}	σ_{θ_b}	σ_{ϕ_b}	Performance
200	250	200	30%	0.38	2.37	6.22	Poor
200	250	200	37%	0.36	2.27	6.11	Poor
200	250	225	23%	0.44	2.79	6.66	Poor
200	250	225	30%	0.43	2.76	6.53	Poor
200	250	225	37%	0.41	2.69	6.44	Poor
200	275	125	23%	0.21	1.21	4.35	Good
200	275	125	30%	0.20	1.21	4.29	Good
200	275	125	37%	0.20	1.21	4.18	Good
200	275	150	23%	-	-	-	Infeasible
200	275	150	30%	-	-	-	Infeasible
200	275	150	37%	-	-	-	Infeasible
200	275	175	23%	0.26	1.70	5.37	Average
200	275	175	30%	0.26	1.68	5.25	Average
200	275	175	37%	-	-	-	Infeasible
200	275	200	23%	0.32	2.22	5.74	Average
200	275	200	30%	0.29	2.04	5.62	Average
200	275	200	37%	0.27	1.95	5.52	Average
200	275	225	23%	0.36	2.50	6.08	Poor
200	275	225	30%	0.35	2.47	5.97	Poor
200	275	225	37%	0.33	2.36	5.86	Average
200	300	125	23%	0.18	1.04	4.49	Good
200	300	125	30%	-	-	-	Infeasible
200	300	125	37%	0.17	1.06	4.45	Good
200	300	150	23%	-	-	-	Infeasible
200	300	150	30%	-	-	-	Infeasible
200	300	150	37%	-	-	-	Infeasible
200	300	175	23%	-	-	-	Infeasible
200	300	175	30%	-	-	-	Infeasible
200	300	175	37%	-	-	-	Infeasible
200	300	200	23%	0.26	1.76	6.12	Average
200	300	200	30%	0.26	1.80	6.07	Average
200	300	200	37%	-	-	-	Infeasible
200	300	225	23%	0.32	2.27	6.51	Poor
200	300	225	30%	0.30	2.15	6.45	Average
200	300	225	37%	0.30	2.24	6.30	Poor
300	225	125	23%	0.18	1.06	3.69	Good
300	225	125	30%	0.17	1.04	3.62	Good
300	225	125	37%	0.17	1.05	3.56	Good
300	225	150	23%	0.23	1.34	4.06	Good
300	225	150	30%	0.22	1.35	4.00	Good
300	225	150	37%	0.21	1.30	3.94	Good
300	225	175	23%	0.26	1.51	4.32	Good
300	225	175	30%	0.26	1.52	4.27	Good
300	225	175	37%	0.26	1.51	4.21	Good
300	225	200	23%	0.28	1.67	4.50	Average
300	225	200	30%	0.28	1.67	4.45	Average
300	225	200	37%	0.28	1.68	4.41	Average
300	225	225	23%	0.30	1.93	4.66	Average
300	225	225	30%	0.30	1.89	4.61	Average
300	225	225	37%	0.30	1.87	4.56	Average
300	250	125	23%	0.21	0.79	3.49	Good
300	250	125	30%	0.22	0.80	3.46	Good
300	250	125	37%	0.22	0.81	3.48	Good
300	250	150	23%	0.20	0.93	3.86	Good
300	250	150	30%	0.21	0.91	3.83	Good
300	250	150	37%	0.22	0.97	3.83	Good
300	250	175	23%	0.27	1.36	4.16	Good
300	250	175	30%	0.26	1.37	4.12	Good

Table D.2: Boom parameters during straight and level flight in medium turbulence

FL	V_c	m_r	CG _r	σ_{ℓ_b}	σ_{θ_b}	σ_{ϕ_b}	Performance
300	250	175	37%	0.22	1.26	4.12	Good
300	250	200	23%	0.36	1.28	4.37	Average
300	250	200	30%	0.36	1.31	4.34	Average
300	250	200	37%	0.35	1.30	4.33	Average
300	250	225	23%	0.38	1.34	4.52	Average
300	250	225	30%	0.38	1.34	4.49	Average
300	250	225	37%	0.39	1.32	4.48	Average
300	275	125	23%	0.16	0.73	3.45	Good
300	275	125	30%	0.16	0.73	3.55	Good
300	275	125	37%	0.16	0.72	3.49	Good
300	275	150	23%	0.13	0.99	3.83	Good
300	275	150	30%	0.13	0.93	3.94	Good
300	275	150	37%	0.13	0.88	3.88	Good
300	275	175	23%	0.21	1.25	4.24	Good
300	275	175	30%	0.20	1.24	4.33	Good
300	275	175	37%	0.19	1.20	4.26	Good
300	275	200	23%	0.32	1.47	4.58	Average
300	275	200	30%	-	-	-	Infeasible
300	275	200	37%	0.32	1.49	4.60	Average
300	275	225	23%	0.28	1.23	4.83	Good
300	275	225	30%	-	-	-	Infeasible
300	275	225	37%	-	-	-	Infeasible
300	300	125	23%	0.12	0.82	6.45	Good
300	300	125	30%	0.12	0.83	6.71	Good
300	300	125	37%	0.12	0.83	6.91	Good
300	300	150	23%	0.13	1.02	7.57	Good
300	300	150	30%	0.13	1.02	7.79	Good
300	300	150	37%	0.13	1.02	7.94	Good
300	300	175	23%	0.14	1.15	8.45	Average
300	300	175	30%	0.14	1.15	8.59	Average
300	300	175	37%	0.14	1.18	8.67	Average
300	300	200	23%	0.18	1.32	8.99	Average
300	300	200	30%	0.16	1.32	9.10	Average
300	300	200	37%	0.17	1.31	9.11	Average
300	300	225	23%	0.23	1.53	9.10	Average
300	300	225	30%	0.22	1.62	9.50	Average
300	300	225	37%	-	-	-	Infeasible

Bibliography

- [1] Airbus. Definition of an autonomous air-to-air refueling mode for the A330 MRTT during receiver's phases. (September 2006), 2007.
- [2] Airbus. Requirements for an automatic AAR function Technical Report. (0):1–16, 2008.
- [3] A W Bloy and M Kouma'a. Lateral and Directional Stability and Control in Air-to-Air Refueling. In *Proceedings of the Institution of Mechanics Engineers*, 1995.
- [4] A W Bloy, P J Lamont, H A Abu-Assaf, and K A M Ali. The Lateral Dynamic Stability and Control of a Large Receiver Aircraft During Air-To-Air Refuelling. *Aeronautical Journal*, 90:237–243, 1986.
- [5] A W Bloy and K A Lea. Directional Stability of a Large Receiver Aircraft in Air-to-Air Refueling. *Journal of Aircraft*, 32(2):453–455, 1994.
- [6] a W Bloy and V Trochalidis. The Performance and Longitudinal Stability and Control of a Large Receiver Aircraft During Air-To-Air Refueling. *Aeronautical Journal*, 93:367–378, 1989.
- [7] A W Bloy and M G West. Interference Between Tanker Wing Wake with Roll-Up and Receiver Aircraft. *Journal of Aircraft*, 31(5):1214–1216, 1994.
- [8] A W Bloy, M G West, K A Lea, and M Jouma'a. Lateral Aerodynamic Interference Between Tanker and Receiver in Air-To-Air Refueling. *Journal of Aircraft*, 30(5):705–710, 1993.
- [9] Christopher Bolkcom. CRS Report for Congress Received through the CRS Web Air Force Aerial Refueling Methods : Flying Boom versus Hose-and-Drogue. Technical report, 2006.
- [10] J. Bradley. *The Handling and Performance Trials Needed to Clear an Aircraft to Act as a Receiver during Air-to-Air Refueling.* 1984.
- [11] DoD. Flying Qualities of Piloted Aircraft. pages 1–717, 1997.
- [12] James Doebbler, Theresa Spaeth, John Valasek, Mark J. Monda, and Hanspeter Schaub. Boom and Receptacle Autonomous Air Refueling Using Visual Snake Optical Sensor. *Journal of Guidance, Control, and Dynamics*, 30(6):1753–1769, November 2007.
- [13] A Dogan and TA Lewis. *Flight Data Analysis and Simulation of Wind Effects During Aerial Refueling.* PhD thesis, 2008.

- [14] Atilla Dogan and William Blake. Modeling of Bow Wave Effect in Aerial Refueling. In *AIAA Guidance, Navigation and Control Conference and Exhibit*, August 2010.
- [15] Atilla Dogan, William Blake, and Christian Haag. Bow Wave Effect in Aerial Refueling: Computational Analysis and Modeling. *Journal of Aircraft*, 50(6):1856–1868, August 2013.
- [16] Atilla Dogan, Christopher M Elliot, Fransell Riley, and William Blake. Effects of Mass and Size on Control of Large Receiver in Aerial Refueling. In *AIAA Atmospheric Flight Mechanics Conference*, August 2009.
- [17] Atilla Dogan, Eunyoung Kim, and William Blake. Control and Simulation of Relative Motion for Aerial Refueling in Racetrack Maneuver. *Journal of Guidance, Control, and Dynamics*, 30(5):1551–1557, 2007.
- [18] Atilla Dogan, Shinya Sato, and William Blake. Flight Control and Simulation for Aerial Refueling. In *AIAA Guidance, Navigation and Control Conference and Exhibit*, 2005.
- [19] Atilla Dogan, Sriram Venkataramanan, and William Blake. Modeling of Aerodynamics Coupling Between Aircraft in Close Proximity. *Journal of Aircraft*, 42(4):941–955, 2005.
- [20] C Favre. Fly-by-wire for commercial aircraft: the Airbus experience. *International Journal of Control*, 59:139–157, 1994.
- [21] M Fravolini, a Ficola, G Campa, M Napolitano, and B Seanor. Modeling and control issues for autonomous aerial refueling for UAVs using a probe/drogue refueling system. *Aerospace Science and Technology*, 8(7):611–618, October 2004.
- [22] Abbas Emami-Naeini Gene Franklin, J.D. Powell. *Feedback Control of Dynamic Systems*. Pearson.
- [23] EH Hoganson. *A Study of the Aerodynamic Interference Effects During Aerial Refueling*. PhD thesis, Airforce Institute of Technology, 1984.
- [24] Eunyoung Kim. *Control and Simulation of Relative Motion for Aerial Refueling in Racetrack Maneuver*. PhD thesis, The University of Texas at Arlington, 2007.
- [25] S.C. Kriel, J.A.A. Engelbrecht, and T. Jones. Receptacle normal position control for automated aerial refueling. *Aerospace Science and Technology*, 29(1):296–304, August 2013.
- [26] Marco Mammarella, Giampiero Campa, M.R. Napolitano, Brad Seanor, M.L. Fravolini, and L. Pollini. GPS/MV based Aerial Refueling for UAVs. In *AIAA Guidance, Navigation and Control Conference and Exhibit*, August 2008.
- [27] C. McFarlane, T.S. Richardson, and CDC Jones. Cooperative Control During Boom Air-to-Air Refueling. In *AIAA Guidance, Navigation and Control Conference and Exhibit*, August 2007.
- [28] Joseph P Nalepka and Jacob L Hinchman. Automated Aerial Refueling: Extending the Effectiveness of Unmanned Air Vehicles. In *AIAA Guidance, Navigation and Control Conference and Exhibit*, August 2005.

- [29] JUAN C. NARVID. Tanker-Force Structure Recapitalization of the KC-135. Technical Report 32, 2004.
- [30] Wendy Okolo, Atilla Dogan, and William Blake. Determination of Sweet Spot for Trailing Aircraft in Formation Flight. In *AIAA Atmospheric Flight Mechanics Conference and Exhibit*, Portland, Oregon, August 2011.
- [31] Sanghyuk Park, John Deyst, and Jonathan P How. Performance and Lyapunov Stability of a Nonlinear Path-Following Guidance Method. *Journal of Guidance, Control, and Dynamics*, 30(6):1718–1728, 2007.
- [32] Anton Johan Runhaar. Autonomous Airborne Refueling: Relative State Estimation. Master's thesis, Stellenbosch University, 2011.
- [33] GW Ryan. Developing Aerial Refueling Simulation Models from Flight Test Data Using Alternative PID Methods. In *System Identification for Integrated Aircraft Development and flight Testing*, number May, 1998.
- [34] Brian L Stevens and Frank L Lewis. *Aircraft Control and Simulation*. Wiley, 2003.
- [35] U.S. Air Force. An air force special operations command hc-130p refuels a hh-60 pave hawk helicopter in the sky over southern louisiana. air force search and rescue crews have been searching for hurricane rita survivors. its in-flight refueling capability allows the helicopter crews to continue search and rescue missions for several hours.
- [36] U.S. Air Force photo by Staff Sgt. Jerry Morrison. An f-16 fighting falcon from the 40th flight test squadron, eglin air force base, florida, refuels from a kc-10 extender during air & space power expo '99. the expo was put on for congress to show how ready the us air force is for the next millenium., 1999.
- [37] John Valasek, Kiran Gunnam, Jennifer Kimmett, M.D. Tandale, J.L. Junkins, and Declan Hughes. Vision-based sensor and navigation system for autonomous air refueling. *Journal of Guidance, Control, and Dynamics*, 28(5):979, September 2005.
- [38] Sriram Venkataramanan and Atilla Dogan. Dynamic Effects of Trailing Vortex with Turbulence & Time-varying Inertia in Aerial Refueling. In *AIAA Atmospheric Flight Mechanics Conference and Exhibit*, 2004.
- [39] Sriram Venkataramanan, Atilla Dogan, and William Blake. Vortex Effect Modelling in Aircraft Formation Flight. In *AIAA Atmospheric Flight Mechanics Conference and Exhibit*, 2003.
- [40] Jiang Wang, Vijay V Patel, Chengyu Cao, Naira Hovakimyan, and Eugene Lavretsky. Novel L1 Adaptive Control Methodology for Aerial Refueling with Guaranteed Transient Performance. *Journal of Guidance, Control, and Dynamics*, 31(1):182–193, 2008.
- [41] Walton R. Williamson, Gregory J. Glenn, Vu T. Dang, Jason L. Speyer, Stephen M. Stecko, and John M. Takacs. Sensor Fusion Applied to Autonomous Aerial Refueling. *Journal of Guidance, Control, and Dynamics*, 32(1):262–275, January 2009.